

# A quantum simulator with long strings of trapped ions

Thesis submitted to the  
Faculty of Mathematics, Computer Science and Physics  
of the Leopold-Franzens University of Innsbruck  
in partial fulfillment  
of the requirements for the degree of

Doctor of Philosophy  
(Physics)

by

**Christine Maier**

Innsbruck, October 2020

This work was carried out at the

Institute for Quantum Optics and Quantum Information (IQOQI)  
of the Austrian Academy of Sciences  
Technikerstraße 21a, 6020 Innsbruck, Austria

under the supervision of

o. Univ.-Prof. Dr. Rainer Blatt and  
Dr. Christian F. Roos

---

## Abstract

This thesis presents experiments on a quantum simulator, based on up to 20 individually addressable  $^{40}\text{Ca}^+$  ions, that are confined in a linear Paul trap. The focus lies on the application of state characterization tools for large quantum systems and the demonstration of three quantum simulation experiments.

The increasing research interest in large quantum systems raises the demand on efficient tools for their characterization. The first two projects of this thesis study entanglement and state estimations of large, locally correlated quantum states. Utilizing only 27 measurement bases, we witness genuine multipartite entanglement of up to 5 neighbouring qubits in a 20-qubit system. The same set of measurement bases is used to realize the first experimental application of matrix product state tomography. We reconstruct and certify the quantum state of 14 entangled qubits, and measure an overlap of  $(74 \pm 5)\%$  between the state in the laboratory and the reconstructed state.

The third project is concerned with the quantum simulation of quantum transport in a 10-qubit network. The network nodes are represented by 10 trapped ions, coupled via long-range spin-spin interaction. Integrating an arbitrary waveform generator into our single-ion addressing setup allows us to disturb the interaction through static energy mismatch (disorder) and even with dynamic noise of practically any desired spectrum. Under strong energy disorder and in absence of noise, we observe effects of Anderson localization. At intermediate noise levels, the transport efficiency is enhanced by an effect called environment-assisted quantum transport (ENAQT). Under coupling to strong noise quantum transport is suppressed, indicating the transition to the quantum Zeno regime. We find that coherences dominate only under the localizing conditions, while in the ENAQT regime they decay quickly and the transport becomes mainly diffusive. Furthermore, we observe that the transport efficiency is strongly influenced by the spectral structure of the applied noise.

The last two projects correspond to experimental realizations of variational quantum simulation. In the first experiment we simulate the molecular ground-state potentials of  $\text{H}_2$  and  $\text{LiH}$ . We apply different trotterized transformations to map the target Hamiltonian to our ion system, compare the simulation results and study the impact of entangling gate errors. In the last simulation experiment, the target Hamiltonian is not directly mapped onto the laboratory system. Instead, the variational circuit is assembled heuristically in order to leverage the unique capabilities of our quantum simulator, and at the same time preserve the symmetries of the target model. This allows us to variationally simulate the lattice Schwinger model with up to 20 qubits - a previously intractable problem. We determine ground states and the energy gap to the

first excited state, and observe a quantum phase transition. Finally, we provide algorithmic error bars for the obtained energies and prove self-consistency of the quantum simulator. With this we address the long-standing challenge of verifying the results of a quantum simulator.

## Zusammenfassung

Diese Dissertation behandelt Experimente an einem Quantensimulator mit bis zu 20 einzel-adressierbaren  $^{40}\text{Ca}^+$  Ionen, die in einer linearen Paulfalle gefangen sind. Der Fokus liegt auf Methoden zur Zustands-Charakterisierung für große Quantensysteme, sowie der Demonstration dreier Quantensimulationsexperimente.

Mit wachsendem Forschungsinteresse an großen Quantensystemen steigt auch der Bedarf an effizienten Methoden zu deren Charakterisierung. Die ersten beiden Projekte dieser Arbeit beschäftigen sich mit der Quantifizierung von Verschränkung sowie der Zustandsbestimmung großer, lokal-korrelierter Quantenzustände. Unter Auswertung von nur 27 Messbasen gelingt uns der Nachweis von Vielteilchen-Verschränkung von bis zu fünf benachbarten Qubits in einem System von 20 Qubits. Wir verwenden dieselbe Anzahl an Messbasen, um erstmals die Methode der Matrix-Produktzustands-Tomographie experimentell anzuwenden. Damit bestimmen wir den Quantenzustand von 14 verschränkten Qubits inklusive Fehlerabschätzung und messen eine Übereinstimmung von  $(74 \pm 5)\%$  mit dem Zustand im Labor.

Das dritte Projekt zeigt die Quantensimulation von Quantentransport durch ein Netzwerk von 10 Qubits. Die Knotenpunkte des Netzwerks werden durch 10 Ionen repräsentiert, welche über langreichweitige Spin-Spin Wechselwirkungen gekoppelt sind. Diese Wechselwirkung kann mit beliebigen statischen Energiebarrieren (Unordnung) und dynamischen Rauschspektren gestört werden. Dazu erweitern wir die Einzelionen-Adressierung um einen Signalgenerator, welcher beliebige Wellenformen generieren kann. Bei starker energetischer Unordnung und in Abwesenheit von Rauschen beobachten wir Effekte der Anderson-Lokalisierung. Rauschen mittlerer Stärke steigert die Effizienz des Quantentransports – ein Effekt der als Umgebungs-unterstützter Quantentransport (ENAQT) bekannt ist. Koppelt das Netzwerk an starkes Rauschen, so sehen wir eine Unterdrückung des Quantentransports, was den Übergang in das Quanten-Zeno Regime einleitet. Kohärenzen sind fast ausschließlich im lokalisierten Fall zu beobachten, während sie im ENAQT-Regime schnell zerfallen und der Transport größtenteils diffusiv verläuft. Weiters sehen wir, dass die Effizienz des Quantentransports stark von der spektralen Struktur des Rauschens beeinflusst wird.

Die letzten vorgestellten Projekte sind experimentelle Realisierungen variationeller Quantensimulation. Im ersten Experiment simulieren wir die Potentiale molekularer Grundzustände von  $H_2$  und  $LiH$ . Wir bilden den Ziel-Hamiltonoperator mit verschiedenen digitalen Transformationsmethoden auf unser Ionensystem ab, vergleichen die Simulationsergebnisse und untersuchen die Auswirkung von Gatterfehlern. Im letzten Simulationsexperiment wird der Ziel-Hamiltonoperator hingegen nicht direkt auf das Laborsystem abgebildet. Stattdessen ist die variationelle Quantenschaltung heuristisch aufgebaut, um die einzigartigen Fähigkeiten unseres Quantensimulators zu nutzen und gleichzeitig die Symmetrien des Ziel-Hamiltonoperators zu erhalten. Diese Vorgehensweise erlaubt uns die, bisher nicht durchführbare, Quantensimulation des Schwingermodells mit bis zu 20 Qubits. Wir bestimmen die Grundzustände und den Energieabstand zum ersten angeregten Zustand und beobachten einen Quantenphasenübergang. Schließlich ermitteln wir algorithmische Fehlerbalken für die erhaltenen Energien und belegen die Selbstkonsistenz des Quantensimulators. Dies ist ein Weg, um die Ergebnisse des Quantensimulators zu verifizieren.

## List of acronyms and abbreviations

AC	alternating current
AOD	acousto-optic deflector
AOM	acousto-optic modulator
AQS	analog quantum simulation
AWG	arbitrary waveform generator
BK	Bravyi-Kitaev
CD	direct current
COM	center of mass
CPU	central processing unit
DDS	direct digital synthesizer
DFE	direct fidelity estimation
DIRECT	DIviding RECTangles
DQS	digital quantum simulation
ED	exact diagonalization
EIT	electromagnetically induced transparency
EMCCD	electron multiplying charged coupled device
ENAQT	environment-assisted quantum transport
FWHM	full width at half maximum
GME	genuine multipartite entanglement
GPR	Gaussian process regression
HF	Hartree Fock
IQOQI	Institute for Quantum Optics and Quantum Information
JW	Jordan-Wigner
LCAO	linear combinations of atomic orbitals
MLE	maximum likelihood estimation
MPS	matrix product state
MS	Mølmer-Sørensen (gate operation)
NEG	non-evaporative getter
OCBA	optimal computing budget allocation
OTOCs	out-of-time-ordered correlators
PBS	polarizing beam splitter
PG	polarization-gradient
PID	proportional–integral–derivative
PhD	philosophiae doctor (doctor of philosophy)

QFP	quantized fluorescence program
QST	quantum state tomography
RAP	rapid adiabatic passage
RF	radio frequency
RGA	residual gas analyzer
S&H	sample-and-hold
SVD	singular value decomposition
STO	Slater-type orbital
TTL	transistor-transistor logic
UCC	unitary coupled-cluster
UCCSD	unitary coupled-cluster singles and doubles
VQE	variational quantum eigensolver
VQS	variational quantum simulation



# Contents

<b>List of acronyms and abbreviations</b>	<b>iv</b>
<b>1. Introduction</b>	<b>1</b>
<b>2. Theoretical framework</b>	<b>5</b>
2.1. Quantum information science . . . . .	5
2.1.1. Quantum bit . . . . .	5
2.1.2. Quantum logic gate operations . . . . .	10
2.1.3. Quantum state tomography . . . . .	14
2.2. Trapped $\text{Ca}^+$ as qubit and pseudospin . . . . .	18
2.2.1. Atomic structure of $\text{Ca}^+$ . . . . .	18
2.2.2. Ion trapping . . . . .	21
<b>3. Quantum simulation with trapped ions</b>	<b>25</b>
3.1. Quantum simulation . . . . .	25
3.1.1. Digital quantum simulation (DQS) . . . . .	26
3.1.2. Analog quantum simulation (AQS) . . . . .	27
3.1.3. Variational quantum simulation (VQS) . . . . .	28
3.2. Laser interaction with a harmonically trapped, two-level atom . . . . .	30
3.2.1. Laser light and a two-level atom . . . . .	30
3.2.2. Experimental realization of single-qubit rotations . . . . .	32
3.2.3. Spin-motion coupling in a trapped ion . . . . .	36
3.3. Simulating effective spin-spin interactions . . . . .	39
3.3.1. Radial motional modes of long ion strings . . . . .	39
3.3.2. Spin-spin interaction with tunable interaction range . . . . .	42
<b>4. Experimental setup and technical innovations</b>	<b>51</b>
4.1. Overview . . . . .	51
4.2. 51 Doppler cooled and coherently manipulated ions . . . . .	54
4.3. Sample-and-hold laser intensity stabilization . . . . .	57
4.3.1. Single-ion addressing path . . . . .	58

4.3.2.	Collective qubit-manipulation path . . . . .	58
4.4.	Simultaneous single-ion addressing . . . . .	59
4.4.1.	The arbitrary waveform generator . . . . .	59
4.4.2.	Characterization and experimental application . . . . .	60
4.5.	Automatized addressing calibration . . . . .	63
4.6.	Sub-Doppler cooling of long ion strings . . . . .	63
4.6.1.	Electromagnetically Induced Transparency (EIT) cooling . . . . .	65
4.6.2.	Polarization-gradient (PG) cooling . . . . .	67
<b>5.</b>	<b>Characterization of quantum many-body states</b>	<b>73</b>
5.1.	Large, locally correlated quantum states . . . . .	74
5.1.1.	Correlation spread in light-like cones . . . . .	75
5.1.2.	Entanglement studies . . . . .	77
5.2.	Matrix Product State Tomography . . . . .	84
5.2.1.	Matrix Product States . . . . .	84
5.2.2.	MPS reconstruction scheme . . . . .	88
5.2.3.	Direct fidelity estimation . . . . .	94
5.3.	Conclusion . . . . .	96
<b>6.</b>	<b>Environment-assisted quantum transport</b>	<b>99</b>
6.1.	Experimental implementation . . . . .	100
6.2.	Markovian dephasing baths . . . . .	102
6.2.1.	Coherence and diffusion dynamics . . . . .	104
6.3.	Non-Markovian dephasing baths . . . . .	108
6.4.	Conclusion . . . . .	109
<b>7.</b>	<b>Variational Quantum Simulations</b>	<b>111</b>
7.1.	Quantum-classical feedback loop . . . . .	112
7.2.	Application I: Molecular ground state potentials . . . . .	114
7.2.1.	Theoretical background . . . . .	115
7.2.2.	Experimental results . . . . .	123
7.2.3.	Impact of gate imperfections and decoherence . . . . .	126
7.3.	Application II: The Lattice Schwinger Model . . . . .	131
7.3.1.	Theoretical background . . . . .	132
7.3.2.	Optimization algorithm . . . . .	136
7.3.3.	Variational Schwinger ground state search for 20 qubits . . . . .	138
7.3.4.	Quantum phase transition for 8 qubits . . . . .	141

---

7.3.5. Algorithmic error bars . . . . .	142
7.4. Conclusion . . . . .	143
<b>8. Summary and Outlook</b>	<b>147</b>
<b>Acknowledgements</b>	<b>151</b>
<b>A. List of publications</b>	<b>153</b>
<b>B. Experimental implementation of MS gates</b>	<b>155</b>
B.1. Implementation of full Mølmer-Sørensen gates . . . . .	155
B.2. Determining the gate fidelity . . . . .	157
B.3. Implementation of half-entangling gates on three ions . . . . .	159
<b>C. Composite pulse sequences for single-qubit rotations</b>	<b>161</b>
<b>D. Tutorial for simultaneous single-ion addressing with an AWG</b>	<b>163</b>
<b>E. Automated addressing calibration</b>	<b>167</b>
<b>F. Implementation of Rapid Adiabatic Passage</b>	<b>169</b>
<b>G. Classical rate equation for transport dynamics under dephasing noise</b>	<b>173</b>
<b>H. Generating Gaussian Random Processes with arbitrary spectra</b>	<b>175</b>
<b>I. Measuring local reductions for MPS tomography</b>	<b>178</b>
<b>J. Singular Value Decomposition</b>	<b>180</b>
<b>K. Hartree-Fock method for deriving molecular orbitals</b>	<b>181</b>
<b>L. Translating UCC operators to quantum gates</b>	<b>184</b>
<b>M. Estimation of the energy gap via quantum subspace expansion</b>	<b>185</b>
<b>Bibliography</b>	<b>187</b>



# 1. Introduction

Quantum theory is the most accurately tested description of the microscopic world. A deep understanding of our world at the nanoscale level allows us to explain observations and predict processes of the macroscopic, daily life. For example, in material science and condensed matter physics [1], chemistry [2] and biology [3] quantum mechanical theories are applied to characterize complex systems and even predict their behaviour. Many of these systems are very challenging to access, control and manipulate directly. As a result, many fields of research focus on efficient modelling and simulation of complex systems. However, already for systems with tens of particles quantum mechanical calculations become computationally demanding for classical computers. As an example, the simple storage of a quantum state with 69 particles requires more memory than what is available in all technological devices on earth nowadays [4]. Furthermore, the time-evolution of such a state would require the exponentiation of a  $2^{69} \times 2^{69}$  matrix.

At this point, the concept of a *Quantum Simulator* comes into play, as proposed in the early 1980's by Richard Feynman and others [5]. The idea is to employ a highly controllable, well accessible system, which itself obeys quantum mechanical laws, to model and simulate another quantum system. In other words, one utilizes the intrinsic capacity of the simulator system to contain and process an exponentially large amount of information in a relatively small amount of physical space. To date, proof-of-principle quantum simulators have been experimentally realized on various platforms such as superconducting circuits, neutral atoms, polar molecules, electrons in semiconductors, nuclear spins, photonic systems, and ions. Each experimental platform has its advantages and weaknesses with respect to scalability as well as individual control and readout [6]. Our research group's expertise lies in experimenting with laser-cooled, trapped ions, which allows us to repeatedly and reliably prepare a quantum state, to control their dynamical evolution, create entanglement and carry out quantum measurements with high efficiency. A lot of research in our group is dedicated to the development of scalable ion trap architectures as well as quantum error correction schemes. The excellent control over all quantum degrees of freedom and the comparably simple mechanism for trapping and manipulating tens of qubits, makes trapped ions a suitable platform for quantum simulators [7].

Nowadays, much research is actively aiming at the realization of quantum devices with tens of qubits [8–11], to show the first practical application in which quantum simulators outperform their classical counterparts. For many years, the general definition of quantum simulation distinguished between *digital* and *analog* quantum simulation. However, recently pioneering experiments [12–15] applied a novel approach to quantum simulation, namely Variational Quantum Simulation (VQS). This method allows for studying a wide variety of previously intractable target models, beyond the capabilities of analog and digital quantum simulation. In VQS, complex quantum states are prepared variationally, using a feedback loop between a classical optimization algorithm and our quantum computer. This approach forgoes the requirement of realizing the targeted system directly in the laboratory, and allows one to use only quantum operations that are well tailored to the available quantum hardware. However, scalability represents a key challenge also for VQS. On the one hand, scaling to larger system sizes is limited by the available quantum computing hardware. On the other hand the number of variational parameters and the number of required measurements increases rapidly with system size. Those challenges can be tackled by exploiting intrinsic symmetries of the system to be simulated, and by using advanced global optimization algorithms suited for high-dimensional and noisy problems [16]. As soon as quantum simulators succeed to solve classically intractable problems, we will be concerned with important tasks: Can we trust the result and how can we verify it? This goes hand in hand with the necessity to develop efficient tools to characterize large quantum systems.

This thesis focuses on quantum simulation, quantum state estimation, entanglement propagation and state characterization in a quantum system of up to 20 trapped ions. The first two chapters introduce the reader to the theoretical background of quantum theory and ion trapping, as well as the methods for quantum simulations with trapped ions. This is followed by a chapter which demonstrates the experimental setup and the technical innovations that pave the way to more complex quantum simulations with even longer strings of ions. The last three chapters report on experimental work in the context of quantum simulation with long ion strings. The appendix focuses on the implementation of certain gates, pulse and measurement sequences and other mathematical and experimental tools which were applied in the projects discussed in the previous chapters. In more detail, the thesis is organized as follows.

**Chapter 2** discusses the theoretical framework of quantum information science and how trapped  $^{40}\text{Ca}^+$  ions can be employed as qubits and pseudospins.

**Chapter 3** firstly introduces the three methods of quantum simulation. Secondly, it contains both the theory and experimental tools for the realization of quantum

---

simulation with trapped ions, from the bare laser-atom interaction, over the coupling to the motion of a trapped ion, to laser-induced spin-spin interactions with tunable interaction range.

**Chapter 4** describes the technical innovations to the existing setup. These innovations allow Doppler cooling and coherent manipulation of up to 51 qubits, in-sequence intensity stabilization of the addressing and the collective qubit-manipulation path, as well as simultaneous and automatized single-ion addressing. Further, the application of EIT cooling and PG cooling are presented – two efficient methods for sub-Doppler cooling of long ion strings.

**Chapter 5** gives a detailed characterization of large states in our quantum simulator. We perform measurements for constructing the reduced density matrices of all groups of three neighbouring particles. This small set of measurements is used to study the spread of correlations and to extract witnesses for genuine multipartite entanglement. The second part of this chapter focuses on MPS tomography, a scheme that can accurately estimate many-qubit states of a broad class of quantum systems with an effort that scales at most polynomially with the number of particles. We apply MPS tomography to reconstruct and verify dynamical states of our quantum simulator with up to 14 entangled and individually-controlled spins – a size beyond the practical limits of full quantum state tomography.

**Chapter 6** investigates the transport behaviour of a spin-excitation through a 10-node network of interacting qubits. We study the interplay between coherent transport, energy disorder and environment-induced Markovian noise. Not only, we find effects of Anderson localization under strong disorder. We also observe, that coupling to intermediate noise levels can increase the transport efficiency and that the transport is suppressed under strong noise due to the quantum Zeno effect. The chapter further examines the influence of the spectral structure of non-Markovian noise to the quantum transport.

**Chapter 7** introduces the quantum-classical feedback loop, building the basis of variational quantum simulation. This is followed by two experimental applications of this novel technique: The first application presents the variational simulation of molecular ground states. Using the variational quantum eigensolver method, we study molecular energy potentials of  $H_2$  and  $LiH$  as a function of the internuclear separation. We investigate the influence of measurement noise and decoherence on this trotterized way of VQS. The second part of this chapter focuses on an

alternative approach, which only uses quantum operations that are well tailored to the available quantum hardware. This method allows us to study ground states of the lattice Schwinger model for up to 20 qubits. The chapter closes targeting the long-standing challenge of verifying the results of our variational quantum simulator.

## 2. Theoretical framework

The experiments presented in this thesis are performed on a state-of-the-art quantum simulator, based on trapped calcium ions interacting with laser light. The aim of this chapter is to introduce foundations of quantum theory as well as basic concepts of our experimental system. First, I define a few technical terms from quantum information science, concerning quantum states, their manipulation and tomography. This is followed by an introduction of the atomic level structure of calcium and a theoretical discussion on trapping ions in a linear Paul trap.

### 2.1. Quantum information science

Classical information is processed with digital computers, transmitted via electronic signals and manipulated with algorithms. Analogous concepts apply to quantum information science: Quantum information can, for example, be transmitted via photons and manipulated with algorithms based on quantum logic gates. The following sections cover an introduction of pure, mixed and entangled quantum states as well as single- and multiple qubit gates. Further, I discuss methods to estimate the state of a quantum system in the laboratory.

#### 2.1.1. Quantum bit

The smallest unit of information in classical computers is represented by binary digits or *bits*. A bit can take the value of logical 0 or 1, commonly corresponding to two discrete voltage levels in a transistor. In analogy with their classical counterparts, quantum computers identify their smallest unit of information as quantum bits or *qubits*, again based on two distinguishable states, typically indicated in the Dirac notation as  $|0\rangle$  and  $|1\rangle$ , or equivalently  $|\uparrow\rangle$  and  $|\downarrow\rangle$ . These states can be quantum-mechanical properties, e.g. the polarization of photons, the excitation state of atoms or the magnetic flux of artificial structures like superconducting circuits. The key difference to classical bits is that qubits can also be in superposition states, so in both states  $|0\rangle$  and  $|1\rangle$  at the same time. The properties of a quantum bit are described by its so-called wave function  $|\psi\rangle$ .

### Pure states

For a single qubit, the wavefunction of a pure state takes the form:

$$|\psi\rangle = c_0 |0\rangle + c_1 |1\rangle, \quad (2.1)$$

with the normalization condition  $|c_0|^2 + |c_1|^2 = 1$ . The linear combination explicitly expresses that the system is in a coherent superposition of both the states  $|0\rangle$  and  $|1\rangle$ . The coefficients  $c_0$  and  $c_1$  are complex and can not be measured directly. Only repetitive measurements permit the determination of the occupation probabilities  $|c_0|^2$  and  $|c_1|^2$  of the qubit states  $|0\rangle$  and  $|1\rangle$ , respectively. For  $N$  measurement repetitions, also called measurement cycles, the corresponding uncertainty of the probability  $p \in [0, 1]$  is given by

$$\Delta p = \sqrt{\frac{p(1-p)}{N}} \quad (2.2)$$

and is known as quantum projection noise.

A useful way to write down a pure state is by identifying the two levels as column vectors  $|0\rangle = \begin{pmatrix} 1 \\ 0 \end{pmatrix}$  and  $|1\rangle = \begin{pmatrix} 0 \\ 1 \end{pmatrix}$ , such that a pure state takes the form  $|\psi\rangle = \begin{pmatrix} c_0 \\ c_1 \end{pmatrix}$ . This vector representation simplifies the formal treatment of a quantum state: a logic gate that is applied to a qubit corresponds to a rotation operation of the qubit vector on the Bloch sphere (see next paragraph), which mathematically is realized by matrices.

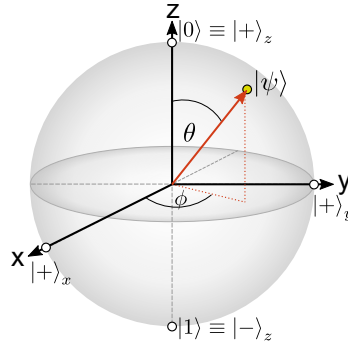


**Figure 2.1.:** The Bloch sphere is a tool to visually represent single-qubit states. A pure quantum state  $|\psi\rangle$  lies on the surface of the unit sphere and is defined by two angles  $(\theta, \phi)$ . A fully mixed state, instead, lies in the center of the sphere.

A good graphical representation of a qubit vector and its rotations is provided by the so-called *Bloch sphere*. Figure 2.1 illustrates the Bloch sphere together with a pure qubit state  $|\psi\rangle$ , mapping out a vector of length one and thus lying on the surface of the unit sphere. Each point on the Bloch sphere is specified by the polar angles  $(\theta, \phi)$

with the North pole ( $\theta = 0$ ) and the South pole ( $\theta = \pi$ ) defining the states  $|0\rangle$  and  $|1\rangle$ , respectively. Replacing the coefficients  $c_0$  and  $c_1$  by the polar angle representation, Eq. (2.1) can be rewritten as

$$|\psi\rangle = \cos\left(\frac{\theta}{2}\right) |0\rangle + e^{i\phi} \sin\left(\frac{\theta}{2}\right) |1\rangle. \quad (2.3)$$

States along other values of  $\theta$  and  $\phi$ , thereby correspond to superposition states of  $|0\rangle = |+\rangle_z$  and  $|1\rangle = |-\rangle_z$ , e.g.

$$\begin{aligned} |+\rangle_x &= \frac{1}{\sqrt{2}}(|+\rangle_z + |-\rangle_z) = \frac{1}{\sqrt{2}} \begin{pmatrix} 1 \\ 1 \end{pmatrix}, \text{ and} \\ |+\rangle_y &= \frac{1}{\sqrt{2}}(|+\rangle_z + i|-\rangle_z) = \frac{1}{\sqrt{2}} \begin{pmatrix} 1 \\ i \end{pmatrix}. \end{aligned} \quad (2.4)$$

Now, we want to extend this formalism to multiple ions: The total Hilbert-space  $\mathcal{H}^{(N)}$  for  $N$  qubits is constructed by expanding the individual single-qubit Hilbert spaces  $\mathcal{H}_n$  with the tensor product:

$$\mathcal{H}^{(N)} = \bigotimes_{n=1}^N \mathcal{H}_n = \mathcal{H}_n \otimes \mathcal{H}_{n-1} \otimes \cdots \otimes \mathcal{H}_1, \quad (2.5)$$

following the convention to count qubits from right to left, according to the computational, binary representation of numbers. Analogously, a pure state of  $N$  qubits is described by the tensor product of the individual states of the subsystems  $|\psi\rangle_n$  (see Eq. (2.1)):

$$|\psi\rangle^{(N)} = |\psi\rangle_n \otimes |\psi\rangle_{n-1} \otimes \cdots \otimes |\psi\rangle_1. \quad (2.6)$$

A state that can be written in this *fully separable* form is called a *product state*. An example for such a product state of a two-qubit system is

$$\begin{aligned} |\psi\rangle^{(2)} &= (c_{01} |0\rangle_1 + c_{11} |1\rangle_1) \otimes (c_{02} |0\rangle_2 + c_{12} |1\rangle_2) \\ &= c_{00} |00\rangle + c_{01} |01\rangle + c_{10} |10\rangle + c_{11} |11\rangle = \begin{pmatrix} c_{00} \\ c_{01} \\ c_{10} \\ c_{11} \end{pmatrix}. \end{aligned} \quad (2.7)$$

Here, the notation  $|ij\rangle$  implies that qubit 1 is in the state  $i$  and qubit 2 in state  $j$ . The linear combination, again, specifies the superposition of all four possible combinations

of states for two qubits. In the vector representation one simply extends the length of the column vector. This description can be generalized to any number of qubits such that an  $N$ -qubit register is described by  $2^N$  coefficients  $c$ . This means, that the amount of information stored in these coefficients grows exponentially with the size of the register, which is the basis of the huge benefit of quantum computation.

### Mixed states and density matrix formalism

The most general way to describe any quantum mechanical system is the *density matrix*  $\rho$  [17]:

$$\rho = \begin{pmatrix} \langle |c_1|^2 \rangle & \langle c_1 c_2^* \rangle \\ \langle c_1^* c_2 \rangle & \langle |c_2|^2 \rangle \end{pmatrix} = \sum_i p_i |\psi_i\rangle \langle \psi_i|. \quad (2.8)$$

For a conceptual explanation, consider an ensemble of  $N$  identical two-level particles, with the two levels again represented by  $|0\rangle$  and  $|1\rangle$  and their occupation probabilities  $|c_0|^2$  and  $|c_1|^2$ . The  $\langle \bullet \rangle$  in Eq. (2.8) indicates the average value for the ensemble and  $p_i$  the probability of finding the quantum system in a pure state  $|\psi_i\rangle$ , with  $\sum_i p_i = 1$ . Expression (2.8) allows us to describe not only pure superposition states, as in Eq. (2.1), but also statistical mixtures of states  $|0\rangle$  and  $|1\rangle$ . An ensemble with  $N_1$  particles in state  $|0\rangle$  and  $N_2$  particles in state  $|1\rangle$  is an example for a fully mixed state, described by:

$$\rho_{\text{mix}} = \begin{pmatrix} N_1/N & 0 \\ 0 & N_2/N \end{pmatrix}. \quad (2.9)$$

Here, each individual particle either has  $|c_1| = 1$  and  $|c_2| = 0$  or vice versa. For particles in coherent superposition states, instead, both  $|c_1|$  and  $|c_2|$ , and thus  $\langle c_1 c_2^* \rangle$  and  $\langle c_1^* c_2 \rangle$ , are non-zero. Therefore, non-zero off-diagonal elements in the density matrix identify the presence of quantum coherences in a system. A parameter which refers to the degree of mixture of a quantum state is e.g. the purity  $P(\rho) = \text{Tr}(\rho^2)$ , with  $P \in [\frac{1}{2^N}, 1]$ , where  $P(\rho) = 1$  refers to a pure state and  $P(\rho) = \frac{1}{2^N}$  to a fully mixed state of an  $N$ -qubit system.

With the above mentioned properties of pure states, the different  $|\psi_i\rangle$  in Eq. (2.8) represent an orthonormal basis of a vector space called *Hilbert space*  $\mathcal{H}$ . A convenient set of orthonormal bases is the Pauli group

$$\mathbb{1} = \begin{pmatrix} 1 & 0 \\ 0 & 1 \end{pmatrix}, \quad \sigma_x = \begin{pmatrix} 0 & 1 \\ 1 & 0 \end{pmatrix}, \quad \sigma_y = \begin{pmatrix} 0 & i \\ -i & 0 \end{pmatrix}, \quad \sigma_z = \begin{pmatrix} 1 & 0 \\ 0 & -1 \end{pmatrix}. \quad (2.10)$$

With this, the density matrix of a single-qubit, as defined in Eq. (2.1), takes the form

$$\rho = \frac{1}{2}(\mathbb{1} + \vec{n} \cdot \vec{\sigma}), \quad \text{with } \vec{n} = \begin{pmatrix} \langle \sigma_x \rangle \\ \langle \sigma_y \rangle \\ \langle \sigma_z \rangle \end{pmatrix} \quad \text{and } \vec{\sigma} = \begin{pmatrix} \sigma_x \\ \sigma_y \\ \sigma_z \end{pmatrix}, \quad (2.11)$$

where  $\langle \sigma_i \rangle = \text{Tr}(\sigma_i \rho)$  denotes the expectation value of the density matrix for the respective Pauli operator  $\sigma_i$ . This closes the loop to the Bloch vector representation of a quantum state: the components of the vector correspond to projections onto the three axis and are equivalent to the expectation values  $\langle \sigma_i \rangle$ . For example, the state  $|+\rangle_x = \frac{1}{\sqrt{2}}\begin{pmatrix} 1 \\ 1 \end{pmatrix}$  as defined in Eq. (2.4), corresponds to the eigenstate with eigenvalue +1, of the  $\sigma_x$  Pauli operator.

Consider dividing a general quantum system  $\rho$  into two subsystems  $A$  and  $B$ . The state of system  $A$  is then defined as the partial trace of  $\rho$  over the basis states  $|j\rangle_B$  of system  $B$

$$\rho_A = \sum_j \langle j|_B \rho |j\rangle_B = \text{Tr}_B \rho, \quad (2.12)$$

where  $\rho_A$  is also called the *reduced density matrix* of  $\rho$  on subsystem  $A$ . In words, we “trace out” system  $B$  to be left with the reduced state on  $A$ .

## Entanglement

One of the most counter-intuitive concepts of the quantum world is *entanglement*, a feature which is impossible to simulate within any classical formalism. Formally, an entangled state is defined as a state which cannot be decomposed into a product of states of its constituents, as in Eq. (2.7). The total Hilbert space, however, is the product Hilbert space of the subsystems. A system is in a fully entangled state (with respect to all its subsystems), if and only if all bipartite partitions generate mixed reduced density matrices [18], as defined in Eq. (2.12). A popular example for maximally entangled states in a two-qubit system are the Bell states:

$$|\Phi^\pm\rangle = \frac{1}{\sqrt{2}}(|00\rangle \pm |11\rangle), \quad |\Psi^\pm\rangle = \frac{1}{\sqrt{2}}(|01\rangle \pm |10\rangle). \quad (2.13)$$

The entangled, non-decomposable, form of the Bell states implies that the measurement of the state of one qubit immediately reveals the state in which the other qubit is. Einstein describes this property a “spooky action at a distance”.

The characterization and measurement of entanglement is a wide field of current research and is also addressed in Chapter 5 of this thesis. In principle, one can extract

any information, including entanglement properties, from the full density matrix of a system. An example for an entanglement measure which is relevant with respect to the experiments presented in this thesis is the *bipartite negativity*  $\mathcal{N}(\rho)$ . While it is difficult to verify entanglement between several subsystems, the negativity is an efficient tool to verify entanglement in a bipartite mixed state  $\rho_{AB}$ , consisting of the subsystems  $\rho_A$  and  $\rho_B$ .

$$\mathcal{N}(\rho_{AB}) = \frac{\|\rho^{TA}\|_1 - 1}{2} = \left| \sum_n \mu_n \right|, \quad (2.14)$$

where  $\mu_n$  are the negative eigenvalues of  $\rho^{TA}$ , the partial transpose of  $\rho_{AB}$ . Negative eigenvalues  $\mu_n$  are a distinct feature of entanglement between  $\rho_A$  and  $\rho_B$ , while  $\mathcal{N}(\rho_{AB})$  vanishes for unentangled states [19]. So, if and only if  $\mathcal{N}(\rho_{AB}) > 0$  then the subsystems  $\rho_A$  and  $\rho_B$  are entangled.

With increasing number of qubits in a system it gets soon impossible to reconstruct its full density matrix (see Subsection 2.1.3). Therefore it is often preferable to describe a quantum state by other means, for example by its *fidelity*, which quantifies the overlap of a given quantum state with another known quantum state.

### 2.1.2. Quantum logic gate operations

The processor of a classical computer performs millions of binary logic gate operations (like NOT or NAND) on single or two bits of information. A computer program determines how to link the gate operations to a logical circuit in order to perform the requested task. Finally, the results are output as a new set of bits.

The basic functioning of a quantum computer is much the same. Quantum logic gate operations (in the following abbreviated as “gates”) are connected to quantum circuits, which carry out operations on an input register of  $N$  qubits. Finally, measurements on the new set of output qubits are performed to obtain a set of  $N$  classical bits of information. At this stage it appears that quantum computation has no advantage over its classical counterpart. However, the key point is that with an input register of  $N$  qubits the quantum processor effectively manipulates  $2^N$  amplitude coefficients. For specific tasks and clever programming, a quantum computer can therefore process and obtain information much more efficient than a classical machine. A detailed presentation of quantum algorithms would go beyond the scope of this thesis, but I want to cite the first algorithm which demonstrated that a quantum computer can be exponentially faster than a classical one, namely Deutsch’s algorithm [20]. The simulation of complex quantum systems is another class of tasks which benefits from the use of a quantum computer (in this context also called *quantum simulator*). A more detailed discussion

on quantum simulation follows in Chapter 3.

Just as with its classical counterpart, it turns out that one only needs a very small number of quantum logic gates (a few single-qubit gates and one multiple-qubit gate) to perform any quantum computation task [17]. In the following I give a few examples for the most relevant quantum logic gates with respect to the projects presented in this thesis.

### Single- qubit gate operations

Following the column vector representation of a qubit, a single-qubit gate is described by a  $2 \times 2$  matrix  $\mathbf{M}$

$$\begin{pmatrix} c'_0 \\ c'_1 \end{pmatrix} = \begin{pmatrix} M_{11} & M_{12} \\ M_{21} & M_{22} \end{pmatrix} \begin{pmatrix} c_0 \\ c_1 \end{pmatrix}. \quad (2.15)$$

The requirement on matrix  $\mathbf{M}$  is unitarity  $\mathbf{M}\mathbf{M}^\dagger = \mathbb{1}$ , which implies that all quantum gates must be reversible [17]. The effect of a single-qubit gate is to change the amplitude coefficients  $c_i$  in the qubits wave function such that

$$|\psi\rangle = c_0 |0\rangle + c_1 |1\rangle \xrightarrow{\text{gate } U} |\psi'\rangle = c'_0 |0\rangle + c'_1 |1\rangle. \quad (2.16)$$

The change of a qubit's amplitude coefficients corresponds to altering the position of the vector which represents the qubit on the Bloch sphere (Fig. 2.1). In other words, gate operations amount to rotations of the qubit Bloch vector.

The Pauli matrices defined in Eq. (2.10) provide a convenient way to describe rotations around the axes  $k = \{x, y, z\}$  of the Bloch sphere. The Pauli eigenstates  $|\pm\rangle_k$  (see Eq. 2.4) correspond to the points where the respective axis  $k$  intersects the surface of the Bloch sphere. A rotation by an amount  $\theta$  about an axis  $k$  can thereby be expressed as rotation operator  $R_k(\theta) = \cos\left(\frac{\theta}{2}\right) \mathbb{1} - i \sin\left(\frac{\theta}{2}\right) \sigma_k$ . More generally, a rotation by  $\theta$  about an arbitrary unit vector  $\vec{n} = (n_x, n_y, n_z)$  is given by [21]

$$R_{\vec{n}}(\theta) = e^{-i\frac{\theta}{2}\vec{n}\vec{\sigma}} = \cos\left(\frac{\theta}{2}\right) \mathbb{1} - i \sin\left(\frac{\theta}{2}\right) (n_x\sigma_x + n_y\sigma_y + n_z\sigma_z). \quad (2.17)$$

Furthermore, it follows from Euler's theorem, that it is possible to decompose an arbitrary single qubit operator  $U$  into a concatenation of three rotations:

$$U = e^{i\alpha} R_z(\delta) R_y(\gamma) R_z(\beta), \quad (2.18)$$

where  $R_z$  and  $R_y$  are rotations about the  $y$ - and  $z$ -axes by the angles  $\beta, \gamma, \delta$ . The

global phase shift  $\alpha$  can be discarded, since the absolute phase of a wave function is not observable.

To give an example, a  $\theta = \pi/2$  rotation around the  $x$ -axis, applied to the basis state  $|\psi\rangle = |1\rangle$  brings the qubit to the coherent superposition state  $|+\rangle_y = \frac{1}{\sqrt{2}}(|0\rangle + i|1\rangle)$ :

$$\begin{aligned} R_x(\pi/2) |\psi\rangle &= e^{-i\frac{\pi}{4}\sigma_x} |1\rangle = \left[ \cos\left(\frac{\pi}{4}\right) \mathbb{1} - i \sin\left(\frac{\pi}{4}\right) \sigma_x \right] \begin{pmatrix} 0 \\ 1 \end{pmatrix} \\ &= \frac{1}{\sqrt{2}} \begin{pmatrix} 1 & -i \\ -i & 1 \end{pmatrix} \begin{pmatrix} 0 \\ 1 \end{pmatrix} = \frac{1}{\sqrt{2}} \begin{pmatrix} -i \\ 1 \end{pmatrix} = \frac{e^{-i\pi/2}}{\sqrt{2}} \begin{pmatrix} 1 \\ i \end{pmatrix} \stackrel{\text{Eq. (2.4)}}{=} |+\rangle_y. \end{aligned}$$

Another important gate maps the basis state  $|0\rangle$  onto the superposition state  $|+\rangle_x = \frac{1}{\sqrt{2}}(|0\rangle + |1\rangle)$  and is referred to as Hadamard gate  $H$ :

$$H = e^{-i\frac{\pi}{2}\left(\frac{\sigma_x + \sigma_z}{\sqrt{2}}\right)} = \frac{1}{\sqrt{2}} \begin{pmatrix} 1 & 1 \\ 1 & -1 \end{pmatrix}. \quad (2.19)$$

Considering the example where the qubit is represented by a two-level atom, arbitrary single-qubit gates can be performed by resonant light-atom interactions, where the amplitude and phase of the electromagnetic pulse determine the angles of the vector rotation and thereby the applied gate (details follow in Section 3.2.1).

### Multiple- qubit gate operations

Together with the arbitrary single-qubit operations, defined in Eq. (2.17), only one multi-qubit gate is necessary in order to perform any quantum computation task [17, 22]. The Mølmer-Sørensen (in the following abbreviated as MS) gate is an example for such a multi-qubit operation [23–25]:

$$U_{\text{MS}}(\phi) = e^{-i\frac{\pi}{4}S_\phi^2} = \exp\left(-i\frac{\pi}{4}\sum_{i<j}\sigma_\phi^{(i)}\otimes\sigma_\phi^{(j)}\right), \quad (2.20)$$

where  $\sigma_\phi^{(i)} = \cos(\phi)\sigma_x^{(i)} + \sin(\phi)\sigma_y^{(i)}$ . The angle  $\phi$  defines the rotation axis, and  $\sigma_x^{(i)}$  and  $\sigma_y^{(i)}$  denote the corresponding Pauli operator acting on qubit  $i$ . The effect of the MS gate is to drive collective state rotations of the involved qubits, as shown in the following example: Consider two qubits, starting in the state  $|\psi\rangle = |1\rangle \otimes |1\rangle = |11\rangle = \begin{pmatrix} 0 \\ 0 \\ 0 \\ 1 \end{pmatrix}$ .

Applying the MS gate with  $\phi = 0$  generates an entangled state:

$$\begin{aligned}
 U_{\text{MS}}(\pi/2, 0) |11\rangle &= e^{-i\frac{\pi}{4}\sigma_x^{(1)}\sigma_x^{(2)}} |11\rangle = \frac{1}{\sqrt{2}} \begin{pmatrix} 1 & 0 & 0 & -i \\ 0 & 1 & -i & 0 \\ 0 & -i & 1 & 0 \\ -i & 0 & 0 & 1 \end{pmatrix} \begin{pmatrix} 0 \\ 0 \\ 0 \\ 1 \end{pmatrix} \\
 &= \frac{1}{\sqrt{2}} \begin{pmatrix} -i \\ 0 \\ 0 \\ 1 \end{pmatrix} = \frac{1}{\sqrt{2}} (|11\rangle - i|00\rangle). \tag{2.21}
 \end{aligned}$$

The advantage of the MS gate over some other entangling gates such as the Cirac-Zoller gate [26], is its insensitivity to the motional state of the qubit [27]. A more thorough description of the effects of the MS gate is given in Section 3.3.2 and instructions for the experimental implementation of MS gates in our setup are given in Appendix B.

### Decoherence and error correction

The manipulation of *coherent* superposition states builds the basis for reliable quantum computation. Uncontrolled coupling to the environment introduces noise that triggers random behaviour. For example, thermal motion of surrounding particles could cause a qubit to flip its logical state randomly and thereby lose the stored quantum information [17]. This fragility of qubits is due to what is called *decoherence*. Traditionally we distinguish between two types of decoherence processes, quantified by the time constants  $T_1$  and  $T_2$ : (i) The  $T_1$  process describes coherence loss due to spontaneous, stochastic decay, or “relaxation”, of the excited qubit state. The relaxation rate is governed by the lifetime of the excited level. (ii) The  $T_2$  constant describes a dephasing process, where the phase of the qubits wavefunction is scrambled e.g. due to laser intensity noise.

The number of gates that can be performed before decoherence destroys superposition states, is given by  $N_G = \frac{\min(T_1, T_2)}{T_G}$ , with  $T_G$  denoting the required time to perform the gate operation. Table 2.1 compares  $N_G$  for a few physical systems commonly used for quantum computation. Apparently a trade-off has to take place: On the one hand a strongly isolated quantum system, which barely interacts with its environment, is preferable. On the other hand such a system is unsuitable for quantum computation, as we have to efficiently interact with it to perform gate operations. Therefore, the development of fault-tolerant quantum computation protocols has drawn great attention

System	$T_2$ (s)	$T_G$ (s)	$N_G$ (s)
Trapped ions [28]	60	$10^{-6}$	$10^6$
Superconducting flux qubits [29]	$10^{-4}$	$10^{-8}$	$10^4$
Quantum dots [30]	$10^{-4}$	$10^{-7}$	$10^3$

**Table 2.1.:** Decoherence times  $T_2$ , two-qubit gate operation times  $T_G$  and number of gate operations  $N_G$  before decoherence occurs. The listed physical systems are potentially scalable and therefore commonly considered as suitable for quantum computation [17].

over the last two decades: Analogously to classical error-checking protocols, there exist quantum error correction algorithms to correct for decoherence effects [31, 32]. The idea is to use additional *ancilla* qubits, and to apply *syndrome* measurements to retrieve information about a potential error, without disturbing the quantum information in the encoded state. The syndrome measurement tells us not only whether a qubit has decohered but also which qubit was corrupted and in which way (state or phase flip). Based on this, correction operations can be applied to reconstruct the original quantum state. Experimental demonstrations of quantum error correction in ion trap systems have already been carried out, e.g. in Refs. [33, 34].

### 2.1.3. Quantum state tomography

*Quantum state tomography* denotes the experimental determination of a density matrix by performing measurements on the system, without any initial information about it. The knowledge of the precise density matrix allows one to answer any question about the state of a quantum system (e.g. regarding entanglement or purity). Full state tomography is based on the concept given in Eq. (2.11) for the case of a single qubit: Any quantum state can be decomposed into a sum of operators  $\mathcal{O}$  (which form a basis of the Hilbert space), that are multiplied by their respective expectation values. Typically, the Pauli group is chosen as the set of orthonormal bases of the Hilbert space:  $\mathcal{O} \in \{\sigma_x, \sigma_y, \sigma_z\}$ . Therefore, by measuring the expectation values  $\langle \sigma_i \rangle = \text{Tr}(\sigma_i \rho)$  for the respective Pauli operators, the density matrix  $\rho$  of the quantum system can be reconstructed. For an  $N$ -qubit system this amounts to applying  $3^N$  measurement settings, which is highly demanding for large systems.

### Linear reconstruction

A straight-forward linear reconstruction of the quantum state

$$\rho_{\text{lin}} = \frac{1}{2} (\mathbb{1} + \langle \sigma_x \rangle \sigma_x + \langle \sigma_y \rangle \sigma_y + \langle \sigma_z \rangle \sigma_z) \quad (2.22)$$

is mathematically correct, however, experimentally it is not possible to determine the expectation values, and thereby the quantum state, with absolute precision. For example, to estimate  $\langle \sigma_x \rangle$  the observable  $\sigma_x$  is measured a large, but only finite number of times,  $m$ , and the outcomes  $x_1, x_2, \dots, x_m$  are all equal to  $+1$  or  $-1$ . For large  $m$ , the distribution of the outcomes is approximately Gaussian, with the mean  $\sum_i x_i/m$  being an estimate for  $\langle \sigma_x \rangle$  [21]. The related uncertainty is determined by quantum projection noise, given in Eq. (2.2) and imperfect experimental control. Employing Monte-Carlo simulations [35], the mean density matrix and its standard deviation is derived. A drawback of the linear reconstruction method is that the obtained density matrices may not necessarily be physical (i.e. result in normalized and positive hermitian matrices). Fig. 2.2 a) visualizes the problem for a single-qubit quantum state: In particular for pure states, the finite number of measurements and imperfect experimental control may result in unphysical density matrices with negative eigenvalues, i.e.  $\text{Tr}(\rho^2) > 1$ .

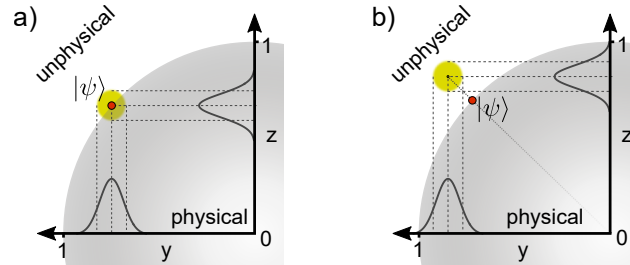


**Figure 2.2.:** Sector of a Bloch sphere (gray) with two axes of coordinates. A physical quantum state has to lie on (red point) or within the Bloch sphere. The coordinates of the point correspond to the states expectation values of  $\sigma_x, \sigma_y, \sigma_z$ . **a)** Projection noise and imperfect experimental control induce uncertainties on the expectation values (yellow halo). A bare linear reconstruction may return a density matrix which lies outside the Bloch sphere. **b)** Simply restricting the reconstruction of a quantum state to a physical density matrix may return a state without overlap with the actually measured state.

### Maximum likelihood reconstruction

One solution to the possible predictions of unphysical density matrices from a simple linear reconstruction is the *maximum likelihood estimation* (MLE) [36]. It implements the constraint on the estimated density matrix  $\rho_{\text{MLE}}$  to be physical, directly in the

evaluation: A likelihood function  $\mathcal{L}$  is maximized, to find a physical density matrix which fits the measured data best [37, 38]

$$\rho_{\text{MLE}} = \arg \max_{\rho} \{\mathcal{L}(\mathcal{M}, \rho) \mid \rho \geq 0\}. \quad (2.23)$$

Here,  $\mathcal{L}(\mathcal{M}, \rho) = \prod_i (\text{Tr}[M_i \rho])$  denotes the likelihood of the semipositive density matrix  $\rho$  to generate the measured data  $\mathcal{M} = \{M_1, M_2, M_3, \dots, M_m\}$ , with  $M_i$  representing the operator of the  $i$ -th observation. Since  $\mathcal{L}$  has a unique local maximum at  $\rho_{\text{lin}}$ , it can be shown that if  $\rho_{\text{lin}}$  lies outside of the closed region of physical states,  $\rho_{\text{MLE}}$  must lie on the boundary of that region (see Fig. 2.3) [38]. In other words, MLE is a minimal fix for tomography, returning the physical state that is closest to  $\rho_{\text{lin}}$ . MLE is the commonly

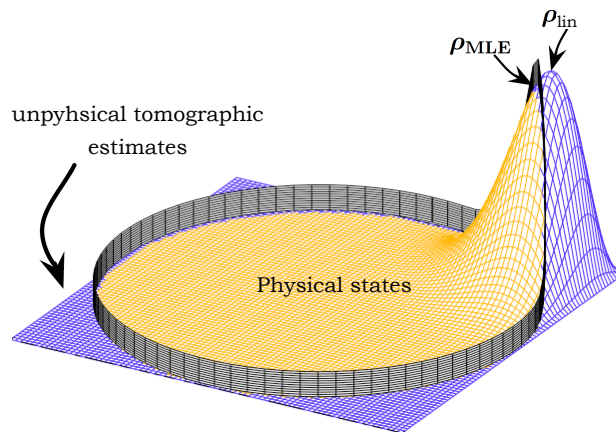


**Figure 2.3.:** Comparison of single-qubit state estimations reconstructed via different methods. The shown domain is a cross section of the Bloch sphere (e.g. along the equator). The density matrix  $\rho_{\text{lin}}$ , resulting from straight-forward linear reconstruction, lies in the unphysical area (blue). The constrained state  $\rho_{\text{MLE}}$ , reconstructed via MLE, lies on the boundary between the physical (orange) and unphysical region. (Picture adapted from Ref. [38])

used tomography method in Innsbruck, even though it has some flaws; e.g. it typically yields a density matrix estimate with one or more zero eigenvalues. Such an estimate implies that some measurement outcomes are impossible, which can not be justified by any finite amount of data.

An alternative tomography procedure, also not without drawback, is Bayesian mean estimation (BME). In contrast to MLE, it does not search a unique maximally likely state, but additionally considers other states that are slightly less plausible. The basic principle is that the final estimate is an average over all states which are consistent with the data, weighted by their likelihood. Further discussion can be found in Refs. [38, 39].

### Matrix Product State tomography

Experimentally, it is highly demanding to obtain the full density matrix of a multiple-qubit system, as the matrix grows exponentially with the number of qubits. Therefore, both full tomography methods discussed above soon become impractical for many-body systems with more than a few qubits. An alternative approach is Matrix Product State (MPS) tomography [40], which accurately estimates many-qubit states of a broad class of quantum systems, with an effort that increases at most polynomially with the number of constituents [41].

MPS tomography is suited for states in which significant quantum correlations only exist over a maximum distance. The information required to identify such states is typically accessible locally. MPS tomography recognizes this property and requires only measurements on subsets of qubits of the same neighbourhood, in order to estimate the state in the laboratory. Such locally correlated states are e.g. generated during the dynamical evolution of systems with short-ranged interactions. In Chapter 5 I present the MPS tomography scheme and its experimental application in more detail. Note that the applied protocol expects pure states and also returns pure state estimates. The scheme is in principle also applicable to mixed states, but without the possibility of certifying the estimated states.

### Quantum compressed sensing

Quantum compressed sensing is another technique to reconstruct a quantum state by measuring only a subset of all  $3^N$  observables. This mitigates the unfavourable scaling of the measurement and computation effort with increasing system size. The method relies on “compressed sensing”, a technique that is widely used in the field of classical data analysis with applications in image processing, seismology, wireless communication and many more [42]. This technique recovers a vector with only a few non-zero entries in a specified basis, using a small number of measurements that are linear functions of the vector entries. Choosing a small number of measurements randomly (in a certain precise sense), allows one to uniquely determine the vector by an efficient convex optimization algorithm [43, 44].

Quantum compressed sensing is most effective on density matrices with a small number of dominating eigenvalues – this is, quantum states which are close to pure states. This is usually the case, as most quantum information experiments apply near-unitary processes to pure states, which again generate quantum states close to pure states, described by a low-rank density matrix. The reconstruction of such a matrix with

dimension  $d$  and rank  $r \ll d$ , requires only  $\mathcal{O}(rd \log^2(d))$  measurement settings. Despite the still exponential scaling, the improvement can be considerable, compared to standard full tomography methods that require  $d^2$  parameters. The acquired data is also used to certify that the state is close to pure, so no a priori assumptions are required [42]. Quantum compressed sensing protocols have been experimentally implemented on diverse quantum platforms to characterize quantum states [45, 46] as well as quantum gates [47, 48].

### Direct Fidelity Estimation

In contrast to quantum state tomography, *state verification* checks by how much an arbitrary experimental state overlaps with another given quantum state. While state verification requires less resources than tomography and may be up to exponentially faster [49, 50], a priori assumptions are necessary to find a reasonable state to which the overlap is measured. An example for a verification method is *direct fidelity estimation*, which is discussed in Section 5.2.3, on the basis of an experiment.

## 2.2. Trapped $\text{Ca}^+$ as qubit and pseudospin

Our experimental platform is based on  $^{40}\text{Ca}^+$  ions confined in a linear Paul trap. In the following I will present the atomic structure of the singly ionized calcium ion and explain why it represents a suitable qubit/pseudospin<sup>1</sup> for quantum computation/simulation. The chapter closes with a discussion on the techniques and consequences of confining ions in a linear Paul trap.

### 2.2.1. Atomic structure of $\text{Ca}^+$

$^{40}\text{Ca}$  is an alkaline-earth element with two outer valence electrons in the 4s shell and no nuclear spin, so no hyperfine splitting. The singly charged  $^{40}\text{Ca}^+$  ion has a single outer valence electron and therefore a hydrogen-like electronic level structure. The three lowest orbitals, shown in Fig. 2.4 a), can be coupled with commercially available solid state lasers. The spectroscopic notation  $n^{(2S+1)}L_J$  used here, defines an electronic level by its quantum numbers  $n, L, S, J$ . Here,  $n$  is the principal quantum number and the capital letter  $L$  designates the electronic orbital<sup>2</sup>,  $(2S+1)$  denotes the spin multiplicity,

<sup>1</sup>The terms qubit and pseudospin-1/2 are equivalent, but are typically used in the context of quantum computation and simulation, respectively.

<sup>2</sup>The electronic orbitals are identified with quantum numbers  $L$  or capital roman letters  $L$ :  
 $0 \hat{=} S, 1 \hat{=} P, 2 \hat{=} D, 3 \hat{=} F \dots$

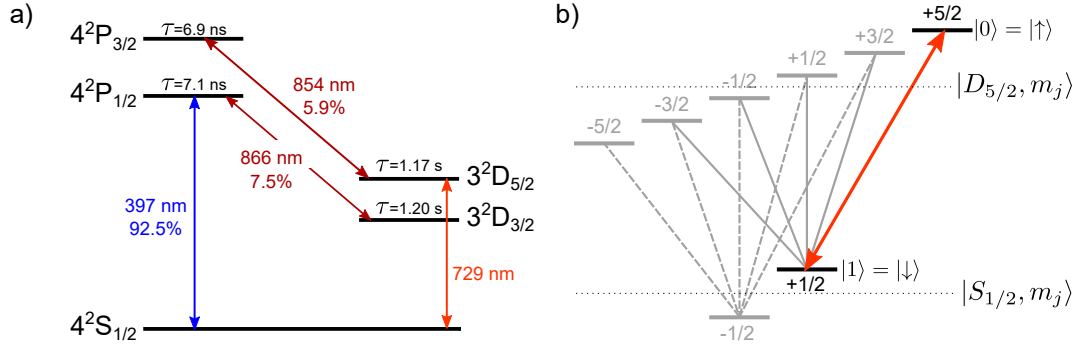


**Figure 2.4.: Reduced energy level scheme of  $^{40}\text{Ca}^+$ .** **a)** Schematic level scheme with wavelengths and decay probabilities (in %) for the relevant transitions with regards to the experiments presented in this thesis. Doppler cooling and state detection are carried out on the fast cycling dipole transition  $S_{1/2} \leftrightarrow P_{1/2}$  with 397 nm laser light. The qubit is encoded in two Zeeman sublevels of the  $S_{1/2} \leftrightarrow D_{5/2}$  quadrupole transition with a linewidth of  $\Gamma/(2\pi) = 136$  mHz and is manipulated with 729 nm laser light. Two infrared lasers pump out the metastable D-states to prevent population trapping. **b)** A magnetic field of about 4 G lifts the degeneracy of the Zeeman states, identified by the quantum numbers  $m_j$ . In all experiments discussed in this thesis the qubit is encoded in the states  $|1\rangle = |\downarrow\rangle \equiv |S_{1/2}, m_j = 1/2\rangle$  and  $|0\rangle = |\uparrow\rangle \equiv |D_{5/2}, m_j = 5/2\rangle$ .

in which the spin quantum number  $S$  for a system with a single valence electron is  $S = 1/2$ . The spin-orbit interaction<sup>3</sup> induces energy shifts such that a level with the orbital quantum number  $L$  splits into two sublevels  $J = L \pm 1/2$ . The electronic levels addressed within this thesis are distinguishable even without mentioning the quantum numbers  $n$  and  $S$ , which justifies an abbreviated notation:  $n^{(2S+1)}L_J \rightarrow L_J$ , e.g.  $4^2S_{1/2} \rightarrow S_{1/2}$ .

Additionally, an external magnetic field induces the so-called Zeeman effect, lifting the degeneracy of each electronic level, which is split into  $m_j$  sublevels ranging from  $-J$  to  $+J$  (Fig. 2.4 b)). The corresponding energy shift for a magnetic field  $B_z$  along an axis  $z$  (the quantization axis) is given by

$$\Delta E = -\mu_z B_z = g_J \mu_B m_j B_z. \quad (2.24)$$

The  $z$ -component of the magnetic dipole,  $\mu_z$ , of the atom is given by the Landé factor  $g_J = 1 + \frac{J(J+1)+S(S+1)-L(L+1)}{2J(J+1)}$ , the Bohr magneton  $\mu_B$  and the number of the corresponding Zeeman level  $m_j$ . As an example, for the magnetic field typically used in our experiment  $B_z = 4.18$  G, the ground state  $S_{1/2}$  splits into two sublevels with  $m_j = \pm 1/2$  with a frequency difference of  $\Delta_S = 11.7$  MHz.

<sup>3</sup>This can be understood as the interaction between the magnetic field induced by the motion of the electron in its orbit, and the magnetic dipole associated with the spin of the electron.

Considering the *criteria of David P. DiVincenzo* [51], trapped  $^{40}\text{Ca}^+$  ions represent suitable candidates for quantum computation and simulation:

1. **Well characterized qubits:** An optical qubit/pseudospin-1/2 can be encoded in the ground state  $|1\rangle = |\downarrow\rangle \equiv |S_{1/2}, m_j = 1/2\rangle$  and the metastable excited state  $|0\rangle = |\uparrow\rangle \equiv |D_{5/2}, m_j = 5/2\rangle$ . The latter has a lifetime<sup>4</sup> of  $\tau = 1.168(7)\text{ s}$  [53], which is 4 – 5 orders of magnitude longer than the duration of typical quantum gates. Although this stretched state is more sensitive to magnetic field noise, we use it for most experiments presented in this thesis as it has two major advantages over other Zeeman levels: (i) Its motional mode spectrum has less overlap with other levels. This reduces the chance of undesired coupling to other levels, which becomes important in spin-spin interaction experiments with many ions. (ii) It can be efficiently used for sideband cooling. More detailed considerations on spin-spin interactions and motional mode coupling can be found in Sections 3.2.3 and 3.3.

2. **The ability to initialize a simple fiducial state:** The fast-cycling electric dipole transition  $S_{1/2} \leftrightarrow P_{1/2}$  at 397 nm is used to perform Doppler cooling [54, 55], aided by a laser beam at 866 nm which repumps population from the metastable  $D_{3/2}$  state back into the cooling cycle. The minimum achievable temperature (Doppler limit) for  $^{40}\text{Ca}^+$  is  $T_D \approx 0.5\text{ mK}$ .

Sideband cooling [56, 57] to the motional ground state is achieved by exciting the red sideband of the  $|D_{5/2}, m_j = 5/2\rangle$  level (see Section 3.3.1) and quenching on the  $D_{5/2} \leftrightarrow P_{3/2}$  transition with 854 nm light.

Finally, the electronic state can be initialized reliably using the frequency-resolved 729 nm-optical pumping technique, which transfers population from the  $|S_{1/2}, m_j = -1/2\rangle$  to the  $|D_{5/2}, m_j = 3/2\rangle$  state. Following the dipole selection rules, 854 nm light pumps the population to the  $|P_{3/1}, m_j = +3/2\rangle$  and  $|P_{3/1}, m_j = +1/2\rangle$  levels from where it decays predominantly to the  $|S_{1/2}, m_j = 1/2\rangle$  ground state. In our experiment, the  $|S_{1/2}, m_j = 1/2\rangle$  state is initialized after repeating this pumping cycle for 200  $\mu\text{s}$ .

3. **A universal set of quantum gates** can be realized with arbitrary single-qubit rotations (Section 3.2.2) and the MS entangling gate (Section 3.3), with typical

---

<sup>4</sup>Defining the qubit on a quadrupole transition reduces the spontaneous decay rate of the excited qubit state (and therefore extends its lifetime) by a factor  $f \approx (ka_0)^2$  compared with a dipole transition [52]. Here,  $k = 2\pi/\lambda$  is the wave number and  $a_0$  is the Bohr radius.

gate operation times between  $2 - 100 \mu\text{s}$ .

4. **Coherence times much longer than the gate operation time:** In our experiment, the transition between the qubit states is driven using a laser at  $729 \text{ nm}$  with a linewidth of  $\Delta\nu_{\text{FWHM}} = 12 \text{ Hz}$ , measured over  $50 \text{ s}$  [58]. Together with Samarium-Cobalt permanent magnets<sup>5</sup> defining our quantization axis, the qubit has a coherence time of over  $60 \text{ ms}$  [60].
5. **Qubit measurement capability:** The quantum state can be detected with almost unity fidelity [61], using the electron shelving technique [62]: If the electron populates the  $S_{1/2}$  state, a  $397 \text{ nm}$  laser can drive the strong  $S_{1/2} \leftrightarrow P_{1/2}$  transition. Additional  $866 \text{ nm}$  light repumps on the  $D_{3/2} \leftrightarrow P_{1/2}$  transition and causes millions of  $397 \text{ nm}$ -photons to be scattered per second – the ion fluoresces. If the electron populates the  $D_{5/2}$  state instead, the  $397 \text{ nm}$  laser can not drive any transition and no photons will be scattered – the ion remains dark. A back-lit electron multiplying charged coupled device (EMCCD) camera detects the fluorescence, and is able to spatially resolve the individual emitters simultaneously such that the actual quantum state of the entire string can be identified. Qubit rotations prior to the state detection allow us to measure quantum states in arbitrary bases.

More details on Doppler cooling, state detection, optical pumping and  $^{40}\text{Ca}^+$  spectroscopy performed in our experiment can be found in C. Hempel’s PhD thesis [63].

### 2.2.2. Ion trapping

The first step to confine  $^{40}\text{Ca}$  in an ion trap is to ionize them in a two-step photoionization process: We run a current of  $\sim 2.6 \text{ A}$  through a commercial calcium source<sup>6</sup> to evaporate neutral calcium in a beam directed towards the ion trap. A tunable laser at  $422.79 \text{ nm}$  excites an outer valence electron from the  $4s^2 \ ^1S_0$  ground state to the excited  $4s4p \ ^1P_1$  level. Note that the wavelength of this first ionization step selects which calcium isotope<sup>7</sup> will be ionized and subsequently trapped. The second ionization step transfers the electron into continuum and thus requires a wavelength below  $390 \text{ nm}$  (we use a laser at  $375 \text{ nm}$ ).

<sup>5</sup>  $\text{Sm}_2\text{Co}_{17}$  permanent magnets from BVI-Magnet GmbH have a remanence of  $> 1 \text{ T}$  with a temperature dependence of  $0.015\%/K$  - the lowest value known to us for common permanent magnets. Thereby, the provided magnetic field, and with that the transitions between the Zeeman levels, are insensitive to temperature changes in the laboratory, resulting in longer coherence times [59].

<sup>6</sup> Alvatec AS-2-Ca-50-C

<sup>7</sup> There are six naturally occurring Ca isotopes  $^{40}\text{Ca}$ ,  $^{42}\text{Ca}$ ,  $^{43}\text{Ca}$ ,  $^{44}\text{Ca}$ ,  $^{46}\text{Ca}$ ,  $^{48}\text{Ca}$ , where  $^{40}\text{Ca}$  has the highest natural abundance of  $96.94(16)\%$ . The isotope shifts on the relevant transition for the first ionization step lie between  $393 - 1513 \text{ MHz}$  [64].

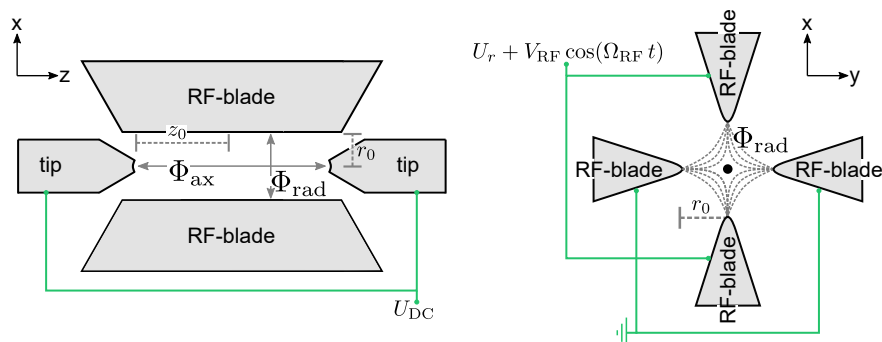


**Figure 2.5.: Schematic of a linear Paul trap from two perspectives.** A DC voltage  $U_{\text{DC}}$  applied on tip-shaped electrodes generate a static electric potential  $\Phi_{\text{ax}}$  along the  $z$ -axis. In our experiment, the tip electrodes have holes of 0.5 mm in diameter for optical access along the principal axis of the ion string. A time-dependent voltage  $U_r + V_{\text{RF}} \cos(\Omega_{\text{RF}} t)$  applied to one pair of radio frequency electrodes (RF-blades) creates a confining quadrupole potential  $\Phi_{\text{rad}}$  in the  $xy$ -plane. The distance from the trap center to the surface of the radial and tip electrodes is denoted by  $r_0$  and  $z_0$ , respectively.

The singly ionized  $^{40}\text{Ca}^+$  is then confined by a Paul trap [65, 66], which creates a quadrupole potential for charged particles. This section only offers a brief summary of the equations and dynamics of linear Paul traps as the topic has already been discussed in great detail in literature (for example, Refs. [67, 68]). Typical linear Paul traps consist of two pairs of electrodes which provide the confinement of an ion string in the radial or  $x, y$ -plane, using dynamic electric fields (radio frequency). An additional pair of tip-shaped electrodes provides axial confinement using a static electric field (see Fig. 2.5). The trapping potential  $\Phi$  can be decomposed into a static axial part  $\Phi_{\text{ax}}$  and a time-dependent radial part  $\Phi_{\text{rad}}$  which varies sinusoidally with the radio frequency  $\Omega_{\text{RF}}$  applied to the RF-blades. The lowest-order terms of a Taylor expansion around the center of the trap, are good approximations<sup>8</sup> for the trapping potential:

$$\begin{aligned} \Phi_{\text{rad}}(x, y, z, t) &= \frac{U_r + V_{\text{RF}} \cos(\Omega_{\text{RF}} t)}{2r_0^2} (\alpha_x x^2 + \alpha_y y^2 + \alpha_z z^2) \\ \Phi_{\text{ax}}(x, y, z) &= \frac{U_{\text{DC}}}{2z_0^2} (\beta_x x^2 + \beta_y y^2 + \beta_z z^2). \end{aligned} \quad (2.25)$$

Here,  $V_{\text{RF}}$  and  $\Omega_{\text{RF}}$  are the peak amplitude and frequency of the RF drive, respectively.  $U_r$  is a DC bias voltage optionally applied to one of the RF-blade pairs and  $r_0$  denotes the distance from the trap axis to the surface of the RF-blades (see Fig. 2.5).  $U_{\text{DC}}$  describes the static voltage applied to the tip electrodes for axial confinement and  $z_0$

<sup>8</sup>Higher order terms (anharmonicities) only become important when the size of the trapped particle or the amplitude of its motion are comparable to the spacing between the particle and the electrodes.

the distance from the center of the trap to the surface of the tip electrodes. Every potential in freespace has to fulfill the Laplace equation  $\Delta\Phi = 0$  at any instant in time, which leads to restrictions in the geometry factors:  $\sum_i \alpha_i = 0 = \sum_i \beta_i$ . Ideal linear Paul traps obey these conditions by choosing

$$\begin{aligned} \alpha_x &= -\alpha_y, \quad \alpha_z = 0 \quad \text{and} \\ -(\beta_x + \beta_y) &= \beta_z > 0 \quad \text{e.g.} \quad \beta_x = \beta_y = -\frac{1}{2}\beta_z. \end{aligned} \quad (2.26)$$

Classically, the motion of a particle with mass  $m$  and charge  $Q$ , trapped in the potentials (2.25), can be described by Mathieu's differential equations

$$\begin{aligned} \frac{d^2x}{d\xi^2} + [a_x - 2q_x \cos(2\xi)]x &= 0, \quad \text{with the substitutions} \\ \xi = \frac{\Omega_{\text{RF}} t}{2}, \quad a_x = \frac{4Q}{m\Omega_{\text{RF}}^2} \left( \alpha_x \frac{U_r}{r_0^2} - \beta_x \frac{U_{\text{DC}}}{z_0^2} \right), \quad q_x = \alpha_x \frac{2QV_{\text{RF}}}{m\Omega_{\text{RF}}^2 r_0^2} \end{aligned} \quad (2.27)$$

and analogously for the other directions  $y, z$ . Considering the relations in Eq. (2.26), stable solutions for a trapped particle in a linear Paul trap are found in all three dimensions. The resulting particle trajectory is approximately

$$r_i(t) \approx A_i \cos(\omega_i t) \left( 1 - \frac{q_i}{2} \cos(\Omega_{\text{RF}} t) \right), \quad (2.28)$$

with  $i \in \{x, y, z\}$ . This trajectory corresponds to a superposition of two motions: harmonic oscillations with amplitude  $A_i$  and frequency  $\omega_i = \Omega_{\text{RF}}/2 \cdot \sqrt{a_i + q_i^2/2}$ , called *secular motion*, and fast, driven excursions at the trap drive frequency  $\Omega_{\text{RF}}$ , called *micromotion*. Using the relations from Eq. (2.27), the secular frequencies are given by:

$$\begin{aligned} \omega_z &= \sqrt{\frac{2\beta_x Q U_{\text{DC}}}{m z_0^2}}, \\ \omega_x &= \sqrt{\frac{\alpha_x Q U_r}{m r_0^2} + \frac{(q_x \Omega_{\text{RF}})^2}{8} - \frac{\omega_z^2}{4}}, \quad \omega_y = \sqrt{-\frac{\alpha_x Q U_r}{m r_0^2} + \frac{(q_x \Omega_{\text{RF}})^2}{8} - \frac{\omega_z^2}{4}}. \end{aligned} \quad (2.29)$$

From these equations we can see that the axial trapping voltage  $U_{\text{DC}}$  directly influences the radial motional modes: a stronger axial confinement decreases the radial frequencies. Further, a DC bias voltage  $U_r$  applied to one pair of RF-blades, lifts the degeneracy of the two radial motional frequencies  $\omega_x, \omega_y$ .

In the quantum-mechanical picture, an ion confined in a quadratic potential can be

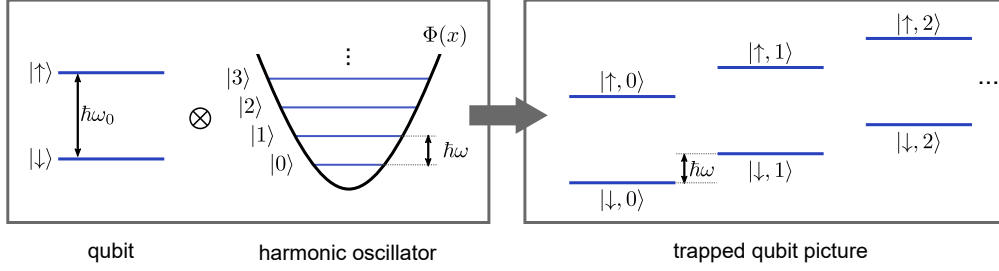


**Figure 2.6.:** **Left panel:** The simplified two-level picture of a qubit with two electronic levels defining the states  $|\downarrow\rangle, |\uparrow\rangle$ , split by an energy  $\hbar\omega_0$ , is combined with the harmonic oscillator eigenstates  $|0\rangle, |1\rangle, \dots$  of a trapped particle. **Right panel:** Combined level picture of a harmonically trapped qubit.

described as harmonic oscillator in a static potential [69–71] with the Hamiltonian

$$H_{\text{osc}} = \frac{p_i^2}{2m} + \frac{1}{2}m\omega_i^2 x_i^2 = \hbar\omega_i \left( \hat{n}_i + \frac{1}{2} \right) \quad , \quad i \in \{x, y, z\}. \quad (2.30)$$

The number operator  $\hat{n}_i = \hat{a}_i^\dagger \hat{a}_i$  is defined by the harmonic oscillator raising and lowering operators  $\hat{a}_i^\dagger, \hat{a}_i$  with the properties

$$a^\dagger |n\rangle = \sqrt{n+1} |n+1\rangle \quad , \quad a |n\rangle = \sqrt{n} |n-1\rangle. \quad (2.31)$$

The quantized harmonic oscillator eigenstates  $|n\rangle$ , called *Fock states*, indicate the number of motional quanta (phonons)  $n$  in the system. Combined with the electronic levels defining the qubit states (Section 2.2.1) a trapped-ion qubit has a ladder-like level structure (Fig. 2.6).

The alignment of multiple ions in a linear Paul is governed by the balance between the mutual Coulomb repulsion of the ions and the force provided by the axial trapping potential  $\Phi_{\text{ax}}$ . Typically, the axial potential is chosen such that the ions align as a string along the trap axis. The frequencies for the center-of-mass motion of the ion string in all three directions are equivalent to Eqs. (2.29). Already for four ions, the determination of the other motional mode frequencies involves numerical calculations [72]. However, the harmonic oscillator picture from Eq. (2.30) and Fig. 2.6 holds for all common motional modes. Laser coupling to these collective motional modes allow the qubits to interact and share information independent of their location in the ion chain (see Chapter 3).

## 3. Quantum simulation with trapped ions

In contrast to other linear Paul trap experiments in our group, we concentrate more on quantum simulation instead of quantum computation. More precisely, we specialize on spin-spin interactions using the transverse motional modes of long ion strings. In the first part of this chapter I introduce different approaches to quantum simulation. The second part discusses how we realize effective spin-spin interactions with tunable interaction range in our laboratory.

### 3.1. Quantum simulation

Quantum theory is the most accurate and best-tested description of the microscopic world, from which many observations of our macroscopic world can be deduced. Many systems in material-science and condensed matter physics, chemistry and biology are extremely difficult to access, control and manipulate directly, such that efficient modelling and simulation has become a great cornerstone in research during the past two decades [6]. However, already for systems with rather few constituents (tens of quantum particles), quantum mechanical calculations become extremely demanding for classical computers. Already the simple storage of a quantum state of 69 particles requires more memory<sup>9</sup> than what is available in all technological devices on earth nowadays (based on estimates in Ref. [4]). Simulating the time evolution of a quantum system with  $N$  constituents is even more challenging, as it corresponds to solving a differential equation represented by a  $2^N \times 2^N$  matrix.

This is when the concept of a *Quantum Simulator* comes into play, as proposed in the early 1980's by Richard Feynman and others [5]. The idea is to employ a highly controllable, well accessible system which itself obeys quantum mechanical laws, to simulate a complex quantum system of interest. Trapped ions allow experimenters to repeatedly and reliably prepare a quantum state, control its dynamical evolution, create entanglement and carry out quantum measurements with high efficiency (cf.

---

<sup>9</sup>A quantum state vector for  $N = 69$  qubits, has  $2^N$  complex coefficients. Storing these as  $2^{N+1}$  double-precision floating numbers (8 bytes per number), requires  $2^{N+1} \cdot 8$  bytes  $\approx 9$  ZB of memory.

Section 2.2). This control over all quantum degrees of freedom makes trapped ions suitable candidates for realizing quantum simulators [7].

As soon as quantum simulators solve classically intractable problems, an important question arises: Can we trust the result or how can we verify it? One possible solution is to perform checks across different quantum platforms and simulation techniques. In the following I present three approaches to quantum simulation, differing in the way in which the Hamiltonian of interest is implemented, in error sensitivity and also in the requirements for the available gates and interactions.

### 3.1.1. Digital quantum simulation (DQS)

The time evolution of a quantum system under a certain (time-independent) Hamiltonian  $H_{\text{sys}}$  is defined as a unitary operator  $U$  acting on an initial state  $|\psi(0)\rangle$ :  $|\psi(t)\rangle = U(t)|\psi(0)\rangle = e^{-iH_{\text{sys}}t}|\psi(0)\rangle$ . The direct implementation of the evolution operator  $U$  is only possible in specific cases (cf. analog quantum simulation). A digital quantum simulator, however, encodes the initial state of the system of interest in qubits and translates its unitary dynamics into a circuit of elementary universal quantum gates [73]. The underlying principle is, that any Hamiltonian can be approximated by a sum of local<sup>10</sup> Hamiltonians  $H_j$ , such that  $H_{\text{sys}} \approx \sum_j^m H_j$ . For the case that all individual local terms commute,  $[H_j, H_k] = 0$ , the unitary dynamics can be decomposed into

$$U(t) = e^{-iH_{\text{sys}}t} = e^{-i\sum_j^m H_j t} = \prod_j^m e^{-iH_j t}, \quad (3.1)$$

corresponding to a sequential application of  $H_j$ 's, which are realized with circuits of single- and multi-qubit gates. For general Hamiltonians, however, the commutation relation above does not hold and the decomposition of the unitary into local gates has to be performed using the Trotter expansion [21, 74]:

$$U(t) = e^{-iH_{\text{sys}}t} = e^{-i\sum_j^m H_j t} = \lim_{n \rightarrow \infty} \left( \prod_j e^{-iH_j t/n} \right)^n, \quad n \in \mathbb{N}. \quad (3.2)$$

In words, the evolution under each local Hamiltonian  $H_j$  is divided into discrete time steps,  $t/n$ , and the sequential application of all truncated  $H_j$ 's defines one block, or Trotter step (see Fig. 3.1). This block is repeated  $n$  times to add up to a total simulation time  $t$ . The finer the temporal slicing, the more Trotter steps  $n$  have to be performed

<sup>10</sup>The terminology *local Hamiltonian* refers to Hamiltonians whose interaction strength decays with increasing distance.

and the better the time dynamics of the system is approximated. For infinitely small time steps  $t/n \xrightarrow{\text{for } n \rightarrow \infty} 0$ , the approximation of  $H_{\text{sys}}$  becomes exact. Theoretically, the

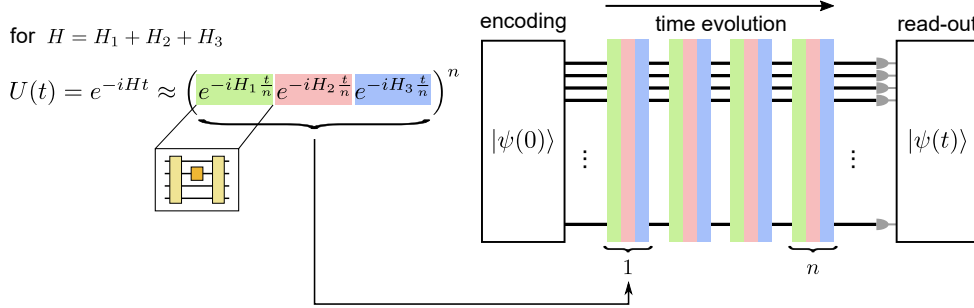


**Figure 3.1.: Digital quantum simulation based on Trotter expansion.** The initial state  $|\psi(0)\rangle$  is encoded in a set of qubits. The states time evolution under a Hamiltonian  $H$  is approximately simulated using the Trotter expansion of order  $n$ .  $H$  is decomposed into a sum of local Hamiltonians  $H_1, H_2, H_3$ , realized by a combination of single- and multi-qubit gates (denoted by orange and yellow blocks in the inset). All local interactions are subsequently applied, each for a time  $t/n$ , defining one Trotter step. This sequence is repeated  $n$  times to add up to a total simulation time  $t$ , and finally the evolved state  $|\psi(t)\rangle$  is measured.

digital quantum simulation scheme allows for simulating the evolution of any system with local interactions, while the complexity of the simulation grows only polynomially with the number of qubits [75]. In practise,  $n$  is finite and the related approximation errors can be minimized only at the expense of an increasing number of concatenated gates. Unfortunately, experimental gates have errors themselves and a trade-off between approximation errors and cumulative gate errors has to be found. To utilize its full universality potential, a freely programmable, universal quantum computer with correction schemes for gate errors would be desirable. Moreover, the simulation of quantum systems with many particles requires scalable quantum computer architectures, whose development is still a long-term goal [76, 77]. In terms of a practical implementation in the near future, *analog quantum simulation* (see next subsection) is more advantageous.

### 3.1.2. Analog quantum simulation (AQS)

An analog quantum simulator mimics the evolution of the system of interest,  $H_{\text{sys}}$ , directly. That is, by mapping  $H_{\text{sys}}$  onto controllable interactions and parameters, naturally available in the simulator:  $H_{\text{sys}} \leftrightarrow H_{\text{sim}}$ . The main task in this scheme is to identify the accessible control parameters in the simulator system and relate them with the relevant variables of the simulated system. Sometimes it even requires additional externally applied fields or ancillary systems to mediate various interactions [6]. The

accuracy of AQS is mainly limited by the quality of the state preparation, the read-out of the result and the degree to which the simulator can reproduce the dynamics of the system of interest. Moreover, analog quantum simulators lack error correction protocols. However, an important advantage over DQS is the smaller sensitivity to errors, because valuable qualitative answers (e.g. the occurrence of a quantum phase transition [78]) can be obtained even without perfect parameter control or full quantitative agreement between simulator and simulated system. The drawback of this approach is that simulator and simulated system have to be sufficiently similar, such that the class of problems that can be simulated is limited by the available simulator interactions [73]. A demonstration of AQS on our experimental apparatus is presented in Chapter 6.

### 3.1.3. Variational quantum simulation (VQS)

Variational quantum simulation represents a third, new method of quantum simulation, based on quantum-classical hybrid algorithms which variationally optimize a given cost function. The VQS feedback loop (Fig. 3.2) basically consist of three steps:

1. The simulator prepares a quantum state  $|\psi(\boldsymbol{\theta})\rangle$  by applying a quantum circuit, which is based on the naturally available gates of the simulator and a related set of control parameters  $\boldsymbol{\theta}$ .
2. The cost function of interest is measured. For example, the cost function to simulate the ground state of a target Hamiltonian,  $\hat{H}_T$ , corresponds to the expectation value:  $E = \langle \psi(\boldsymbol{\theta}) | \hat{H}_T | \psi(\boldsymbol{\theta}) \rangle$ .
3. A classical computer calculates the cost function from the measurement results. Further, it employs an optimization algorithm to minimize the cost function by varying the parameter set  $\boldsymbol{\theta}$ , which is then handed over to the quantum simulator.

Steps 1 – 3 are repeated until the optimization converges. The variational principle implies that, in the absence of experimental imperfections, the cost function  $E$  is always bigger or equal to the lowest eigenvalue of  $\hat{H}_T$ .

In summary, the quantum device performs the computationally expensive generation and evaluation of potentially highly entangled states. The classical computer, instead, is employed to solve noisy, high-dimensional and gradient-free optimization problems. In this quantum simulation scheme, the target Hamiltonian only exists as a measurement prescription and is never realized physically in the experimental quantum device. This endows the approach with great flexibility in the models which can be simulated.

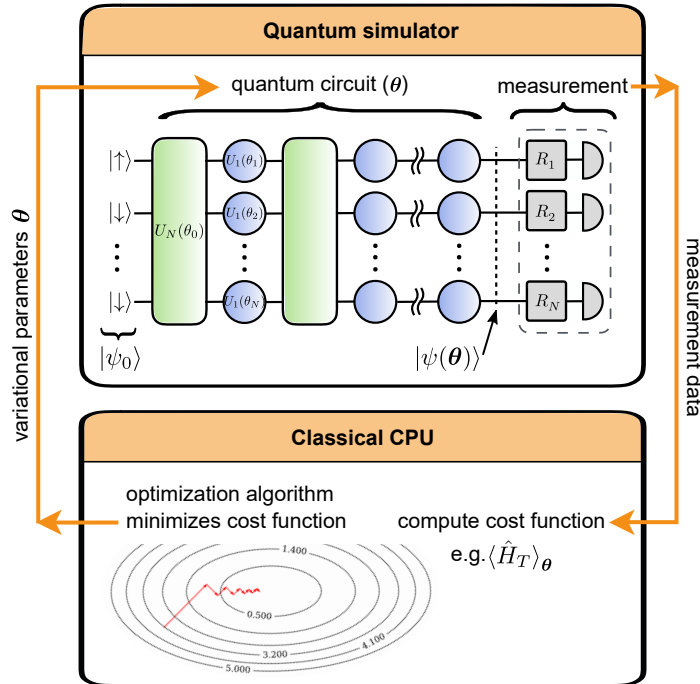


**Figure 3.2.: VQS quantum-classical feedback loop.** A quantum simulator generates a state  $|\psi(\theta)\rangle$  by applying a sequence of gates, e.g. multi-qubit entangling gates (green boxes) and single-qubit rotations (blue circles). Individual gate settings are controlled by a set of parameters  $\theta$ . State read-out is performed in the measurement bases (gray boxes) relevant for the reconstruction of the cost function of interest. A classical CPU runs an optimization algorithm to minimize the cost function and hands over new parameters  $\theta$  to the quantum device.

The requirements that the quantum device has to meet are high experimental repetition rates, a fast exchange between the classical- and quantum co-processors and an advanced classical optimization algorithm.

Pioneering experiments employed VQS on 2 to 6 qubits, to successfully tackle complex problems in quantum chemistry [13, 14, 79, 80], as well as condensed matter and high-energy physics [12, 15]. Combining quantum variational techniques with a state-of-the-art, potentially scalable, analog quantum simulator unites the advantages of DQS and AQS. This enables the simulation of large, complex Hamiltonians, which are out of reach for AQS and DQS, as we could show in Ref. [16]. A more thorough discussion on variational quantum simulation and the respective experiment performed in our laboratory, follows in Chapter 7.

## 3.2. Laser interaction with a harmonically trapped, two-level atom

This section presents an overview on the interaction of coherent laser light with a two-level atom, confined in a harmonic trap. First, a review of the manipulation of the bare electronic states, and the experimental realization of single-qubit rotations is given. Finally, I discuss the manipulation of motional levels and the coupling of electronic and motional degrees of freedom.

### 3.2.1. Laser light and a two-level atom

First, we focus on the case where a two-level atom, representing a qubit, is held at a fixed position in space and excited by a laser beam. The full Hamiltonian, describing the bare atom  $H_a$  and the atom-light interaction  $H_{al}$  is given by [68]

$$H = H_a + H_{al} = \frac{\hbar\omega_0}{2}\sigma_z + \hbar\Omega(\sigma_+ + \sigma_-) \cos(\omega_l t + \phi_l). \quad (3.3)$$

The two atomic levels are typically labelled as  $|g\rangle = |-\rangle_z$  (ground state) and  $|e\rangle = |+\rangle_z$  (excited state). They correspond to the eigenstates of the  $\sigma_z$  Pauli operator (cf. Section 2.1.1) and are split by an energy  $\hbar\omega_0$ . Frequency and phase of the laser light are denoted  $\omega_l$  and  $\phi_l$ , respectively. The operators  $\sigma_+$ ,  $\sigma_-$  describe the excitation and de-excitation of the electronic state:  $\sigma_+ = |e\rangle\langle g|$ ,  $\sigma_- = |g\rangle\langle e|$ . Finally, the Rabi frequency  $\Omega$  accounts for the coupling strength between the atom and the laser field. More precisely, for the optical qubit used in our experiments (see Section 2.2.1) the coupling mechanism is defined by the interaction of the atomic quadrupole moment  $\hat{Q}$  with the electric field gradient  $H_l = \hat{Q} \cdot \nabla \mathbf{E}$ , which yields the form as in Eq. (3.3) with the Rabi frequency defined as [52, 72]

$$\Omega = \frac{eE_0}{2\hbar} \sqrt{\frac{15\lambda^3 A}{c\alpha 8\pi^3}} \cdot \Lambda(m_g, m_e) g_{\Delta m_j} \quad (3.4)$$

Here,  $E_0$  is the electric field amplitude, related to the laser intensity  $I$  via  $E_0 \propto \sqrt{I}$ .  $\alpha$  is the fine structure constant,  $A$  the spontaneous decay rate (or natural linewidth) of the excited state,  $\lambda$  the laser beam's wavelength and  $\Lambda(m_g, m_e)$  the corresponding Clebsch-Gordan coefficient [81] of the transition between the two chosen atomic levels  $|g\rangle$ ,  $|e\rangle$  with corresponding Zeeman levels  $m_g$ ,  $m_e$ . The geometric factor  $g_{\Delta m_j}$  accounts for the polarization and the angle between the laser beam's wave vector and the magnetic field quantization axis [63, 82]. The two transitions relevant for the experiments

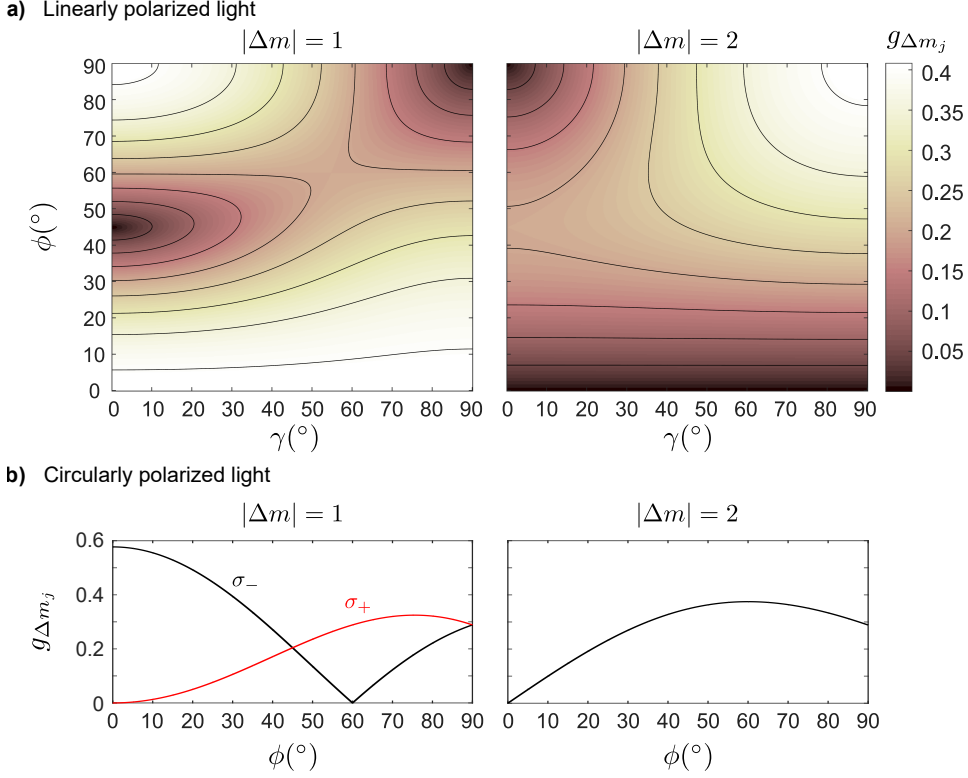


**Figure 3.3.: Geometric factor charts.** The geometric factor  $g_{\Delta m_j}$  influences the coupling efficiencies for transitions between different Zeeman levels  $\Delta m$ . It depends on the wave vector and polarization of the incident beam with respect to the quantization axis. Here,  $\phi$  denotes the angle between the laser beam's  $\mathbf{k}$  vector and the quantization axis and  $\gamma$  is the angle between a linear polarization and the plane of incidence, which is spanned by the quantization axis and the laser's  $\mathbf{k}$  vector.

presented in this thesis are  $|S_{1/2}, m_j = 1/2\rangle \leftrightarrow |D_{5/2}, m_j = 5/2\rangle$ , where  $|\Delta m| = 2$ , and  $|S_{1/2}, m_j = 1/2\rangle \leftrightarrow |D_{5/2}, m_j = 3/2\rangle$ , where  $|\Delta m| = 1$ . Following the geometric factor charts in Fig. 3.3, we choose right-circular polarized light ( $\sigma_-$ ), travelling along the quantization axis ( $\phi = 0^\circ$ ) to drive the  $\Delta m = 1$  transition,  $|S_{1/2}, m_j = 1/2\rangle \leftrightarrow |D_{5/2}, m_j = 3/2\rangle$ , with maximum strength. To efficiently drive the  $\Delta m = 2$  transition,  $|S_{1/2}, m_j = 1/2\rangle \leftrightarrow |D_{5/2}, m_j = 5/2\rangle$ , we use a laser beam that travels perpendicular to the quantization axis ( $\phi = 90^\circ$ ), with a linear polarization whose vector encloses  $\gamma = 90^\circ$  with the plane of incidence (spanned by the quantization axis and the laser's  $\mathbf{k}$  vector).

### 3.2.2. Experimental realization of single-qubit rotations

After transforming Hamiltonian  $H$  from Eq. (3.3) to the interaction picture<sup>11</sup> with respect to  $H_a$  and applying the rotating wave approximation<sup>12</sup> the atom-light interaction Hamiltonian reads as:

$$H_{\text{int}} = \frac{\hbar\Omega}{2} \left( e^{-i(\Delta \cdot t + \phi_l)} \sigma_+ + e^{i(\Delta \cdot t + \phi_l)} \sigma_- \right), \quad (3.5)$$

where  $\Delta = \omega_l - \omega_0$  describes the detuning of the laser frequency from the transition between the two atomic levels. The  $\sigma_{\pm} = (\sigma_x \pm i\sigma_y)/2$  terms show that the perturbation induced by the laser field leads to single-qubit rotations around different axes on the Bloch sphere. Generally, we need to distinguish between two different cases: resonant and non-resonant laser field.

**(i) Resonant laser field  $\Delta = 0$ :** The interaction induces coherent population exchange between the qubit states  $|g\rangle$  and  $|e\rangle$ , with the related unitary operation

$$U(\theta, \phi) = e^{-iH_{\text{int}}t/\hbar} = \begin{pmatrix} \cos\left(\frac{\theta}{2}\right) & -ie^{-i\phi_l} \sin\left(\frac{\theta}{2}\right) \\ -ie^{i\phi_l} \sin\left(\frac{\theta}{2}\right) & \cos\left(\frac{\theta}{2}\right) \end{pmatrix}. \quad (3.6)$$

By comparing with Eq. (2.17), we can identify this unitary as a rotation by an angle  $\theta = \Omega \cdot t$ , around an axis  $\sigma_{\phi_l} = \cos(\phi_l)\sigma_x + \sin(\phi_l)\sigma_y$  in the equatorial plane of the Bloch sphere (cf. Fig. 2.1). In other words, the rotation angle of a resonant single-qubit rotation is defined by the duration  $t$  for which the laser is applied to the atom and the Rabi frequency  $\Omega$ , which includes the light intensity and coupling efficiency to the corresponding transition, cf. Eq. (3.4). The rotation axis is determined by the optical phase  $\phi_l$  of the light field. A full qubit flip from  $|g\rangle$  to  $|e\rangle$  is commonly called  $\pi$ -pulse, which is realized by applying a resonant laser for the duration  $t = \pi/\Omega$ . Continuous population exchange between  $|g\rangle$  and  $|e\rangle$  under continuous application of the laser is called *Rabi oscillation* (Fig. 3.4 a)).

**(ii) Non- resonant laser field  $\Delta \neq 0$ :** Also a non-resonant light field induces population transfer between  $|g\rangle$  and  $|e\rangle$ . After preparing the atom initially in  $|g\rangle$ , the

<sup>11</sup>It is convenient to change into the interaction picture [83], to investigate the dynamics induced by the laser-atom Hamiltonian  $H_{at}$ . This way, the time evolution driven by the laser-interaction is separated from the evolution of the unperturbed system. The transformation into the interaction Hamiltonian  $H_{\text{int}}$  is performed via  $H_{\text{int}} = U_a^\dagger H U_a$  with  $U_a = e^{-iH_a t/\hbar}$ . Further,  $|\psi(t)\rangle = U_a e^{-iH_{\text{int}}t/\hbar} U_a^\dagger |\psi(0)\rangle$ .

<sup>12</sup>The rotating wave approximation (RWA) neglects terms rotating at the sum frequency  $\omega_l + \omega_0$  as they oscillate much faster than  $\Delta = \omega_l - \omega_0$ , and thereby average out over the time scale of the induced dynamics.

probability amplitude  $p_e$  to find it in the excited state is quantified by solving the optical Bloch equations [84, 85]

$$p_e(t) = \frac{\Omega^2}{\Omega^2 + \Delta^2} \sin^2 \left( \frac{\sqrt{\Omega^2 + \Delta^2} t}{2} \right) = \frac{\Omega^2}{\Omega_{\text{eff}}^2} \sin^2 \left( \frac{\Omega_{\text{eff}} t}{2} \right), \quad (3.7)$$

with an effective oscillation frequency  $\Omega_{\text{eff}} = \sqrt{\Omega^2 + \Delta^2}$ . Panel a) in Fig. 3.4 shows the effect of a non-resonant laser field on the Rabi oscillations. Apart from suppressed population transfer, an off-resonant light field also induces a shift of the atomic levels, the so-called *AC-Stark shift*. The related Hamiltonian is derived by transforming Eq. (3.3) to the interaction picture with respect to the applied laser frequency:

$$H_{\text{int}}^{\text{AC}} = -\frac{\hbar\Delta}{2}\sigma_z + \frac{\hbar\Omega}{2}\sigma_x. \quad (3.8)$$

The corresponding eigenvalues,  $\lambda_{\pm} = \pm\frac{\hbar}{2}\sqrt{\Omega^2 + \Delta^2}$  determine how much the energy of a level is shifted by the AC-Stark shift. For the case of large laser detuning,  $\Delta \gg \Omega$ , the eigenvalues are approximated by  $\lambda_{\pm} \approx \pm\left(\frac{\hbar\Delta}{2} + \frac{\hbar\Omega^2}{4\Delta}\right)$  and the related energy shift becomes  $\delta = \lambda_{\pm} - \lambda_{\pm}(\Omega = 0) = \pm\frac{\hbar\Omega^2}{4\Delta}$ , where the sign of the detuning also determines the sign of the shift for the individual levels. For example, a blue detuned laser ( $\Delta > 0$ ) shifts the upper level downwards and the lower level upwards (see Fig. 3.4 b)) such that the overall AC-Stark shift of the transition frequency becomes

$$\delta_{\text{AC}} = -\frac{\Omega^2}{2\Delta}. \quad (3.9)$$

For this case of large detuning, rapidly oscillating terms in the Hamiltonian can be neglected [86], resulting in the effective Hamiltonian  $H_{\text{eff}}^{\text{AC}}$ , with the corresponding unitary  $U(\delta_{\text{AC}})$ :

$$H_{\text{eff}}^{\text{AC}} = \frac{\hbar}{2}\delta_{\text{AC}}\sigma_z, \quad U(\delta_{\text{AC}}) = e^{-iH_{\text{eff}}^{\text{AC}}t/\hbar} = \begin{pmatrix} e^{-i\frac{\delta_{\text{AC}}}{2}t} & 0 \\ 0 & e^{i\frac{\delta_{\text{AC}}}{2}t} \end{pmatrix}. \quad (3.10)$$

Comparing with Eq. (2.17), this unitary is identified as a rotation by an angle  $\phi = \delta_{\text{AC}} \cdot t$ , around the  $z$ -axis of the Bloch sphere. Also in this case one can define AC-Stark Rabi oscillations  $\Omega_{\text{AC}}$ . Note that for a real atom the calculation of the induced AC-Stark shift is quite complex, as the laser couples far off-resonantly to many electronic levels (Section 2.2.1), which all contribute to the effective energy level shift. For a detuning  $\Delta$  of tens of MHz, we typically observe AC-Stark shifts of tens of kHz, which are predom-

inantly caused by off-resonant coupling to electric dipole transitions in the calcium ion. The corresponding AC-Stark Rabi frequencies are in the order of  $\Omega_{AC} \approx (2\pi) 100$  kHz.

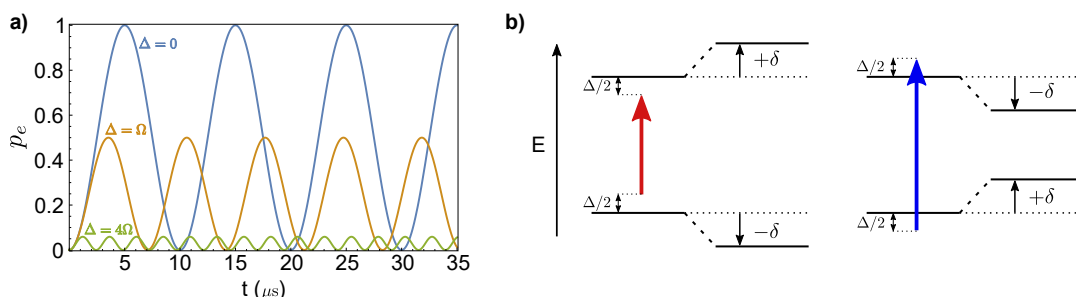


**Figure 3.4.:** Effects of resonant and non-resonant laser interaction. **a)** Rabi oscillations with  $\Omega = (2\pi) 100$  kHz for different laser detunings  $\Delta = 0$  (blue),  $\Delta = \Omega$  (orange) and  $\Delta = 4\Omega$  (green). The probability  $p_e$  to find the atom in the excited state is plotted as a function of the laser application time  $t$ . **b)** Energy level shifts  $\pm\delta$  induced by a red detuned ( $\Delta < 0$ ) or blue detuned ( $\Delta > 0$ ) laser light with respect to the atomic transition.

### Pulse sequence for single-qubit rotations

In our experiments we typically use a combination of (i) resonant laser pulses and (ii) a far off-resonant, tightly focused laser beam, in order to realize single-qubit rotations<sup>13</sup>:

1. A global pulse, resonant with the qubit transition at 729 nm, is applied for the duration  $t_1 = \pi/(2\Omega)$  to rotate every qubit's state vector from  $|\downarrow\rangle$  to the equatorial plane of the Bloch sphere.
2. A tightly focused laser beam, with a frequency detuned between  $\Delta = -60$  MHz and  $\Delta = -90$  MHz from the qubit transition, addresses a single ion. The pulse is applied for a duration  $t_2$ , such that it's AC-Stark shift rotates the state vector within the equatorial plane, by an angle  $\phi = \delta_{AC} \cdot t_2$ .
3. The final, global laser pulse of duration  $t_3 = \pi/(2\Omega)$  is again resonant to the qubit transition, but its optical phase  $\phi_l$  is shifted by  $\pi$  with respect to the pulse in step 1. Therefore, it effectively undoes the first  $\pi/2$  - pulse for all ions which were not addressed while completing the single-qubit rotation for the addressed ion.

<sup>13</sup>The sequence presented here is based on AC-Stark shift pulses, which leads to a narrowed effective beam width compared to resonant pulses, and therewith minimizes crosstalk. A detailed discussion on single-ion addressing can be found in C. Hempel's thesis [63].

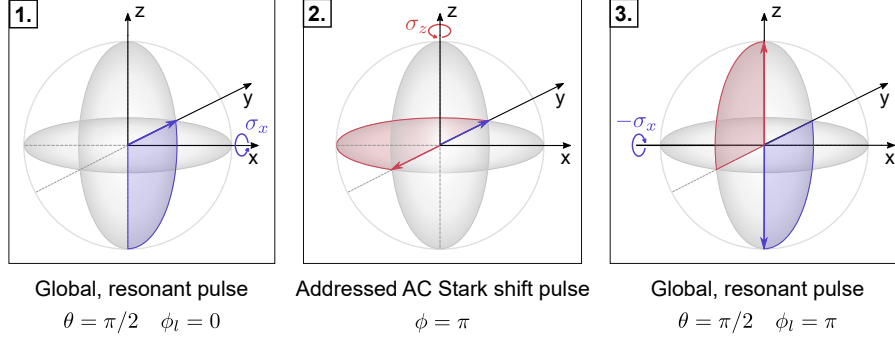


**Figure 3.5.: AC-Stark shift sequence for realizing single-qubit spin flips.** (1) All qubits are rotated into the equatorial plane by a global, resonant laser beam. (2) An addressed, far detuned laser pulse rotates the state vector of a single qubit by an angle  $\phi = \pi$ . (3) A second global, resonant pulse completes the single-qubit rotation for the addressed ion, while all other qubits are flipped back to the initial state.

### Composite pulse sequence for single-qubit rotations

For experiments with a large number of ions ( $N > 10$ ) the global beam driving collective, resonant qubit rotations (steps 1. and 3.) has a weaker coupling to the ions at the ends of the chain, due to its intrinsic Gaussian intensity profile. This causes the state vectors of these outer qubits to be under-rotated, compared to the qubits close to the center of the chain. Using cylindrical lenses, the beam is shaped elliptically (see P. Jurcevic’s thesis [87]), which improves the situation: the remaining difference in beam intensity between the center and the outermost ion is 30%, for  $N = 20$  ions (axial trapping frequency  $\omega_z = (2\pi) 217$  kHz). This corresponds to up to 15% discrepancy in the Rabi frequencies, and single-qubit flip errors of  $\sim 5\%$ . An advanced, composite pulse sequence is more robust against these inhomogeneities, resulting in improved single-qubit flip fidelities of up to 99.7% (Appendix C). The idea is to turn the under-rotated state vector into the equatorial plane and thereby convert the rotation error mainly into an offset on the equator. This is achieved by two additional pulses (step 2. and 4.) in the sequence:

1. A global, resonant  $\pi/2$  - pulse with phase  $\phi_l = 0$  and small under-rotation  $\epsilon$  is applied.
2. A global, resonant  $\pi/2$  - pulse with phase  $\phi_l = \pi/2$  converts the under-rotation to an offset in the equatorial plane. Note that all resonant pulses suffer the same under-rotation  $\epsilon$ .
3. A tightly focused laser beam pulse, with a frequency detuned between  $\Delta = -60$  MHz and  $\Delta = -90$  MHz from the qubit transition, addresses a single ion. The

pulse is applied for a duration  $t_2$ , rotating the state vector within the equatorial plane, by an angle  $\phi = \delta_{AC} \cdot t_2 = \pi$ .

4. A global, resonant  $\pi/2$  - pulse with phase  $\phi_l = -\pi/2$  flips the qubit vectors back into the z-y plane.
5. A global, resonant  $\pi/2$  - pulse with phase  $\phi_l = \pi$  completes the single-qubit rotation for the addressed ion, up to a small error, caused by the imperfect global rotations. All other ions are rotated back to the initial state without remanent error.

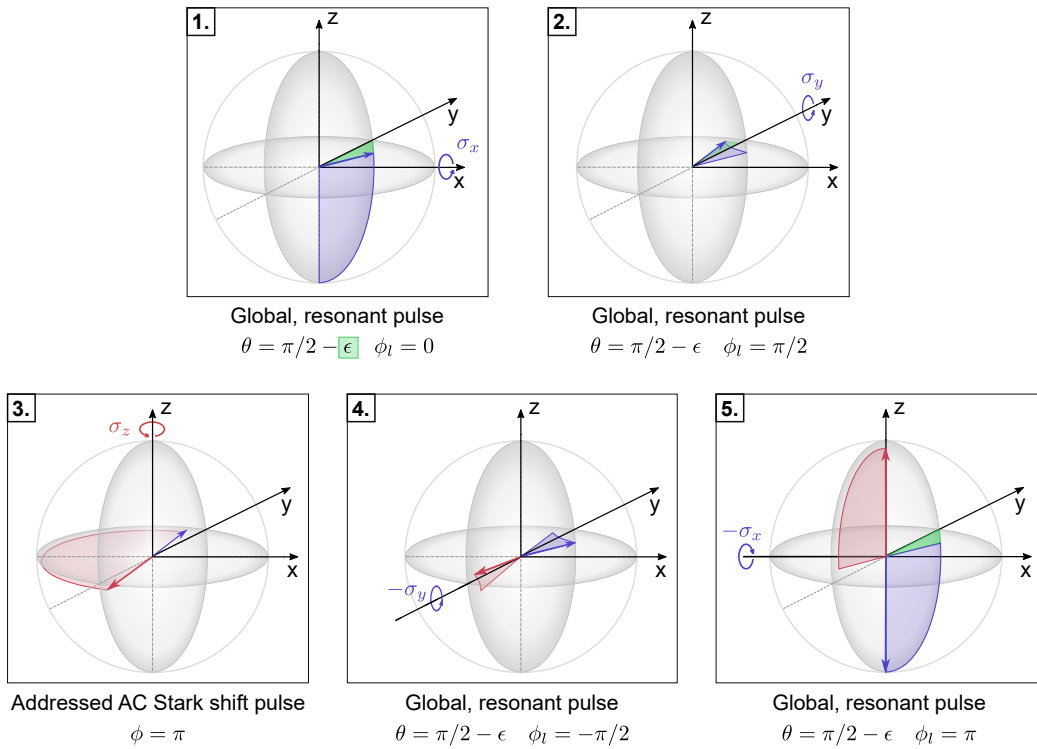


**Figure 3.6.: Advanced AC-Stark shift sequence for realizing single-qubit rotations.** Pulse sequence as in Fig. 3.5 extended by two pulses (2) and (4) in order to convert an under-rotation,  $\epsilon$ , by the global, resonant beam into an offset in the equatorial plane. This composite sequence diminishes the single-qubit flip errors from 5% to 0.3%.

### 3.2.3. Spin-motion coupling in a trapped ion

Now, we consider the case where the two-level atom, or ion, interacts with a laser, while it is trapped in a harmonic potential (symbolizing an ion trap, cf. Section 2.2). In the ion's rest frame, its oscillating motion at frequency  $\omega$  alters the phase  $\phi_l$  of the

incident light field depending on the ion's position. The associated Doppler shift results in an effective frequency modulation which appears as motional sideband transitions at  $\omega_0 \pm \omega$  and allows for a joint manipulation of the ion's electronic ("spin") and external (motional) degrees of freedom (Fig. 3.7).

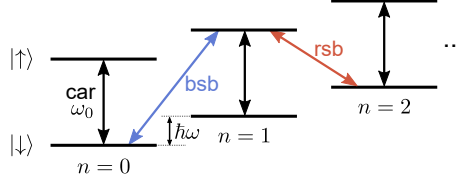


**Figure 3.7.: Energy levels of a harmonically trapped, two-level ion.** The combined state picture has a ladder-like structure, with  $|\downarrow\rangle, |\uparrow\rangle$  denoting the electronic and  $n$  the motional states, split by multiples of the motional energy  $\hbar\omega$ . Black arrows indicate carrier (car) transitions, blue (bsb) and red (rsb) arrows the corresponding sideband transitions.

For a formal description, we extend Hamiltonian (3.3) from the previous discussion with a position operator  $\hat{x}$  and the motional term from Eq. (2.30),

$$\begin{aligned} H &= H_a + H_{al} + H_m \\ &= \frac{\hbar\omega_0}{2}\sigma_z + \hbar\Omega(\sigma_+ + \sigma_-)\cos(k\hat{x} - \omega_l t - \phi_l) + \hbar\omega(a^\dagger a + \frac{1}{2}), \end{aligned} \quad (3.11)$$

where  $k$  is the laser's wave vector,  $\omega$  is the oscillation frequency of the ion in the harmonic potential,  $\omega_0$  is the bare atomic transition frequency and  $\omega_l$  is the laser frequency. Transforming this Hamiltonian to an interaction picture with respect to the atomic terms  $H_a + H_m$ , and after applying the rotating wave approximation (getting rid of terms that oscillate at optical frequencies), one arrives at:

$$H_{\text{int}} = \frac{\hbar\Omega}{2} \left( \sigma_+ e^{-i(\Delta t + \phi_l)} e^{i\eta(ae^{-i\omega t} + a^\dagger e^{i\omega t})} + \sigma_- e^{i(\Delta t + \phi_l)} e^{-i\eta(ae^{-i\omega t} + a^\dagger e^{i\omega t})} \right). \quad (3.12)$$

Here, the *Lamb-Dicke* parameter  $\eta$  was introduced in order to express the position operator  $\hat{x}$  in terms of the creation and annihilation operators  $a, a^\dagger$  of the harmonic oscillator. The Lamb-Dicke parameter relates the spatial extension  $x_0$  of the harmonic oscillator's ground state with the wavelength of the atomic transition. In other words, it describes how well the impinging light field, which encloses the angle  $\alpha$  with the direction of ion motion, couples to the motion in the harmonic trap:

$$k\hat{x} = \eta(a + a^\dagger), \quad \text{with} \quad \eta = |\mathbf{k}| \cos(\alpha)x_0 = |\mathbf{k}| \cos(\alpha) \sqrt{\frac{\hbar}{2m\omega}}. \quad (3.13)$$

An ion is said to be in the Lamb-Dicke regime, if the extent of the motional wave packet is small compared to the laser's wavelength<sup>14</sup>. With this assumption we can simplify the exponential in  $H_{\text{int}}$  by a Taylor expansion,  $e^{i\eta(ae^{-i\omega t} + a^\dagger e^{i\omega t})} = \mathbb{1} + i\eta(ae^{-i\omega t} + a^\dagger e^{i\omega t}) + \mathcal{O}(\eta^2)$ , resulting in:

$$H_{\text{int}} = \frac{\hbar\Omega}{2} \left( \sigma_+ e^{-i(\Delta t + \phi_l)} \left[ 1 + i\eta(ae^{-i\omega t} + a^\dagger e^{i\omega t}) + \mathcal{O}(\eta^2) \right] + h.c. \right). \quad (3.14)$$

In the resolved sideband limit, the fundamental Rabi frequency  $\Omega$  is small compared to the oscillation frequency  $\Omega \ll \omega$ . In this regime, a second rotating wave approximation can be performed, neglecting terms which oscillate at  $\omega$  or higher. Depending on the detuning  $\Delta = \omega_l - \omega_0$ , three important types of transitions can be distinguished [68], which can be independently driven if the linewidth of the driving laser is small compared to the trap frequency,  $\omega_l \ll \omega$ :

- **Carrier transition  $\Delta = 0$ :** Absorption of resonant laser light does not change the motional quantum number  $n$  of the ion by coupling  $|\downarrow, n\rangle \leftrightarrow |\uparrow, n\rangle$ . Taking into account terms up to second order in  $\eta$ , Hamiltonian (3.14) turns into

$$H_{\text{car}} = \frac{\hbar\Omega_{n,n}}{2} \left( \sigma_+ e^{-i\phi_l} + \sigma_- e^{i\phi_l} \right), \quad \text{with} \quad \Omega_{n,n} = \Omega(1 - \eta^2 n), \quad (3.15)$$

corresponding to the single-qubit rotation Hamiltonian introduced in Section 3.2.2. Note that population of higher motional states  $n > 0$  reduces the coupling strength.

- **Red sideband transition  $\Delta = -\omega$ :** Absorption of red detuned laser light decreases the motional quantum number  $n$ , by coupling  $|\downarrow, n\rangle \leftrightarrow |\uparrow, n-1\rangle$  with a coupling strength that scales as  $\Omega_{n-1,n} = \eta\sqrt{n}\Omega$  [68]:

$$H_{\text{rsb}} = \frac{i\hbar\Omega_{n-1,n}}{2} \left( \sigma_+ a e^{-i\phi_l} - \sigma_- a^\dagger e^{i\phi_l} \right). \quad (3.16)$$

In our experiment, we perform sideband cooling by driving red sideband transitions, alternated with a dissipative process (repumping) to bring the spin state back to  $|\downarrow\rangle$  while the motional quantum number remains mostly unchanged. The state  $|\downarrow, 0\rangle$  remains uncoupled.

- **Blue sideband transition  $\Delta = +\omega$ :** Absorption of blue detuned laser light

<sup>14</sup>This holds as long as  $\eta^2(2\bar{n} + 1) \ll 1$ . This can be achieved by cooling the ion close to the motional ground state such that the mean vibrational quantum number  $\bar{n}$  is small. Experimentally, this is usually satisfied after Doppler cooling with  $\bar{n} \approx 10 - 20$ .

increases the motional quantum number  $n$ , by coupling  $|\downarrow, n\rangle \leftrightarrow |\uparrow, n+1\rangle$  with a coupling strength that scales as  $\Omega_{n,n+1} = \eta \sqrt{n+1} \Omega$  [68]:

$$H_{\text{bsb}} = \frac{i\hbar\Omega_{n,n+1}}{2} \left( \sigma_+ a^\dagger e^{-i\phi_i} - \sigma_- a e^{i\phi_i} \right). \quad (3.17)$$

In the case of multiple ions confined in the same trapping potential, they influence each other due to their Coulomb interaction. This results in  $3N$  sidebands, describing the motion of the ion chain in all 3 dimensions. The sideband transitions, as described above, allow one to convert the spin excitation of an ion into a collective motion of the ion chain and to transfer this excitation to any other ion that shares the motional mode. In other words, the motion acts as a bus system, which mediates the interaction between multiple ions in a chain.

### 3.3. Simulating effective spin-spin interactions

This section contains the theoretical background about spin-spin interactions and the tools for their experimental realization in trapped-ion experiments. In the first part, I introduce the radial motional spectrum of long ion strings and explain their crucial role in our experiment. In the second part, I summarize how to realize effective spin-spin interactions between multiple ions, using a light field with three frequency components (trichromatic beam). Further experimental techniques for trapping and manipulating long ion strings are discussed in P. Jurcevic’s thesis [87].

#### 3.3.1. Radial motional modes of long ion strings

As mentioned in the previous section, motional sidebands are crucial in trapped-ion experiments, since they are used as the bus system to mediate an interaction between multiple ions. In a linear Paul trap such as the one we use in our experiment, the axial motional modes<sup>15</sup> have well-separated frequencies and an intrinsically high stability. Therefore, they are well suited to realize Mølmer-Sørensen entangling gates by coupling the laser to a distinct mode (see below and Appendix B). The radial motional mode spectrum, instead, is more bunched, which opens up the possibility to induce more flexible and complex interactions by coupling the laser to multiple modes. However, the motional frequencies need to be stabilized, which requires the RF-voltage across the RF-blades to be measured and controlled. Further, all involved modes need to be ground-

<sup>15</sup>The term “axial motional modes” denotes the sideband spectrum which belongs to the motion along the principal axis of the ion string.

state cooled in order to reduce fluctuations in coupling strength and AC-Stark shifts, and thereby assure controlled time evolution of the interaction gate (see Ref. [87]). Ground-state cooling of all  $2N$  radial modes is achieved by the resolved sideband cooling (SBC) technique, where a narrow laser is tuned to the lower (red) motional sideband to reduce the motional state by one phonon in each step [88, 89]. Other methods to cool the motional state below the Doppler cooling limit are electromagnetically induced transparency (EIT) cooling or polarization-gradient (PG) cooling (Chapter 4).

The theoretical description of the motional mode spectrum for multiple ions involves numerical calculations via the equilibrium positions of all ions [72]. However, measuring the spectrum with resolved sidebands is an easy task in our experiment. The few Hertz narrow [58] 729 nm beam used for sideband probing, sideband cooling, entanglement operations and collective qubit rotations, is shaped elliptically with  $16.5 \mu\text{m} \times 190 \mu\text{m}$  by using cylindrical lenses [87]. This allows us to probe the red sideband spectrum of a string of 20 ions, trapped at an axial frequency of  $\omega_z = (2\pi) 219.4 \text{ kHz}$ . Fig. 3.8 shows the resulting spectrum with and without applied sideband cooling pulses. A bias voltage on one pair of RF-blades (see Section 2.2.2) allows us to lift the degeneracy of the two sets of modes, which are linked to the two radial directions of motion of the ion string. In our Paul trap, a bias voltage of 0.5 V results in a mode splitting of about  $(2\pi) 30 \text{ kHz}$  such that the two radial center-of-mass (COM) modes have frequencies  $\omega_{\text{rad}}^{\text{COM1}} = (2\pi) 2.712 \text{ MHz}$  and  $\omega_{\text{rad}}^{\text{COM2}} = (2\pi) 2.681 \text{ MHz}$ . All 40 radial modes are cooled to the ground state by four consecutive pulses, denoted by the red arrows in Fig. 3.8, in a total cooling time of 11 ms.

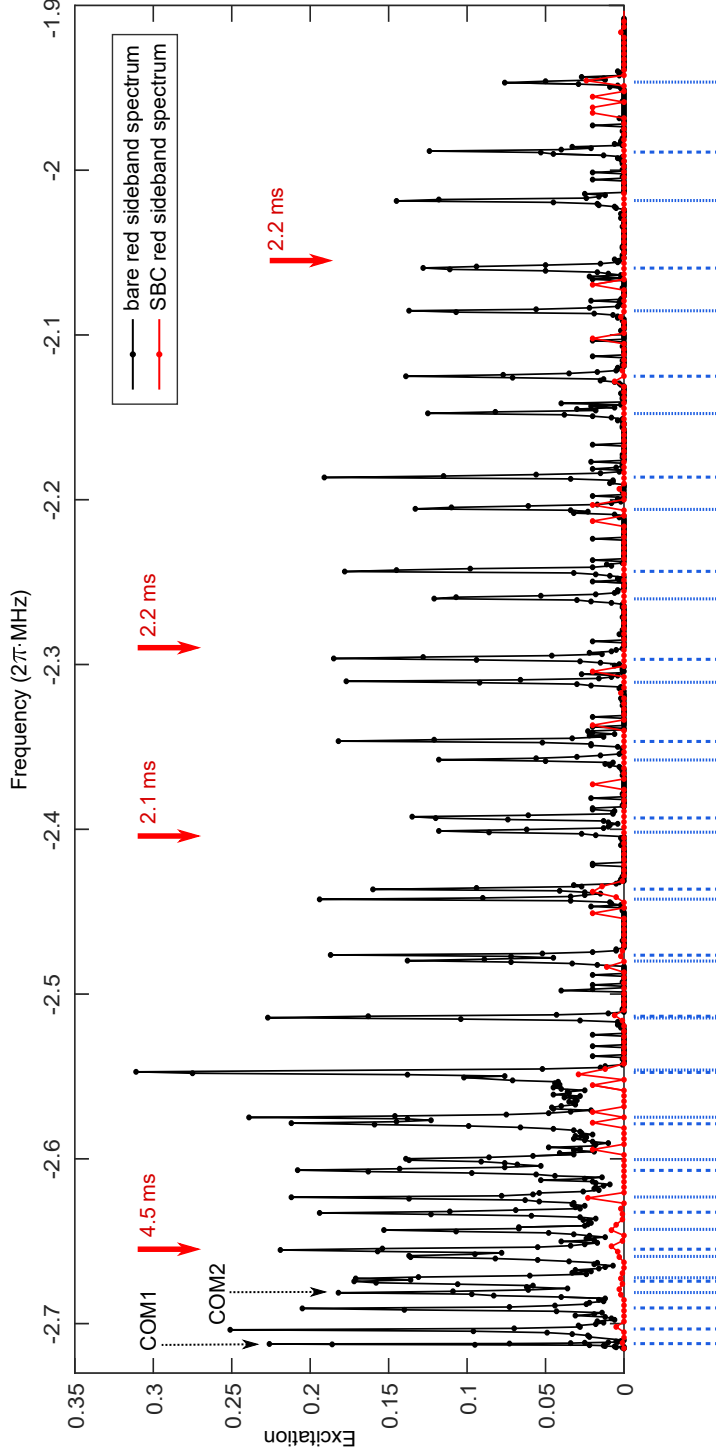


**Figure 3.8.:** Red sideband spectrum of the radial motional modes of 20 ions. The spectrum is shown without (black) and with (red) sideband cooling. Red arrows indicate the frequencies of the four sideband cooling pulses and the pulse duration. The trapping frequencies of the ion string are  $\omega_z = (2\pi) 219.4 \text{ kHz}$ ,  $\omega_{\text{rad}}^{\text{COM1}} = (2\pi) 2.712 \text{ MHz}$  and  $\omega_{\text{rad}}^{\text{COM2}} = (2\pi) 2.681 \text{ MHz}$ . The two center-of-mass modes, linked to the two radial directions of motion, are highlighted with COM1 and COM2. The dashed and dotted blue lines below the graph denote the spectrum of both sets of radial motional modes, calculated via the equilibrium positions of the ions in the trap.

### 3.3.2. Spin-spin interaction with tunable interaction range

The red and blue motional sideband of an ion can be excited simultaneously, by applying a bichromatic light field (Fig. 3.10 a)) with frequencies  $\omega_l^\pm = \omega_0 \pm (\omega + \Delta)$ . Both, the resonant ( $\Delta = 0$ ) and off-resonant ( $\Delta \neq 0$ ) case result in very interesting ion-light interactions.

#### Resonant bichromatic field

When the red and blue motional sideband are excited simultaneously and resonantly, the arising interaction is described by the sum of the two Hamiltonians (3.16) and (3.17), with the coupling strengths  $\Omega_{n-1,n} = \Omega_{n,n+1} = \Omega$  made equal:

$$H_{\text{bic}} = i\hbar\eta\frac{\Omega}{2} (\sigma_+ a e^{-i\phi_r} - \sigma_- a^\dagger e^{i\phi_r}) + i\hbar\eta\frac{\Omega}{2} (\sigma_+ a^\dagger e^{-i\phi_b} - \sigma_- a e^{i\phi_b}), \quad (3.18)$$

with  $\phi_r$  and  $\phi_b$  denoting the phases of the red and blue detuned light fields, respectively. Using the definitions

$$\phi_+ = \frac{\phi_r + \phi_b}{2} - \frac{\pi}{2} \quad \text{and} \quad \phi_- = \frac{\phi_r - \phi_b}{2}$$

we can rewrite Hamiltonian (3.18)

$$H_{\text{bic}} = \hbar\eta\frac{\Omega}{2} \{\sigma_x \cos(\phi_+) + \sigma_y \sin(\phi_+)\} \{(a^\dagger + a) \cos(\phi_-) + i(a^\dagger - a) \sin(\phi_-)\}. \quad (3.19)$$

In this form, we immediately see that the Hamiltonian simultaneously couples all states

$$\begin{aligned} |\downarrow, 0\rangle &\leftrightarrow |\uparrow, 1\rangle \leftrightarrow |\downarrow, 2\rangle \leftrightarrow |\uparrow, 3\rangle \leftrightarrow \dots \quad \text{and} \\ |\uparrow, 0\rangle &\leftrightarrow |\downarrow, 1\rangle \leftrightarrow |\uparrow, 2\rangle \leftrightarrow |\downarrow, 3\rangle \leftrightarrow \dots \end{aligned}$$

It effectively describes an oscillating force, which resonantly drives the harmonic oscillator representing the ion's motional state. Fig. 3.9 a)-b) shows, how a resonant driving force displaces the motional ground state  $|0\rangle$  in phase space to a coherent motional state

$$|\alpha\rangle = \sum_n e^{-|\alpha|^2/2} \frac{\alpha^n}{\sqrt{n!}} |n\rangle, \quad (3.20)$$

where  $|n\rangle$  are the Fock states, indicating the number of phonons  $n$  in the system, and  $\alpha$  contains the amplitude, frequency and phase information of the driving field [17, 84]. In contrast to the standard model of a driven quantum harmonic oscillator, the driving

force in Eq. (3.19) is spin-dependent and displaces the two electronic eigenstates  $|\pm\rangle_x$  of Hamiltonian  $H_{\text{bic}}$  into opposite directions in phase space [90], as depicted in Fig. 3.9 c). Consider the case where  $\phi_r = \phi_b = \pi/2$  such that  $\phi_+ = \phi_- = 0$ , and apply Hamiltonian  $H_{\text{bic}}$  to a qubit in an equal superposition of eigenstates  $|\downarrow\rangle = \frac{1}{\sqrt{2}}(|+\rangle_x - |-\rangle_x)$  and in the motional ground state  $|0\rangle$ . The corresponding unitary time evolution  $U(t)$  can be written in terms of the displacement operator  $\hat{D}(\alpha) = e^{\alpha a^\dagger - \alpha^* a}$ , with  $\alpha = -\frac{i\eta\Omega t}{2}$ :

$$\begin{aligned} |\psi(t)\rangle &= U(t) |\downarrow\rangle |0\rangle = e^{-iH_{\text{bic}}t} \frac{1}{\sqrt{2}} (|+\rangle_x - |-\rangle_x) |0\rangle \\ &= \frac{1}{\sqrt{2}} e^{-i\frac{\eta\Omega}{2}\sigma_x(a^\dagger+a)t} (|+\rangle_x - |-\rangle_x) |0\rangle = \frac{1}{\sqrt{2}} \hat{D}(\alpha) (|+\rangle_x - |-\rangle_x) |0\rangle \\ &= \frac{1}{\sqrt{2}} (|+\rangle_x |\alpha\rangle - |-\rangle_x |-\alpha\rangle), \end{aligned} \quad (3.21)$$

The resulting state  $|\psi(t)\rangle$ , referred to as motional Schrödinger cat state [91, 92], is a superposition of coherent states  $|\pm\alpha\rangle$  that are maximally entangled with the qubit states  $|\pm\rangle_x$ . The situation becomes particularly interesting, when the bichromatic light field is applied to multiple ions, as will be discussed in the following subsections.

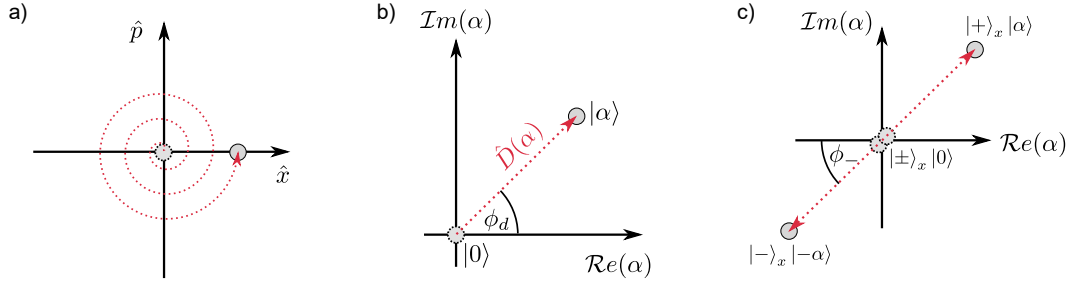


**Figure 3.9.: Effect of a resonant driving force.** **a)** Phase space picture of the particle trajectory for a resonantly driven harmonic oscillator, initially at rest. The amplitude of the trajectory is steadily increasing with time. The size of the grey circle represents the particles uncertainties in position and momentum. **b)** Phase space picture in the co-rotating frame. The motional ground state  $|0\rangle$  is displaced by the operator  $D(\alpha)$  on a straight line, to a coherent state  $|\alpha\rangle$ .  $\phi_d$  is the phase relation between the harmonic oscillator and the driving force. **c)** A resonant bichromatic light field pushes the two eigenstates  $|\pm\rangle_x$  of  $H_{\text{bic}}$  in opposite directions. The angle of the trajectories is determined by the phase difference  $\phi_-$  between the red and blue light field component.

### Off-resonant bichromatic field - MS entangling gate

We now consider the case, in which the applied bichromatic laser field is detuned by an amount  $\Delta$  from the red and blue motional sidebands (Fig. 3.10 c)), such that  $\omega_l^\pm = \omega_0 \pm (\omega + \Delta)$ . The additional detuning expresses itself as additional, time-

dependent light phase in the red and blue sideband transitions, (3.16) and (3.17):  $\phi_r = \phi_{r,0} - \Delta t$ ,  $\phi_b = \phi_{b,0} + \Delta t$ . Therefore, the motional phase becomes time-dependent  $\phi_- = (\phi_{r,0} - \phi_{b,0})/2 - \Delta t$  such that eigenstates of  $\sigma_x$  are no longer displaced on a straight line in phase space as in Fig. 3.9, but their direction changes continuously with  $\Delta t$ , such that they evolve along circles and return to their initial position after the time  $\tau = 2\pi/|\Delta|$  (Fig. 3.10 b)). This situation effectively describes an off-resonantly driven harmonic oscillator. In contrast to a classical oscillator, however, the enclosed area appears as accumulated phase in the quantum mechanical wave function (see definition of  $\Phi$  in Eq. (3.24)). Choosing  $\phi_{r,0} = \pi$  and  $\phi_{b,0} = 0$  for simplicity, the corresponding interaction Hamiltonian reads as

$$H_{\text{MS}}^{(1)} = i\hbar\eta\frac{\Omega}{2}\sigma_x(a^\dagger e^{-i\Delta t} - ae^{i\Delta t}). \quad (3.22)$$

We now apply this detuned, bichromatic field to two ions and focus on coupling to the sidebands of the center-of-mass (COM) mode of the ion pair. This configuration was first studied by A. Sørensen and K. Mølmer as well as E. Solano [23–25] and allows for entangling the internal states of the qubits via their joint motional mode. Detailed derivations of the Hamiltonian and its application to trapped ions are thoroughly covered in Ref. [82, 93]. Here, I will briefly summarize the important equations and effects, starting from the two-qubit Mølmer-Sørensen (MS) interaction Hamiltonian, directly deduced from Eq. (3.22):

$$H_{\text{MS}}^{(2)} = i\hbar\eta'\frac{\Omega}{2}S^x(a^\dagger e^{-i\Delta t} - ae^{i\Delta t}), \quad (3.23)$$

with  $S^x = \sigma_1^x + \sigma_2^x$ , where  $\sigma_1^x$  and  $\sigma_2^x$  denote the Pauli spin-operators for ion 1 and 2, respectively, and  $\eta'$  is the Lamb-Dicke parameter of the respective two-qubit system. The corresponding unitary evolution of this time-dependent Hamiltonian is given by

$$U_{\text{MS}}(t) = \hat{D}(\alpha(t)S^x)e^{i\Phi(t)(S^x)^2}, \quad (3.24)$$

with  $\alpha(t) = i\left(\frac{\eta'\Omega}{2\Delta}\right)(e^{-i\Delta t} - 1)$  and  $\Phi(t) = \left(\frac{\eta'\Omega}{2\Delta}\right)^2(\sin(\Delta t) - \Delta t)$ .

The time-dependent displacement operator is again defined by  $\hat{D}(\alpha) = e^{\alpha a^\dagger - \alpha^* a}$ . As mentioned above, and shown in Fig. 3.10 b), qubits in the eigenstates  $|++\rangle_x$  and  $|--\rangle_x$  are displaced on circles in phase space. The enclosed area is proportional to the accumulated phase  $\Phi$ , called geometrical or Berry phase. States  $|+-\rangle_x$  and  $|-+\rangle_x$

instead, remain stationary, since the net force cancels<sup>16</sup>.

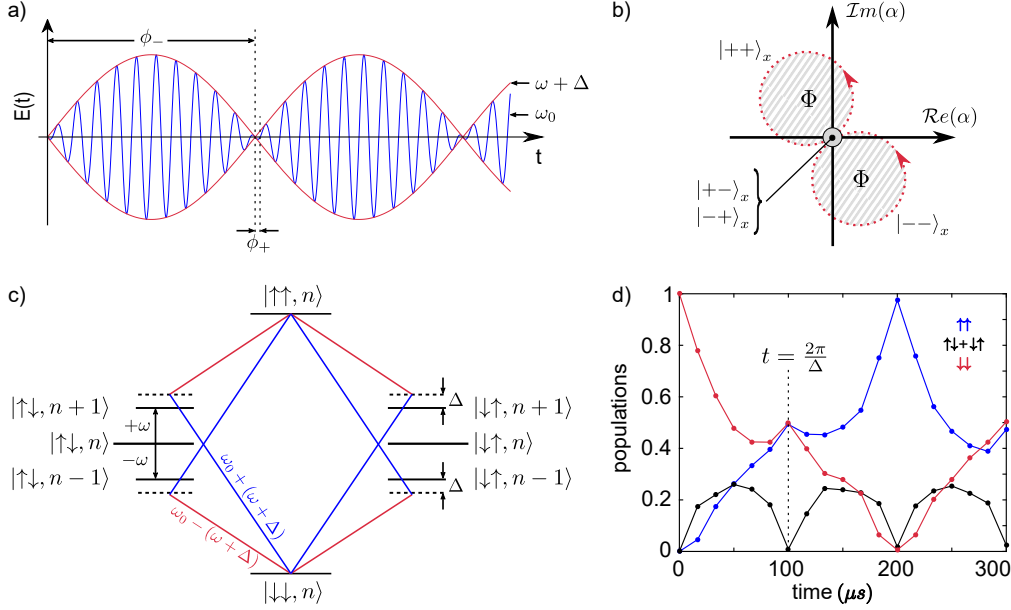


**Figure 3.10.: Schematics to the Mølmer-Sørensen gate.** **a)** Electric field of the beat signal  $E(t) \propto \cos(\omega_0 t + \phi_+) \cos((\omega + \Delta)t + \phi_-)$ , resulting from a bichromatic laser field with frequency components  $\omega_t^\pm = \omega_0 \pm (\omega + \Delta)$ . **b)** The state-dependent force displaces the two-qubit states,  $|++\rangle_x$  and  $|--\rangle_x$ , on circular trajectories with the same direction of rotation but on opposite sites in phase space. The picked up geometric phase is denoted  $\Phi$  and visualized as gray dashed area. For states  $|+-\rangle_x$  and  $|-+\rangle_x$  the net force cancels such that they remain stationary in phase space. **c)** Spin-motion level manifold for two qubits, coupled to a bichromatic laser field with detuning  $\Delta$  from the red and blue motional sidebands  $\pm\omega$ . Motional states are denoted by  $|n\rangle$ , electronic qubit states by  $|\downarrow\rangle$  and  $|\uparrow\rangle$ . The transition  $|\downarrow\downarrow\rangle \leftrightarrow |\uparrow\uparrow\rangle$  is coupled via constructive interference of the four paths. The states  $|\downarrow\uparrow\rangle \leftrightarrow |\uparrow\downarrow\rangle$  are coupled equivalently. **d)** Experimental data of the electronic state population in the z-basis as a function of time, for two ions driven by a bichromatic light field with detuning  $\Delta = (2\pi) 9.9$  kHz. An entangled state is created after  $t \approx 100 \mu\text{s}$ .

When applying the unitary (3.24) for a multiple of the time  $\tau_{\text{gate}} = 2\pi/|\Delta|$ , the displacement operator becomes one and the accumulated phase  $\Phi$  is left in the electronic states:

$$U(\tau_{\text{gate}}) = e^{-i\left(\frac{\eta'\Omega}{\Delta}\right)^2 \pi \sigma_1^x \sigma_2^x}.$$

This means, that the motional state returns to its initial state and the transition states are not populated any more. At this point spin and motion have disentangled and the gate is independent of the motional state of the qubits. Moreover, a Rabi frequency of  $\Omega = |\Delta|/(2\eta')$  yields the unitary of the MS entangling gate, as it was introduced in

<sup>16</sup>Note that this is only true for the COM mode, whereas for the 2-qubit stretch mode the exact opposite statement holds.

Section 2.1.2:

$$U_{\text{MS}} = e^{-i\frac{\pi}{4}\sigma_1^x\sigma_2^x\text{sign}(\Delta)}, \quad (3.25)$$

with corresponding Hamiltonian

$$H_{\text{MS}}(\tau_{\text{gate}}) = \hbar\frac{\pi}{4}\text{sign}(\Delta) \cdot \sigma_1^x\sigma_2^x. \quad (3.26)$$

When applied to the states  $|\downarrow\downarrow\rangle$ ,  $|\downarrow\uparrow\rangle$ ,  $|\uparrow\downarrow\rangle$  or  $|\uparrow\uparrow\rangle$ , this corresponds to a maximally entangling gate. In order to keep the coupling to the carrier transition low, the Rabi frequency  $\Omega$  has to be small compared to the detuning  $(\omega + \Delta)$  from the carrier. Considering the above mentioned condition for a maximally entangling gate,  $\Omega \propto \eta^{-1}\tau_{\text{gate}}^{-1}$ , the question of whether  $\Omega \ll (\omega + \Delta)$  holds, becomes crucial in the limit of desirable fast gate operations. Additional shaping of the laser pulse as a Blackman window, suppresses off-resonant carrier excitation further [82].

Fig. 3.10 d) shows the temporal evolution of the initial state  $|\downarrow\downarrow\rangle$  under unitary (3.24) with a detuning  $\Delta = (2\pi) 9.9$  kHz. The plotted electronic state populations arise from the interference of the four paths in Fig. 3.10 c). An entangled state, close to the Bell state  $|\Psi\rangle = 1/\sqrt{2}(|\downarrow\downarrow\rangle - i|\uparrow\uparrow\rangle)$ , is generated at time  $t = 2\pi/\Delta \approx 100 \mu\text{s}$ . A short tutorial of how to experimentally set up a MS entangling gate in our experiment is given in Appendix B.

### Ising and XY-Hamiltonian

We now introduce an additional asymmetric detuning  $\delta \ll \Delta$ , named centerline detuning, to the bichromatic laser field such that the two laser components have frequencies  $\text{bic}_{\pm} = \pm(\omega + \Delta) + \delta$  as shown in Fig. 3.11 a). As in the previous subsections, we can derive the Hamiltonian for this configuration by summing (3.16) and (3.17), with the corresponding laser frequencies and choosing  $\phi_+ = \phi_- = 0$ :

$$H_{\text{asym.bic}} = \hbar\eta\frac{\Omega}{2}(ae^{i\Delta t} + a^\dagger e^{-i\Delta t})(\sigma^+ e^{-i\delta t} + \sigma^- e^{i\delta t}).$$

For  $N$  ions,  $\sigma^\pm$  are extended to global spin operators,  $S^\pm = \sum_i^N \sigma_i^\pm$ , where  $\sigma_i^\pm$  denotes the spin raising and lowering operator acting on ion  $i$ . Assuming that we couple to a center-of-mass mode of the  $N$ -ion string, the coupling parameter  $\eta$  is equal for all ions and reduces by a factor  $1/\sqrt{N}$ :

$$H_{\text{asym.bic}} = \hbar\frac{\eta}{\sqrt{N}}\frac{\Omega}{2}(ae^{i\Delta t} + a^\dagger e^{-i\Delta t})(S^+ e^{-i\delta t} + S^- e^{i\delta t}), \quad (3.27)$$

If the coupling strength of the bichromatic light field on the sidebands is much weaker than the detuning from the sidebands,  $\eta\Omega \ll \Delta$ , the system is said to be in the weak coupling regime. In this regime, the qubit-light interaction hardly changes the motional state, and consequently spin and motion of the qubit are only virtually entangled at all times, not only at  $\tau_{\text{gate}}$ . An excellent approximation for such an interaction is an effective Hamiltonian which describes correlated spin flips and results from (3.27) after applying the Magnus expansion and Taylor approximation in  $\delta/\Delta$  [87, 90]:

$$H_{\text{spin-spin}} = \hbar J \sum_{i,j}^N \left( \sigma_i^+ \sigma_j^+ e^{-2i\delta t} + \sigma_i^+ \sigma_j^- + \sigma_i^- \sigma_j^+ + \sigma_i^- \sigma_j^- e^{2i\delta t} \right), \quad (3.28)$$

with the spin-spin coupling strength  $J = \Omega\eta/(\sqrt{N}2\Delta)$ . The experiments presented in this work were performed in two different regimes, accessible by tuning the parameter  $\delta$ :

- $\delta \approx J$ : The transformation into the interaction picture with respect to the Hamiltonian  $H_0 = -\frac{\delta}{2} \sum_i \sigma_i^z$  yields a time-independent form of (3.28), the so-called transverse field Ising-Hamiltonian

$$H_{\text{Ising}} = U_0^\dagger (H_{\text{spin-spin}} - H_0) U_0 = \hbar J \sum_{i,j}^N \sigma_i^x \sigma_j^x + B \sum_i \sigma_i^z, \quad (3.29)$$

where  $B = \delta/2$  corresponds to an effective transverse magnetic field, directly depending on the detuning  $\delta$ .

- $\delta \gg J$ : Here, we can apply the rotating wave approximation, neglecting terms oscillating at  $\delta$  such that the interaction simplifies to an effective XY-Hamiltonian

$$H_{\text{XY}} = \hbar J \sum_{i,j}^N \left( \sigma_i^+ \sigma_j^- + \sigma_i^- \sigma_j^+ \right). \quad (3.30)$$

The energy spectrum of this Hamiltonian with the ground state  $|\downarrow\downarrow \dots \downarrow\rangle$ , is split into  $N+1$  subspaces, identified by the number of excitations  $|\uparrow\rangle$  in the system [94]. Transitions between subspaces involve additional spin flips, which become energetically more and more unfavourable, with increasing detuning  $\delta$ . Therefore, Hamiltonian (3.30) is excitation conserving. In our experiment, we typically work in the regime where transitions between energy subspaces are strongly suppressed.

So far, we only considered the case where the bichromatic laser field couples to the COM mode of an ion string. In this mode all ions move with the same amplitude

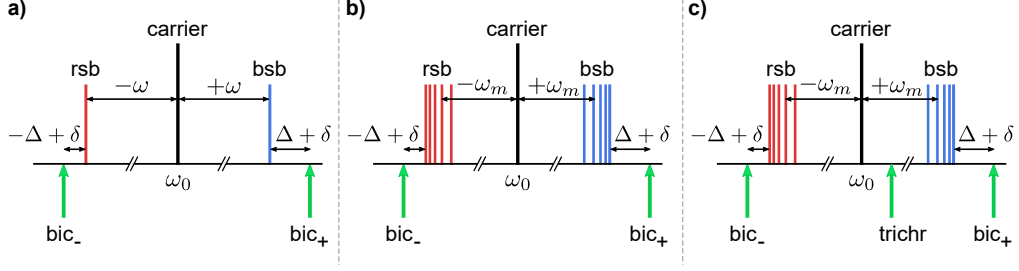


**Figure 3.11.: Schematic transition spectrum and arrangement of the interaction beams.** The carrier transition is denoted as high black line at frequency  $\omega_0$ , red (rsb) and blue (bsb) radial sidebands are denoted as red and blue lines at frequencies  $\pm\omega$ . Green arrows represent the laser fields, inducing interesting spin-spin interactions. **a)** Bichromatic laser field with asymmetric detuning  $\delta \ll \Delta$  from the COM mode. For  $\delta = 0$ , the field induces the MS-interaction. Tuning  $\delta > 0$  induces the transverse field Ising-Hamiltonian or the XY-Hamiltonian. **b)** If  $N$  motional modes couple to a bichromatic field, the spin-spin interaction strength decays approximately as  $J_{ij} \propto 1/|i-j|^\alpha$ , where the interaction range  $\alpha$  can be tuned by the parameter  $\Delta$ . **c)** A third frequency component (trichr) is added to the laser field in order to compensate the AC-Stark shifts arising from the asymmetric coupling of the bichromatic field to the ion's transitions.

and phase, which reflects in a single Lamb-Dicke parameter,  $\eta$ , for all ions. If the bichromatic light field couples to several motional modes (Fig.3.11 b)), we need to introduce a generalized, non-uniform Lamb-Dicke parameter  $\eta_{i,m}$  for each ion  $i$  and each mode  $m$ . The coupling,  $J_{ij}$ , between a pair of ions  $i$  and  $j$ , is then given by the sum over all couplings mediated by the different motional modes. In other words,  $\eta_{i,m}$  imprints the structure of each motional mode  $m$ , with frequency  $\omega_m$  onto the coupling matrix  $J_{ij}$  [90, 95]:

$$J_{ij} = \frac{\Omega^2}{2} \sum_m \eta_{i,m} \eta_{j,m} \cdot \frac{\omega_m}{(\omega + \Delta)^2 - \omega_m^2}, \quad \text{with} \quad (3.31)$$

$$\eta_{i,m} \eta_{j,m} = b_{i,m} b_{j,m} \frac{\hbar k^2}{2M\omega_m}. \quad (3.32)$$

Here,  $b_{i,m}$  represent the eigenvectors of the motional modes and  $M$  is the ion mass. The coupling matrix  $J_{ij}$  approximately follows a power law decay with ion-ion distance  $|i-j|$  [96, 97]:

$$J_{ij} \propto \frac{1}{|i-j|^\alpha}. \quad (3.33)$$

where the interaction range  $\alpha$  can be tuned, by changing the detuning  $\Delta$  and thereby modifying the relative contribution of each mode. In the limit of small  $\Delta$ , the laser field mainly couples to the COM mode, inducing an infinite range interaction with  $\alpha = 0$ . For a large detuning  $\Delta$ , however, all modes are degenerate and couple equivalently

strong, which results in an interaction with dipolar decay at  $\alpha = 3$ . Note that those extreme cases are difficult to achieve experimentally: For a very small detuning  $\Delta$ , the system would no longer be in the weak coupling regime<sup>17</sup>, while for a very large detuning, the overall coupling strength would decrease to zero.

One technical innovation that was realized within my doctoral studies, was the modification of the single-ion addressing unit, such that the effective magnetic field  $B$  in Hamiltonian (3.29) is not restricted to be time-independent and homogeneous over all ions. Instead, it is now possible to disturb the spin-spin interaction dynamically and for each ion independently:  $H_{\text{Ising}} = \hbar J \sum_{i,j}^N \sigma_i^x \sigma_j^x + \sum_i B_i(t) \sigma_i^z$ . Section 4.4 presents details on the modification and Chapter 6 discusses an experimental application.

### Trichromatic light field

In an ideal two-level system, the AC-Stark shift, induced by the off-resonant bichromatic light field on the carrier transition would cancel, since the detuning is symmetric with respect to that transition. However, in real ions the light field additionally couples off-resonantly to all available energy levels of the ions. That is, it couples to the dipole transitions and the other quadrupole transitions within the  $S_{1/2} \leftrightarrow D_{5/2}$  Zeeman manifold such that a net AC-Stark shift remains. The solution in our experiment is to add a third, off-resonant frequency component to the light field (Fig. 3.11 c)), whose intensity is chosen such that it counteracts the undesired shift [98]. Experimentally, this trichromatic light field is realized by applying three frequencies to a fiber-coupled acousto-optic modulator (AOM)<sup>18</sup>. Furthermore, the intensity distribution of the global laser field which induces the interaction, is non-uniform (but elliptical Gaussian) over the ion string and thus induces spatially dependent AC-Stark shifts. Since all three light fields of the trichromat are coupled to the same fiber, their spatial modes are identical which enables the compensation field to also cancel these spatially dependent AC-Stark shifts. Typical parameters for an experimentally realized spin-spin interaction on 20 ions with trapping frequencies  $\omega_z = (2\pi) 217 \text{ kHz}$ ,  $\omega_{\text{rad}}^{\text{COM1}} = (2\pi) 2.71 \text{ MHz}$  and  $\omega_{\text{rad}}^{\text{COM2}} = (2\pi) 2.68 \text{ MHz}$ , are: detuning  $\Delta = (2\pi) 40 \text{ kHz}$ , centerline detuning  $\delta = (2\pi) 3 \text{ kHz}$  and trichromat frequency  $\Delta_{\text{trichr}} = (2\pi) 1.2 \text{ MHz}$ . A detailed description on how to experimentally set up the spin-spin interactions and calibrate the AC-Stark shift compensation beam, can be found in P. Jurcevic's thesis [87].

<sup>17</sup>To achieve long-range interactions,  $\alpha \approx 0$ , a better strategy is to use a bichromatic beam along the principle axis of the ion string and thereby induce the interaction over the axial COM mode, instead of the radial modes.

<sup>18</sup>Gooch&Housego, model SFO4912-T-M150-0.5C2W-3-F2P-01



## 4. Experimental setup and technical innovations

All experiments presented in this work, have been carried out at the Institute of Quantum Optics and Quantum Information (IQOQI). The linear Paul trap, the vacuum system, the basic laser system and the computer control were set up by my predecessors, and to a large extent, their original setups are still used. Detailed descriptions can be found in the corresponding diploma and PhD theses [63, 82, 99–101]. In the following I focus on those significant modifications of the experimental setup and software, which substantially contributed to the results presented in Chapters 5, 6 and 7.

### 4.1. Overview

The macroscopic linear Paul trap, shown in Fig. 4.1 a) forms the heart of the experiment. It is based on a blade design [102], with an electrode-ion distance of  $565\ \mu\text{m}$  and additional holes, with  $0.5\ \text{mm}$  diameter, through the tip electrodes allowing for direct optical access along the principal axis of the ion string. Stray electric fields on the linear Paul trap can push the ion out of the RF null along the trap's symmetry axis, and therefore induce excess micromotion. Additional micromotion compensation electrodes along the axial direction are used to counter these stray fields and minimize micromotion (for details see Ref. [63]).

The vacuum vessel, illustrated in Fig. 4.1 b), encloses the ion trap. It is an octagon made of 316 stainless steel, with eleven flanges for optical access, three connected vacuum pumps and a residual gas analyzer (RGA), allowing for in-situ vacuum diagnostics. The trap holder is attached to the top flange, together with the RF power feedthrough that connects to the helical resonator. The voltages for the tip and compensation electrodes are provided through a low-pass filter board on an adjacent high-voltage feedthrough. The commercial calcium oven is mounted on the bottom flange, next to a non-evaporative getter (NEG). A six-way cross on the western horizontal flange carries a titanium sublimation pump, an ion pump and a Bayard-Alpert ion gauge. See C. Hempel's thesis [63] for more details. The optical access points of the vacuum chamber

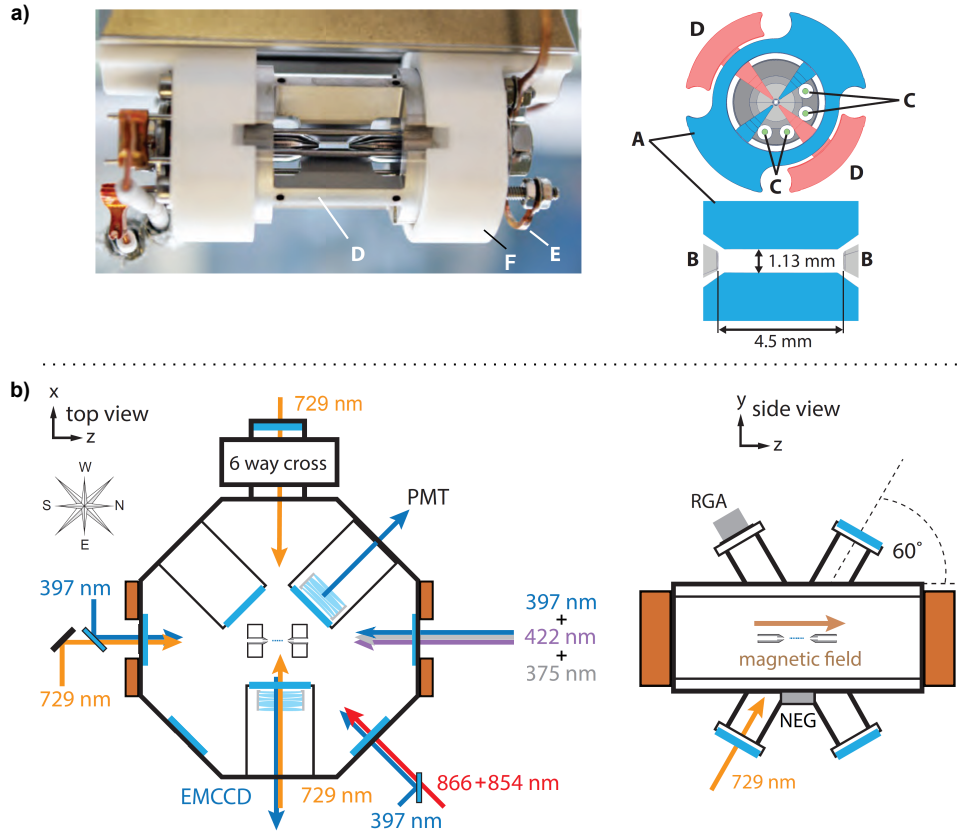


**Figure 4.1.:** a) **Linear Paul trap.** Photograph and schematic drawing, showing the ground (A) and RF (D) blades, the tip shaped electrodes (B) and the micromotion compensation electrodes (C). The RF blades are connected in series by a copper bridge (E). All parts are kept together by a Macor holder (F). b) **Schematic drawings of the vacuum vessel with beam and imaging directions.** The compass rose on the top left and the laboratory coordinate system (x,y,z), depict the orientation of the chamber and the points of view. Copper holders (brown boxes) on the north and south viewports encase 40 permanent magnets each, which provide a magnetic field along the axial (z) direction of the trap. The originals of these modified pictures are taken from C. Hempel's thesis [63], the photograph was taken by M. Rambach.

and the corresponding laser beams are shown in Fig. 4.1 b). The duration and relative timing of all laser pulses is coordinated with an FPGA-based device, the so-called “Pulse box”. It is equipped with 2 digital inputs and 16 digital outputs and two independent direct digital synthesizers (DDS). The DDSs are used to set the frequency, phase and pulse shape of the RF signals sent to the AOMs for coherent qubit manipulation and single-ion addressing. As part of my doctoral work, the following major changes were implemented with respect to the setup reported in previous theses [63, 87]:

- **East viewport, single-qubit addressing:** The single-qubit addressing path

was upgraded with a sample-and-hold intensity stabilization. The circuit reduces laser intensity fluctuations during pulsed gate sequences, right before the beam enters the ion trap (see Section 4.3). Further, within the master project of L. Perntaler [103], the addressing unit was redesigned and subsequently integrated into the ion trap apparatus. The improved optical setup and a new acousto-optic deflector<sup>19</sup> (AOD) enable individual-qubit addressing of up to 50 ions. The new AOD has a process time of  $11.3 \mu\text{s}$ , which required adding a delay in the start time for single-ion addressing pulses<sup>20</sup>. Finally, we found that our Pulse box switches off the RF to the AOD (DDS2 in the Pulse box), for about 300 ms after each data point. This leads to a varying temperature level of the AOD, which results in intensity variations in the addressing beam. To circumvent this problem, we installed an additional DDS (DDS60), which continuously sends an RF of 80 MHz and 29.5 dBm to the AOD, whenever it is not controlled by the Pulse box itself<sup>21</sup>.

- **North-East viewport:** This beam path is used for Doppler cooling (397 nm) and repumping (854 nm and 866 nm). We facilitated the alignment of the repumping lasers by overlapping of the 854 nm and 866 nm laser beams through a customized dichroic beam combiner<sup>22</sup> and coupling both to a single photonic crystal fiber<sup>23</sup>. Further, the fiber coupler of the 397 nm was replaced with customized anamorphic beam shaping optics<sup>24</sup>. This generates an elliptical beam with  $147 \mu\text{m} \times 375 \mu\text{m}$  full axes lengths at the position of the ions, which enables homogeneous Doppler cooling and fluorescence detection of long ion strings (see Section 4.2).
- **North viewport:** We overlapped the beam paths for the two photoionization lasers (375 nm and 422 nm) and a 397 nm beam and coupled all three beams into a single fiber to facilitate their alignment through the holes in the tip electrodes of the Paul trap. Here, the latter beam is used to cool the axial ion motion of the ion string using polarization-gradient cooling (see Section 4.6.2). A combination of two achromatic lenses<sup>25</sup>, allows us to focus all three beams to the center of

<sup>19</sup>Acal BFi, Acousto-optic deflector LS55-NIR.

<sup>20</sup>Using the variable “add\_add\_time”, we added a  $11.3 \mu\text{s}$  time delay to the “start\_time” of each pulse which uses the AOD (e.g. the class “rf\_pulse”). This was done in the file “user\_function.py” lying in the folder “C:\IQOQI\expcontrol\python\innsbruck”.

<sup>21</sup>The switch used for this, is toggled by “TTL1”.

<sup>22</sup>Schäfter&Kirchhoff, Multicube 48MC-LI-19.5 with polarization beam cube 48PM-CC-B.

<sup>23</sup>NKT Photonics, aeroGUIDE-5-PM-A LMA-PM-5, with FC/APC connectors.

<sup>24</sup>Schäfter&Kirchhoff, 60SMS-1-4-A11-01 coupler with anamorphic beam shaping optics 5AN-3-V-35 and micro-focusing optics 5M-S325-33-S.

<sup>25</sup>Edmund Optics, NUV 12.5 X 40 UV-VIS CTD #65-973 and NUV 50 x 200 UV-VIS TS #35-997.

the ion trap with minimized deviation of the focal points caused by the different wavelengths.

- **West viewport, collective qubit-manipulation:** This beam path is used to drive collective spin-rotations and to realize spin-spin interactions by applying three RF signals to an AOM, generating a trichromatic laser beam (see Section 3.3.2). A new fiber-AOM<sup>26</sup>, where both the input and output path are fiber-coupled, was integrated into the setup. This bilateral fiber-coupled AOM eliminates anti-correlated intensity fluctuations between the three frequency components, that are caused by beam pointing drifts when coupling free space into an AOM. Since the new fiber AOM runs at a center frequency of 150 MHz (instead of 80 MHz), we installed two new DDSs: DDS27 drives the fiber AOM at 145.5 MHz and 0 dBm, with the option of toggling a trichromatic field, where frequency components are added through RF combiners. The second DDS (DDS26) continuously drives an upstream AOM at 65.5 MHz and  $-1.5$  dBm, to achieve a frequency shift of 80 MHz<sup>27</sup>. Further, this path was upgraded with sample-and-hold intensity stabilization (see Section 4.3).
- **South viewport:** The 397 nm beam constitutes the second arm of the polarization-gradient cooling setup (Section 4.6.2). Its fiber coupler was replaced such that the foci of the two counter-propagating beams match.

## 4.2. 51 Doppler cooled and coherently manipulated ions

Customized anamorphic beam shaping optics generates an elliptical beam profile (Fig 4.2 a)) for the 397 nm laser, used for Doppler cooling and state detection. This enables homogeneous illumination, and thereby homogeneous Doppler cooling and detection fluorescence of long ion strings, at reduced intensity losses. Unfortunately, the wavelength difference is too large to get a comparable optical effect on 397 nm, 866 nm and 854 nm light simultaneously, as shown in Fig. 4.2 b)-c). This prevents the insertion of the two repumping lasers through the same fiber coupler as the 397 nm beam.

The second technical challenge is the uniform and single-ion resolved detection of a long ion string, using our custom imaging objective<sup>28</sup> and a back-lit EMCCD camera<sup>29</sup>.

<sup>26</sup>Gooch&Housego, SFO4912-T-M150-0.5C2W-3-F2P-01.

<sup>27</sup>All qubit manipulation lasers obtain a frequency shift of 80 MHz by the final single-pass AOMs used for fast pulse switching.

<sup>28</sup>Sill Optics, S6 ASS 2241

<sup>29</sup>Andor iXon “blue” DU-897-DCS-BBB, with custom AR-coated front window with 89.27 % transmission at 397 nm.

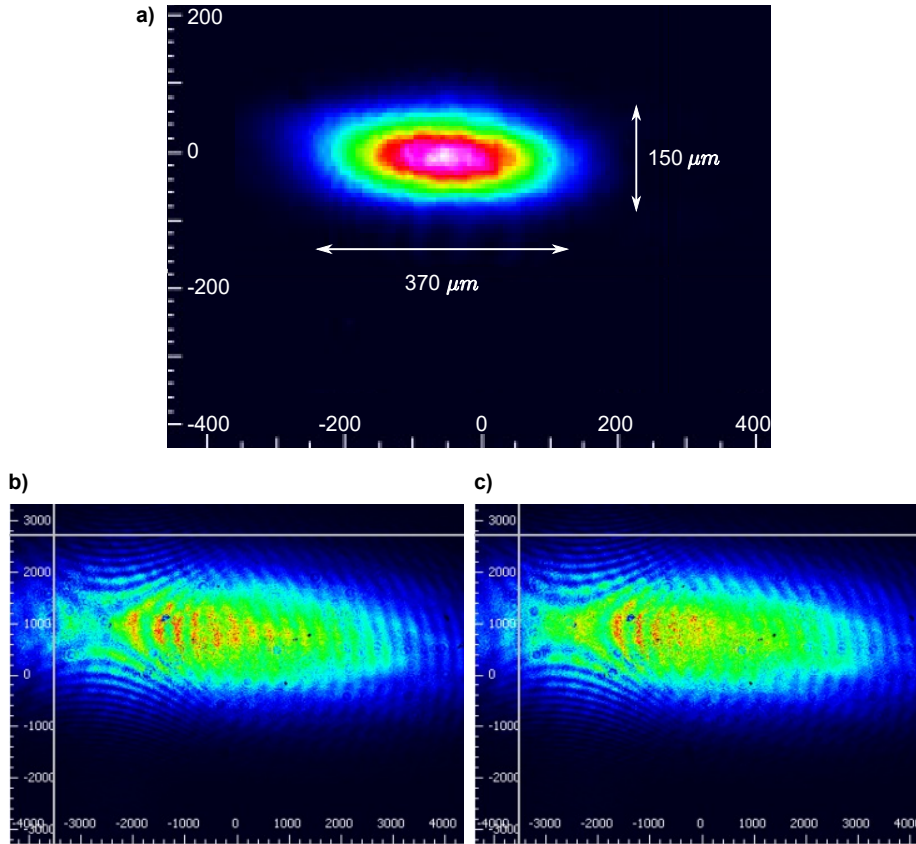


**Figure 4.2.: Effect of the elliptical beam shaping optics.** **a)** The 397 nm beam measures Gaussian diameters of  $147 \mu\text{m}$  and  $375 \mu\text{m}$ , at the position of the ions. **b)** Effect on the 854 nm beam:  $8300 \mu\text{m} \times 2800 \mu\text{m}$ . **c)** Effect on the 866 nm beam:  $8300 \mu\text{m} \times 2900 \mu\text{m}$ . All profiles were recorded with the Thorlabs camera beam profiler BC106-VIS.

A Labview program associates pixels of interest to each ion, based on a maximum likelihood detection algorithm (see C. Hempel's thesis [63] for details). Depending on the maximum detected fluorescence, the program assigns all pixels whose fluorescence level lies above an adjustable *brightness threshold* (for 10 ions we typically choose 35% of the maximum value). From these regions of interest for each ion, the software determines the individual quantum states.

The imaging path was originally designed to map a  $<100 \mu\text{m}$  long object to the camera chip. Straight ion strings with 50 ions, however, extend over more than  $200 \mu\text{m}$ . Hence, the fluorescence of the outermost ions is not efficiently captured and the state detection program fails at assigning pixels of interest to those ions, for reliable quantum state detection (Fig. 4.3 a)). Simply increasing the brightness threshold for all ions, overexposes the center ions, which results in overlapping regions of interest and thereby

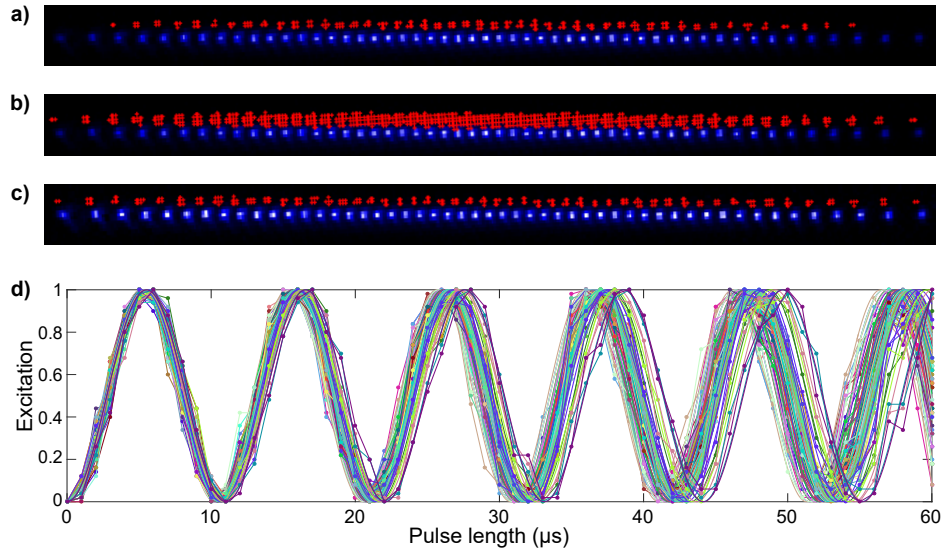


**Figure 4.3.:** Imaging of long ion strings. **a)** Section of a camera image without correction multiplier, brightness threshold 35 %. Pixels of interest (red dots) are only assigned to 48 out of 51 ions (light blue). For better visualization, the computed array of pixels of interest is shifted by two pixels left and five pixels up, with respect to the ion picture. The selected image section contains about  $22 \times 380$  pixels. **b)** Image without correction multiplier, brightness threshold 15 %. All 51 ions are identified, but the pixels of interest of the center ions overlap. **c)** Image with correction multiplier, brightness threshold 35 %. All 51 ions are identified and pixels of interest are assigned without overlap. **d)** Collective Rabi flops on 51 ions. Connected points are experimental data, solid lines are fits of the type  $y = \sin^2(\alpha \cdot x)$ . The elliptical but still Gaussian beam profile of the driving laser causes lower Rabi frequencies for the outer ions in the chain. This is observable as fanning out of the individual Rabi flops.

wrong quantum state assignment (Fig. 4.3 b)). In order to solve this problem, the entire detection image is multiplied<sup>30</sup> with a correction function  $C$  that varies over the length  $l$  of the ion string. The best performance for 50 ions is observed with the function  $C = a \cdot |l|^b + 1$ , with  $a = 1.7$ ,  $b = 2.5$ . This function amplifies the brightness for the outer ions by a factor 2.7, while leaving the value of the innermost ion unchanged. Fig. 4.3 c) shows a successful assignment of pixels of interest to all ions in the string. Finally, this allowed us to drive and detect collective, coherent qubit-rotations on 51 ions, as shown in Fig. 4.3 d).

During the writing of this work, an aperture in the imaging path, right in front of the camera chip, was expanded such that the fluorescence of the outermost ions is no longer shielded (see T. Brydges’ thesis [60]). Nevertheless, we use the image correction feature

<sup>30</sup>This image correction can be turned on or off using the “Ion image correction” button at the lower right corner of the camera program, while variables  $a$  and  $b$  are adjustable in the “Reference Pictures” tab. The SubVI that executes the correction is called “pictureMultiplier.vi” and is integrated in “PikTURE.vi”, which evaluates the raw camera images.

for strings of  $\sim 50$  ions, where the regions of interest for the middle ions can overlap and compromise correct quantum state assignment. In the long-term we should replace the imaging software by a more advanced program, which assigns regions of interest to each ion individually, independent of the maximum fluorescence level, and which can deal with overlapping regions of interest.

### 4.3. Sample-and-hold laser intensity stabilization

We stabilize the laser intensity on both the single-ion addressing path and the laser path perpendicular to the principal axis of the ion crystal, used for collective qubit-manipulation. In both paths, a pellicle beamsplitter is used to reflect 8% of the beam onto a 2.5 MHz USB-photodiode, which provides the control variable for a sample-and-hold stabilization circuit<sup>31</sup>. A trigger, fed through the “PID” input, toggles the sampling and holding functions. This allows us to stabilize the laser intensity right before the beams enter the vacuum vessel and even during the pulsing of the lasers in experimental sequences. In the *sampling mode*, the photodiode signal is sampled and the optical intensity is stabilized, by adjusting a voltage-variable attenuator, which regulates the RF amplitude to the last AOM in the optical path. With the trigger’s falling slope, the *holding mode* of the stabilization circuit is initiated and the last value of the correcting variable is applied till the next rising slope of the trigger. Setpoint and gain of the proportional–integral–derivative (PID) control unit are adjustable using external trim-pots, while observing the error signal on an oscilloscope. In both paths, the pellicles are installed after polarizing optics, as shown in Fig. 4.4 a)-b). This way, also polarization fluctuations of the laser beams are reduced, after their transformation into intensity fluctuations. Moreover, the polarization of the two counter propagating beams is chosen such that the collective qubit-manipulation laser has maximum coupling efficiency (Fig. 3.3), while the polarization for the single-ion addressing laser is perpendicular to it<sup>32</sup>. Once each beam passed through the ion trap, the polarization optics of the other path withdraws it. This prevents the two counter-propagating beams from being reflected by some optical components back onto the ions, causing uncontrolled qubit manipulation.

<sup>31</sup>The circuit “PID Controller with S+H V1.1 Chicken 2015” was designed and built by Gerhard Hendl.

<sup>32</sup>Single-ion addressing in our experiment is based on AC-Stark pulses (see Section 3.2.2), for which the polarization of the light field does not play any role.

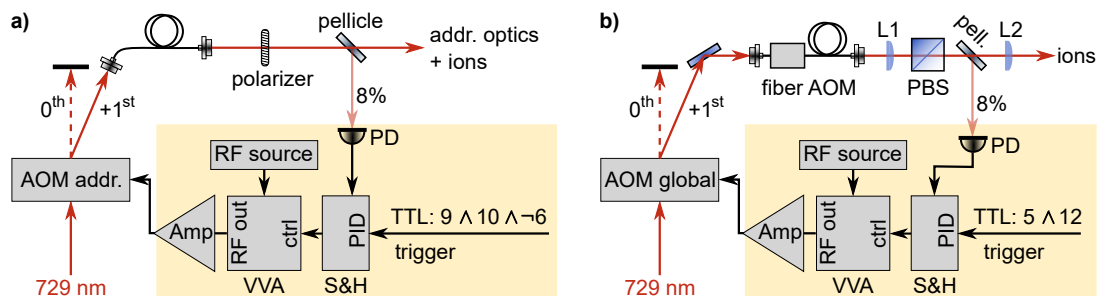


**Figure 4.4.:** Simplified optical and electronic configuration (yellow background) for sample-and-hold (S&H) intensity stabilization. **a)** Single-ion addressing setup. The stabilization optics, consisting of a polarizer and a pellicle, is mounted right before the single-ion addressing optics. A logic circuit, combining three pulse box TTLs, triggers the sampling function during Doppler cooling. **b)** Collective qubit-manipulation setup. The stabilization optics, consisting of a polarizing beam splitter (PBS) cube and a pellicle, is mounted inbetween two cylindrical lenses L1 and L2 [87]. A logic circuit, combining two pulse box TTLs, triggers the sampling function during sideband cooling.

### 4.3.1. Single-ion addressing path

Fig. 4.4 a) shows the optical and electronic arrangement for the intensity stabilization of the single-ion addressing beam. We chose a pellicle<sup>33</sup> as beamsplitter, in order to minimize the influence on the sensitive, tightly focused laser beam. The sampling part is performed in each sequence during Doppler cooling, by including an addressing pulse at 50 MHz RF to the Doppler cooling script<sup>34</sup>. The corresponding trigger consists of three combined transistor-transistor logic (TTL) signals from the pulse box:  $9 \wedge 10 \wedge \neg 6$ . This assures that sampling is performed if and only if the single-ion addressing path carries light (TTL  $9 \wedge 10$ ) and Doppler cooling is executed (inverted TTL 6). Finally, the stabilization circuit reduces intensity fluctuations measured over five minutes from 1.8% to 0.2%.

### 4.3.2. Collective qubit-manipulation path

The optical and electronic configuration is shown in Fig. 4.4 b). Here, the sampling part is triggered by two combined pulse box TTLs:  $5 \wedge 12$ . In an experimental sequence, TTL 5 activates the “Listmode” of the RF function generator used for sideband cooling<sup>35</sup>, and TTL 12 assures that the collective qubit-manipulation path carries light.

<sup>33</sup>Thorlabs BP108

<sup>34</sup>The corresponding Doppler cooling python sequence is called “DopplerCooling40\_sampling.py”.

<sup>35</sup>The “Listmode” in function generator “Rhode&Schwarz SMB 100A” allows us to apply many sideband cooling pulses consecutively, using only one out of the 16 available transitions objects in our control software. The corresponding sequence is called “SBCooling40\_bic.py”.

The beam intensity is therefore sampled during sideband cooling of each sequence. The stabilization circuit reduces intensity fluctuations from 2% to 0.3%.

## 4.4. Simultaneous single-ion addressing

The single-ion addressing beam is used for preparing initial quantum states or performing measurements on individual qubits. For these applications it is sufficient to apply a single radio frequency at a time to the acousto-optic deflector (AOD). This refracts the laser to a single beam which is then tightly focused and subsequently steered towards an ion. Application of multiple radio frequencies to the AOD generates multiple beams and allows us to address multiple ions at the same time. This enables new, interesting experiments, for which simultaneous single-qubit manipulation is required. In the following, I describe the technical extension which was implemented for achieving multiple-ion addressing and highlight important guidance concerning its usage. The final subsection contains some applications and characterization measurements.

### 4.4.1. The arbitrary waveform generator

The most flexible way to generate multiple-frequency waveforms is by an arbitrary waveform generator (AWG). In our experiment, we use a model<sup>36</sup> which is installed on a PCI Express interface and which can be controlled directly by a PC. The AWG has an onboard memory for a fast replay of waveforms, 16 bit resolution, an output rate of 1.25 GS/s, a bandwidth of 400 MHz, and external trigger and clock inputs. Arbitrary waveforms are programmed via a python-interface and output can be obtained in different modes: *single-start*, *continuous loop*, *gated* or *sequenced*. The generated waveform is then sent to an RF switch, which is triggered by the pulse box TTL 11: at low trigger voltage, the AOD receives a single-tone RF from DDS2 of the pulse box. At high trigger voltage, the multi-tone waveform from the AWG is supplied, instead.

Applying a waveform with multiple frequency components

$$y = \sum_{i=1}^N A_i \cdot \sin(\omega_i^{RF} \cdot t) \quad (4.1)$$

to the AOD, generates multiple laser beams, each targeting a different ion and shifted by 60 – 90MHz with respect to the qubit transition (see Fig. 4.5). The RF amplitude  $A_i$  for each beam can be regulated independently, resulting in individually adjustable

---

<sup>36</sup>Spectrum M4i.6631-X8.

AC-Stark shifts on all ions simultaneously, reaching up to a few kHz. Static waveforms, for constant AC-Stark shifts, are programmed with a *gated* trigger. These waveforms consist of a single time segment of typically  $100 \mu\text{s}$ . The gated trigger will continuously replay the waveform during the high voltage period of TTL 11.

Moreover, the AWG allows us to program temporally modulated AC-Stark shifts, by concatenating time segments with different RF amplitudes  $A_i$  in a phase-coherent manner (see I-III in Fig. 4.5). Each segment is typically  $10 \mu\text{s}$  long. For temporally-modulated waveforms, we use the *single-start* trigger, which plays a waveform once, after a single trigger event from TTL 11. Note that a temporally-modulated waveform with a total length of tens of ms, and a resolution of 1 ns, takes several minutes to be generated by the python program. Therefore, it is nice to outsource this task to a separate computer, while running the experiment. Appendix D contains the most important considerations and programs for performing simultaneous single-ion addressing with the AWG in our experiment.

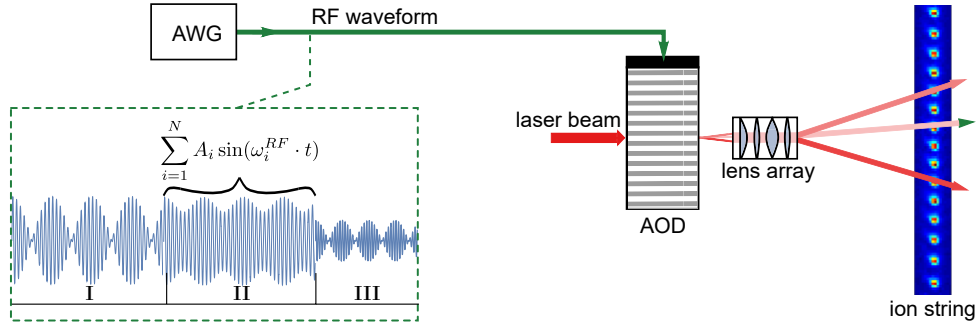


**Figure 4.5.: Schematic AWG setup.** The AWG sends a multi-tone RF waveform to the AOD, which results in multiple laser beams. An array of lenses focuses all beams, such that finally each beam targets a single ion in the string. The RF waveform is composed of time segments (denoted as I-III), each of which consists of a sum of sine-functions with multiple frequencies  $\omega_i^{RF}$ . For each time segment, the RF amplitudes  $A_i$  can be set independently.

#### 4.4.2. Characterization and experimental application

The intensities of the addressing beams are not homogeneous over the ion string. This is mainly caused by clipping of the largely expanded addressing beam on the focusing optics. Due to the inhomogeneity, the ions have different pi-times, as shown in Fig. 4.6 a). These pi-time differences are “calibrated out” with an according correction factor for each RF amplitude  $A_i$  in Eq. (4.1). With this, we can then apply arbitrary AC-Stark shift patterns, e.g. we can homogenize the Rabi frequencies as shown in Fig. 4.6 b). Comparing the pulse box DDS2 with the AWG as RF source, no quality differences

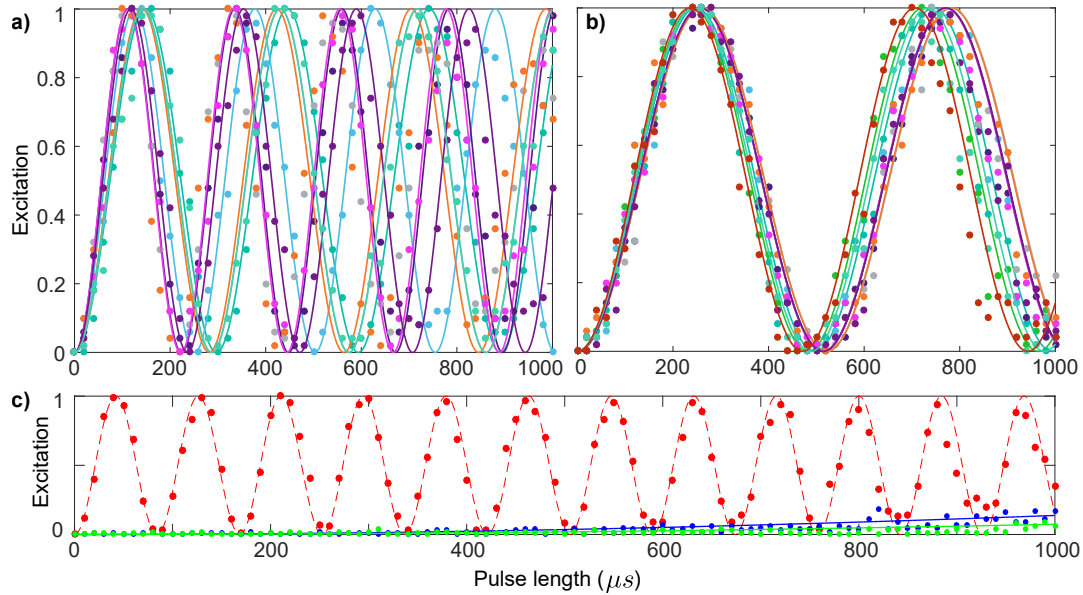


**Figure 4.6.:** Addressed AC-Stark Rabi flops using the AWG. **a)** Simultaneous addressed Rabi flops on a 10-ion string. The inhomogeneous intensity profile over the ion string causes a multiplicity of Rabi frequencies. **b)** Example of equalized Rabi frequencies after calibration (step 2 above). Here, the collective Rabi frequency was chosen to be 60 % of the lowest frequency measured in a). **c)** Addressing error associated with cross-talk for a 10-ion string, trapped at  $\omega_z = (2\pi) 217$  kHz axial frequency. Every second ion in string is addressed, but only ion 4 (blue), 5 (red) and 6 (green) are shown, for simplicity.

in the single-ion addressing pulses are detected: Short-term fluctuations<sup>37</sup> appear only after multiple Rabi flops, e.g. around  $800 \mu\text{s}$  in Fig. 4.6 c). Long-term drifts are not discernible<sup>38</sup> from quantum projection noise, and hence lie below 3 %. Fig. 4.6 c) shows the cross-talk between neighbouring ions, when driving AC-Stark Rabi flops on every second ion in a 10-ion string. The associated addressing error  $\epsilon = \Omega_{i\pm 1}/\Omega_i$  is given by the ratio of the Rabi frequencies  $\Omega_i$  of the considered ions, and lies below 1 %.

An interesting application for temporally modulated addressing of arbitrary ions, is the suppression and/or recovery of spin-spin interaction (c.f. Section 3.3.2) for determined ions in the chain. The interaction can be suppressed by applying a magnetic field gradient over the ion string, using a pair of current-carrying coils. This shifts the qubit's energy-levels out of resonance with respect to each other. If this energy

<sup>37</sup>Fluctuations on the order of a few kHz could be caused by noise on the RF source or by intensity fluctuations of the laser beam, e.g. due to vibration-induced beam pointing instabilities.

<sup>38</sup>Drifts are detected by observing the excitation at a pulse length which is associated with a slope of the Rabi oscillations (e.g.  $700 \mu\text{s}$  in Fig. 4.6 c)). We choose the longest possible pulse length, which is still not affected by short-term fluctuations, and observe the excitation at 200 measurement repetitions (sequence cycles) for several minutes.

difference is larger than the laser-induced spin-spin coupling strength, the interaction is suppressed. On the other hand, the coupling blockade can be lifted, by applying a modulated AC-Stark shift to one of the ions, with the modulation rate corresponding to the energy-level difference. This induces modulation sidebands, over which the interaction occurs. Fig. 4.7 shows a proof of principle experiment with two ions and a spin-spin coupling strength of  $J_{ij} = (2\pi) 83$  Hz: At first, one of the qubits is excited to the  $|\uparrow\rangle$  spin state. The spin-spin coupling to the second qubit is suppressed, by sending a current of 95 mA through the coils, corresponding to  $\Delta\nu = (2\pi) 111$  Hz difference between the carrier transitions of the two qubits. Finally, the interaction is successfully recovered by addressing one of the ions with the single-qubit addressing beam modulated at a rate of about  $(2\pi) 110$  Hz. The modulation is carried out by switching the addressing beam on and off at a period of 1.4 ms.

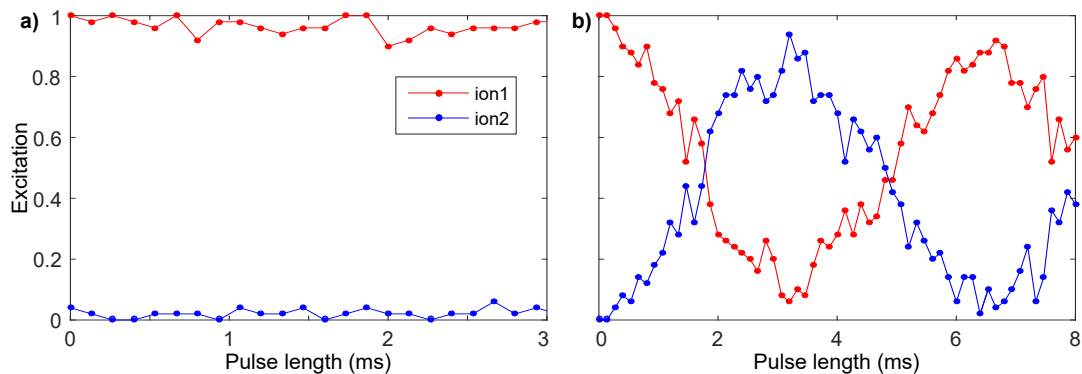


**Figure 4.7.:** Controlled suppression and recovery of spin-spin interaction for two qubits. **a)** A magnetic field gradient induces a difference of  $\Delta\nu = (2\pi) 111$  Hz between the qubit transitions of the two ions. Therefore the laser-induced spin-spin interaction, at a strength of  $J_{ij} = (2\pi) 83$  Hz, is suppressed. Consequently, the spin excitation of ion 1 (red) is not transferred to ion 2 (blue). **b)** Modulating the single-qubit addressing beam at a rate of about  $(2\pi) 110$  Hz bridges the interaction barrier and enables the interchange of spin excitation.

The experimental application presented in Chapter 6 goes one step further: In a chain of 10 interacting ions, single-qubit AC-Stark shifts are applied to multiple ions simultaneously. The shifts can be (i) static to suppress the spin-spin interaction, or (ii) temporally modulated to recover the interaction. With this, we mimic static energy disorder and dynamic noise in an interacting spin chain, or in other words, we simulate excitation transport in a disordered network and noisy environment. The flexibility of the AWG allows us to apply practically any desired spectral noise properties. Another application can be gleaned in Ref. [104], where we report on the temporal evolution of entanglement entropy in an interacting quantum system with and without disorder: For the unperturbed system, we observed linear (ballistic) entropy growth. In the presence

of disorder, however, we found a many-body localized phase, in which the system does not thermalize and the entropy grows strongly restrained.

## 4.5. Automated addressing calibration

Over a time of 10 minutes, the positions of the ions in our Paul trap drift<sup>39</sup> by about 40 nm along the principal axis of the chain, and 5 nm along the perpendicular direction. Measurements suggest that these drifts are caused by surface charging effects triggered by the Doppler cooling beam (397 nm). To counter this, we detect the changes of the ion positions every 10 minutes using the camera. Then we feed back on the voltage of the trap tip electrodes in order to cancel the shifts. Finally, we also recalibrate the addressing Rabi frequency of each ion, to make sure that the coupling of the addressed beam with the ion is maximized.

For long ion strings and when performing contiguous experiments over many hours, it is beneficial to automatize the calibration procedures, so the experiment can run stand-alone and overnight. For example, for the measurements presented in Section 7.3 this automatized calibration was essential. Using the *script* function in QFP<sup>40</sup>, we program the experimental scans to be automatically interlaced by a clock-measurement<sup>41</sup> every 2-3 minutes, and a calibration of the individual ion pi-times every 10 minutes. Appendix E shows an example of such a qsc-script.

## 4.6. Sub-Doppler cooling of long ion strings

Sub-Doppler cooling of long ion strings is a prerequisite for most entanglement-generating atom-light interactions, employed in quantum information processing, quantum simulation and quantum metrology. The challenge is, to efficiently cool many modes (possibly spread over hundreds of kHz) close to the motional ground state, in the shortest possible time. As a reference, the typically sequentially applied resolved-sideband cooling technique requires about 10 ms to cool all radial modes of a 20-ion string. This is already 50% of the line-cycle<sup>42</sup> time. In our experiment we investigated

<sup>39</sup>Measurements performed with 10 ions at  $(2\pi) 217$  kHz axial trapping frequency.

<sup>40</sup>Quantized Fluorescence Program (QFP) is the multi-threaded Labview software for controlling the experiment.

<sup>41</sup>Two qubit-transitions are measured every few minutes and a feedback to the laser is applied, such that it is locked on resonance with the current qubit-transitions [63].

<sup>42</sup>The alternating current (AC) in our electric power grid, has a nominal oscillation frequency of 50 Hz. Or in other words, a line-cycle with a period of 20 ms. Every experimental sequence is triggered to start at the same phase within this line-cycle to secure reproducibility.

two methods for sub-Doppler cooling: EIT cooling (Section 4.6.1) and polarization-gradient cooling (Section 4.6.2). After a short overview on motional states for single ions and ion strings, the basic principle and results of the two cooling methods are presented.

### Methods for motional state analysis

There exist several methods to analyze the achieved motional state of a single ion or an ion string, for example:

- Rabi oscillations of the carrier transition. The amplitude of the carrier oscillations is damped due to the weak dependency of the Rabi frequency on the phonon number  $n$ . In the case of a single ion, and coupling to a single motional mode, the relation is well approximated by:  $\Omega_{n,n} = (1 - \eta^2 n)\Omega_0$ . The mean phonon number  $\bar{n}$  is then extracted by fitting the probability amplitude  $p^{\text{carr}}(t)$  to find the ion in the excited state:

$$p^{\text{carr}}(t) = \frac{1}{2} \left( 1 - \sum_{n=0}^{n_{\text{max}}} \tilde{p}_n \cos(\Omega_{n,n} t) \right), \text{ with } \tilde{p}_n = \frac{\bar{n}^n}{(\bar{n} + 1)^{n+1}},$$

where phonon numbers up to  $n_{\text{max}} \gg \bar{n}$  are considered and  $\tilde{p}_n$  is the respective thermal probability distribution of the motional state. In the case of a single motional mode, this fitting method is simple and works well for Doppler- or sub-Doppler cooled ions, not too close to the motional ground-state.

However, the fitting complexity increases for an ion string, where the Rabi flops are influenced by the coupling to multiple motional modes: Following the atom-light interaction as derived in Eq. (3.15), the Rabi frequency of the carrier transition is influenced by each motional mode  $m$  according to:

$$\Omega_{n,n}^{(j)} = \Omega_0 \prod_m \left( 1 - \eta_{m,j}^2 n \right), \quad (4.2)$$

where the Lamb-Dicke parameter  $\eta_{m,j}$  varies for different modes as well as for different ions  $j$ . The fitting of such a multi-variable function does hardly converge such that sophisticated fitting techniques have to be used to estimate the motional state of a long ion string using this method. One solution is to fit the experimental data via a combined simulation and least-squares optimization approach as described in Ref. [105].

- The idea of extracting the motional state by fitting to Rabi oscillations is also

applicable to the sideband transition of a particular motional mode. For example, the Rabi frequency of the blue sideband transition of mode  $m$  is given by:  $\Omega_{n,n+1}^m = \sqrt{n+1}\eta_m\Omega_0$ . The respective probability amplitude  $p_m^{\text{bsb}}(t)$  to find the ion in the excited state is given by:

$$p_m^{\text{bsb}}(t) = \frac{1}{2} \left( 1 - \sum_{n=0}^{n_{\text{max}}} \tilde{p}_n \cos(\Omega_{n,n+1}^m t) \right).$$

The advantage of the sideband-method is, that it reveals the motional state of a particular mode. Note that this scheme is also applicable to ion strings, if the laser is focused to address only a single ion such that the mode- and ion-dependent coupling parameter  $\eta_m$  stays a single fitting parameter.

- Instead of the Rabi flops, one can also analyze the ratio between the red and blue sideband population of a particular mode  $m$ . Here, the  $k$ -th order of a sideband is excited on its red and blue component, using an arbitrary pulse length (but the same for red and blue). The mean phonon number  $\bar{n}_m$  is then given by the ratio  $R_k$  between the population of the red ( $p_m^{\text{rsb}}$ ) and blue ( $p_m^{\text{bsb}}$ ) sideband:

$$\bar{n}_m = \frac{(R_k)^{1/k}}{1 - (R_k)^{1/k}}, \text{ with } R_k = \frac{p_m^{\text{rsb}}}{p_m^{\text{bsb}}}.$$

This relation is only valid for thermal states and small phonon numbers. Further, the method is most sensitive for sideband orders  $k$  close to  $\bar{n}_m$ , which is disadvantageous because the laser-ion coupling scales as  $\eta_m^k$ . However, also this method can be extended to ion strings using a single-ion addressing beam.

- An alternative method is the rapid adiabatic passage [106] on a red motional sideband, in which the phonon number  $\bar{n}_m$  is directly mapped to the number of collective electronic excitations in the ion string. This method requires a number of ions  $N \geq \bar{n}_m$ , it is suited for long ion chains, large phonon numbers and is not constrained to thermal states. A more detailed description of the method, especially the implementation in our setup, is given in Appendix F.

#### 4.6.1. Electromagnetically Induced Transparency (EIT) cooling

In the following, I summarize the results of the method and defer to the PhD thesis of R. Lechner [107] for a detailed discussion on the theoretical background, experimental setup and results.

We applied EIT cooling to the radial vibrational modes, as most of our experiments employ this part of the motional spectrum to perform spin-spin entangling gates. The EIT technique can be implemented in an atomic three-level system in lambda-configuration [108], represented in our system by Zeeman sublevels  $|S_{1/2}, m_j = 1/2\rangle$ ,  $|S_{1/2}, m_j = -1/2\rangle$  and  $|P_{1/2}, m_j = 1/2\rangle$ , and coupled by two 397 nm laser beams. The laser detunings are chosen such that they pump the atomic system into a dark state, which does not couple to the laser fields, to first order. For this reason, spontaneous photon emission rates, and therefore the related heating processes, are very low. Transitions that change the motional state are generally allowed, however red-sideband transitions are strongly favoured above blue-sideband transitions. Consequently, the frequency range over which the ion motion is cooled is wider, and the achievable cooling rates are higher, as compared to resolved-sideband cooling [109]. The good optical access to our ion trap allowed us to arrange the two EIT beams such that the overlap between the resulting Raman wave vector is equal with both radial directions of motion: The  $\sigma^+$ -polarized EIT dressing beam was oriented anti-parallel to the magnetic field axis, while the  $\pi$ -polarized EIT probe beam propagated at an angle of  $60^\circ$  with it<sup>43</sup>. In summary, we achieved sub-Doppler cooling of all radial motional modes of an 18-ion string with a single cooling pulse. Applying the rapid adiabatic passage, we found a cooling rate of  $(19 \pm 3)10^3 s^{-1}$ , resulting in mean phonon numbers between 0.01 – 0.03 after 300  $\mu s$  of EIT cooling.

However, the beam arrangement in our EIT cooling setup also caused an overlap of the Raman  $k$ -vector with the axial direction of motion of the ion string. For the axial trapping frequencies around  $\omega_z = (2\pi) 217$  kHz, which we typically use for trapping long ion strings, we observed heating of the axial motional modes, during optimum EIT cooling of the radial modes. The mean phonon number of the axial motion increased from  $\langle n \rangle_{\text{Doppl}} \approx 180$  after Doppler cooling, to  $\langle n \rangle_{\text{EIT}} \approx 320$  after EIT cooling. This affected the coupling efficiency and fidelity of our single-qubit rotation gates<sup>44</sup>. A possible explanation is the high vibrational excitation of the axial modes after Doppler cooling. This might lift the suppression of the carrier transition, which is usually provided by the EIT method, resulting in off-resonant scattering processes that heat up the ions. One could overcome this problem, by avoiding an overlap of the Raman  $k$ -vector with the axial direction of motion. For this, we would need to rearrange the beam access and change the magnetic field axis, such that the  $k$ -vector propagates

<sup>43</sup>See Refs. [107, 109] for schematics of the optical setup.

<sup>44</sup>The wave-function of a high Fock state has a smaller overlap with the Gaussian laser beam, than the ground state wave-function. This reduces the coupling efficiency. The thermal distribution of the Fock state results in fluctuations of the coupling strength, which reduces the gate fidelity.

perpendicular to the axial direction of motion. As we don't want to drastically change the setup for the time being, we decided to continue using resolved-sideband cooling.

#### 4.6.2. Polarization-gradient (PG) cooling

Sisyphus cooling by means of polarization-gradients (PG), is another technique for cooling multi-ion crystals from far outside the Lamb-Dicke regime to below the Doppler cooling limit [110–112]. Here, I summarize the basic idea and the achieved results for PG cooling of the axial vibrational modes of a single ion and large ion crystals. Section 4.1 in this work, addresses the experimental setup. Detailed discussions on the theoretical background and results can be found in Refs. [105, 113].

The underlying idea is to create an optical field with periodically varying polarization gradient, along the desired cooling direction (labelled as  $z$ -axis in the following). Experimentally we achieve this by two counter-propagating laser beams at 397 nm, with mutually orthogonal linear polarizations, both blue detuned from the  $S_{1/2} \leftrightarrow P_{1/2}$  transition by 210 MHz. This generates an optical field along the  $z$ -axis, with periodic right-hand circular and left-hand circular (lin-perp-lin) polarization, as depicted in Fig. 4.8. An ion that moves along this axis, experiences a periodic light shift between the two Zeeman energy levels  $|S_{1/2}, m_j = -1/2\rangle$  and  $|S_{1/2}, m_j = 1/2\rangle$ . The ion loses kinetic energy when travelling along the optical field, as it climbs up the optical potential hill. Furthermore, the transition rules for the involved energy levels and the chosen laser beams are such that the population transfer between the two sublevels is maximum, whenever the ion reaches a peak of the potential energy curve. This way, the ions' state is transferred to the lower lying energy level via optical pumping and the procedure starts again. So in summary, the interplay between the spatially dependent light shifts and pumping rates gives rise to an efficient cooling mechanism.

The optimum cooling performance is achieved if the ion is positioned at the steepest part of the optical potential [110]. However, in our experiment it is not feasible to reliably place the ion within tens of nm of a particular position in the *static* standing-wave. Therefore, we detune one of the two cooling beams with respect to the second beam, by a frequency smaller than the lowest motional frequency (we choose 60 kHz). The resulting *travelling* standing-wave ensures that the ion is not positioned at a poor cooling point but rather samples multiple phases of the polarization gradient field during the cooling pulse. For long ion chains this consideration is not essential, as the ions are spatially spread over many positions of the standing wave. Hence, it is likely that at least one ion lies at the optimum position to climb the potential hill and sympathetically cools the chain.

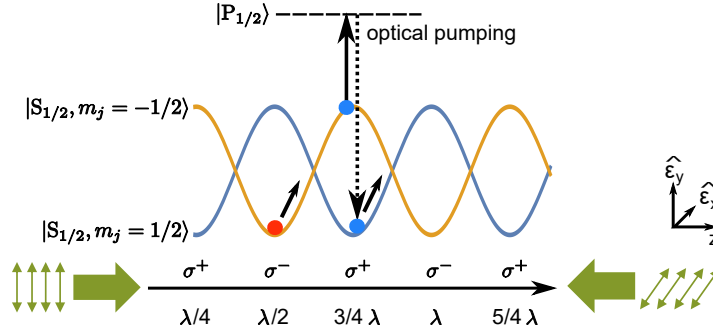


**Figure 4.8.: Schematics on polarization-gradient cooling.** Two counter-propagating laser beams (broad green arrows) with mutually orthogonal linear polarizations generate an optical field along the  $z$ -axis with periodic right hand circular,  $\sigma^-$ , and left hand circular polarization,  $\sigma^+$ . This field couples the two Zeeman ground states to an excited state and causes a polarization gradient varying at a periodicity of  $\lambda/2$  along the propagation direction  $z$ . An ion travelling along that direction experiences a periodic shift of the Zeeman sublevels  $|S_{1/2}, m_j = \pm 1/2\rangle$ , reducing the kinetic energy of the ion as it climbs the potential hill. At the peaks of the potential curve the population is transferred to the lower lying energy level via optical pumping.

In our experiment, we investigate PG cooling along the principal axis of the ion trap. Sub-Doppler cooling is achieved on (i) a single ion and (ii) long strings of calcium ions as well as two-dimensional ion Coulomb crystals in a linear Paul trap. The phonon numbers and cooling rates are estimated by fitting to the decaying Rabi flops on the carrier transition, as well as Rabi flops on the sideband transition probed on a single ion in the chain [105].

**(i) Single ion:** A single ion, strongly confined at  $\omega_z = (2\pi) 1.1$  MHz axial frequency, reaches phonon numbers below 2 after  $200 \mu\text{s}$  of PG cooling. The cooling rate measures  $6.6 \cdot 10^4/\text{s}$ . At trap frequencies below  $(2\pi) 400$  kHz, the cooling rate is lower because the Lamb-Dicke regime is left. At  $\omega_z = (2\pi) 217$  kHz, we measure 8-10 phonons after  $200 \mu\text{s}$  of PG cooling.

**(ii) Long ion strings:** We apply PG cooling on a linear ion string with 22 ions, confined at an axial trapping frequency of  $\omega_z = (2\pi) 217$  kHz. The effect on the motional spectrum of a long chain is shown in Fig. 4.9 a)-b). It shows the excitation of each ion, for all first order red and blue sidebands of the axial motion, as well as the carrier transition. For the case of a Doppler cooled ion chain (a), all sidebands are strongly excited and the spectrum is crowded, indicating the occupation of high lying phonon states for all motional modes. After 1 ms of PG cooling (b), the spectrum is noticeably less crowded and we observe an asymmetry between the red and blue sidebands, which indicates the occupation of low lying phonon states. Fig. 4.9 c)-d) visualize the effect of PG cooling onto coherent laser manipulation. We resonantly drive the carrier transition

using the global beam and perform Rabi spectroscopy. In the case where the ions are only Doppler cooled (b), the Rabi flops dephase already after  $20 \mu\text{s}$  due to the occupation of high vibrational states. Applying PG cooling for 1 ms additionally (c), improves the time scale for coherent control significantly, inferring successful cooling of the ion crystal. Note that the reduced Rabi frequency of outer ions in the chain, is attributed to their coupling to micromotion along the principal trap axis.

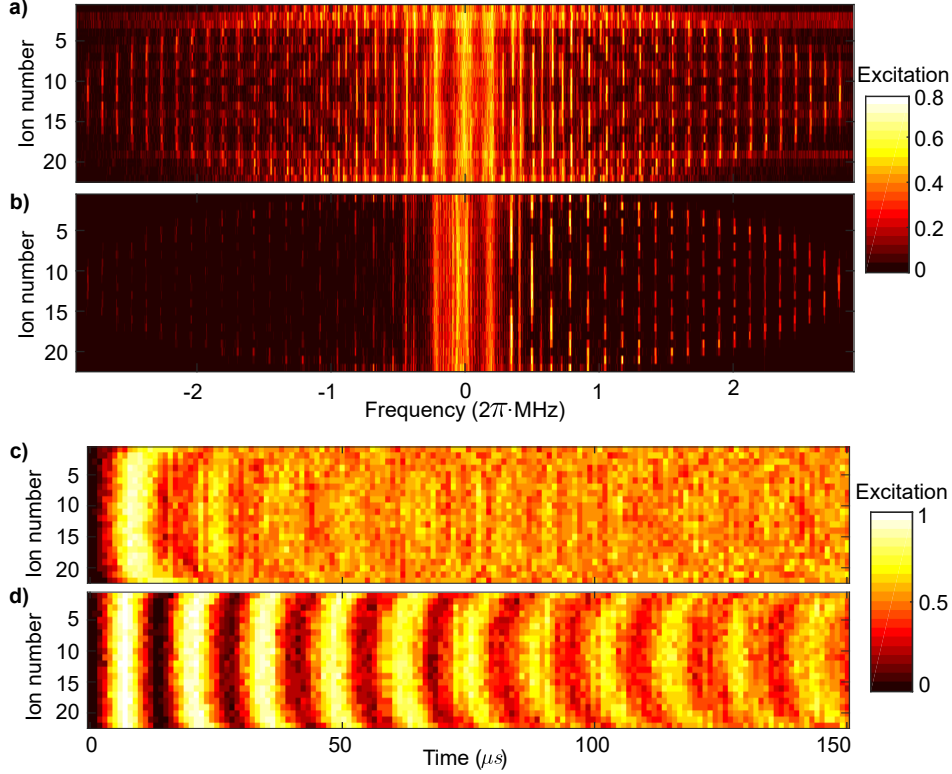


**Figure 4.9.: Effect of PG cooling on a 22-ion chain.** a) Individual qubit excitations as a function of the laser frequency shift, after Doppler cooling for 3 ms. The blue (left hand) and red (right hand) sidebands are strongly and equally excited, indicating the occupation of high lying phonon states. b) Spectrum after additional 1 ms of PG cooling, the blue sidebands are excited noticeable less, indicating cooling to low lying phonon states. c) Resonant qubit excitation with the global laser beam, after 3 ms Doppler cooling, results in quickly decohering Rabi flops. d) Additional PG cooling for 1 ms improves the coherent control significantly.

Finally, we also estimate the mean phonon numbers after PG cooling [105]: In a linear Paul trap, long strings of ions have to be trapped at a weak axial confinement  $\omega_z \approx (2\pi) 100 \text{ kHz}$ , prone to high motional heating by electric field noise, in particular for the COM mode. Given a heating rate of about 1400 quanta/s, for a single ion, we estimate a heating rate on the order of 30 000 quanta/s for 22 ions. Consequently, PG cooling achieves mean phonon numbers between 25-45 for the COM mode, while

other modes are cooled down to 1-10 phonons. These numbers are estimated with single-ion resolved Rabi flops on individual motional sidebands. Least-square fitting on carrier Rabi flops confirms the result for the COM mode, but overestimates the phonon numbers for high-frequency modes. We assign this discrepancy to the thermal occupation of the high-frequency modes, affecting the shape of the carrier oscillations only weakly. Moreover, we apply PG cooling to a 51-ion chain and observe that the cooling performance is quantitatively the same as for the 22-ion chain. This indicates, that the presented cooling technique is scalable.

When working with strings of about 50 ions, sub-Doppler cooling of the axial modes of motion is essential: Large phonon numbers result in a large spatial spread of the individual ions. This again, affects the single-ion addressing quality as the ions' wavepackets extend beyond the addressing beam. Fig. 4.10 compares single-ion addressing with and without PG cooling. Finally, we find that the PG cooling method also succeeds in cooling the in-plane modes of a two-dimensional 22-ion crystal (see [105]).

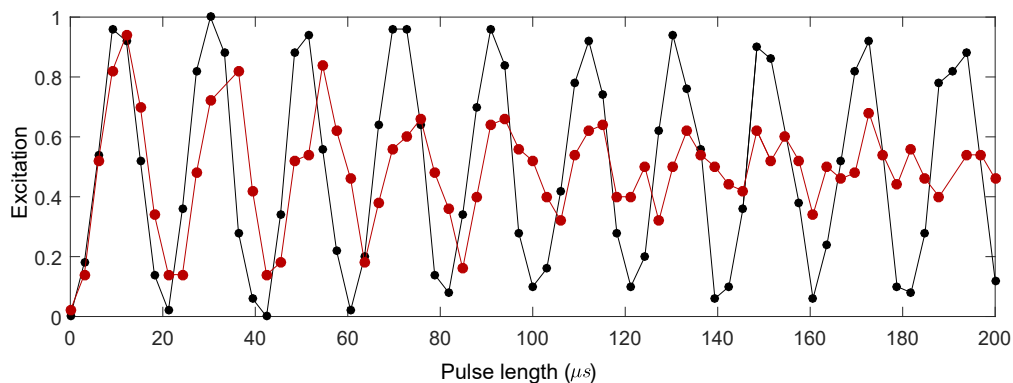


**Figure 4.10.:** AC-addressed Rabi flops of ion 30 in a 51 ion chain, with and without polarization-gradient cooling. Without sub-Doppler cooling of the axial motional modes, addressed Rabi flops decay quickly (red circles), while the phase coherence is well maintained for the PG cooled case (black circles).

In conclusion, we demonstrate efficient sub-Doppler cooling of trapped ions. For high trapping frequencies, phonon numbers between 1-2 are achieved. At low trapping frequencies, the cooling rates compete with motional heating by electric field noise, resulting in higher phonon numbers for the COM mode. Our investigation shows that PG cooling is scalable to large ion crystals and is efficient to simultaneously cool a broad frequency range even from outside the Lamb-Dicke regime.

While PG cooling cannot compete with EIT cooling when it comes to cooling multiple modes close to the ground state, EIT cooling achieves high cooling rates only over a comparatively small frequency range. This is due to the narrow dressed state that

facilitates cooling. Moreover, the highest EIT cooling rate scales with  $W_{\text{cool}} \sim \omega$  [114], such that EIT cooling becomes slow for low-frequency modes.



## 5. Characterization of quantum many-body states

The studies presented here are published in:  
[Nature Physics](#) **13**, 1157-1162 (2017) &  
[Phys. Rev. X](#) **8**, 021012 (2018)

Quantum state tomography (QST) is the gold standard technique for estimating the state of small quantum systems. Applying this technique to systems with more than a few qubits soon becomes impractical as the required effort grows exponentially with the number of particles. At the same time, the generation and understanding of complex states in large quantum systems is of fundamental importance to a broad range of current research fields, including quantum computing, quantum simulation, quantum communication, and quantum metrology. With this, more and more precisely-controllable quantum systems, well beyond the reach of QST, are emerging in today's laboratories. Therefore, there is a considerable ongoing effort to develop more efficient tools for the characterization of large quantum systems [40–42, 47, 49, 50, 115].

At the beginning of the chapter I describe the generation of large, locally correlated quantum states in our laboratory. These states have been characterized within two separate experimental projects, published in the journals mentioned above. The first project focuses on witnessing genuine multipartite entanglement in our states and is discussed in the first part of this chapter. General properties of the quantum states as well as entanglement estimates are extracted from a practical number of measurements. The second part of the chapter focuses on Matrix Product State (MPS) tomography, a technique, which is theoretically proven to accurately estimate the states of a broad class of quantum systems, with an effort that increases efficiently with the number of qubits [40]. After an introduction of the concept of MPS, I present the MPS tomography scheme and its application to an experiment. We successfully reconstructed quantum states of up to 14 entangled qubits. This achievement is far beyond the practical limits of quantum state tomography. Moreover, the presented MPS scheme allows one to assess the lower bound of the fidelity between the reconstructed state and the state

generated in the laboratory. The last section describes the experimental implementation of "direct fidelity estimation", a technique that allows for measuring the real overlap of the estimated state with the laboratory state.

## 5.1. Large, locally correlated quantum states

In our laboratory, we trap one-dimensional strings of up to 20  $^{40}\text{Ca}^+$  ions in a linear Paul trap. Two electronic states of each ion encode a spin-1/2 particle (Section 2.2). Using a trichromatic laser beam, we engineer interactions between the spins (Section 3.3), such that the entire system is well described by the Hamiltonian

$$H_{XY} = \hbar \sum_{i < j} J_{ij} (\sigma_i^+ \sigma_j^- + \sigma_i^- \sigma_j^+) + \hbar B \sum_j \sigma_j^z. \quad (5.1)$$

Here,  $J_{ij}$  describes the  $N \times N$  spin-spin coupling matrix of spins  $i$  and  $j$ , where  $N$  denotes the number of qubits.  $\sigma_i^+$  ( $\sigma_i^-$ ) is the spin raising (lowering) operator and  $\sigma_j^z$  is the Pauli  $Z$  matrix for spin  $j$ . The interactions decrease with distance  $|i - j|$ , approximately following a power-law  $J_{ij} \propto 1/|i - j|^\alpha$ . To quantify the interaction range  $\alpha$  in our system we find a best fit between the eigenmode spectrum of  $H_{XY}$  in the one-excitation subspace, with the eigenmode spectrum of an interaction that reduces with  $1/|i - j|^\alpha$ . The decay parameter  $\alpha$  of the best fit, yields an effective interaction range of  $\alpha = 1.58$  (8 spins),  $\alpha = 1.27$  (14 spins) and  $\alpha = 1.1$  (20 spins). For these interaction ranges, one can observe spreading wave packets of quantum correlations [94, 116, 117]. Applying MPS tomography to such complex out-of-equilibrium states, generated by interactions that are not strictly of finite range, represents a stringent test of its scope of application.

The ground state of the model Hamiltonian (5.1) corresponds to the state with all spins down  $|\downarrow_z\rangle^{\otimes N}$ . Spin-up states  $|\uparrow_z\rangle$  are quasiparticle excitations, which disperse and scatter in the system [94]. We choose the Néel state as the initial state in our experiment, as it is highly excited ( $N/2$  excitations) and leads to the emergence of locally correlated entangled states involving all  $N$  particles. After evolving this state under the XY-Hamiltonian for a desired time  $t$ , the spin interactions are abruptly turned off, freezing the generated state and allowing for spin measurements. At the end of every such experimental run, the state of each spin is determined using the standard electron shelving technique and a single-ion resolving CCD camera. This measurement setting corresponds to measuring each spin in the  $Z$ -basis, that is, projecting each spin into either of the two eigenstates of the Pauli  $\sigma^z$  operator. Moreover, we can measure any

spin in any single-spin basis via laser-driven spin rotations that map the eigenstates of the desired single-spin-operators onto the eigenstates of the Pauli  $\sigma^z$  operator. After this, electron shelving detection is carried out as in the Z-basis measurements. In this way we measure arbitrary combinations of single-spin bases, e.g. the first spin in the Z basis, the second in X, the third in Y, etc.

### 5.1.1. Correlation spread in light-like cones

Consider an  $N$ -component quantum system in a separable pure state (e.g. the Néel state) in which the spin-spin interactions (5.1) are turned on abruptly (quench). In the case of finite-range interactions, information and correlations spread over the system with a strict maximum group velocity [118–120]. As we do not have finite-range interactions in our experiment, information does not spread at a strict maximum speed. However, light-cone like trajectories provide a practically useful description of the correlation dispersal. Fig. 5.1 a) to d) show the spread of spin excitations over the entire ion chain. The lines  $t = d/v$  delineate the light-like cones, where  $d = |i - i_c|$  denotes the distance of the ion sites  $i = 1 \dots N$  to the centre ion  $i_c$ . The spread velocity  $v$  is estimated by considering a nearest-neighbour model of our system, where the homogeneous coupling strength  $J = \frac{1}{N-1} \sum_{i=1}^{N-1} J_{i,i+1}$  is given by the average nearest-neighbour coupling of the original (full) coupling matrix  $J_{ij}$ . Then, we calculate the corresponding eigenmode spectrum of this truncated system, and determine the gradient between every pair of consecutive eigenvalues. The largest of these gradients corresponds to the maximum velocity  $v_{\max}$  at which energy and correlations disperse in the system. Finally we renormalize  $v_{\max}$  by the algebraic tail of the original coupling matrix: Specifically, we choose the central ion  $i_c = 5$  (7) respectively for 8 (14) ions and average between the left and right algebraic tail, resulting in the normalization factor  $G = \frac{1}{2J} \sum_{i \neq j} (J_{j,i_c} + J_{i_c,j})$  such that  $v = \frac{v_{\max}}{G}$ .

After a finite evolution time under the interaction Hamiltonian, there is a maximum distance over which correlations have spread across the system. Beyond this so-called *correlation length*  $L$ , correlations decay exponentially in distance. The information required to describe the corresponding quantum state is largely contained in the *local reductions* – the reduced density matrices of all groups of neighbouring particles contained within  $L$  (see Fig. 5.1 e)). In 1D systems, such states are well described by a compact MPS [121, 122] and one only needs to perform the measurements required to reconstruct the local reductions, to identify the entire  $N$ -component state at a certain point in time (Section 5.2.2). The light-like cones presented in Fig. 5.1 serve as a guide to interpret correlation spreading in our system. This way they help to estimate the

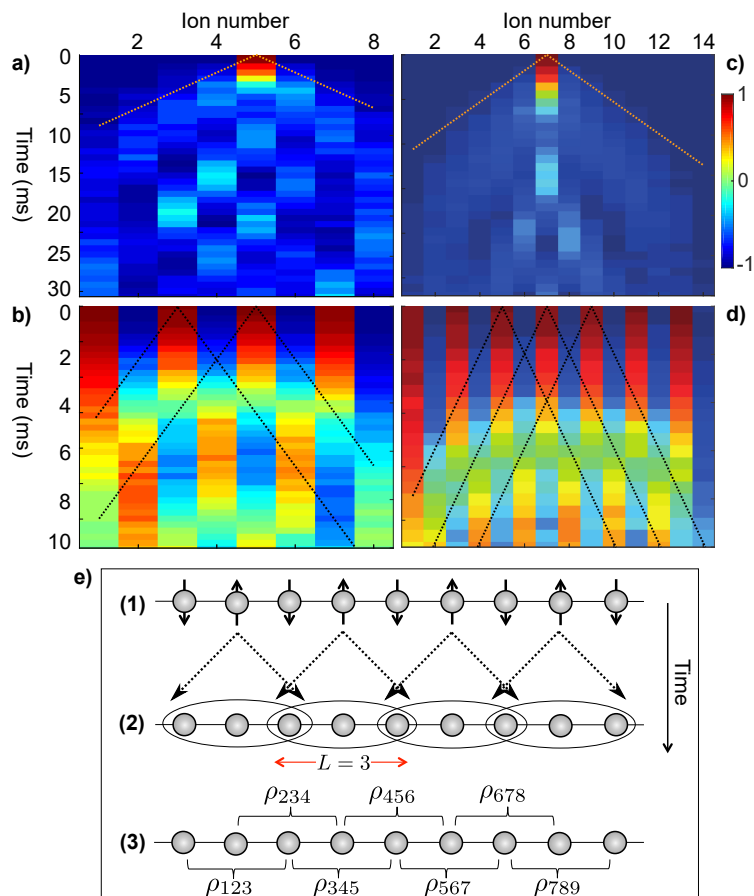


**Figure 5.1.: Generation and evolution of locally correlated quantum states.** **a), b)** Single-spin magnetization dynamics  $\langle \sigma_i^z(t) \rangle$  during a quench of Hamiltonian (5.1) for 8 ions. Light-light cones are visualized as orange dotted line for the initial state with a single spin excitation, and analogously as black dotted lines for the Néel initial state. The cones exemplify an estimate for the maximum speed at which correlations spread. **c), d)** Same as in a) and b) for a 14 ion chain. **e)** (1) Quantum spins arranged in a one-dimensional chain, are initialized into the Néel state. Finite-range spin-spin interactions are turned on abruptly, and quantum correlations spread out with a maximum group velocity. Black arrows (only a few are shown) denote the light-like cones of the correlation spread, producing a locally correlated entangled state. (2) After a particular evolution time, quantum correlations have spread to neighbouring spin triplets, expressed via the correlation length  $L = 3$ . The correlation length increases at most linearly in time. The total  $N$ -spin state is accurately described by a compact MPS. (3) It suffices to reconstruct all  $N - L + 1$  neighbouring spin triplet reduced density matrices  $\rho_{i,j,k}$ , in order to obtain an accurate MPS estimate for the state in the laboratory. At any given evolution time, the experimental effort therefore increases linearly in spin number  $N$ .

correlation length at each time step and reveal when measurements over larger sites become necessary for successful MPS tomography. For the state reconstruction in our

experiment, we measure the local reduced density matrices  $\rho^{(k)}$  of all blocks<sup>45</sup> of individual spins ( $k = 1$ ), neighbouring spin pairs ( $k = 2$ ) and spin triplets ( $k = 3$ ). For each neighbouring  $k$ -spin block we measure all  $3^k$  bases, corresponding to all combinations of single-qubit Pauli operators (see details in Appendix I).

The set of measurements for reconstructing all reduced density matrices of up to three neighbouring spins, contains 27 measurement bases with 1000 repetitions per basis. These data reveal a large set of correlations between spin-pairs all over the ion chain. Examples of two-qubit correlation matrices in a 20-qubit system are shown in Fig. 5.2: Panel a) shows the development and spread of correlations  $\langle Y_i(t)Y_j(t) \rangle - \langle Y_i(t) \rangle \langle Y_j(t) \rangle$ , between spins  $i$  and  $j$ , as a function of time. Here,  $Y$  is the standard Pauli spin operator  $\sigma_y$ . The second term in this correlation function removes pure-state classical correlations such as those present in the initial state. Therefore, the correlation matrix at time  $t = 0$  ms contains all zero entries to within the error limits. Panels b) to d) present correlation matrices after  $t = 2$  ms interaction time, where strong pairwise correlations have emerged beyond next-nearest neighbours, in different bases.

### 5.1.2. Entanglement studies

The data set for the reconstruction of  $k$ -qubit local density matrices allows us to extract interesting properties:

1. We can reconstruct each local  $k$ -spin reduced density matrix  $\rho^{(k)}$  via full quantum state tomography and standard maximum likelihood estimation [37]. From this we obtain arbitrary information about all neighbouring two- and three-body states, e.g. entanglement measures [123].
2. The experimental data allow us to define genuine multipartite entanglement witnesses, beyond the fully reconstructed states of three neighbouring qubits [124].

#### 1. Two- and three-body properties:

We reconstruct the density matrices of all subsets of two and three neighbouring qubits. From these local reductions we can extract dynamical properties of all neighbouring spin pairs and spin triplets. Fig. 5.3 a) shows an example for a reconstructed density matrix of two spins after 3 ms quench dynamics on an 8-ion Néel initial state. Fig. 5.3 b) shows the Von Neumann entropy  $S(\rho) = -\text{Tr}(\rho \ln(\rho))$ , quantifying the degree of mixing of some selected local reductions  $\rho_{i,j,k}$  of the three-qubit system  $(i, j, k)$ . Note

<sup>45</sup>A 1D chain of  $N$  spins has  $N - k + 1$  blocks of  $k$  neighbouring spins. We can measure them simultaneously, requiring a total of  $3^k$  measurements bases for the entire string.

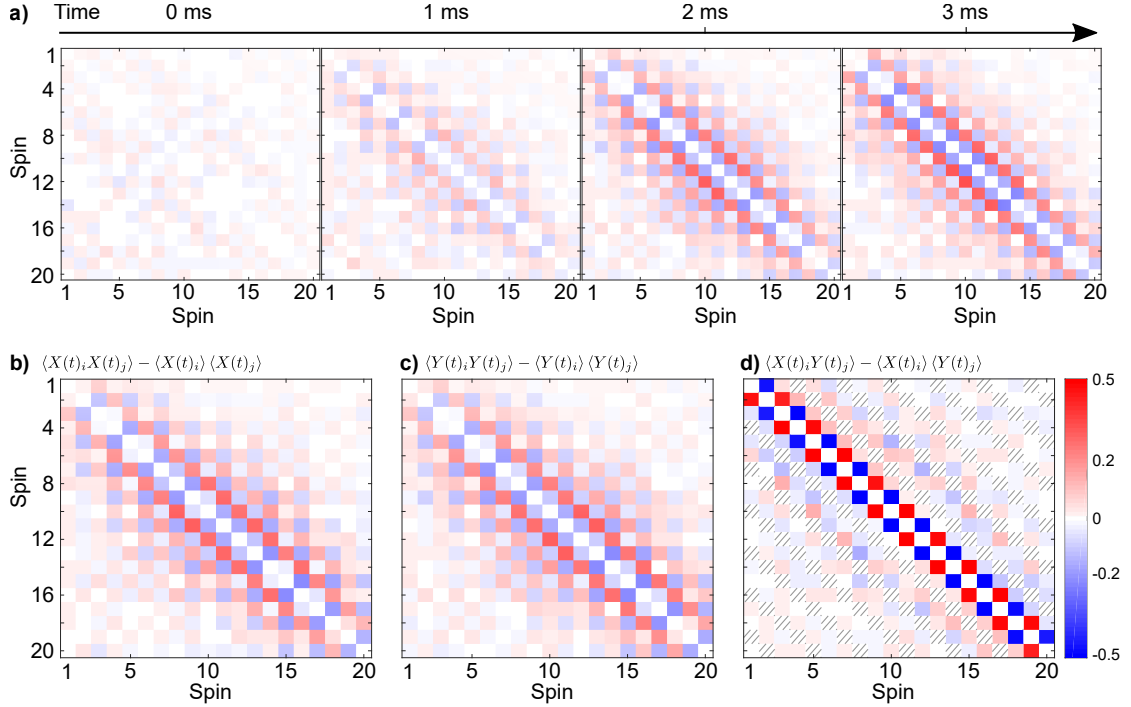


**Figure 5.2.: Spin pair correlation matrices in a 20-spin system.** a) Development of correlations  $\langle Y_i(t)Y_j(t) \rangle - \langle Y_i(t) \rangle \langle Y_j(t) \rangle$ , between spins  $i$  and  $j$ , as a function of time. At time  $t = 0$  ms there are no correlations to within the error limits. b) - d) Correlation matrices at time  $t = 2$  ms in different bases, as stated in the panel titles. The performed measurements for the reconstruction of 3-qubit density matrices do not contain all spin-spin correlations. Missing data is denoted by hatched squares.

that the von Neumann entropy vanishes for a pure state and reaches the maximum value  $\ln(2^N)$  for a maximally mixed state of  $N$  qubits. Finally, we calculate the overlap<sup>46</sup> between all neighbouring spin-pair states and a maximally entangled two-qubit state, the  $|\Psi^+\rangle = (|01\rangle + |10\rangle)/\sqrt{2}$  Bell state. Fig. 5.3 c) shows that the overlap reaches its maximum around 3 ms.

We quantify entanglement by the bipartite logarithmic negativity  $LN_2$  for spin pairs, and tripartite logarithmic negativity  $LN_3$  for spin triplets. Logarithmic negativity  $LN(\rho) = \log_2 \|\rho^{TA}\|_1$  is an entanglement measure that can be computed for a generic bipartite mixed state  $\rho$ , from the trace norm of its partial transpose  $\rho^{TA}$  [126]. This expression vanishes for unentangled states and we use it to quantify the degree of

<sup>46</sup>Quantifying entanglement in terms of the overlap with a maximally entangled two-qubit state has an operational meaning: two-qubit states with fidelities above 50% are distillable. That is, from many copies of qubit-pairs with fidelities above this threshold, local actions on each qubit can distill a smaller number of states with higher quality entanglement [125].

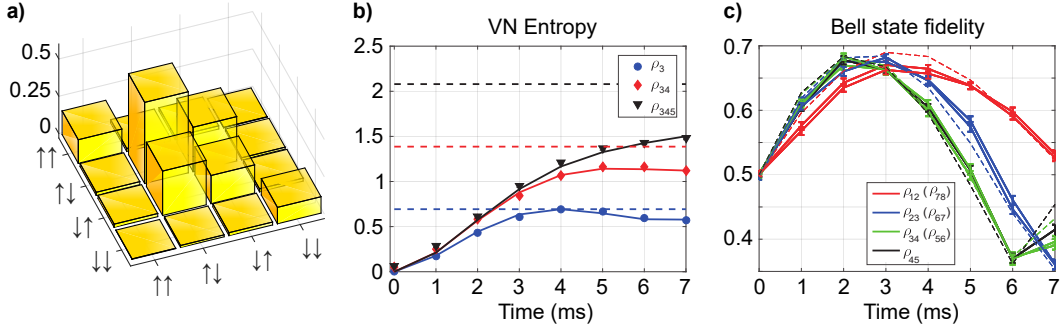


**Figure 5.3.: Properties extracted from local reductions in an 8-spin system.** **a)** Absolute value of the reduced density matrix of spins 3 and 4 at time  $t = 3$  ms, reconstructed via full QST and standard maximum likelihood estimation. **b)** Von Neumann entropy in example local reductions of a single spin (blue), two spins (red) and three spins (black). Shapes: entropy of the experimentally measured local reductions. Error bars are of similar size as the symbols. Solid lines: theoretical model based on ideal quantum simulator states. Dashed lines: the maximum entropy for a fully mixed state of  $N$  qubits. **c)** Overlap of the maximally entangled  $|\Psi^+\rangle$  Bell state with the absolute value of all experimentally reconstructed neighbouring 2-spin density matrices. Spin pairs symmetrically distributed around the centre of the string are shown in the same color. Solid lines connecting points with error bars: experimental data. Error bars represent one standard deviation obtained via the Monte Carlo simulation of quantum projection noise. Dashed lines: theory from ideal model of the simulator.

entanglement in the reduced 2-qubit density matrices  $\rho^{(2)}$  of neighbouring spin pairs,

$$LN_2(\rho^{(2)}) = \log_2 \|\rho^{TA}\|_1 = \log_2 \left( 2 \cdot \left| \sum_n \mu_n \right| + 1 \right), \quad (5.2)$$

where  $\mu_n$  are the negative eigenvalues of  $\rho^{TA}$ . For a qualitative discussion of entanglement evolution in neighbouring spin triplets  $\rho^{(3)}$ , we define tripartite logarithmic negativity  $LN_3$  as the geometric mean of the three bipartite logarithmic negativities (similar to the definition of tripartite negativity in [127]):

$$LN_3(\rho^{(3)}) = \sqrt[3]{LN_2(\rho_{I-JK}) \cdot LN_2(\rho_{J-IK}) \cdot LN_2(\rho_{K-IJ})}, \quad (5.3)$$

where  $LN_2(\rho_{I-JK}) = \log_2 (2 \cdot |\sum_i \tilde{\mu}_i| + 1)$ , with  $\tilde{\mu}_i$  as negative eigenvalues of  $\rho^{TI}$ , the partial transpose of  $\rho^{(3)}$  with respect to subsystem  $I$ . Fig. 5.4 reveals that entanglement between neighbours maximizes at 2 ms, and spin-triplet entanglement around 3 ms. As the simulator evolves further, entanglement reduces first in pairs, as correlations have then spread out to include more distant spins. Then, entanglement reduces in spin triplets, in agreement with the continuing spread of correlations in the system.

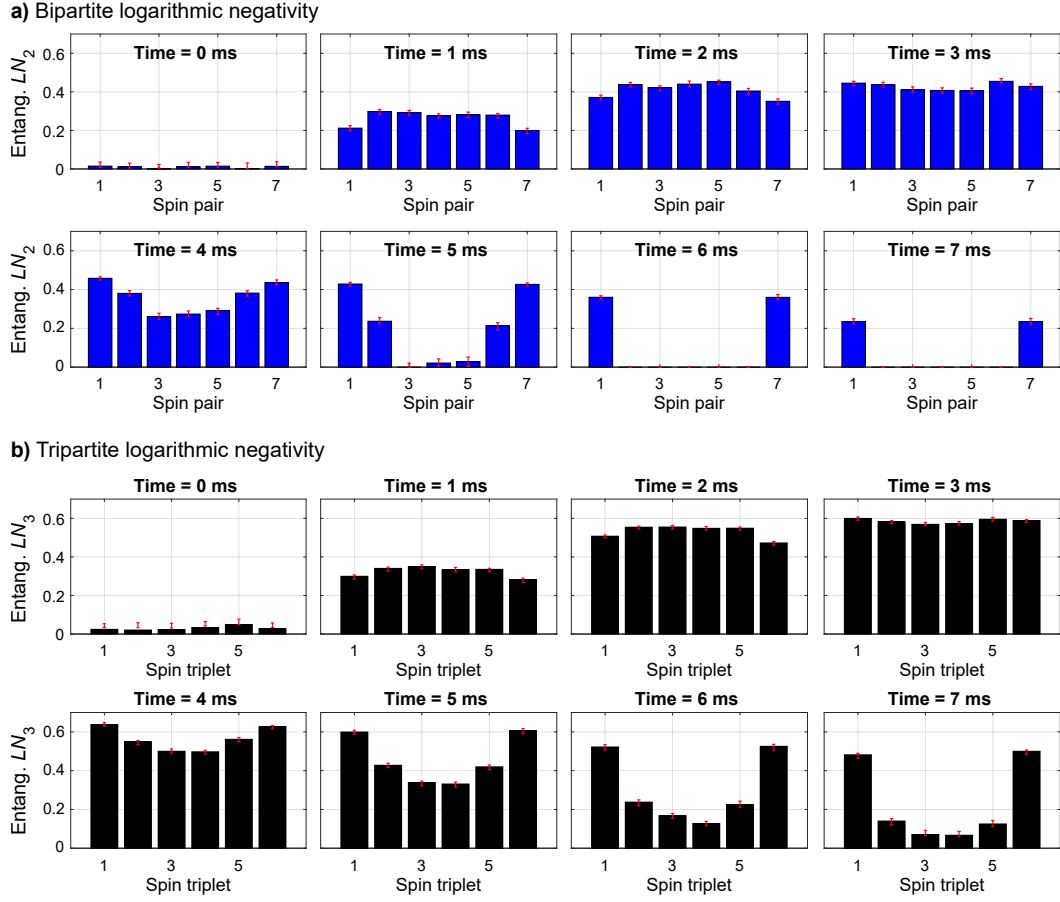


**Figure 5.4.:** Temporal evolution of two- and three-body entanglement in an 8-spin system. a) Bipartite logarithmic negativity  $LN_2$  for neighbouring spin pairs and b) tripartite logarithmic negativity  $LN_3$  for neighbouring spin triplets. The evolution time under the XY-Hamiltonian is given in each panel. The values are extracted from the measured  $k$ -spin local reductions. Error bars represent one standard deviation derived from Monte Carlo simulation of quantum projection noise.

## 2. Genuine multipartite entanglement witnesses:

The acquired data for the reconstruction of all neighbouring 3-qubit density matrices can also be used to design multipartite entanglement witnesses. Every qubit added to the system doubles the Hilbert space dimension, in which the collective quantum state is described. This makes it challenging to determine *if* and *how* an  $N$ -qubit quantum system is entangled. For an arbitrary mixed state, the problem is at least NP hard, such that a mixed 5-qubit state is already at the practical limit of our available computers and algorithms [128]. One may ask, is multipartite entanglement not implied if e.g. every neighboring qubit pair is entangled as we know that this applies to our

system (c.f. Fig. 5.4)? The answer to this question is no. There are states that feature entanglement in every 2-qubit reduction, yet still feature only bipartite entanglement. Nonetheless, it is often possible to detect genuine multipartite entanglement (GME)<sup>47</sup> purely from inspection of the reduced density matrices of overlapping groups of qubits.

In Ref. [124] we report on the partial characterization of a 20-qubit system via custom-build witnesses to detect GME. The designed witnesses are not a function of every element of the density matrix and therefore require only a limited number of measurements. For any group  $i$  of  $k$  neighbouring qubits we aim to find a witness operator  $Q_i^{(k)}$ , whose expectation value provides a lower bound on the  $k$ -qubit genuine multipartite negativity  $\mathcal{N}_g$  [129, 130]. The constraints are

- (i) that it can be written as a linear function of the 27 projectors that we measured in our experiment,
- (ii) it maximizes the inequality

$$-\text{Tr}(Q_i^{(k)} \rho_i^k) \equiv \mathcal{S}_i^{(k)} \leq \mathcal{N}_g(\rho_i^k), \quad (5.4)$$

where  $\mathcal{S}_i^{(k)}$  is the witness expectation value for a specific  $k$ -qubit state  $\rho_i^k$  and

- (iii) inequality (5.4) has to be satisfied for all possible  $k$ -qubit states.

We employ a numerical search to find  $k$ -qubit witnesses for GME. This search is computationally demanding, as the used optimization resources increase exponentially with  $k$ . Theoretical details on the analytical derivation of the GME witnesses are given in Ref. [124]. Here, I want to summarize the experimental results when applying the established methods to a 20-qubit state.

The experimental results in Fig. 5.5 present the witness expectation values  $\mathcal{S}_i^{(k)}$  for the  $i$ th group of up to  $k = 5$  neighbouring qubits, for different time steps in the dynamics. The witness detects  $k$ -qubit GME ( $\mathcal{N}_g > 0$ ) if it is larger than zero. We find, that between 2-3 ms the majority of all neighbouring groups of 3, 4 and 5 qubits shows GME, to within at least 1 standard deviation of experimental uncertainty. We further compare the experimental results with two different theoretical models:

1. The “pure” model assumes the preparation of a perfect initial product state and a pure time-evolved state. Although this model succeeds in describing the en-

<sup>47</sup>A pure state  $|\psi\rangle$  is called biseparable if there exists a bipartition  $A|B$  such that  $|\psi\rangle = |\phi\rangle_A |\chi\rangle_B$  for some  $|\phi\rangle_A$  and  $|\chi\rangle_B$ , and is called genuinely multipartite entangled otherwise. Mixed states are GME if their density operators cannot be written as convex combinations of biseparable pure states [124].

tanglement dynamics qualitatively, the experimental data are generally offset to lower values.

2. A more sophisticated “mixed” model includes known imperfections<sup>48</sup> in the preparation of the Néel-ordered initial state. This model is able to explain part of the experimental data offset, the remaining difference is attributed to additional mixing processes during the laser-induced spin-spin interactions.

The theory error bars in Fig. 5.5 indicate one standard deviation of the mean and originate from a finite number (1000) of numerically simulated measurements per basis. These errors denote that the fluctuations in the data are well explained by statistical noise. Amongst the 27 measurement bases, 3-qubit measurements are repeated (duplicated) more often in the measurement pattern than 4-qubit or 5-qubit measurements - leading to the observed variations in the statistics. We conclude that we could benefit from taking more measurements, in order to witness 4- and 5-qubit GME with greater statistical significance.

---

<sup>48</sup>Out of 1000 attempts to generate the Néel state, we observe the correct output state 829 times. In the remaining 171 cases, 146 correspond to single qubit flip errors and the rest to errors with two or more qubit flips. We model these errors as leading to the preparation of a statistical mixture of those different logical initial states, with corresponding weights. The error source is attributed to uncontrolled fluctuations in laser intensity and frequency.

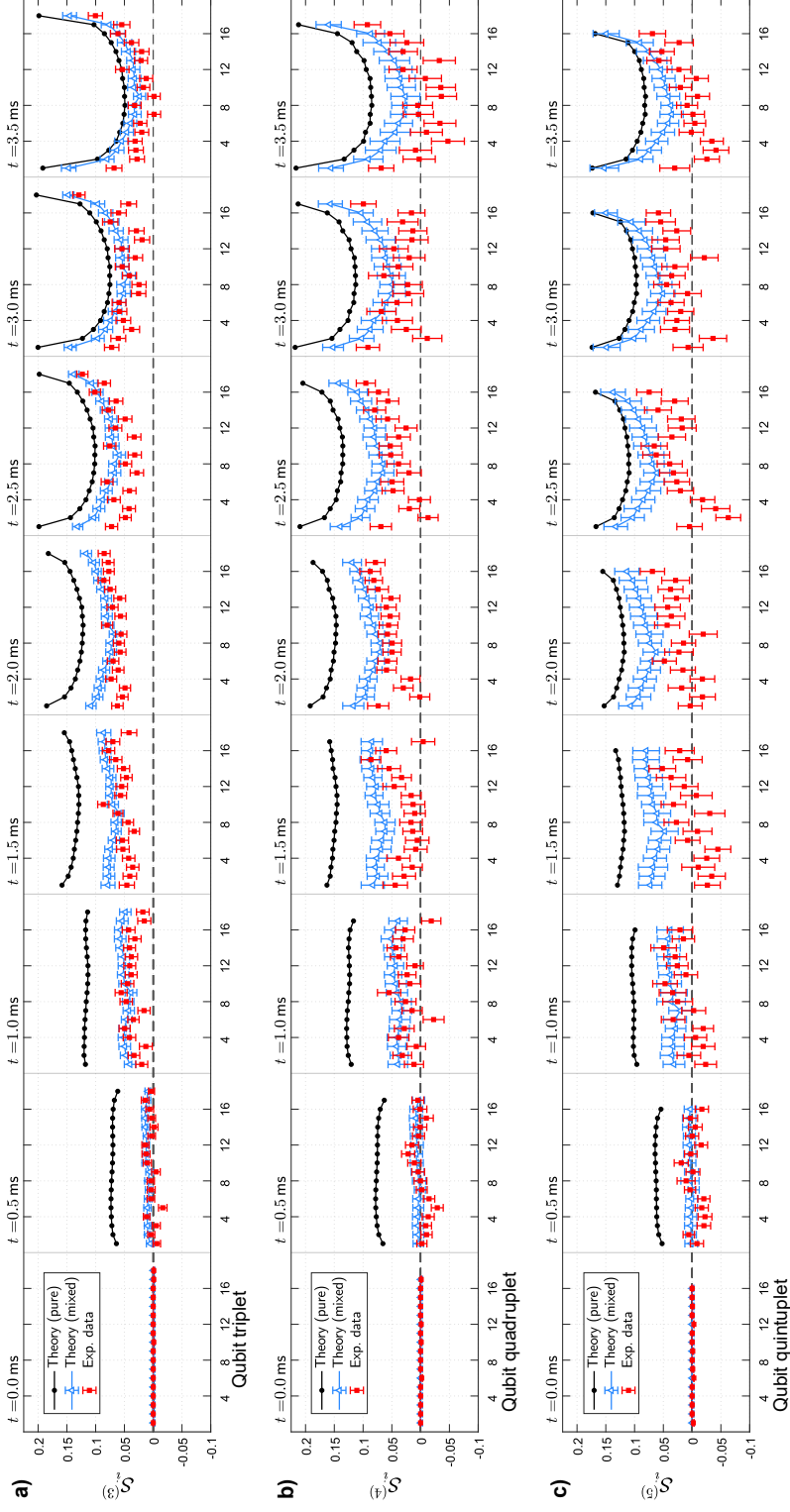


**Figure 5.5.: Genuine multipartite entanglement witnesses for a 20-qubit system.** Witnesses  $S_i^{(3)}$ ,  $S_i^{(4)}$  and  $S_i^{(5)}$  are shown in panels a) to c), respectively. The connected subpanels show increasing time steps in the dynamics, with intervals of 0.5 ms, starting with 0 ms (the initial state). The shapes represent results for a given triplet [a]  $k = 3$ ], quadruplet [b]  $k = 4$ ], or quintuplet [c]  $k = 5$ ] of neighboring qubits. GME is detected if the witness is positive. The different theory plots correspond to a pure model (black circles) and a mixed model (blue triangles). Red squares show experimental data. Error bars denote 1 standard deviation of the mean and originate from a finite number (1000) of measurements per basis.

## 5.2. Matrix Product State Tomography

So far, the largest application of full QST was on an 8-qubit W-state, requiring ten hours of measurements in 6561 different bases [131]. In our experiment, we applied MPS tomography to study complex out-of-equilibrium states on 8- and 14-qubits, generated by quench dynamics under the XY-Hamiltonian. We succeeded to accurately reconstruct entangled states using measurements in only 27 bases taken over a few tens of minutes.

MPS tomography is most efficient for states with a maximum distance over which significant quantum correlations exist. Example states are the 2D cluster states (universal resource states for quantum computing) and the ground states of a broad class of 1D systems. MPS tomography recognizes that the information needed to identify these states is accessible locally – that is, it only requires measurements on subsets of neighbouring particles. In this case, the total effort to obtain a reliable estimate for the state in the laboratory increases at most polynomially in system components [40, 41].

### 5.2.1. Matrix Product States

Matrix Product State representation is a way to parametrize a many-particle wave function. MPS are hierarchical, that is, the matrix size is related to the degree of entanglement. In principle, any state can be expressed as MPS. However, for locally-correlated states – representing a broad class of physical states – it offers a compact description with a number of parameters that increases only polynomially in system components. A great advantage of MPS is, that it is mathematically easy to apply operators onto and that they are efficient to search through (e.g. for finding the lowest energy for a given Hamiltonian). In the following I explain first intuitively, then mathematically, how to derive a compact MPS from the well-known density matrix representation [132]:

Let us consider a general pure quantum state, given by  $L$  particles on a one-dimensional lattice, where each particle can be in  $d$  local states  $|\sigma_i\rangle$  (e.g. for spin-1/2 particles  $\{|\sigma_i\rangle\} = \{|\uparrow_i\rangle, |\downarrow_i\rangle\}$ ). The state is described by

$$|\psi\rangle = \sum_{\sigma_1, \dots, \sigma_L} c_{\sigma_1 \dots \sigma_L} |\sigma_1, \dots, \sigma_L\rangle ,$$

with  $d^L$  coefficients  $c_{\sigma_1 \dots \sigma_L}$ . While the following discussion holds for lattices of arbitrary dimension, the most natural and intuitive picture is a 1D lattice.

**Intuitive derivation:** The first step in the construction of an MPS is the division

of the quantum system into two parts (bipartition), such that the first qubit  $|\sigma_1\rangle$  is set apart from the rest of the lattice  $|a_{L-1}\rangle$ , as depicted in iteration 1 of Fig. 5.6. The information about the correlations between the two subsystems is condensed into a Matrix  $A^{\sigma_1}$  and the remanent subsystem  $|a_{L-1}\rangle$ , such that the state is described by

$$|\psi\rangle = \sum_{a_{L-1}, \sigma_1} \langle a_{L-1}, \sigma_1 | \psi \rangle |a_{L-1}\rangle |\sigma_1\rangle \equiv \sum_{a_{L-1}, \sigma_1} A^{\sigma_1} |a_{L-1}\rangle |\sigma_1\rangle .$$

This bipartition and matrix decomposition is recursively swept over the entire quantum system until all qubits are transformed:  $|\psi\rangle = \sum_{\sigma_1, \dots, \sigma_L} A^{\sigma_1} A^{\sigma_2} \dots A^{\sigma_L} |\sigma_1, \dots, \sigma_L\rangle$ .

**Mathematical derivation:** The transformation of a the density matrix into an MPS representation is based on a tool from linear algebra, the so-called Singular value decomposition (SVD) (see Appendix J). There are three related methods to generate MPS, indicating that the MPS representation of a state is not unique. In the following I focus on the generation of so-called “*left-canonical matrix product states*”<sup>49</sup>:

1. Bipartition: Reshape the state vector with  $d^L$  entries, into a matrix  $\Psi$  of dimension  $[d \times d^{L-1}]$  such that  $\Psi_{\sigma_1, (\sigma_2 \dots \sigma_L)} = c_{\sigma_1 \dots \sigma_L}$ . Applying SVD onto matrix  $\Psi$ , results in:

$$\Psi_{\sigma_1, (\sigma_2 \dots \sigma_L)} = \sum_{a_1}^{r_1} U_{\sigma_1, a_1} S_{a_1, a_1} (V^\dagger)_{a_1, (\sigma_2 \dots \sigma_L)},$$

with the rank  $r_1 \leq d$ . The matrix  $S$  is diagonal with non-negative entries  $S_{a,a}$  – the so-called *singular values* – and describes the *bond* between the two subsystems of the bipartition.

2. Matrix decomposition: Now, the matrix  $U$  is decomposed into a collection of  $d$  row vectors  $A^{\sigma_1}$ , with the entries  $A_{a_1}^{\sigma_1} = U_{\sigma_1, a_1}$ . Further, matrices  $S$  and  $V^\dagger$  are multiplied and reshaped into a new matrix  $\Psi_{(a_1 \sigma_2), (\sigma_3 \dots \sigma_L)}$  of dimension  $[r_1 d \times d^{L-2}]$ . In summary the original coefficient vector of Eq. (5.2.1) turns into:

$$c_{\sigma_1 \dots \sigma_L} = \sum_{a_1}^{r_1} A_{a_1}^{\sigma_1} \Psi_{(a_1 \sigma_2), (\sigma_3 \dots \sigma_L)} .$$

The combination of reshaping (step 1.) and matrix decomposition (step 2.) corresponds to one iteration of the conversion into a matrix product state, as depicted graphically in Fig. 5.6. In the second iteration, the new matrix  $\Psi_{(a_1 \sigma_2), (\sigma_3 \dots \sigma_L)}$  is decomposed into

<sup>49</sup>In contrast to “right-canonical matrix product states” and “mixed-canonical matrix product states”, where the state decomposition starts from the right side, or simultaneously from the left and from the right.

its singular values:

$$\Psi_{(a_1\sigma_2),(\sigma_3\dots\sigma_L)} = \sum_{a_2}^{r_2} U_{(a_1\sigma_2),a_2} S_{a_2,a_2} (V^\dagger)_{a_2,(\sigma_3\dots\sigma_L)}.$$

Again,  $U$  is replaced by a set of matrices  $A^{\sigma_2}$  as in step 2, such that the original coefficient vector turns into

$$c_{\sigma_1\dots\sigma_L} = \sum_{a_1}^{r_1} \sum_{a_2}^{r_2} A_{a_1}^{\sigma_1} U_{(a_1\sigma_2),a_2} S_{a_2,a_2} (V^\dagger)_{a_2,(\sigma_3\dots\sigma_L)} = \sum_{a_1}^{r_1} \sum_{a_2}^{r_2} A_{a_1}^{\sigma_1} A_{a_1,a_2}^{\sigma_2} \Psi_{(a_2\sigma_3),(\sigma_4\dots\sigma_L)},$$

where  $A^{\sigma_2}$  is of dimension  $[r_1 \times r_2]$  with entries  $A_{a_1,a_2}^{\sigma_2} = U_{(a_1\sigma_2),a_2}$ . Upon further iterations we obtain

$$c_{\sigma_1\dots\sigma_L} = \sum_{a_1,\dots,a_{L-1}} A_{a_1}^{\sigma_1} A_{a_1,a_2}^{\sigma_2} \dots A_{a_{L-2},a_{L-1}}^{\sigma_{L-1}} A_{a_{L-1}}^{\sigma_L} = A^{\sigma_1} A^{\sigma_2} \dots A^{\sigma_L},$$

such that an arbitrary quantum state is represented in the form of an exact *matrix product state*:

$$|\psi\rangle = \sum_{\sigma_1,\dots,\sigma_L} A^{\sigma_1} A^{\sigma_2} \dots A^{\sigma_L} |\sigma_1, \dots, \sigma_L\rangle. \quad (5.5)$$

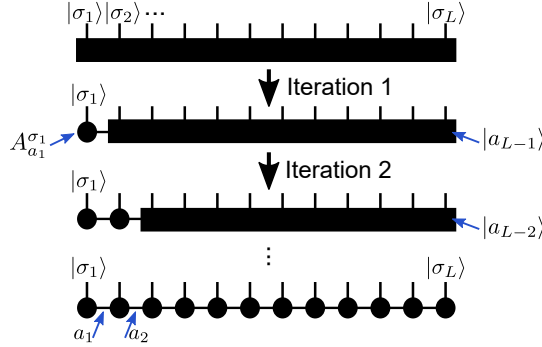


**Figure 5.6.:** Graphical representation of the iterative MPS construction from a pure quantum state. The first black rectangular block represents the coefficients  $c_{\sigma_1\dots\sigma_L}$  of state  $|\psi\rangle$ , from which the physical states  $|\sigma_1\rangle$  to  $|\sigma_L\rangle$  stick out vertically. After the first iteration we obtain a matrix  $A_{a_1}^{\sigma_1}$ , represented by a black circle and a reduced block, identified as  $|a_{L-1}\rangle$  (c.f. Eqs. (5.8)). The connecting horizontal arms correspond to the matrix indices  $a_1, \dots, a_L$ . They are auxiliary degrees of freedom, connecting the subsystems of each bipartition.

### Compression of MPS

The matrices in an MPS representation can be exponentially large, as e.g. states with long-range correlations have many non-negative eigenvalues and thereby large singular value matrices  $S$ . For exponentially decaying singular values  $S_{a,a}$ , it is possible to reduce the matrix dimension without appreciable loss of precision [132]. The following section summarizes the process of compressing an MPS, which is explained easiest using another form of matrix product representation, the so-called mixed-canonical representation.

Analogously to left-canonical MPS, the decomposition of the state can be performed likewise from the right side of the lattice, setting apart qubit  $|\sigma_L\rangle$  at first, and decomposing  $(V^\dagger)_{a_{L-1},\sigma_L}$  (instead of the matrix  $U$ ) into matrices  $B_{a_{L-1}}^{\sigma_L}$ . The states build in this manner are called “*right-canonical matrix product states*”. One can also mix the decomposition from the left and from the right, constructing a “*mixed-canonical matrix product state*”: Assume a bipartition of the system universe into a subsystem  $A$ , running from lattice site  $[1, \ell]$ , and subsystem  $B$  running from  $[\ell + 1, L]$ . We apply a decomposition of system  $A$  from the left up to site  $\ell$ , such that

$$c_{\sigma_1 \dots \sigma_L} = \sum_{a_\ell} (A^{\sigma_1} \dots A^{\sigma_\ell}) S_{a_\ell, a_\ell} (V^\dagger)_{a_\ell, (\sigma_{\ell+1} \dots \sigma_L)}.$$

Hereupon we carry out successive SVD on  $V^\dagger$ , from the right side up to site  $\sigma_{\ell+1}$  such that

$$\begin{aligned} (V^\dagger)_{a_\ell, (\sigma_{\ell+1} \dots \sigma_L)} &= \sum_{a_{\ell+1}, \dots, a_{L-1}} B_{a_\ell, a_{\ell+1}}^{\sigma_{\ell+1}} \dots B_{a_{L-1}}^{\sigma_L} \text{ and thereby} \\ |\psi\rangle &= \sum_{\sigma_1, \dots, \sigma_L} A^{\sigma_1} \dots A^{\sigma_\ell} S B^{\sigma_{\ell+1}} \dots B^{\sigma_L} |\sigma_1 \dots \sigma_L\rangle. \end{aligned} \quad (5.6)$$

Introducing two orthonormal bases states  $|a_\ell\rangle_A$ ,  $|a_\ell\rangle_B$  for subsystems  $A$  and  $B$ , we can read off the Schmidt decomposition (see Appendix J) of the state:

$$\begin{aligned} |a_\ell\rangle_A &= \sum_{\sigma_1, \dots, \sigma_\ell} (A^{\sigma_1} \dots A^{\sigma_\ell})_{1, a_\ell} |\sigma_1 \dots \sigma_\ell\rangle \\ |a_\ell\rangle_B &= \sum_{\sigma_{\ell+1}, \dots, \sigma_L} (B^{\sigma_{\ell+1}} \dots B^{\sigma_L})_{a_\ell, 1} |\sigma_{\ell+1} \dots \sigma_L\rangle \\ |\psi\rangle &= \sum_{a_\ell} |a_\ell\rangle_A S_{a_\ell, a_\ell} |a_\ell\rangle_B \end{aligned} \quad (5.7)$$

For exponentially decaying singular values  $S_{a_\ell, a_\ell}$ , we can cut the spectrum at the  $D_b$

largest values, without appreciable loss of precision. This reduction of the *bond dimension* goes along with compressing the matrices  $A^{\sigma_\ell}$  and  $B^{\sigma_{\ell+1}}$ , by retaining the first  $D_b$  columns of  $A^{\sigma_\ell}$  and the first  $D_b$  rows of  $B^{\sigma_{\ell+1}}$ . In summary, we obtain an efficient approximate representation of the state.

### 5.2.2. MPS reconstruction scheme

As discussed above, the representation as MPS is suitable for states with a maximum distance over which significant quantum correlations exist between constituents. In particular, we find that MPS tomography is well-suited to characterize the states generated in our experiment from the dynamical evolution of a Néel initial state under the XY-Hamiltonian. As described in section 5.1, the spread of information and correlations is well described by a maximum group velocity. Therefore, after a finite evolution time, we identify a maximum distance over which correlations extend in the system – the correlation length  $L$ . Beyond this length, correlations decay exponentially in distance. The information required to describe the state is largely contained locally: in the density matrix reductions of all groups of neighbouring particles contained within  $L$ . MPS tomography recognizes this fact and requires only measurements on subsets of particles that lie in the same neighbourhood. Each local reduction can be determined by full quantum state tomography (QST), requiring measurements in at most  $3^L$  bases.

In our experiment, we perform measurements up to  $L = 3$ , amounting to a maximum of 27 measurement bases. The reduced state estimates are then passed to a classical algorithm which finds an MPS estimate in a time polynomial in the number of qubits  $N$ . In the following, I give an overview on how the experimental data is processed to reconstruct a pure MPS estimate of the unknown state in the laboratory, and how we construct a fidelity certificate. The development of the reconstruction process, as well as the application to our data was performed in the team of Prof. Martin Plenio (University of Ulm). The Supplementary Material of Ref. [123] provides a more detailed mathematical description of the process.

The experimental data comprises up to 27 different measurement settings, each repeated 1000 times. These samples are split into two parts of 500 samples (Part 1 and Part 2 in Fig. 5.7). The first part is used to obtain a pure MPS estimate  $|\psi_c^k\rangle$  of the unknown state  $\rho_{\text{lab}}$  in the laboratory. The second part is used to obtain a certificate, that is, an assumption-free lower bound on the fidelity between the unknown state and our MPS estimation of this state. The motive to split the data is to ensure statistical independence of the process of obtaining the MPS estimate  $|\psi_c^k\rangle$ , and the process of

obtaining the certificate.

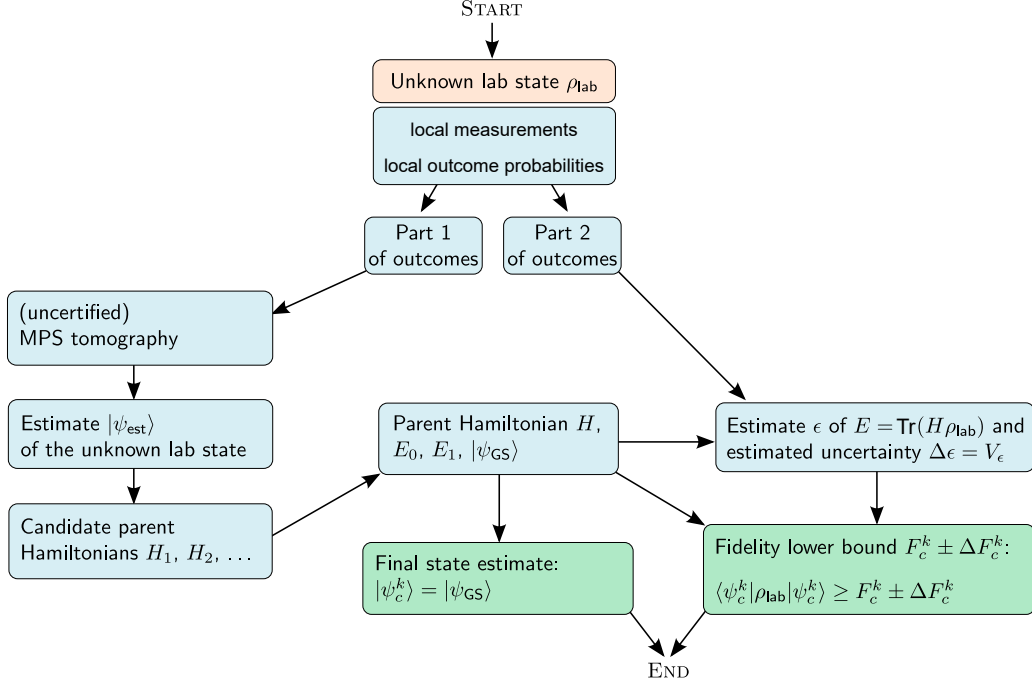


**Figure 5.7.:** Flow process chart of certified MPS tomography. Measurement data from the unknown state in the laboratory  $\rho_{\text{lab}}$  is split into two parts. The first part is used to obtain a certified MPS estimate  $|\psi_c^k\rangle$  and a parent Hamiltonian  $H$ . The second part is processed to obtain a fidelity lower bound  $F_c^k \pm \Delta F_c^k$ .

**Part 1. Identify an initial MPS estimate:** The first part of the experimental data is processed with linear inversion to obtain estimates of the local  $k$ -spin reduced density matrices. These reduced density matrices are processed by the modified singular value thresholding (SVT) algorithm from Ref. [40], to return a pure MPS estimate. This pure state is used as the start vector for the iterative likelihood maximization algorithm over pure states [115], which uses the  $6^k$  outcome probabilities<sup>50</sup> as input and returns an initial MPS estimate  $|\psi_{\text{est}}\rangle$  of the unknown lab state. Both algorithms search for an MPS that is compatible with the local outcome probabilities, and has a small bond dimension  $D_b$ . For the 8 qubit experiment, we use  $D_b = 2$  for  $t \leq 2$  ms and  $D_b = 4$  for other times. For 14 qubits we use  $D_b = 16$  for all times. The initial estimate  $|\psi_{\text{est}}\rangle$  reproduces the local outcome probabilities well but it may or may not be close to the unknown state  $\rho_{\text{lab}}$  in the laboratory. Therefore, an additional step is necessary to

<sup>50</sup>Each of the  $3^k$  settings has  $2^k$  distinguishable outcomes, which amounts to  $3^k \times 2^k = 6^k$  outcome probabilities.

verify the correctness of the result.

**Part 2. Certify an MPS estimate:** We use the second part of the experimental data to obtain estimates for the fidelity lower bound  $F_c^k$  and its statistical uncertainty  $\Delta F_c^k$ , caused by the finite number of measurements. We start with finding the so-called parent Hamiltonian of the initial estimate  $|\psi_{\text{est}}\rangle$ . A parent Hamiltonian of a pure state  $|\psi_{\text{GS}}\rangle$  is any hermitian linear operator  $H$  such that  $|\psi_{\text{GS}}\rangle$  is the ground state of  $H$ . If  $H$  is a sum of local terms – that is, terms acting only on  $k$  neighbouring spins – the  $3^k$  measurements described above suffice to define it, and obtain its energy spectrum. We define a set of candidates  $H_1, H_2, \dots$  for parent Hamiltonians, for which the overlap between their ground states and  $|\psi_{\text{est}}\rangle$  lies above a certain threshold. For all candidate parent Hamiltonians we compute the ground state  $|\psi_{\text{GS}}\rangle$  as well as the smallest and second smallest eigenvalues  $E_0$  and  $E_1$ . In order to return the highest fidelity lower bound, the final parent Hamiltonian has to provide the best compromise between two conditions:

1. The related ground state  $|\psi_{\text{GS}}\rangle$  must be close to the initial MPS estimate  $|\psi_{\text{est}}\rangle$ . This means, the Hamiltonian has to minimize

$$\mathcal{D}(|\psi_{\text{est}}\rangle, |\psi_{\text{GS}}\rangle) = (E_1 - E_0), \quad (5.8)$$

where  $\mathcal{D}(|\psi\rangle, |\tilde{\psi}\rangle) = \frac{1}{2} \|\ |\psi\rangle\langle\psi| - |\tilde{\psi}\rangle\langle\tilde{\psi}| \|_1 = \sqrt{1 - |\langle\psi|\tilde{\psi}\rangle|^2}$  is the trace distance [21].

2. The gap between the two smallest eigenvalues  $E_1 - E_0$  must be much bigger than the measurement uncertainty of the energy  $E$  of the unknown state  $\rho_{\text{lab}}$  in terms of the parent Hamiltonian  $H$ :  $E = \text{Tr}(H\rho_{\text{lab}})$

Finally, we denote by  $|\psi_c^k\rangle$  the ground state of the chosen parent Hamiltonian, and define it as the final estimate of the unknown state in the laboratory  $\rho_{\text{lab}}$ . Since the ground state is non-degenerate, i.e.  $E_0 < E_1$ , a lower bound to the fidelity between the state  $|\psi_c^k\rangle$  and any pure or mixed state  $\rho_{\text{lab}}$  is given by [40]

$$\langle\psi_c^k|\rho_{\text{lab}}|\psi_c^k\rangle \geq 1 - \frac{E - E_0}{E_1 - E_0} \Rightarrow F_c^k \mathbb{1} \equiv 1 - \frac{\epsilon(D) - E_0}{E_1 - E_0}. \quad (5.9)$$

The information about the laboratory state is obtained from a finite number of measurement outcomes (distributed according to an unknown probability distribution). This leads to uncertainty in our estimate of the energy  $E$ , which we express by introducing the estimator  $\epsilon(D)$ . The term *estimator* refers to a quantity that is given by

many independent random variables – in our case, the measurement data  $D$  – to obtain an estimate  $\epsilon(D)$  of the true value  $E$  [133]. Our uncertainty about the value of  $E$  is quantified by  $V_\epsilon(D)$ , as the mean squared error of  $\epsilon(D)$  and defines the uncertainty of the fidelity lower bound:

$$\Delta F_c^k = \frac{\sqrt{V_\epsilon(D)}}{E_1 - E_0}. \quad (5.10)$$

### Experimental results

Figure 5.8 a) presents the certified fidelity lower bound  $F_c^k \leq \langle \psi_c^k | \rho_{\text{lab}} | \psi_c^k \rangle$  from MPS tomography during 8-qubit quench dynamics of an Néel-ordered initial state  $|\phi(0)\rangle = |\uparrow, \downarrow, \uparrow, \dots\rangle$ . The results closely match an idealized theoretical model where MPS tomography is applied to exact local reductions of the ideal time-evolved states. Measurements at  $t = 0$  on individual sites ( $k = 1$ ) yield an MPS (pure-state) reconstruction with  $F_c^1 = 0.98 \pm 0.01$  and  $|\langle \psi_c^1 | \phi(0) \rangle|^2 = 0.98$ , indicating that the system is initially well described by a pure product Néel state. The fidelity lower bound based on such single-site measurements rapidly degrades as the simulator evolves with time, falling to 0 by  $t = 2$  ms. Nevertheless, an accurate MPS description is still achieved by measuring on larger ( $k = 2$ ) and larger ( $k = 3$ ) sets of neighbouring sites. The fidelity bounds  $F_c^3$  begin to clearly drop after  $t = 3$  ms, consistent with the time at which the information wavefronts are expected to reach next-nearest-neighbours, developing correlations beyond 3 sites (see light-like cones, in Fig. 5.8 b)). Beyond  $t = 3$  ms it becomes increasingly difficult to uniquely distinguish (and certify) the global state based on 3-site local reductions. This agrees with the growing amount of entanglement with time, as can be seen from the inset in Fig. 5.8 a). It also agrees with the properties measured directly in the local reductions (Fig. 5.4), in which entanglement in spin triplets maximizes around 3 ms. To reconstruct the state in the laboratory beyond  $t = 3$  ms with high fidelity, it would be necessary to measure on an increasing number of sites, demanding measurements that grow exponentially in  $k$ .

Figure 5.9 shows MPS tomography results from a 14-spin quench (panel d)) – a many-body state far beyond the practical limit of full QST, which would require measuring in more than 4 million bases. The state reconstruction presented here uses only 27 local measurement bases instead, to obtain the reduced density matrices of all  $k = 3$  neighbouring sites. Figs. 5.9 a)-c) compare spin-spin correlation matrices at time  $t = 4$  ms from the certified MPS  $|\psi_c^3\rangle$  (lower panels) with those obtained in the laboratory directly via additional measurements (upper panels). The certified pure MPS captures the strong pairwise correlations in the simulator state and correctly predicts the sign and spatial profile of correlations beyond next-nearest neighbour. This means, that the

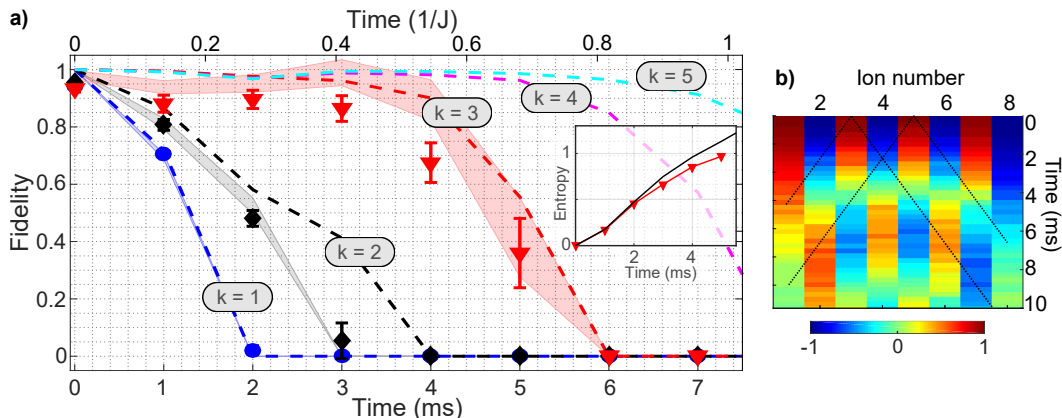


**Figure 5.8.: MPS tomography results for an 8-qubit quench.** a) Lower bound on the fidelity  $F_c^k$  between the certified MPS estimate  $|\psi_c^k\rangle$  and the generated state in the laboratory  $\rho_{\text{lab}}$ , as a function of the simulator evolution time (c.f. panel b)). Shapes: Data points for which the MPS estimate was reconstructed from measurements over  $k$  neighbouring sites. Error bars reflect one standard deviation uncertainty  $\Delta F_c^k$  due to the finite number of measurements and are derived in the certification process. Dashed lines: Theoretical model for which MPS tomography was applied to  $k$ -site local reductions derived from ideal simulator dynamics of perfect Néel initial states. Shaded areas simulate the outcomes of the finite number of measurements per basis used in experiments (1000). Insert: Half-chain von Neumann entropy of the reconstructed state: Red triangles from  $|\psi_c^k\rangle$ , black line from ideal model. b) Single-spin magnetization dynamics  $\langle \sigma_i^z(t) \rangle$  during a quench of the XY-Hamiltonian. Light-like cones are visualized as black dotted lines, exemplifying the maximum speed of correlation spread.

scheme is able to predict state properties beyond those that are measured to reconstruct the state.

The MPS estimate  $|\psi_c^3\rangle$  yields a certified minimum fidelity of  $F_c^3 = 0.39 \pm 0.08$ . However,  $F_c^k$  is only a conservative lower bound and even lies quite far from the one expected from an idealized theoretical model (0.78). It is natural to ask what the true state fidelity is. Using the estimated state  $|\psi_c^3\rangle$  from MPS tomography, we perform Direct Fidelity Estimation (see Section 5.2.3) with the experimentally generated state. This reveals a fidelity of  $F_{\text{DFE}} = 0.74 \pm 0.05$ . In summary, MPS tomography provided an accurate estimate of the 14-spin simulator state, and the fidelity lower bound of  $F_c^3 = 0.39 \pm 0.08$  is correct. We find, that the certification process is compromised by errors in initial state preparation, introducing mixture at the single spin level. The current state initialization error per-spin limits the ability to accurately and efficiently characterize its state. A revised optical addressing setup should improve single-qubit operations and allow for a smaller and constant error-per-spin.

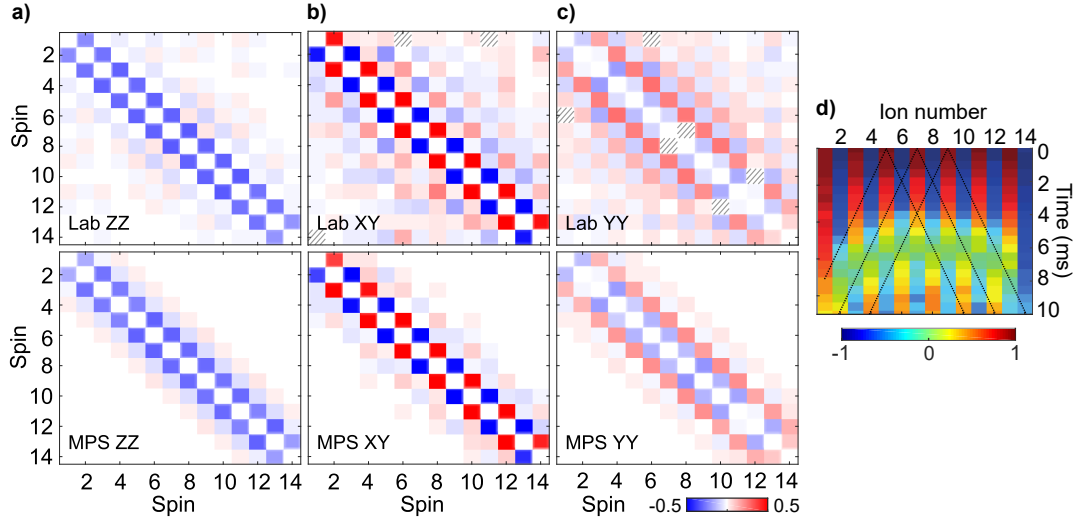


**Figure 5.9.: MPS tomography results for a 14-qubit quench. a)-c)** Two-spin correlation matrices  $\langle A(t)_i B(t)_j \rangle - \langle A(t)_i \rangle \langle B(t)_j \rangle$  at time  $t = 4$  ms in the quench dynamics (c.f. panel d).  $A, B$  as labelled in the graphs, with X, Y and Z denoting standard Pauli spin operators. The correlations of the upper panels are measured directly, with hatched squares denoting non-measured correlations. The lower panels show correlation matrices extracted from the certified MPS estimate  $|\psi_c^k\rangle$ , which captures many of the correlations between spins up to four sites apart. The weak correlations over greater distances in the laboratory state develop effectively instantly in quench dynamics, due to the long-range components of our interactions. **d)** Single-spin magnetization dynamics  $\langle \sigma_i^z(t) \rangle$  during a quench of the XY-Hamiltonian. Light-like cones are visualized as black dotted lines, exemplifying the maximum speed of correlation spread.

### Scalability considerations

We determine the scalability of MPS tomography, by studying the dependency of the estimation error on the number of spins  $N$ , under a constant total number of measurements. The estimation error is quantified with the trace distance  $\mathcal{D} = \sqrt{1 - F}$  between the density matrices of the two pure states, where  $F$  describes the estimation fidelity lower bound. We carried out numerical simulations, estimating states containing a significant amount of entanglement (Half-chain von Neumann entropy  $\sim 0.58$ ). Specifically, we reconstructed states of  $N \in \{8, 20, 32, 48, 64\}$  spins, that would be generated after 3 ms under an quench of an ideal nearest-neighbour model. The couplings and fields of this model are set to the average values of the 8-spin experiment described above. For each state, we simulate  $M$  measurements in each  $k$ -spin basis. The results in Fig. 5.10 show that the estimation error  $\mathcal{D}$  decreases slightly with  $N$ , if we hold the ratio  $c = M/N^2$  constant. This means, that our scheme achieves an (at most) constant estimation error  $\mathcal{D}$ , with a total number of measurements given by  $M_T = cN^2(N - k + 1)3^k$  which is only cubic in  $N$ . The post-processing time to obtain

the state increases with  $\approx N^{1.2}$ . Hence MPS tomography involves an experimental and computational effort that scales polynomially in  $N$  while standard tomography scales exponentially. Unfortunately, we could not experimentally demonstrate the efficiency of MPS tomography beyond 14 spins, for technical reasons: During the preparation of the initial state, addressing errors<sup>51</sup> introduce mixture at the single spin level. These error-per-spin obviously accumulates, such that MPS tomography could not return a useful pure-state description in our 20-qubit quench experiment. Nevertheless, the process was considered successful because it returned a vanishing fidelity lower bound for the state estimate, denoting that the procedure failed.

A generalization of the MPS tomography scheme to higher spatial dimensions and to mixed states is possible, using matrix product operators [41, 115]. However, for mixed states no general certification method is currently known [134].

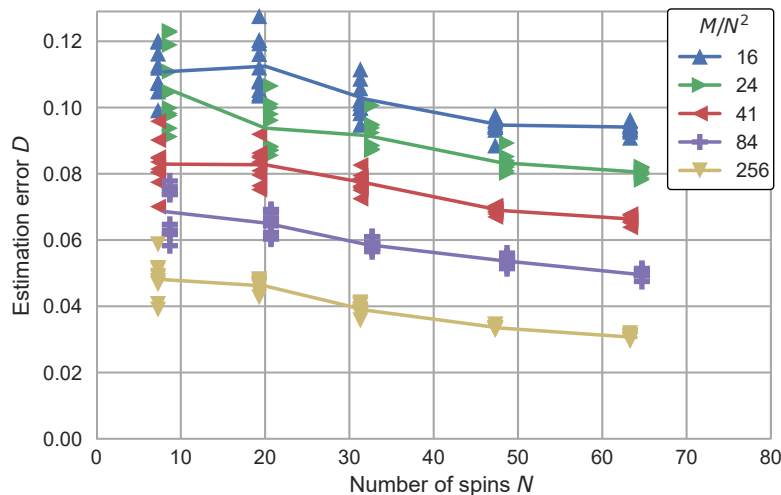


**Figure 5.10.: Resource cost of MPS tomography**, obtained from numerically simulated MPS reconstructions of ideal nearest-neighbour quench states. Shown is the constant estimation error  $\mathcal{D} = \sqrt{1 - \bar{F}}$ , as a function of the number of spins  $N$ . The reconstruction procedure was repeated 10 times to estimate fluctuation errors due to the finite number of measurements  $M$ . Lines show connected average values.

### 5.2.3. Direct fidelity estimation

The fidelity returned by the certification procedure is only a lower bound for the overlap between the state in the laboratory  $\rho_{\text{lab}}$  and the estimated MPS  $|\psi_c^3\rangle$ . The actual overlap between the two states could take any value between the certificate and unity,

<sup>51</sup>The new optical addressing setup, built during the writing of this work [103], yields improved single-qubit operations and should allow for a small constant error-per-spin beyond 20 spins.

and is determined via Direct Fidelity Estimation (DFE) [49, 50]. This method uses a set of measurements on the (generally mixed) laboratory state to determine a fidelity between this state and a given pure state – in our case the output MPS from our tomography scheme. In this section, I provide an overview of DFE with emphasis on the current experiment. Mathematical details, in particular error analysis, can be found in the Supplementary Material of Ref. [123].

In general, the fidelity is given by

$$F(|\psi_c^3\rangle, \rho_{\text{lab}}) = \langle \psi_c^3 | \rho_{\text{lab}} | \psi_c^3 \rangle = \sum_{k=1}^{4^N} \rho_{\text{lab}}^k \sigma^k,$$

where  $\rho_{\text{lab}}^k = \text{Tr}(P^k \rho_{\text{lab}})$  is the lab state's expectation value of the normalized Pauli string operators  $P^k$ , and  $\sigma^k = \langle \psi_c^3 | P^k | \psi_c^3 \rangle$  is the expectation value of the MPS  $|\psi_c^3\rangle$ . The brute force approach of measuring all  $4^N$  observables is impractical for systems composed of more than a few qubits. The DFE method leverages the knowledge of the MPS estimate to overcome this infeasibility: the expression above is replaced by a preferential summation over those values of  $k$  for which MPS-estimate components  $\sigma^k$  are likely to be large. In other words, more measurements are made in those Pauli operators  $P^k$  for which  $|\psi_c^3\rangle$  has a large expectation value. Therefore, we first rewrite the fidelity as the expectation value of the variable  $\rho_{\text{lab}}^k / \sigma^k$  over the probability distribution  $q^k \stackrel{\text{def}}{=} (\sigma^k)^2$ :

$$F = \sum_{k=1}^{4^N} q^k \frac{\rho_{\text{lab}}^k}{\sigma^k}.$$

Next, this expression is evaluated using a Monte Carlo approach: We draw  $M$  random indices  $(k_1, k_2, \dots, k_M)$  with  $k_i \in \{1, 2, \dots, 4^N\}$  according to the distribution  $q^k$  and approximate the fidelity with

$$F \approx \bar{F} = \frac{1}{M} \sum_{i=1}^M \frac{\rho_{\text{lab}}^{k_i}}{\sigma^{k_i}}.$$

In the experiment we set  $M = 250$  and repeat the measurements many times. Specifically, the number of copies  $N_k$  spent to measure a particular Pauli operator  $P^k$  is proportional to the inverse square of its calculated expectation value  $\sigma^{k_i}$ . This way we prevent the error in  $\bar{F}$  to be dominated by those terms for which  $\sigma^{k_i}$  is small. In total we prepare and evaluate  $5 \times 10^5$  copies of the state. Fig. 5.11 shows the distribution of  $\rho_{\text{lab}}^{k_i} / \sigma^{k_i}$  for different  $i$ , from which we infer the fidelity estimate and its error:  $0.74 \pm 0.05$ .

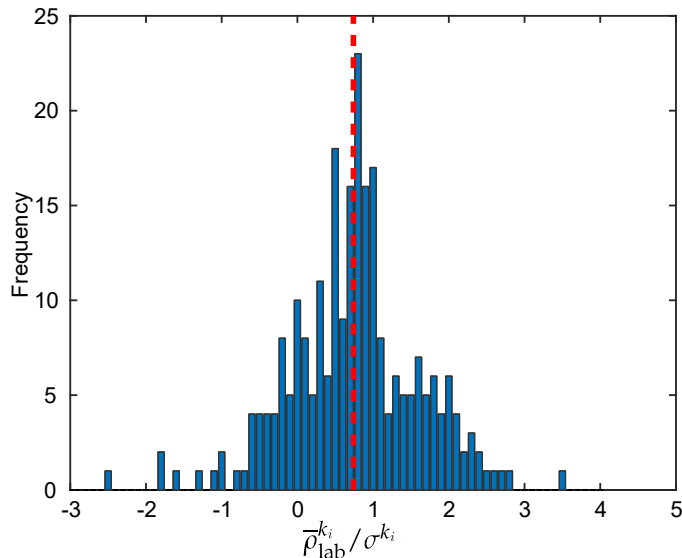


**Figure 5.11.:** Histogram of the DFE-variable  $\bar{\rho}_{\text{lab}}^{k_i} / \sigma^{k_i}$  for different observables. The mean value (red dashed line) and standard deviation are the respective estimators of the fidelity  $F$  and its error.

### 5.3. Conclusion

We applied MPS tomography to successfully reconstruct and verify dynamical states of our quantum simulator towards classically intractable regimes. Performing measurements in only 27 bases, we estimated states comprising up to 14 entangled and individually-controlled spins – a size far beyond the practical limits of QST. Even if the obtained fidelity lower bound was conservative, direct fidelity estimation proved that MPS tomography provided an accurate estimate of the 14-spin quench state.

Our results revealed the dynamical growth of entanglement and description complexity in our quench experiments: As the quantum simulator evolves, the correlation length in the system increases. With this, the number of measurements to estimate local reductions and obtain an accurate pure MPS description, grows exponentially. This puts practical limits on the evolution time until which a state in our quantum simulator can be efficiently characterized via MPS tomography. Once correlations have spread out over the whole system, the effort becomes the same as for full QST.

We determined the scalability of MPS tomography, by studying the dependency of the reconstruction fidelity on the number of spins  $N$ , under a constant total number of measurements. Numerical simulations revealed that for a constant fidelity the required number of measurements scales as the third power in  $N$ . The post-processing time to obtain the state increases with  $\approx N^{1.2}$ . Hence, MPS tomography involves an

experimental and computational effort that scales only polynomially in  $N$ .

The here presented technique for characterizing large quantum states is not restricted to 1D systems nor to those with strictly finite-range interactions. Further, MPS tomography does not require prior assumptions about the state in the laboratory (for example, if it is pure or well-described by a compact MPS), because the obtained state estimate can be certified. Therefore, it could become a standard procedure, to employ MPS tomography to obtain a first estimate of a large quantum state, and then apply direct fidelity estimation or Renyi entropy measurements [104] for further characterization. With this, MPS tomography should find widespread use to study large quantum many-body systems and to benchmark and verify quantum simulators and computers.



## 6. Environment-assisted quantum transport

The work presented here is published in:  
[Phys. Rev. Lett. \*\*122\*\*, 050501 \(2019\)](#)

The way in which energy is transported through a network governs fundamental phenomena in nature, such as thermal and electric conductivity and phase changes. In recent years, investigations of quantum transport have drawn great inspiration from quantum biology, especially from chromophoric light-harvesting complexes [135–140] that are central elements of photosynthesis. The transport through these complexes is governed by a highly non-trivial interplay between coherent quantum dynamics and dissipative environmental noise that destroys the quantum coherence. Energy mismatch in disordered materials leads to destructive interference of the quantum state’s wavefunction, resulting in suppressed transport efficiency [141, 142]. However, the interaction with environmental noise can lift this localization and enhance quantum transport, an effect known as environment-assisted quantum transport (ENAQT) [143]. This intriguing interplay has motivated several recent proof-of-principle experiments in highly-controlled model systems. However, these experiments were limited to at most four network nodes, represented by photonic wave-guides, classical electrical oscillators, superconducting qubits, or trapped ions [144–149].

In this chapter, I present an experimental in-depth study of the interplay between coherent quantum transport, energy disorder, and environment-induced noise on a 10 node network. The chapter begins with the introduction of the experimental realization of a disordered network, which couples to a Markovian dephasing noise. Then, controlled studies of quantum coherences and diffusion dynamics are presented. The second part of the chapter discusses the effect of non-Markovian dephasing baths on the transport behaviour.

## 6.1. Experimental implementation

The nodes of our quantum network are realized by 10 trapped  $^{40}\text{Ca}^+$  ions, where two internal electronic states encode spin-1/2 particles:  $|\downarrow\rangle \equiv |S_{1/2}, m_j = 1/2\rangle$  and  $|\uparrow\rangle \equiv |D_{5/2}, m_j = 5/2\rangle$ . A global, trichromatic laser beam couples the states of all ions, inducing a long-range spin-spin interaction  $H_1 = \hbar \sum_{i \neq j} J_{ij} (\sigma_i^+ \sigma_j^- + \sigma_i^- \sigma_j^+)$  (Section 3.3). This Hamiltonian describes the hopping of spin excitations between sites  $i$  and  $j$ , conserving the number of spins in the excited state  $|\uparrow\rangle$ . The measured hopping rates have a peak strength  $J_{\max}$  between  $(2\pi) 28$  Hz and  $(2\pi) 33$  Hz and an interaction range of  $\alpha = 1.22$ . An important feature of our experimental setup is the individual controllability and detection of the quantum state of each network node. We investigate the transport dynamics by observing the spread of a single electronic excitation over the sites of the network. To do so, we introduce an excitation at time  $t = 0$  at the source site  $i_{\text{source}} = 3$ , by preparing spin  $i_{\text{source}}$  in the  $\sigma^z$  eigenstate  $|\uparrow\rangle$  while keeping all other spins in the eigenstate  $|\downarrow\rangle$  (Fig. 6.1). We observe the transport of the excitation through the network to the target site  $i_{\text{target}} = 8$  under the disturbed spin-spin interaction Hamiltonian (6.1).

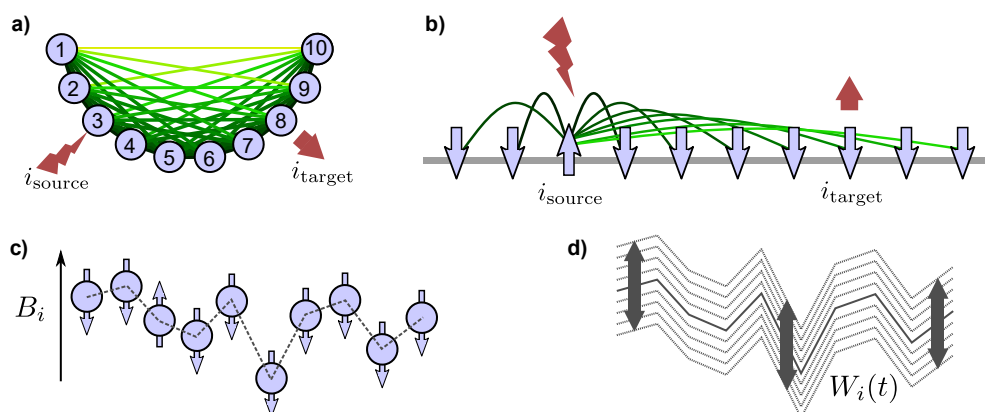


**Figure 6.1.: Sketches of the transport network in different aspects.** **a)** All ions (blue circles) interact with each other through a long-range coupling. Darker and thicker connection lines indicate higher coupling strengths. The red flash denotes the manipulation of the source ion, the red arrow denotes the read-out of the target ion. **b)** The network represented as a chain of spin-1/2 particles, with the spin states denoted as blue arrows. A few green connection lines indicate the long-range spin-spin coupling, spreading of the spin excitation over the network. **c)** Illustration of the static on-site energy disorder  $B_i$  as gray dashed line, inducing energy-mismatch between the network sides. **d)** Illustration of dephasing noise  $W_i(t)$ , as temporally modulated energy-mismatch.

The source and target sites are chosen such that the transport dynamics is not immediately influenced by boundary effects. We define the transport efficiency to a

particular site  $i$  by  $\eta_i \equiv \int_0^{t_{\max}} p_i(t) dt$ . Here,  $p_i(t) = (\langle \sigma_i^z(t) \rangle + 1)/2$  is the instantaneous probability to find the excitation at site  $i$  and  $t_{\max} = 60 \text{ ms} \approx 11.7/J_{\max}$  is the system's evolution time. The time is chosen such that the evolution is long enough to observe ENAQT and short enough to minimize decoherence from amplitude damping due to spontaneous decay [150]. Any residual amplitude damping effect is eliminated by postselecting measurements with a single excitation in the system. Typically more than 77% of the measurements lie within this subspace.

Considering static disorder (energy mismatch) and coupling to the environment, the full spin-spin interaction Hamiltonian reads as [151]:

$$H = \hbar \sum_{i \neq j} J_{ij} (\sigma_i^+ \sigma_j^- + h.c.) + \hbar \sum_i (B_i + W_i(t)) \sigma_i^z. \quad (6.1)$$

Experimentally, the static disorder  $B_i$  and dynamic dephasing noise  $W_i(t)$  are realized by individually tunable on-site AC-Stark shifts, inducing an energy-mismatch between the network sites (Fig. 6.1 c-d)). These AC-Stark shifts are induced during the interaction dynamics, by applying multiple radio frequencies to an acousto-optic deflector. This generates a set of laser beams which are then tightly focused to simultaneously address multiple ions (Section 4.4). The corresponding laser frequency is detuned from the qubit's carrier transition by 60–90 MHz. The RF amplitudes (and thereby the intensity) for each beam can be regulated independently, resulting in individually adjustable AC-Stark shifts of up to a few kHz. Note that cross talk between neighbouring ions and sub-harmonics of the driving frequencies are negligible, such that noise at different sites is uncorrelated. For both static disorder and dephasing noise, we apply up to 40 different instances and average the observations. Therefore, the values  $B_i$  are randomly sampled from a uniform distribution  $[-B_{\max}, B_{\max}]$ , where  $B_{\max}$  can take two different values: weak static disorder  $B_{\max, \text{weak}} = 0.5 \cdot J_{\max}$  and strong static disorder  $B_{\max, \text{strong}} = 2.5 \cdot J_{\max}$ .

The time-varying on-site energies,  $\hbar W_i(t)$ , induce dephasing between the  $|\downarrow\rangle$  and  $|\uparrow\rangle$  states, simulating environmental noise. It is engineered by temporally modulating the intensity (and in turn the applied AC-Stark shift) of each addressing laser beam individually. For this, we use an arbitrary waveform generator with a switching time much faster than any time scale in the dynamics (Section 4.4). It individually modulates the intensity of each frequency component of the multitone RF, driving the acousto-optical deflector. Generally, we simulate a noise process with broadly tunable spectral

power [152, 153]

$$S(\omega) = \lim_{T \rightarrow \infty} \frac{1}{T} \int_0^T \int_0^T \langle \langle W_i(t) W_i(t') \rangle \rangle e^{i\omega(t-t')} dt' dt, \quad (6.2)$$

where  $\langle \langle \bullet \rangle \rangle$  denotes averaging over up to 40 different noise instances.

Strong<sup>52</sup> energy mismatch in an interacting system lead to destructive interference of the wavefunction causing localization of the electronic excitation. Generally, static disorder and environmental coupling are expected to have negative impact on the transport efficiency. However, as we demonstrate in the following, the interaction with the environment can enhance the excitation spread under certain conditions. We investigate the quantum transport behaviour under two types of noise: white, or Markovian noise where  $S(\omega) = \text{const.}$  (Section 6.2) and non-Markovian noise, where  $S(\omega)$  has a Lorentzian shape (Section 6.3).

## 6.2. Markovian dephasing baths

First, we study the effect of static disorder and coupling of the network to white (or Markovian) dephasing noise  $W_i(t)$ , for which  $S(\omega) = \text{const.}$  For this, we randomly sample  $W_i$  between two values  $\{-\frac{W_{\max}}{2}, \frac{W_{\max}}{2}\}$  with equal probabilities, every  $\Delta T = 100 - 200 \mu\text{s}$  in the dynamics. This is equivalent to tossing a coin at a rate  $\lambda = 1/\Delta T$ , which is chosen to be much faster than the maximal hopping  $J_{\max}$ , such that the process is well approximated as white noise with  $S(\omega) = \frac{W_{\max}^2}{\lambda}$ . This constant spectral power defines the noise strength and gives a rate of dephasing  $\gamma = \frac{W_{\max}^2}{\lambda}$ . This dephasing noise is applied to the interacting quantum network under weak static disorder, where  $B_{\max, \text{weak}} = 0.5 \cdot J_{\max} \approx (2\pi) 15 \text{ Hz}$  and strong static disorder, where  $B_{\max, \text{strong}} = 2.5 \cdot J_{\max} \approx (2\pi) 75 \text{ Hz}$ .

Fig. 6.2 shows the measured transport efficiency  $\eta_s$  as a function of the dephasing rate  $\gamma/J_{\max}$ : Weak static disorder (blue markers) does not affect transport considerably. However, with additional noise at a level beyond  $\gamma = J_{\max}$  the transport efficiency gradually decreases. This regime, where noise is the dominant effect and inhibits quantum transport, is known as the quantum Zeno regime. Under strong static disorder (red markers), the phenomenology becomes even richer: At weak dephasing,  $\gamma < J_{\max}$ , excitation transport is suppressed corresponding to Anderson localization. Around  $\gamma \approx J_{\max}$ , the noise cancels the destructive interference causing the localization, and thereby enhances the transport efficiency, which is the hallmark of ENAQT. For strong

<sup>52</sup>The energy mismatch  $B_{\max}$  are to be compared with the peak interaction strength  $J_{\max}$ . We consider the case  $B_{\max} > J_{\max}$  as strong energy mismatch.

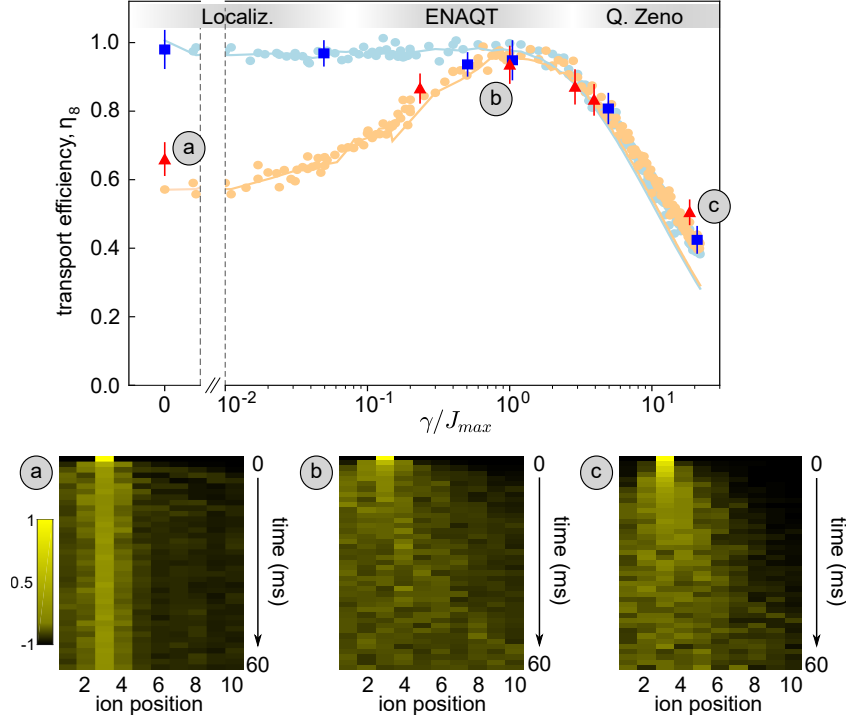


**Figure 6.2.: Quantum transport under Markovian-like dephasing.** Transport efficiency  $\eta_8$  to the target (ion 8) under different strengths of static disorder (blue:  $B_{\max, \text{weak}} = 0.5 \cdot J_{\max}$ , red:  $B_{\max, \text{strong}} = 2.5 \cdot J_{\max}$ ) and dephasing with rate  $\gamma$ . Experimental points (shown as dark squares and triangles) result from averaging over 20 – 40 random realizations of disorder and noise, with 25 experimental repetitions each. Error bars are derived via bootstrapping, based on 1000 samples (see Ref. [154] for details). The regimes of localization, ENAQT and quantum Zeno effect are indicated in shaded gray on the top of the graph. The data agrees well with theoretical simulations of the coin-tossing random process (light blue and orange bullets) realized in the experiment, while simulations with ideal Markovian white noise (lines) underestimate the transport efficiency at large  $\gamma$ . The simulation averages over 300 random realizations. The gray labels a, b, c, mark data points under strong static disorder, for which the magnetization dynamics  $\langle \sigma_i^z(t) \rangle$  is shown in the lower three panels. The suppression or enhancement of excitation spread in the three transport regimes are well depicted.

noise,  $\gamma > J_{\max}$ , the quantum Zeno effect again suppresses transport. The experimental results agree well with theoretical simulations of the coin-tossing process (light bullets in Fig. 6.2). At very strong dephasing, the induced energy shift  $W_{\max}$  becomes comparable to the coin flipping rate  $\lambda$  and the Markovian approximation is no longer fulfilled. In this case, deviations from ideal Markovian white noise (lines) become noticeable, as discussed in [150]. Such non-Markovian effects will be further discussed in Section 6.3.

### 6.2.1. Coherence and diffusion dynamics

The role of coherences in ENAQT has been much discussed in the context of exciton transport in photosynthetic complexes [140, 155–158]. To investigate the existence and development of coherences in our system, we observe the time-resolved dynamics of the excitation probability of spin 8,  $p_8(t)$ , for strong static disorder and several strengths of dephasing noise (see Fig. 6.3). Without dephasing noise,  $\gamma = 0$ , we find strong oscillating behaviour, indicative of quantum coherent transport. Already in the regime where ENAQT becomes relevant,  $\gamma \approx J_{\max}$ , the noise damps out any perceivable coherent oscillations, with spurious oscillations lying in the range of statistical fluctuations. Further, at sufficiently large times,  $t \gg 1/\gamma$ , and for large values of  $\gamma$ , the dynamics of the excitation probability of spin  $i$ ,  $p_i(t)$ , is well described by a classical rate equation (blue solid lines, Fig. 6.3). Here, the coherences between sites have been adiabatically eliminated (see Appendix G), resulting in the equation

$$\dot{p}_i = \sum_{\ell \neq i} \Gamma_{\ell i} (p_\ell - p_i), \quad (6.3)$$

with the classical hopping rate  $\Gamma_{\ell i} = \frac{4\gamma J_{i\ell}^2}{4(B_i - B_\ell)^2 + \gamma^2}$ , derived from the experimental spin-spin coupling matrix  $J_{i\ell}$  and the applied static on-site energies  $B_i$  as well as dephasing noise rate  $\gamma$ . This set of coupled differential equations describes a purely diffusive transport of the spin excitation. For weak dephasing, we observe deviations from rate equation (6.3) at short times, which indicates a temporal crossover from coherent to diffusive transport, similar to what has recently been resolved in classical Brownian motion [159]. With increasing dephasing strength, the observed coherences are damped and the system converges to a diffusive rate equation. This highlights the fact that Anderson localization is a wave phenomenon caused by destructive interference, which is lifted by dephasing.

#### Crossover from ballistic to subdiffusive transport

The transport behaviour can be quantified by examining the spatial dispersal of the excitation, i.e. by measuring the spatial width  $\sigma_{\text{WP}}$  of the excitation wave packet. This analysis is analogous to experiments with ultracold atoms in a momentum space lattice [160] and to experiments in a photonic system on a discrete quantum walk [161]. The width  $\sigma_{\text{WP}}$  is calculated via the single-ion resolved excitation dynamics  $p_i(t)$ , shown in the left panels of Fig. 6.4. We start from the common definition of the wave packet

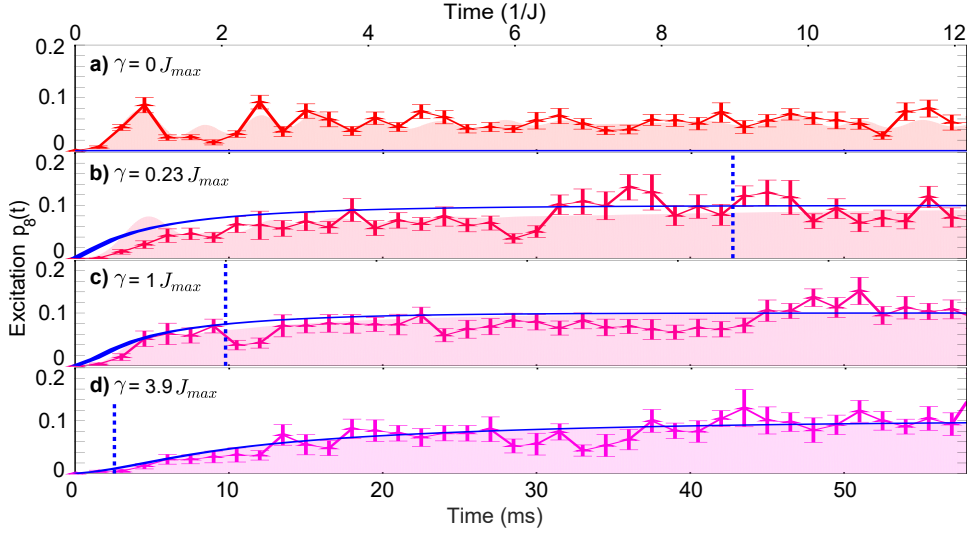


**Figure 6.3.:** Excitation probability at ion 8 as a function of time, for strong static disorder  $B_{\max} = 2.5 \cdot J_{\max}$  and increasing dephasing rate, from (a) to (d). Each data set (red to magenta triangles) results from averaging over 20 – 40 random realizations, with 25 repetitions each. Error bars are derived with bootstrapping [154], based on 1000 samples. With increasing  $\gamma$ , coherent oscillations damp out and the data converges towards a model following diffusive, classical rate equations (blue solid line). This theoretical approximation is valid for times  $t \gg 1/\gamma$ . (The crossover  $t_c = 1/\gamma$  is illustrated by a blue dashed line.) The coloured areas show the time evolution of a theoretical model with ideal Markovian noise, averaged over 100 random realizations.

width

$$\sigma'_{\text{WP}}(t) = \sqrt{\langle \hat{x}^2 \rangle - \langle \hat{x} \rangle^2} = \sqrt{\left( \sum_{i=1}^{10} p_i(t) \cdot i^2 \right) - \left( \sum_{i=1}^{10} p_i(t) \cdot i \right)^2}$$

and rewrite the expression relative to the source site  $i_3$ :

$$\sigma''_{\text{WP}}(t) = \sqrt{\left( \sum_i p_i(t) \cdot (i - i_3)^2 \right) - \left( \sum_i p_i(t) \cdot (i - i_3) \right)^2}.$$

This formula is then modified, in order to reduce boundary effects: Since the excitation is inserted off-center, we can increase the spatial and temporal range over which the width is evaluated. For this, we discard the data between source and the nearer boundary, where boundary effects appear early. Instead, we only consider the region between source and the boundary that is farther away. We mirror this region around  $i_3$ , thus obtaining an imagined system where the excitation spreads symmetrically around  $i_3$ . This description is valid as long as the effects from the nearer boundary do not influence the data in the evaluated region. Mathematically, we split the sums at  $i_3$  and

assume mirror symmetry, which yields

$$\begin{aligned}\sigma_{\text{WP}}(t) &= \sqrt{\left(\sum_{i < i_3} p_i(t) \cdot (i - i_3)^2\right) + \left(\sum_{i > i_3} p_i(t) \cdot (i - i_3)^2\right) - \left(\sum_{i < i_3} p_i(t) \cdot (i - i_3) + \sum_{i > i_3} p_i(t) \cdot (i - i_3)\right)^2} \\ &\approx \sqrt{2 \left(\sum_{i > i_3} p_i(t) \cdot (i - i_3)^2\right)}.\end{aligned}\quad (6.4)$$

A quantitative description of the transport behaviour is gained by fitting a power law  $\sigma_{\text{WP}}(t) = A \cdot t^C$ . In order to exclude data in which effects from the nearer boundary become relevant, we fit the data only up to the time where the excitation has hopped from ion 3 to the left boundary and back to ion 2. We estimate this time through a modified hopping strength  $\tilde{J}_{ij}$ , consisting of the original hopping rate  $J_{ij}$ , reduced by the applied disorder  $B_{\text{max}}$  and dephasing  $\gamma$ ,

$$J_{\text{eff.}} = \min\{\tilde{J}_{ij}, J_{ij}\} \quad , \text{ with } \quad \tilde{J}_{ij} = \frac{J_{ij}^2}{B_{\text{max}}^2 + \gamma^2} \quad (6.5)$$

Based on the hopping rate  $J_{\text{eff.}}$ , we calculate the maximum speed at which an excitation spreads in our system (see [116] and methods in [123]) and visualize it as orange dotted light-like cones in the left panels of Fig. 6.4. Since we do not have finite-range interactions, these are not strict maximum speeds. Still, they provide a practically useful description of the excitation spreading in our system.

Depending on the relationship to time,  $\sigma_{\text{WP}}(t) \propto t^C$ , one distinguishes between ‘normal diffusion’ as it occurs in classical random walks ( $C = 0.5$ ), ‘subdiffusion’ ( $0 < C < 0.5$ ), and ‘superdiffusion’ ( $C > 0.5$ ). The case  $C = 1$  is referred to as ballistic transport. As we show now, we observe ballistic, diffusive, and subdiffusive behavior in our experiment. The excitation dynamics  $p_i(t)$  is displayed in the left panels of Fig. 6.4 for three exemplary parameter values. At small  $\gamma$  an interference pattern is clearly visible. This hallmark for coherence is rapidly washed out as  $\gamma$  increases. We fit a power law of the form  $\sigma_{\text{WP}}(t) = A \cdot t^C$  to the width of the wave packet, as shown in the right panels of Fig. 6.4. However, we only include data up to the time where the excitation has been reflected from the left boundary back to ion 2, as denoted by blue arrows in the left panels of Fig. 6.4. Without any disorder and noise, the width increases linearly in time with  $C = 1.01 \pm 0.09$ , corresponding to ballistic spreading. In the regime around  $\gamma = J_{\text{max}}$  (Fig. 6.3 (b)), where ENAQT is most efficient, we find that within very short times  $t \sim 1/J_{\text{max}}$  the transport evolves from ballistic to mainly diffusive dynamics (as theoretically predicted in Ref. [162]), yielding  $C = 0.76 \pm 0.18$ .

For strong dephasing,  $\gamma = 18.4 \cdot J_{\max}$ , we observe subdiffusive transport with a power exponent  $C = 0.44 \pm 0.02$ .

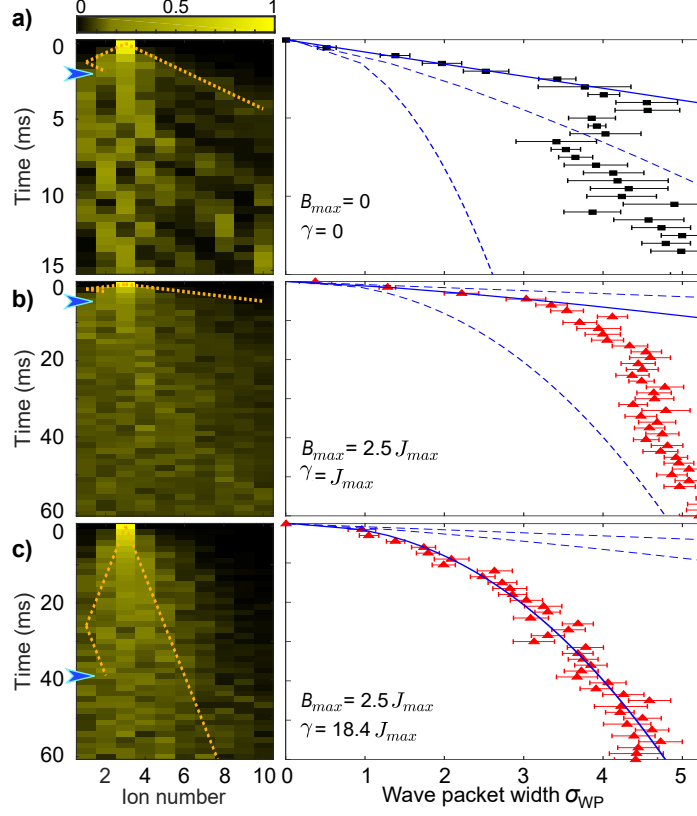


**Figure 6.4.:** **Left panels:** Single-ion resolved excitation dynamics  $p_i(t)$  for (a) the unperturbed system (no static disorder and no noise), (b) static disorder  $B_{\max} = 2.5 \cdot J_{\max}$  with dephasing  $\gamma = J_{\max}$ , and (c) static disorder  $B_{\max} = 2.5 \cdot J_{\max}$  with  $\gamma = 18.4 \cdot J_{\max}$ . The orange dotted line shows the maximum speed at which an excitation spreads in order to estimate up to which time the reflection from the left boundary can be neglected (blue arrows). **Right panels:** Spatial width of the excitation wave packet  $\sigma_{\text{WP}}(t)$ , calculated from the data in the left panels. Blue solid lines are fits of the form  $\sigma_{\text{WP}} = A \cdot t^C$  (fits from the respective other panels are included as dashed lines for comparison). The expected maximum of  $\sigma_{\text{WP}}(t)$  lies at  $\sigma_{\max} = 5.3$ , and corresponds to a single excitation distributed equally over all ions. (a)  $A = (1.2 \pm 0.8) \cdot 10^{-3}$ ,  $C = 1.01 \pm 0.09$  (b)  $A = (5.1 \pm 7.6) \cdot 10^{-3}$ ,  $C = 0.76 \pm 0.18$ . (c)  $A = (3.9 \pm 0.9) \cdot 10^{-2}$ ,  $C = 0.44 \pm 0.02$ . All error bars are derived via bootstrapping [154], based on 100 samples.

The theoretical simulations in Fig. 6.5 compare the temporal evolution of the wave packet width for two different cases: one where the coupling strength corresponds to the experimentally realized coupling matrix  $J_{ij}$ , approximately following a power law  $J_{ij} = J_{\max}/|i - j|^\alpha$  with interaction range  $\alpha = 1.22$ . The second case considers a nearest-neighbour model, where the interaction is averaged between the left and right

algebraic tail  $J_{i,i+1}^{\text{NN}} = \sum_j J_{ij}/2$ . From the observed time relationship  $\sigma_{\text{WP}} \propto t^C$  we conclude that subdiffusive dynamics is a consequence of our long-range interactions.

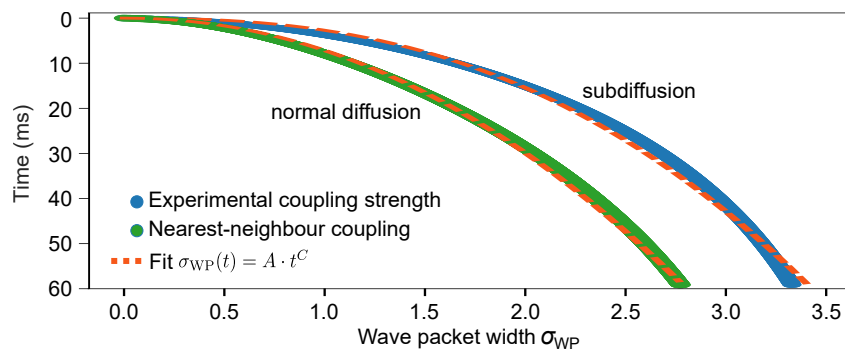


**Figure 6.5.:** Theoretical simulation of the temporal evolution of the wave packet width  $\sigma_{\text{WP}}$  for two different coupling models: (green) Experimentally implemented coupling matrix  $J_{ij}$ , with coupling range  $\alpha = 1.22$ , (blue) nearest-neighbour model. The simulation averages over 100 random realizations of strong disorder  $B_{\text{max}} = 2.5 \cdot J_{\text{max}}$ , and large Markovian dephasing at rate  $\gamma = 18.4 \cdot J_{\text{max}}$ . The spatial width of the excitation wave packet is fitted with a power law (orange dotted line). The obtained fitting parameters are  $A = 0.01, C = 0.49$  (green data) and  $A = 0.04, C = 0.40$  (blue data).

### 6.3. Non-Markovian dephasing baths

In Fig. 6.2, the experimentally observed transport efficiencies for  $\gamma > J_{\text{max}}$  are higher than the simulated values for ideal Markovian noise. This discrepancy could indicate that non-Markovian effects can increase the transport efficiency. To investigate non-Markovian dephasing further, we study ENAQT under noise with a spectral density function  $S(\omega)$  of Lorentzian shape, which we generate using the frequency-domain algorithm described in Ref. [163]. This algorithm allows us to compute the time series of AC-Stark shifts which is required to realize dephasing noise with arbitrary spectral power (see Appendix H). In this study, we choose a single configuration of random static disorder ( $B_{\text{max}} = 2.5 \cdot J_{\text{max}}$ ) in order to have full knowledge of the disordered system and its eigenvalues.

Fig. 6.6 shows that the spectral structure of the noise model has a strong influence on the transport efficiency: Non-Markovian structured noise that covers all difference frequencies of the spin system's eigenenergies (models 3 and 4) can enhance excitation transport as much as white (Markovian) noise (model 1). Moreover, the efficiency for different target ions is equal (Fig. 6.6 (b)). Narrowband noise models, instead, only manage to couple a few eigenstates. In this case, the spectral position determines for which target ions excitation transport is enhanced (cf. models 5 and 6 in Fig. 6.6).

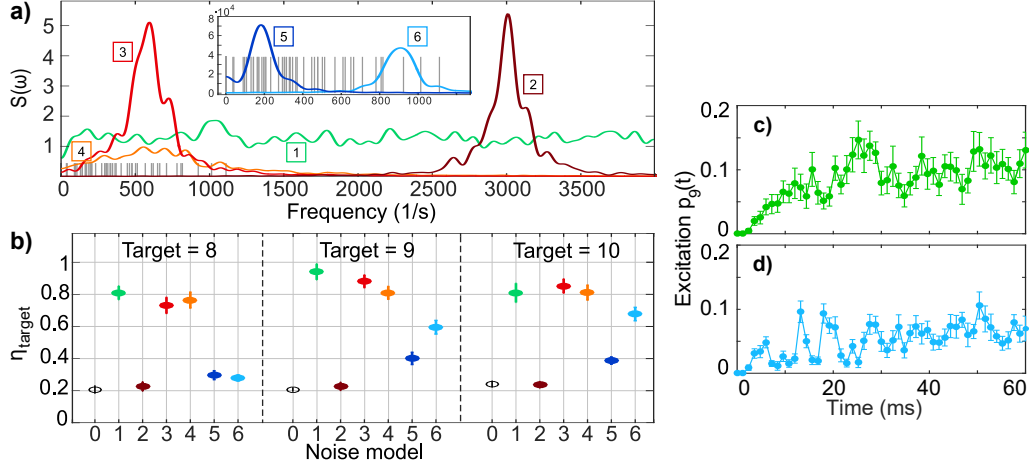


**Figure 6.6.: Excitation transport under strong static disorder and different noise models.** **a)** Spectral density functions  $S(\omega)$  of the applied noise models. [1] white noise, [2]-[6] non-Markovian noise models of Lorentzian shape. All curves are averaged over  $\sim 30$  random realizations, each generated by a Gaussian random process based on 600 sampling points [163]. The inset shows a zoom into the low-frequency domain. Vertical grey lines denote the difference frequencies between all eigenenergies of the disordered system. **b)** Comparison of  $\eta_{\text{target}}$  to target ion 8, 9, and 10 for the noise models shown in (a), as indicated by corresponding colors and numbering. The black circle shows suppressed efficiency under strong static disorder without any noise. While broadband noise in the correct frequency range generically enhances transport efficiencies, for narrowband noise the enhancement depends on the source and target ions. Each data point results from averaging over 25–30 random realizations, with 15 repetitions each. Error bars are derived with bootstrapping [154], based on 1000 samples. **c)-d)** Excitation probability of target ion 9 as a function of time under strong static disorder  $B_{\text{max}} = 2.5 \cdot J_{\text{max}}$ . Panel c) shows the result for the Markovian noise model [1]. Oscillations, indicating coherent dynamics, are strongly damped. Panel d) shows the effects of a narrowband Lorentzian noise model covering only a few eigenstates (model [6]). Here, coherences are maintained stronger and are clearly discriminable from measurement errors up to  $\sim 30$  ms.

Integrating the applied local energy shifts over the entire interaction time, we find that with narrowband non-Markovian noise we can achieve similar transport efficiencies as with Markovian noise, but already at half the energy cost (cf. noise models 1 and 6 in Fig. 6.6 (a)). Further, panels (c) and (d) in Fig. 6.6 show that coherences are maintained better for narrowband noise models than for Markovian-like noise.

## 6.4. Conclusion

Our setup enables us to investigate ENAQT in a controlled quantum network, with arbitrary disorder and dephasing noise. Our network does not have a simple lattice structure restricted to close-neighbour interactions, but has a tunable interaction range. This permits us to microscopically study quantum transport in a tunable, scalable sys-

tem. With the help of an arbitrary waveform generator (Section 4.4), integrated into the single-ion addressing setup, we can disturb the interaction with practically any desired noise spectrum. Under strong static disorder, we observed effects of Anderson localization in the absence of noise, an increased transport efficiency by ENAQT at intermediate noise levels, and finally suppression of quantum transport under strong noise due to the quantum Zeno effect. Further, we found that in the regime where ENAQT is most effective the transport is mainly diffusive, displaying coherences only at very short times. Coherences dominate only in the localized regime (at very low noise strengths). In all other regimes of Markovian noise, the dynamics is well captured through a diffusive rate equation describing a classical random walk. Finally, we observed that the spectral structure of non-Markovian dephasing strongly influences quantum transport, with the possibility to reach efficiencies as high as with white noise while maintaining long-lived coherences.

This work constitutes significant progress in controlled studies of quantum transport, with importance in fields ranging from condensed-matter physics and material science, to quantum chemistry and quantum biology. Our approach allows us to study the possibility of stochastically accelerated hyper-transport, generated, e.g., by time-evolving disorder [164]. Further, we have the possibility to investigate quantum transport with multiple interacting excitations or to study localization using out-of-time-ordered correlators (OTOCs) [165, 166].

## 7. Variational Quantum Simulations

The studies presented here are published in:

[Phys. Rev. X \*\*8\*\*, 031022 \(2018\)](#) &

[Nature \*\*569\*\*, 355 \(2019\)](#)

Quantum simulators are promising instruments for solving classically challenging problems in a broad range of fields, including chemistry, high-energy physics and materials science. Next to digital and analog quantum simulators (Section 3.1), variational quantum simulation (VQS) has recently emerged as a third, new method of quantum simulation. It leverages the unique capabilities of quantum devices by combining them with a classical subroutine: Hybrid quantum-classical algorithms employ a feedback loop between a classical computer and a quantum co-processor. Variational quantum simulators aim at variationally solving optimization problems, while forgoing the requirement of realizing the targeted Hamiltonian directly in the laboratory. As will be shown in this chapter, this allows the study of a wide variety of previously intractable target models using quantum resources as available in today's laboratories.

After an introduction to the quantum-classical feedback loop, two experimental implementations of variational quantum simulation are demonstrated. First, I present the study of molecular ground state potentials, employing up to four ions in our quantum simulator in a digital way. We investigate the potential energy as a function of the internuclear distance for two different molecules. Different methods for mapping the fermionic Hamiltonian to qubits are compared and the effects of measurement noise and decoherence are discussed. The second experimental application focuses on the lattice Schwinger model. In this project, we employed our quantum simulator with up to 20 qubits in an analog way, capable of generating large entangled states while respecting symmetries of the target model. We successfully determined ground states as well as the energy gap to the first excited state, and observed a quantum phase transition. Furthermore, our scheme provides algorithmic error bars for the obtained energies by measuring variances of the target Hamiltonian. This addresses the long-standing challenge of evaluating or verifying the simulation results.

## 7.1. Quantum-classical feedback loop

An efficient quantum-classical feedback loop requires high experimental repetition rates of the quantum device and a fast exchange between the classical computer and the quantum coprocessor. The loop is depicted in Fig. 7.1 and the basic functionality can be divided into three steps:

1. The quantum simulator in the quantum-classical feedback loop prepares an initial state  $|\psi_0\rangle$  and applies a given quantum circuit. This generates a (potentially) highly entangled, variational state, called trial quantum state,  $|\psi(\boldsymbol{\theta})\rangle = U(\boldsymbol{\theta})|\psi_0\rangle$ . The circuit is represented by the unitary operator  $U(\boldsymbol{\theta})$  and consists of quantum gates, e.g. Mølmer-Sørensen entangling gates, spin-spin interaction gates and single-qubit rotation gates (Section 2.1.2). The related set of parameters  $\boldsymbol{\theta}$  controls gate settings such as laser phases and laser pulse lengths. The gate set is chosen such that it efficiently explores the Hilbert space. In particular, the target state of the problem has to lie within the set of possible trial states.

There are different ways for generating suitable trial states: (i) Start from an approximate ground-state wavefunction and apply excitation operations which incorporate the structure of the Hamiltonian of interest and known properties of the solution state. In Section 7.2 (Application I), we used this so-called “unitary coupled cluster” ansatz to simulate molecular ground state potentials. (ii) Another approach applies a quantum circuit which is tailored specifically to the naturally available gates of the corresponding simulator. Section 7.3 presents this ansatz in the simulation of lattice models.

2. The next step is to extract the cost function of interest: The role of the quantum device is to perform the classically difficult task of evaluating observables from potentially highly entangled states. Therefore, a set of measurements – relevant for the reconstruction of the respective cost function – is applied to the state  $|\psi(\boldsymbol{\theta})\rangle$ . For example, the cost function to find the ground state of a target Hamiltonian,  $\hat{H}_T$  corresponds to the energy  $E(\boldsymbol{\theta})$ , given by the expectation value  $E(\boldsymbol{\theta}) = \langle \hat{H}_T \rangle = \langle \psi(\boldsymbol{\theta}) | \hat{H}_T | \psi(\boldsymbol{\theta}) \rangle$ . A generic Hamiltonian

$$\hat{H}_T = \sum_{\ell} c_{\ell} H_{\ell} = \sum_{\ell} c_{\ell} \bigotimes_{j=1}^N \sigma_j^{\alpha_j} \quad (7.1)$$

is decomposed into strings  $H_{\ell} = \sigma_1^{\alpha_1} \otimes \sigma_2^{\alpha_2} \otimes \dots \otimes \sigma_N^{\alpha_N}$  of Pauli operators  $\sigma_j^{\alpha}$ , where  $j$  labels the qubit and  $\alpha$  Cartesian coordinates. With this, the cost

function becomes a sum of expectation values of correlation functions  $E(\boldsymbol{\theta}) = \sum_{\ell} c_{\ell} \langle \Psi(\boldsymbol{\theta}) | H_{\ell} | \Psi(\boldsymbol{\theta}) \rangle$ , which are individually measured on the quantum device. A classical computer then calculates the cost function by adding up the correlation measurements.

Section 7.3 presents an advanced scheme for variational quantum simulation, in which the target Hamiltonian  $\hat{H}_T$  only exists as this set of measurement prescriptions and never needs to be realized physically in the laboratory. This endows us with great freedom in the choice of models to simulate on our quantum device.

3. A classical computer employs an optimization algorithm to minimize the cost function by varying the parameter set  $\boldsymbol{\theta}$ , which is handed over to the quantum simulator. Ritz's variational principle implies that the energy  $E(\boldsymbol{\theta})$  of every trial state  $|\psi(\boldsymbol{\theta})\rangle$  is always bigger or equal to the lowest eigenvalue of  $\hat{H}_T$ . In summary, the feedback loop variationally seeks to prepare the ground state of  $\hat{H}_T$ . A successful and efficient optimization requires an advanced global algorithm, which is specifically suited for noisy<sup>53</sup>, high-dimensional and gradient-free optimization problems. Furthermore, a reuse of measurement data allows one to find ground states of whole classes of Hamiltonians more efficiently.

Steps 1 – 3 are repeated until the optimization algorithm reaches a pre-defined stopping criterion, although the definite determination of this criterion is a challenging open question. A typical stopping criterion for optimization algorithms is the comparison against a fixed goal. However, this only translates the problem to how to define this goal, ideally independent from a-priori knowledge of the system, and not based on comparisons with classical simulations. The stopping criterion we applied in Section 7.3, is to continue the optimization until an allocated resource budget is exhausted: The algorithm is provided with a finite, total measurement budget that it can spend during the optimization process. It autonomously selects how to distribute this budget between new unexplored points and refinement re-evaluations on promising points, to reduce the statistical errors. This selection procedure is based on methods from decision theory and optimal computing budget allocation (OCBA)[167]. Another criterion involves the evaluation of stationarity: the optimization has converged, if the proposed solution is no longer improving as more points in the cost-function landscape are sampled. The proposed solution could for instance be the minimum of the parameter landscape, as predicted by a metamodel. At the termination of the optimization, the final set of

<sup>53</sup>The obtained expectation values will be noisy, due to the limited sampling statistics of the trial quantum states.

experimental parameters corresponds to a simple prescription for the generation of the ground state of the system.

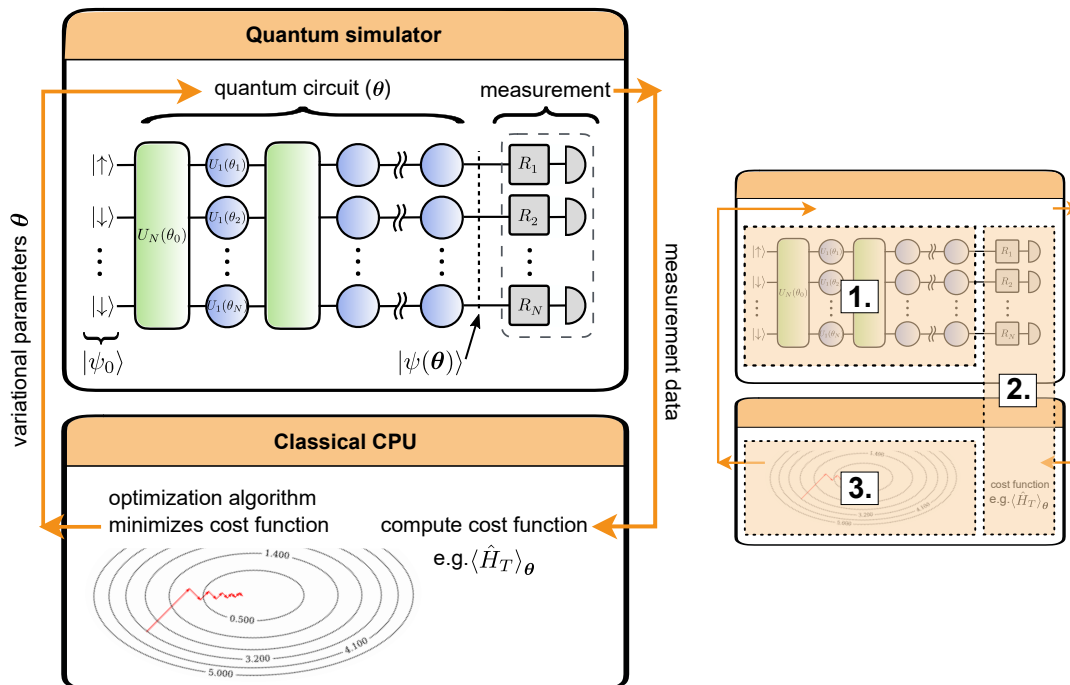


**Figure 7.1.: VQS quantum-classical feedback loop.** A quantum simulator generates a state  $|\psi(\theta)\rangle$  by applying a sequence of gates, e.g. spin-spin interactions (green boxes) and single-qubit rotations (blue circles). Individual gate settings are controlled by a set of parameters  $\theta$ . State read-out is performed in the measurement bases (gray boxes) relevant for the reconstruction of the cost function of interest. A classical CPU runs an optimization algorithm to minimize the cost function and hands over new parameters  $\theta$  to the quantum device. The right panel assigns steps 1-3 as described in the main text.

## 7.2. Application I: Molecular ground state potentials

Particularly compelling applications of quantum simulators are quantum chemistry problems, such as reaction mechanisms or the molecular binding energies [168]. Efficient quantum simulations of classically intractable electronic structures promise breakthroughs in our understanding of basic chemistry and could revolutionize research of new materials, pharmaceuticals, and industrial catalysts<sup>54</sup>. The high potential of vari-

<sup>54</sup>A detailed understanding and prediction of the reaction mechanism for biological nitrogen fixation is of great importance for fertilizer production. The industrial Haber–Bosch method is very energy-intensive, while the naturally occurring FeMoco-process functions at room temperature and standard pressure. To date the mechanism in FeMoco is not understood, but there exist proposals for its investigation using quantum simulators [169].

ational quantum simulation for quantum chemistry applications, has triggered great experimental work over the last years, on architectures ranging from quantum photonics, NV centers, superconducting qubits to trapped ions [12, 14, 79, 80, 170–172]. The beginning of this chapter summarizes the basic method of quantum chemistry for mapping the electronic structure Hamiltonian to a spin Hamiltonian. Furthermore, I discuss the generation and evaluation of the trial quantum states and give an overview on the classical optimization algorithm. In the second part, I report on the experimental implementation of the quantum-classical hybrid algorithm on our trapped-ion quantum simulator. Specifically, we employed the variational quantum eigensolver (VQE) algorithm, to find the electronic ground states for molecular hydrogen and lithium hydride, for given separations between their atoms. From this, we can calculate the related energy and obtain the molecular potential curves. The project discussed here, was published in Ref. [13].

### 7.2.1. Theoretical background

The central problem of theoretical chemistry is the computation of the lowest energy eigenvalue of the molecular electronic structure Hamiltonian. This Hamiltonian encompasses the wave functions and energies of electrons and describes their state of motion in the electrostatic field created by stationary nuclei. It thereby contains all interesting properties of a molecule. The following subsections describe how we find good approximations to a molecular Hamiltonian and its electronic wave function. These approximations then serve as a starting point for the variational quantum simulation, with the goal of finding the electronic ground state and related energy for a given interatomic distance.

#### Hamiltonian mapping

The first-quantized formulation of the molecular Hamiltonian reads as

$$H_I = - \sum_i \frac{\nabla_{R_i}^2}{2M_i} - \sum_i \frac{\nabla_{r_i}^2}{2} - \sum_{i,j} \frac{Z_i}{|R_i - R_j|} + \sum_{i,j>i} \frac{Z_i Z_j}{|R_i - R_j|} + \sum_{i,j>i} \frac{1}{|r_i - r_j|}, \quad (7.2)$$

where  $R_i, M_i, Z_i$  denote the positions, masses and charges of a collection of nuclei, and  $r_i$  describes the position of the electrons in the system. The second-quantized formulation is derived, by applying the Born-Oppenheimer approximation, to treat the nuclei as fixed classical point charges [173]. The electronic wavefunction is represented in a basis  $\phi_i$  of molecular orbitals, which are constructed as linear combinations of

atomic orbitals using the Hartree-Fock method (see Appendix K for details). With this, the electronic structure Hamiltonian in the second-quantized form reads:

$$H_{II} = \sum_{pq} h_{pq} a_p^\dagger a_q + \frac{1}{2} \sum_{pqrs} h_{pqrs} a_p^\dagger a_q^\dagger a_r a_s, \quad (7.3)$$

where the indices  $p, q, r, s$  identify the molecular orbitals. The scalar coefficient  $h_{pq}$  represents the one-electron terms, describing the kinetic energy of the electron and its potential energy in the presence of the nuclei. The coefficient  $h_{pqrs}$  describes the two-electron Coulomb repulsion. These coefficients contain all spatial and spin information of the electrons and can be calculated classically as the overlap integrals of the orbital basis functions  $\phi_i$ :

$$\begin{aligned} h_{pq} &= \int d\sigma \phi_p^*(\sigma) \left( \frac{\nabla_r^2}{2} - \sum_i \frac{Z_i}{|R_i - r|} \right) \phi_q(\sigma) \\ h_{pqrs} &= \int d\sigma_1 d\sigma_2 \frac{\phi_p^*(\sigma_1) \phi_q^*(\sigma_2) \phi_s(\sigma_1) \phi_r(\sigma_2)}{|r_1 - r_2|}. \end{aligned} \quad (7.4)$$

Here,  $\sigma_i = (r_i, s_i)$  encodes the spatial and spin coordinates of the electron. Note that the fermionic nature of the electrons is enforced through the anti-commutator relations of the electron creation and annihilation operators  $a_i^\dagger$  and  $a_j$ .

Before the implementation on our quantum simulator, Hamiltonian (7.3) and its electronic wave functions have to be mapped to qubits. There are two common transformation schemes: (i) The Jordan-Wigner (JW) transformation uses the state of a qubit to encode whether or not a particular basis orbital is occupied [174]. That is, the fermionic creation and annihilation operators are directly mapped to qubit states. (ii) In the Bravyi-Kitaev (BK) transformation instead, even qubits store occupations and odd qubits keep track of the parity of all qubits with smaller indices [175].

For both transformations, the resulting spin Hamiltonians  $H$  take the form

$$H_{II} \xrightarrow{\text{JW, BK}} H = \sum_{\ell} c_{\ell} H_{\ell} = \sum_{\ell} c_{\ell} \bigotimes_{j=1}^N \sigma_j^{\alpha_j}.$$

Here,  $H_{\ell}$  are products  $H_{\ell} = \sigma_1^{\alpha_1} \otimes \sigma_2^{\alpha_2} \otimes \dots \otimes \sigma_N^{\alpha_N}$  of Pauli matrices  $\sigma_j^{\alpha}$ , where  $j$  labels the qubit and  $\alpha$  Cartesian coordinates. The scalar values  $c_{\ell}$  capture the integrals from Eq. (7.4). Those integrals can be pre-calculated classically, for any given internuclear separation  $R$ . Mathematical details on the two transformation methods can be found in Refs. [176, 177] and in the Appendix of Ref. [13].

- **H<sub>2</sub> Hamiltonian under BK:** In the STO-3G basis (Appendix K), each hydrogen atom contributes a 1s orbital to the molecular electronic wavefunction, as depicted in Fig. 7.2 a). The BK transformation maps the molecular ground state wavefunction to the four-qubit state  $\varphi_{\text{HF}} = |0001\rangle$ . In the same basis, Hamiltonian (7.3) transforms to

$$\begin{aligned} H^{\text{BK}} = & a_0\mathcal{I} + a_1\sigma_0^z + a_2\sigma_1^z + a_3\sigma_2^z + a_4\sigma_1^z\sigma_0^z + a_5\sigma_2^z\sigma_0^z + a_6\sigma_3^z\sigma_1^z \\ & + a_7\sigma_2^x\sigma_1^z\sigma_0^x + a_8\sigma_2^y\sigma_1^z\sigma_0^y + a_9\sigma_2^z\sigma_1^z\sigma_0^z + a_{10}\sigma_3^z\sigma_2^z\sigma_0^z + a_{11}\sigma_3^z\sigma_2^z\sigma_1^z \\ & + a_{12}\sigma_3^z\sigma_2^x\sigma_1^z\sigma_0^x + a_{13}\sigma_3^z\sigma_2^y\sigma_1^z\sigma_0^y + a_{14}\sigma_3^z\sigma_2^z\sigma_1^z\sigma_0^z. \end{aligned}$$

Here,  $\{\sigma_j^x, \sigma_j^y, \sigma_j^z\}$  denote Pauli matrices, acting on the  $j$ -th qubit. The coefficients  $a_i$  depend on the internuclear separation  $R$  between the hydrogen atoms and are classically computable from the integrals (7.4). We see, that qubits 1 and 3 are only exposed to identity and  $\sigma^z$  operations. The Hamiltonian stabilizes these qubits, such that they are never flipped throughout the simulation. This allows us to reduce the Hamiltonian above to an effective two-qubit Hamiltonian, with the reference state  $\varphi_{\text{HF}} = |01\rangle$ .

$$H_{\text{eff}}^{\text{BK}} = c_0\mathcal{I} + c_1\sigma_0^z + c_2\sigma_1^z + c_3\sigma_0^z\sigma_1^z + c_4\sigma_0^x\sigma_1^x + c_5\sigma_0^y\sigma_1^y \quad (7.5)$$

- **H<sub>2</sub> Hamiltonian under JW:** Under the JW transformation the electronic ground state is mapped to  $\varphi_{\text{HF}} = |0011\rangle$ , and the Hamiltonian gets

$$\begin{aligned} H^{\text{JW}} = & c_0\mathcal{I} + c_1(\sigma_0^z + \sigma_1^z) + c_2(\sigma_2^z + \sigma_3^z) + c_3\sigma_3^z\sigma_2^z + c_4\sigma_1^z\sigma_0^z \\ & + c_5(\sigma_2^z\sigma_0^z + \sigma_3^z\sigma_1^z) + c_6(\sigma_2^z\sigma_1^z + \sigma_3^z\sigma_0^z) \\ & + c_7(\sigma_3^x\sigma_2^y\sigma_1^y\sigma_0^x + \sigma_3^y\sigma_2^x\sigma_1^x\sigma_0^y) - c_7(\sigma_3^x\sigma_2^x\sigma_1^y\sigma_0^y + \sigma_3^y\sigma_2^y\sigma_1^x\sigma_0^x), \end{aligned} \quad (7.6)$$

with the coefficients  $c_i$  again computed from the integrals (7.4).

- **LiH Hamiltonian under BK:** LiH is a heteronuclear molecule with four electrons. We encode its electronic structure via the Hartree-Fock method, using a STO-6G basis set of the molecular orbitals (Appendix K). A direct BK transformation would lead to a 12-qubit Hamiltonian. We reduce the number of qubits by only considering single- and double excitations and thereby defining an active space of two electrons in three molecular orbitals (Fig. 7.2 b)). Such active spaces average out (or “freeze”) the core electrons, since they are not considered to participate strongly in the molecular bonding. Finally, we select the two dominant

contributions to the active space such that the effective Hamiltonian involves operations on 3 qubits only. Under the BK transformation it takes the form:

$$H = c_0 + c_1\sigma_0^z + c_2\sigma_1^z + c_3\sigma_2^z + c_4\sigma_1^z\sigma_0^z + c_5\sigma_2^z\sigma_0^z + c_6\sigma_2^z\sigma_1^z + c_7\sigma_1^x\sigma_0^x + c_8\sigma_1^y\sigma_0^y + c_9\sigma_2^x\sigma_0^x + c_{10}\sigma_2^y\sigma_0^y + c_{11}\sigma_2^x\sigma_1^x + c_{12}\sigma_2^y\sigma_1^y, \quad (7.7)$$

with the reference electronic ground state  $\varphi = |111\rangle$ .

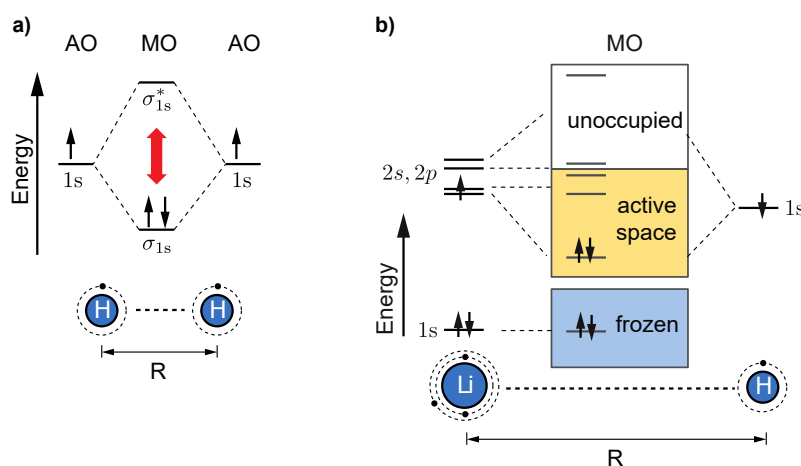


**Figure 7.2.:** Molecular orbitals (MO) constructed from the atomic orbitals (AO) of the individual elements. **a)** H<sub>2</sub> molecular orbitals are built from 1s orbitals, contributed by the two hydrogen atoms. **b)** LiH molecular orbitals generated from the 1s orbital of the hydrogen atom and the 1s, 2s, 2p orbitals from the lithium atom. The three orbitals among which the Hamiltonian's excitation operators act is highlighted in yellow (active space).

### Generation and evaluation of trial wavefunctions

Once the mapping of the fermionic Hamiltonian to qubits is chosen, we need to prepare suitable trial states for the variational quantum simulation, as outlined in step 1. of Section 7.1. A good starting point is the approximate ground state wave function  $|\varphi_{\text{HF}}\rangle$  of the respective Hamiltonian, as indicated in the previous subsection. This electronic wavefunction is derived via the Hartree–Fock method and consists of the lowest-energy set of molecular orbitals (details in Appendix K).

The initial state  $|\varphi_{\text{HF}}\rangle$  is then exposed to a series  $U(\boldsymbol{\theta})$  of quantum operations, generating the trial wave function  $|\varphi(\boldsymbol{\theta})\rangle = U(\boldsymbol{\theta})|\varphi_{\text{HF}}\rangle$ , in order to explore the Hilbert space perturbatively. The ansatz unitary ideally incorporates the structure of the Hamiltonian of interest as well as known properties of the solution state. In the experiment presented here, we parameterize our ansatz using the unitary coupled-cluster method

UCC – a cornerstone method of electronic structure theory [80, 178]. The unitary  $U(\boldsymbol{\theta})$  is constructed by exponentiation of the so-called cluster operator  $T(\boldsymbol{\theta})$  for an  $N$  electron system:

$$U(\boldsymbol{\theta}) = e^{T(\boldsymbol{\theta}) - T^\dagger(\boldsymbol{\theta})}, \text{ where } T(\boldsymbol{\theta}) = \sum_i^N T_i(\boldsymbol{\theta})$$

$$\text{and } T_1(\boldsymbol{\theta}) = \sum_{\substack{i \in \text{occ} \\ j \in \text{unocc}}} \theta_{(i)}^{(j)} \hat{a}_j^\dagger \hat{a}_i, \quad T_2(\boldsymbol{\theta}) = \sum_{\substack{i, j \in \text{occ} \\ l, k \in \text{unocc}}} \theta_{(i, j)}^{(k, l)} \hat{a}_l^\dagger \hat{a}_k^\dagger \hat{a}_j \hat{a}_i, \quad \dots$$

Here,  $\boldsymbol{\theta}$  describes a vector of experimental parameters that are variationally optimized and the coefficients  $\theta_{(i)}^{(j)}$  are the related coupled cluster amplitudes. To date, no efficient implementation of this method has been developed for a classical computer, but in principle, it can be operated efficiently on a quantum device: One can define a reduced cluster operator  $T^{(k)} = \sum_i^k T_i$ , which suggests a set of fermionic operators  $T_i$  up to a given excitation degree  $k$ . This allows one to systematically explore all relevant excited wavefunctions, while sampling only a polynomial number of experimental parameters  $\boldsymbol{\theta}$ . Typically, the cluster expansion is truncated at the double level of excitation (UCCSD)  $T\boldsymbol{\theta} = T_1\boldsymbol{\theta} + T_2\boldsymbol{\theta}$ , which after exponentiation also introduces higher excitations.

$$e^{T(\boldsymbol{\theta})} = 1 + T_1(\boldsymbol{\theta}) + T_2(\boldsymbol{\theta}) + \frac{T_1^2(\boldsymbol{\theta})}{2!} + T_1(\boldsymbol{\theta})T_2(\boldsymbol{\theta}) + \frac{T_2^2(\boldsymbol{\theta})}{2!} + \dots$$

This signifies, that the number of parameters  $\boldsymbol{\theta}$  quickly increases. Thus, the implementation of the UCC method in state-of-the art quantum devices requires further truncations and approximations, involving symmetries of molecular orbitals and quantum number selection rules [13]. Once the relevant unitary coupled cluster operators are determined, they also have to be mapped to qubit operators, using the Jordan-Wigner (JW) or Bravyi-Kitaev (BK) transformation:

- **H<sub>2</sub> unitary under BK:** Considering only single and double excitations as relevant for this molecule, we determine the unitary  $U_{\text{UCCSD}}(\boldsymbol{\theta}) = e^{\theta(a_2^\dagger a_3^\dagger a_1 a_0 - a_0^\dagger a_1^\dagger a_3 a_2)}$ , where the indices correspond to the set of molecular orbitals and  $a, a^\dagger$  to the fermionic annihilation (creation) operator. The BK transformation leads to the effective qubit unitary

$$U_{\text{UCCSD}}^{\text{BK}}(\boldsymbol{\theta}) = e^{-i\theta\sigma_1^x \sigma_0^y},$$

acting on the Hartree-Fock ansatz state  $|\varphi(0)_{\text{BK}}\rangle = |01\rangle$ . Following the relations in Appendix L, the UCCSD operator is translated into a combination of two

Mølmer-Sørensen gates (Appendix B) and a single-qubit rotation:

$$U_{\text{UCCSD}}^{\text{BK}}(\theta) = \exp\left(i\frac{\pi}{4}\sigma_1^x\sigma_0^x\right) \exp(-i(\theta + \pi)\sigma_1^z) \exp\left(i\frac{\pi}{4}\sigma_1^x\sigma_0^x\right).$$

The corresponding quantum circuit is depicted in Fig. 7.3 a).

- **H<sub>2</sub> unitary under JW:** The same fermionic unitary coupled cluster operator  $U_{\text{UCCSD}}(\theta) = e^{\theta(a_2^\dagger a_3^\dagger a_1 a_0 - a_0^\dagger a_1^\dagger a_3 a_2)}$  transforms under the JW mapping into

$$U_{\text{UCCSD}}^{\text{JW}}(\theta) = e^{-i\theta\sigma_3^x\sigma_2^x\sigma_1^x\sigma_0^y},$$

with the related Hartree-Fock state  $|0011\rangle$ . The corresponding quantum circuit also consists of a single-qubit rotation and two MS entangling gates, and is depicted in Fig. 7.3 b).

- **LiH unitary under BK:** The complete UCCSD ansatz for the four electrons in the LiH molecule, contains 32 single and 168 double excitation operators. The number of operators can be reduced, by identifying an active space of two electrons that stay in three molecular orbitals (Fig. 7.2 b)). Considering only excitations from orbital 1 to orbitals 2 and 3 we obtain the approximated unitary coupled cluster operator

$$U_{\text{UCCSD}} = e^{\alpha(a_5^\dagger a_4^\dagger a_3 a_2 - a_2^\dagger a_3^\dagger a_4 a_5)} \cdot e^{\beta(a_7^\dagger a_6^\dagger a_3 a_2 - a_2^\dagger a_3^\dagger a_6 a_7)}.$$

In this notation, spin-orbitals with odd (even) indices correspond to spin-up (spin-down) electrons, such that  $a_2^\dagger a_3^\dagger$  denotes occupation of the first orbital with one spin-up and one spin-down electron. The two angles  $\alpha, \beta$  are two components of the parameter vector  $\theta$  for the variational optimization. After transformation under BK, we find that only three qubits are acted on non-trivially with the dominant subterms being

$$U_{\text{UCCSD}}^{\text{BK}}(\alpha, \beta) = e^{-i\alpha\sigma_2^x\sigma_4^y} \cdot e^{-i\beta\sigma_2^x\sigma_6^y},$$

acting on the HF state  $|111\rangle$ . The corresponding quantum circuit is shown in Fig. 7.3 c), where the lower panel shows the actual implemented circuit using the refocusing technique: A fully entangling MS gate acting on a subsystem is rewritten to a sequence of two global half-entangling gates (Appendix B), interleaved with an addressed  $\pi$  phase shift. The phase-shifted qubit is decoupled from the other qubits, such that it is not participating in the entanglement of the rest of

the register.

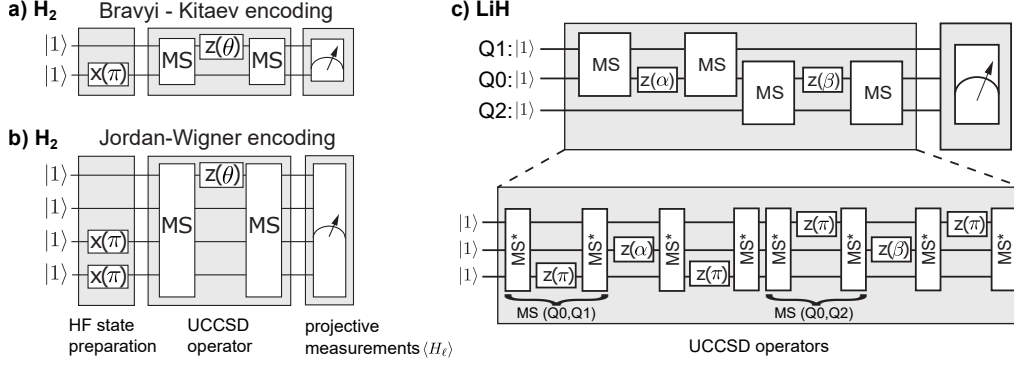


**Figure 7.3.:** Abstract quantum circuits which implement the UCCSD operators. **a)** Encoding of the  $H_2$  molecule with respect to the Hartree-Fock (HF) ansatz state  $|01\rangle$ , mapped from fermions to qubits via BK transformation. Fully entangling gates are denoted by MS, local qubit rotations are denoted as X and Z, with the respective rotation angles  $\pi$  and  $\theta$ . **b)** Encoding of the  $H_2$  molecule with respect to  $|0011\rangle$ , using JW transformation. **c)** Encoding of the LiH molecule with respect to  $|111\rangle$ , mapped from fermions to qubits via BK transformation. The qubits are indexed Q0, Q1, Q2. The lower panel depicts the actual circuit implemented in the experiment. Each locally acting MS gate split up into global half-entangling gates ( $MS^*$ ), and interleaved with a local  $\pi$  phase shift (refocusing). This modified sequence allows us to apply global MS gates, while the entangling operation is restricted to the non-addressed qubit subset, e.g. (Q0,Q1).

In summary, the so constructed unitaries incorporate many properties of the Hamiltonian of interest and are expected to construct suitable trial states, when applied to the ansatz states:  $U(\boldsymbol{\theta})|\varphi_{\text{HF}}\rangle = |\varphi(\boldsymbol{\theta})\rangle$ . Finally, the trial states  $|\varphi(\boldsymbol{\theta})\rangle$  are evaluated by projective measurements, given by the Pauli operators  $H_\ell$  of the respective Hamiltonians (7.5), (7.6) and (7.7). A much simpler approach for generating trial states is presented in Section 7.3, where trial states are generated heuristically.

### The optimization algorithm

The experimental parameters in the preparation of trial states are variationally optimized by a classical optimization algorithm, in order to explore the Hilbert space systematically. The goal of the optimization is to find the ground state wavefunction of the target Hamiltonian  $\hat{H}_T$ , by minimizing its energy at a given interatomic distance  $R$  – the cost function

$$E(R, \boldsymbol{\theta}) = c_0(R)\mathbb{1} + \sum_{\ell} c_{\ell}(R) \langle H_{\ell}(\boldsymbol{\theta}) \rangle. \quad (7.8)$$

We decided to employ the Nelder-Mead direct search algorithm, a common numerical method for finding the minimum of a function in a multidimensional space [179]. However, intrinsic experimental errors<sup>55</sup> lead to fluctuations in the cost function evaluation and can prevent the algorithm from converging. Fig. 7.4 illustrates that the optimization algorithm can be trapped in a local minimum: We simulated the experiment (including quantum projection noise) and repeated the full variational optimization run 10 times, with the same initial guess of variational parameters  $\alpha_0, \beta_0$ . For better visibility, we plotted only the last 20 points of each optimization run, after which the algorithm converged to a stable position. We find, that each repeated run converged to a different local minimum, leading to a deviation from the exact energy value, as predicted by the numerical method of exact diagonalization.

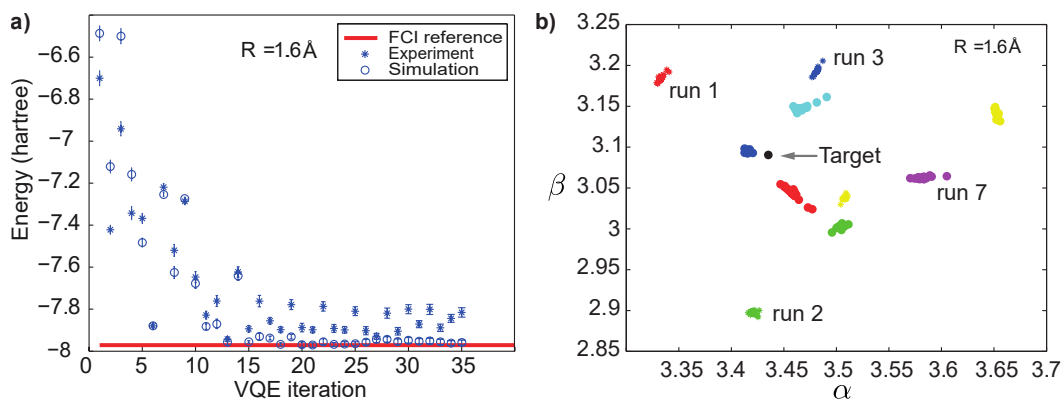


**Figure 7.4.:** a) Exemplary optimization run for LiH under the basic Nelder-Mead search algorithm, for a nuclear separation of  $R = 0.6 \text{ \AA}$ . The graph shows the energy  $\langle \hat{H}_T(\theta) \rangle$  vs the iteration number of the optimization algorithm. Stars represent experimental data with error bars derived from quantum projection noise. Circles depict a theoretical simulation of an ideal experiment (without noise). The red line indicates the target value, calculated numerically (exact diagonalization). b) Simulations of the optimization run, considering quantum projection noise. The colored clusters of symbols represent the 20 final steps of 10 independent repetitions of the same simulation. All runs started at the same initial variational parameter set  $\alpha_0, \beta_0$  but converged to different values. None of the final parameter sets coincides with the optimum combination (black dot) of the global minimum as predicted by exact diagonalization.

We conclude that the basic Nelder-Mead search method is not suitable for an optimization problem in our noisy environment. To combat this, we employed a hybrid algorithm, which combines both the Nelder-Mead algorithm and an element of simulated annealing [180]: The algorithm introduces random perturbations that are sampled from a distribution  $D$  and added to the cost function (7.8). We heuristically choose  $D$

<sup>55</sup>The two main sources are: (i) measurement errors due to quantum projection noise, and (ii) noisy gate operations e.g. due to fluctuations in laser intensity.

to be on the order of the energy error caused by quantum projection noise, such that the perturbations only become dominant in the vicinity of the global minimum. For example, at  $R = 1.6 \text{ \AA}$  of the LiH molecule, the energy error from quantum projection noise after 500 experimental repetitions lies between  $0.01 \text{ Ha} \leq \Delta \langle H \rangle \leq 0.04 \text{ Ha}$ <sup>56</sup>, depending on the specific parameter set  $\{\alpha, \beta\}$ . Hence, we chose to sample from the uniform distribution  $D = [0.01, 0.08] \text{ Ha}$ , with mean  $\bar{D} = 0.045 \text{ Ha}$ , comparable to the range above. This way, the algorithm is forced to continuously sample the surrounding of the minimum, without converging any further. Once the fluctuations of the energy values in the optimization run are on the order of the mean perturbation strength  $\bar{D}$ , we proceed for another 10 – 20 iterations before stopping the algorithm. The large number of samples in the region of interest allows us to fit a convex function to the obtained energy landscape and to extract the minimum. For the example of LiH we compared (1) a Gaussian process regression (GPR) machine learning fit [181] with (2) a two-dimensional quadratic fit to a subset of the VQE iterations (four standard deviations from the median). Comparing the results (Subsection 7.2.2) with the ideal theoretical calculation shows, that the GPR-based fit appears to systematically underestimate the energy, which highlights the impact of the data evaluation method.

### 7.2.2. Experimental results

The ultimate goal is to determine the molecular potential curve – in other words, the ground state energy of the electrons interacting in the fixed external potential of the atomic nuclei, specified by the internuclear distance  $R$ . First, we prepare the trial states  $|\varphi(\boldsymbol{\theta})\rangle$  and measure the expectation values  $\langle H_\ell(\boldsymbol{\theta}) \rangle = \langle \varphi(\boldsymbol{\theta}) | H_\ell | \varphi(\boldsymbol{\theta}) \rangle$ , where  $H_\ell$  consist of tensor products of Pauli matrices (see Eqs. (7.5)–(7.7)). The molecular energy is then obtained, by combining  $\langle H_\ell(\boldsymbol{\theta}) \rangle$  with the respective pre-calculated scalar values  $c_\ell$  and adding up, according to Eq. (7.8).

#### The $\text{H}_2$ molecule

Let us consider the case in which we encode the problem in the two-qubit Bravyi-Kitaev mapping, with the Hartree-Fock reference state  $|\varphi_{\text{HF}}\rangle = |01\rangle$ . As visible from Fig. 7.3 a), the quantum circuit contains two-qubit MS gates and only a single variational parameter  $\theta$  in form of a single-qubit rotation angle. For the entangling gate we measured a fidelity of 99(3)%. With a single variational parameter, it is still possible to efficiently scan the complete parameter space  $\theta = [0, 2\pi]$  with a resolution of

<sup>56</sup>In chemistry, energies are usually expressed in Hartree (Ha), where  $1 \text{ Ha} = \frac{\hbar^2}{m_e a_0} \approx 27.2 \text{ eV}$ , with the electron mass  $m_e$  and the Bohr radius  $a_0$

0.05 and 100 experimental repetitions. Each setting  $\theta$  produces a trial state  $|\varphi(\theta)\rangle$ , which is projected onto three measurement bases, to obtain the five expectation values  $H_\ell^{\text{BK}} = \{Z_0, Z_1, X_0X_1, Y_0Y_1, Z_0Z_1\}$  of Hamiltonian (7.5). The limited resolution scan over the parameter space can be extrapolated by fitting e.g. sinusoidal functions to the individual expectation values (Fig. 7.5 a)). Finally, we obtain the molecular energy of the ground state for each internuclear distance  $R$  by combining the expectation values for each value of  $\theta$  with their respective coefficients  $c_\ell(R)$ , according to Eq. (7.8), and picking the result with the minimal total energy in post-processing. Fig. 7.5 b) shows the resulting potential curve, which represents an experimental reference for the performance of our quantum simulator, and is used to compare the following variational simulation results to.

We implement the VQE algorithm at five different internuclear separations  $R$ , yielding the results in Fig. 7.5 b). For each optimization we start at a random initial value  $\theta_0$  and apply the gate sequence depicted in Fig. 7.3 a) to first prepare the trial state  $|\varphi(\theta_0)\rangle$  and then measure the expectation values  $\langle H_\ell \rangle(\theta_0)$ . Then the associated energy  $E(R, \theta_0)$  is passed to the optimization algorithm, which evaluates the result and suggests a new value for  $\theta$  (Fig. 7.5 c)). Throughout the iterations, the energy maps out a 1D landscape. The corresponding energy minimum is extracted by fitting a sinusoidal function to the parameter space, with each point weighted according to the quantum projection noise from its constituent measurements. Fig. 7.5 d) shows such an example of the explored energy landscape and the associated fitting. The error returned by the fitting routine defines the error bars of the VQE results.

### The LiH molecule

LiH is a heteronuclear molecule with four electrons, which increases the complexity of simulating its ground state energy. Under the BK encoding, with reference state  $|\varphi_{\text{HF}}\rangle = |111\rangle$ , the implementation requires three qubits, and a circuit with 8 half-entangling gates and two variational parameters,  $\alpha$  and  $\beta$ , as shown in Fig. 7.3 c). The MS gate fidelity for three qubits reaches 97(3)%. Again, we first perform a parameter scan to establish a baseline for the performance of our system. We scan over the section  $\alpha = [1.5, 6]$ ,  $\beta = [2, 5]$  of the two-dimensional parameter space in a grid-like pattern, with resolutions 0.1 and 0.15, respectively. For each parameter combination, we perform three projective measurements to determine the expectation values of Hamiltonian (7.7):  $H_\ell = \{Z_0, Z_1, Z_2, Z_1Z_0, Z_2Z_0, Z_2Z_1, X_1X_0, Y_1Y_0, X_2X_0, Y_2Y_0, X_2X_1, Y_2Y_1\}$ . Combining the results via Eq. (7.8), we obtain a two-dimensional energy landscape  $E(\alpha, \beta)$  for each separation  $R$ . Fig. 7.6 a) shows the experimentally scanned

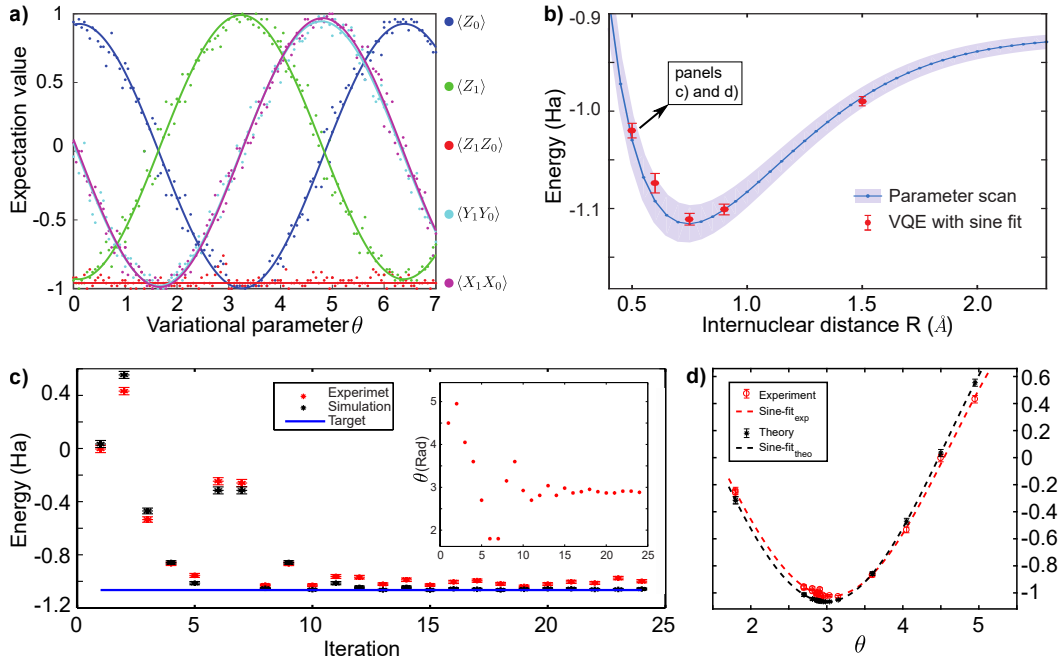


**Figure 7.5.:** H<sub>2</sub> in the two-qubit BK encoding and Hartree-Fock reference state  $|\varphi_{\text{HF}}\rangle = |01\rangle$ . **a)** Expectation values vs. the variational circuit parameter  $\theta$ . Dots denote experimental data with 100 measurement repetitions, while solid lines are fits. Error bars from quantum projection noise are omitted for clarity, but taken into account in the fitting routine. **b)** Blue: Molecular potential curve from a parameter scan with sinusoidal fits, where the shaded area denotes the  $1\sigma$  confidence band. Red: Results from VQE optimizations with final sinusoidal fitting of the energy landscape. **c)** Example for the VQE implementation at internuclear distance  $R = 0.5 \text{ \AA}$ . Energy is shown as a function of optimization iterations. Experimentally data is plotted as red stars with error bars are derived from quantum projection noise. The noise-free circuit simulation (black stars) shows a good convergence to the target value (blue line), obtained by exact diagonalization. The inset shows single-ion rotation angle  $\theta$  vs. the iteration number, illustrating the convergence of the VQE algorithm. **d)** VQE implementation at  $R = 0.5 \text{ \AA}$ . Energy vs. rotation angle  $\theta$  with sinusoidal fitting for extracting the parameters of the energy minimum (black: noise-free simulation, red: experiment).

parameter space, superimposed on a theoretical calculation of the full range. The final molecular potential curve of the ground state is derived by fitting two-dimensional functions to the energy landscapes and extracting the fit minima. We investigated two fitting approaches: (1) a Gaussian process regression (GPR) fit and (2) a two-dimensional quadratic fit  $E(\alpha, \beta) = \langle H(R) \rangle_{\alpha, \beta} = m + (c \cdot \alpha - a)^2 + (d \cdot \beta - b)^2$  to a restricted area around the energy minimum, that is all data points within four standard deviations from the median. While resulting in a smooth potential energy surface, the GPR-based fit systematically underestimates the energy. This highlights how much the data evaluation method influences the result. Fig. 7.6 b) shows the resulting molecular

potential curves, in comparison with an ideal theoretical calculation and data points obtained from VQE implementations.

Despite a significant increase in experiment runtime, it is still possible to sequentially scan the two-dimensional parameter space of LiH. However, scaling up to more complex molecules reveals the true power of the VQE approach: Sparse and adaptive sampling of a potentially very high-dimensional energy landscape. We implement the iterative VQE procedure for two internuclear distances  $R = 1.6$  and  $R = 2.75$ . In contrast to the  $H_2$  molecule, the optimization algorithm is now dealing with two variational parameters  $\alpha$  and  $\beta$ . Fig. 7.6 a) shows how the VQE implementation at  $R = 1.6$  samples over the parameter space. The employed hybrid algorithm ensures a large enough number of data points around the minimum, for successful fitting of all data points within four standard deviations from the mean, as illustrated in Fig. 7.6 c).

### 7.2.3. Impact of gate imperfections and decoherence

We investigate the impact of gate imperfections and decoherence in the context of parameter scans of the  $H_2$  molecule. Depending on the method for mapping the fermionic to spin expressions (Eqs. (7.5 and 7.6)), the variational simulation can be performed on either two qubits (BK) or four qubits (JW), and correspondingly the UCCSD operators contain two- and four-qubit entangling gates. Also the projective measurements for the expectation values  $\langle H_\ell(\boldsymbol{\theta}) \rangle$  depend on the Hamiltonian transformation method: The BK-transformed case requires three measurements to obtain  $H_\ell^{\text{BK}} = \{Z_0, Z_1, X_0X_1, Y_0Y_1, Z_0Z_1\}$ . In the JW-transformed case, we obtain 14 expectation values  $H_\ell^{\text{JW}} = \{Z_0, Z_1, Z_2, Z_3, Z_1Z_0, Z_2Z_0, Z_2Z_1, Z_3Z_0, Z_3Z_1, Z_3Z_2, Y_3Y_2X_1X_0, Y_3X_2X_1Y_0, X_3Y_2Y_1X_0, X_3X_2Y_1Y_0\}$  from 5 different measurements. This spans a great experimental space in which we study four different cases: (1-2) operations within and outside a decoherence-free subspace that is protected against correlated dephasing, and (3-4) implementations with high and low MS gate fidelity.

- (1-2) In the BK mapping, we can perform a basis rotation at the level of the Hamiltonian, which results in a sign changes of the  $c_\ell(R)$  coefficients and a different initial state  $|\varphi_{\text{HF}}\rangle = |11\rangle$ . Note that the UCCSD operator and its circuit implementation are maintained. The initial state  $|01\rangle$  transforms in our gate sequence through a decoherence-free subspace, while  $|11\rangle$  is prone to decoherence.
- (3-4) Within the JW mapping, we compare the results with 97(4)% and 93(3)% MS gate fidelity.

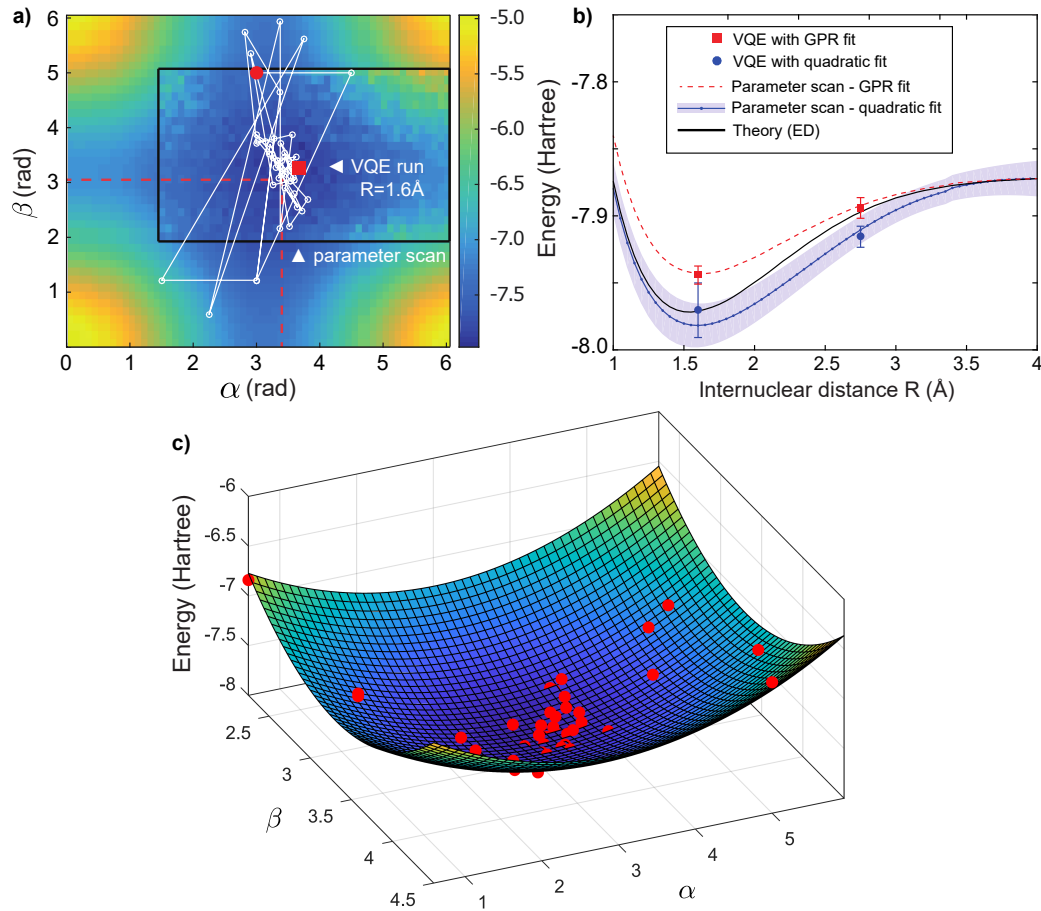


**Figure 7.6.:** LiH results. **a)** Energy landscape at internuclear distance  $R = 1.6 \text{ \AA}$ . The black box inset marks the experimentally scanned parameter range. It is superimposed on a theoretical calculation with dashed red lines marking the coordinates of the targeted energy minimum. Connected white lines show the iterations taken by the VQE algorithm, with the starting point marked by a filled red dot and the abortion point by a red square. **b)** Potential energy curves, obtained from experimentally scanning the parameters (as in a)), in comparison with the theoretical solution, calculated via exact diagonalization (black). The experimental curves are offset in order to overlap at maximum distance  $R$  for a better illustration of the well-depth differences. The data points result from sampling the energy landscape  $\langle H(R) \rangle_{\alpha, \beta}$  with the VQE algorithm. The explored space is fitted with a Gaussian process regression (GPR) based machine learning algorithm (red dashed line) or a 2D quadratic fit (blue solid line), as illustrated in panel c), to extract the minimum energy value. Error bars are obtained from the fits with the underlying data weighted by quantum projection noise. The slight kink close to  $R = 3.5 \text{ \AA}$  is due to the interplay of rounding errors introduced in the fitting routine with small deviations originating in our active space approximation. **c)** VQE data (red) at  $R = 1.6 \text{ \AA}$ , fitted with the two-dimensional quadratic function  $E(\alpha, \beta) = m + (c \cdot \alpha - a)^2 + (d \cdot \beta - b)^2$ .

A comparison of the cases 1-4 is shown in Fig. 7.7 a). It reveals that correlated dephasing errors as well as reduced gate fidelities shift the absolute molecular energy

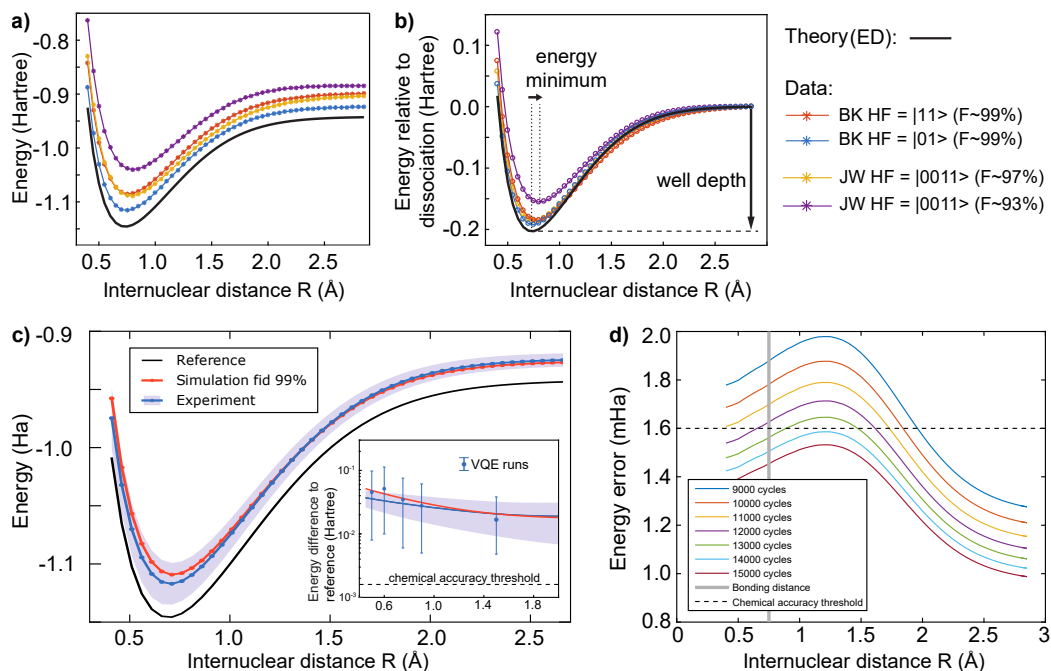


**Figure 7.7.: Impact of gate imperfections and decoherence, on the example of the  $H_2$  molecule.** **a)** Potential energy curve of the ground state for different experimental settings: The data sets vary the number of qubits, the Hartree-Fock reference states and gate fidelities, as denoted in the legend on the right. All colored lines are derived from weighted sinusoidal fits to the energy surface formed from experimental parameter scans. The black line corresponds to the theoretical solution, calculated via exact diagonalization (ED). **b)** Data from panel a), normalized to the theoretical dissociation energy at large internuclear separations  $R$ . The dashed and dotted lines indicate the well depth associated with the binding energy of the molecule and the position of the energy minimum, respectively. **c)** Simulation of decoherence and MS depolarizing errors of 1% (red), compared with the corresponding experimental parameter scan, including error band (blue). The inset shows the data from the main panel with respect to the numerical theory from ED (black line). **d)** Scaling of the energy error, related to quantum projection noise. Each color-coded curve corresponds to a  $1\sigma$  error in the energy calculated from the expectation values  $\langle H_\ell \rangle$ , weighted by the respective scalars  $c_\ell(R)$ .

to higher values. In particular, we observe that a two-qubit ansatz that is not protected against correlated dephasing yields similar results as a decoherence-protected four-qubit ansatz. The latter is significantly more sensitive to correlated dephasing due to the larger number of qubits. This highlights the benefit of employing decoherence-free subspaces in algorithmic implementations. In chemistry, measurements generally refer to energy differences as opposed to absolute values. Therefore, it is common to translate the potential energy curves to their nominal reference value at large separation  $R$  as illustrated in Fig. 7.7 b. This depiction more clearly demonstrates the respective upshift in energy with respect to the calculated binding energy (or well

depth) and the simultaneously occurring shift in the position of the energy minimum towards larger internuclear distances. Fig. 7.7 c) compares a simulation including gate errors and decoherence<sup>57</sup>, with the experimental result for the best conditions (BK mapping,  $|\varphi_{\text{HF}}\rangle = |01\rangle$ , 99% gate fidelity). We observe, that the upshift in energy is largely captured by the gate and coherence infidelities. A recent numerical study [182] reveals the impact of errors in the simulation of the ground state energy of  $\text{H}_2$  and  $\text{LiH}$  in more detail. Possible workarounds to this problem could be the introduction of ancilla qubits, which detect whether the decoherence-free subspace was maintained, or the use of quantum circuits which are tailored to the experimental capabilities.

Finally, we apply the widely used concept of *chemical accuracy* as reference to benchmark our results. In chemistry, an energy error of  $\Delta G = 1.6$  mHa between reactants and the transition state, translates to a chemical event rate that is off by a factor of ten [178]. The inset in Fig. 7.7 c) relates the results for the  $\text{H}_2$  molecule, to this energy error, also known as “chemical accuracy threshold”. Let us assume no other sources of noise, than quantum projection noise. In this case, we can estimate a minimum number of measurements for each observable  $\langle H_\ell \rangle$ , for which the energy error falls below the chemical accuracy threshold. Fig. 7.7 d) illustrates, that one would need to repeat each measurement at least 15000 times in order to reach chemical accuracy. Such a large number of repetitions has a strong impact on the run-time of the experiment. In addition to technical improvements on the hardware side, there are a number of theoretical proposals which appear to significantly reduce the resources required to scale up these simulations. For instance, in Ref. [183] authors introduce a new class of basis functions for the simulation of electronic structure problems. They quadratically reduce the number of terms in the Hamiltonian from  $\mathcal{O}(N^4)$  to  $\mathcal{O}(N^2)$ . Furthermore, an adaptive measurement strategy might also alleviate the resource needs with respect to the required number of averages. This could entail varying the number of repetitions throughout the VQE iterations, based on the observed energy changes in each step. The measurement precision could be gradually increasing as the algorithm converges towards the energy minimum.

In conclusion, further work is needed on both the quantum and classical aspects of this trotterized way of variational quantum simulation. Specifically, the mitigation of gate errors in the quantum circuits promises improved performance. The most significant challenge in trotterized variational simulations remains the circuit depth. A naive application of unitary coupled cluster requires a number of gates that scales

<sup>57</sup>The decoherence channels include single-qubit dephasing of all qubits during state preparation, e.g. due to magnetic field fluctuations, considering a dephasing time  $T_2 = 40$  ms.

as  $\mathcal{O}(N^4)$ , assuming arbitrary connectivity between qubits. This strongly suggests that more scalable variational circuits will be needed if we are to approach classically intractable calculations. An alternative to the unitary coupled cluster ansatz is to employ an unstructured variational circuit, as demonstrated first in [12] and applied in Section 7.3.

### 7.3. Application II: The Lattice Schwinger Model

An alternative approach to the one presented in Section 7.2, is based on the heuristic generation of trial states  $|\varphi(\boldsymbol{\theta})\rangle$  using unitary operations that are more tailored to the available quantum hardware. Specifically, the main quantum resources for the experiment discussed here are single-qubit rotations of arbitrary angles around the z-axis, and spin-spin interactions with variable evolution time. With this, the quantum device efficiently generates possibly highly entangled states that are close to the target state, almost<sup>58</sup> independently of the particular Hamiltonian of interest. In our experiment, we combined quantum variational techniques with our state-of-the-art, potentially scalable, analog quantum simulator. In contrast to analog quantum simulation, this approach forgoes the requirement of realizing the targeted Hamiltonian directly in the laboratory, thus allowing us to study a wide variety of previously intractable target models. Although the results presented below, focus on the simulation of the lattice Schwinger model, the technique is also directly applicable to general lattice models in condensed matter and high-energy physics. Implementing the lattice Schwinger model in a many-qubit system is far out of reach for current analog and digital quantum simulators: The complexity of the Hamiltonian has so far prevented a direct realization using analog quantum simulation. Digital quantum simulation of the model has been reported in [184], however it was restricted to four qubits and four Trotter steps requiring a total of 220 quantum gates. In contrast, we show that variational quantum simulation allows for a well-converged preparation of eigenstates of the lattice Schwinger model, for up to 20 qubits.

A key challenge for variational quantum simulators is the scaling to larger system sizes, which is limited by the available quantum computing hardware, as well as by a rapid increase in the number of variational parameters  $\boldsymbol{\theta}$ . Moreover, the number of measurements needed for the classical computer to successfully navigate the high-dimensional energy landscape, rapidly increases with system size. In the project, published in Ref. [16], we demonstrate how VQS can be scaled up for lattice models by incorporating intrinsic symmetries of the Hamiltonian into the trial states and thus reducing the number of variational parameters. Furthermore, our collaborators from the theory department developed an advanced global optimization algorithm specifically suited for noisy, high-dimensional and gradient-free problems.

Finally, when variational techniques can be scaled up to a regime where classical simulations become intractable, we are facing the long-standing problem of how to

---

<sup>58</sup>The scheme benefits if symmetries of the Hamiltonian are preserved.

verify the produced answers, that is, assessing how close the variational trial states and energies are to the exact values. In the project discussed here, we take a step towards verifying the quantum simulation: By measuring the Hamiltonian variance of the prepared states, we are able to estimate the algorithmic error bars of the final energies, that is, the uncertainty on the approximate ground-state energy. Comparing these to the energy gap to the first excited state, corresponds to a quantitative self-verification of the acquired results on the quantum device itself.

### 7.3.1. Theoretical background

We focus our study on the lattice Schwinger model, a gauge theory of one-dimensional quantum electrodynamics [185, 186]. In simple words, this model describes the interaction of charged matter and antimatter (represented by a fermion field) with a quantized electric field. The Kogut-Susskind encoding maps the fermionic configurations to a spin-1/2 lattice, where a spin down (or spin-up) on an odd (or even) lattice site indicates the presence of a positron (electron), as illustrated in Fig. 7.8. For open boundary conditions, and using the Jordan-Wigner transformation for mapping fermions to spins, our target Hamiltonian reads

$$\hat{H}_T = w \sum_{j=1}^{N-1} [\hat{\sigma}_j^+ \hat{\sigma}_{j+1}^- + \text{H.c.}] + \frac{m}{2} \sum_{j=1}^N (-1)^j \hat{\sigma}_j^z + \bar{g} \sum_{j=1}^N \hat{L}_j^2. \quad (7.9)$$

Here,  $j$  labels the lattice site, for a system of length  $N$ , and  $\hat{\sigma}_j^a$  are Pauli operators. The first term in Eq. (7.9) describes the creation or annihilation of a particle-antiparticle pair, mapped to a spin flip-flop term with coupling  $w$  (which we set to  $w = 1$  as the energy unit). The second term contains the bare mass  $m$  of the matter and the last term is the electric field energy, with coupling  $\bar{g}$ . The 1D character of our model allows the electric field  $\hat{L}_j$  to be eliminated due to Gauss' law [186]  $\hat{L}_j - \hat{L}_{j-1} = \frac{1}{2}(\hat{\sigma}_j^z + (-1)^j)$ , such that  $\hat{L}_j$  is expressed in terms of Pauli operators

$$\hat{L}_j = \epsilon_0 - \frac{1}{2} \sum_{\ell=1}^j (\hat{\sigma}_\ell^z + (-1)^\ell).$$

Here,  $\epsilon_0$  is a background electric field, which is set to zero. With this, the Hamiltonian  $\hat{H}_T$  reduces to an effective spin-1/2 model with exotic long-range interactions originating from squaring  $\hat{L}_j$ . The expectation value of the target Hamiltonian  $\langle \hat{H}_T \rangle$  can be

decomposed into three terms  $\hat{H}_T = \hat{\Lambda}_X + \hat{\Lambda}_Y + \hat{\Lambda}_Z$  with

$$\begin{aligned}
\hat{\Lambda}_X &= \frac{w}{2} \sum_{j=1}^{N-1} \hat{\sigma}_j^x \hat{\sigma}_{j+1}^x, \\
\hat{\Lambda}_Y &= \frac{w}{2} \sum_{j=1}^{N-1} \hat{\sigma}_j^y \hat{\sigma}_{j+1}^y, \\
\hat{\Lambda}_Z &= \frac{m}{2} \sum_{j=1}^N (-1)^n \hat{\sigma}_j^z + \bar{g} \sum_{j=1}^{N-1} \left( \varepsilon_0 - \frac{1}{2} \sum_{\ell=1}^j [\hat{\sigma}_\ell^z + (-1)^\ell] \right)^2 \\
&= \sum_{j=1}^N d_j \hat{\sigma}_j^z + \sum_{j=1}^{N-2} \sum_{j'=n+1}^{N-1} c_{j,j'} \hat{\sigma}_j^z \hat{\sigma}_{j'}^z.
\end{aligned} \tag{7.10}$$

All three components consist of two-spin correlation functions in either the  $x$ -,  $y$ - or  $z$ -basis. Therefore  $\langle \hat{H}_T \rangle$  is obtained by projecting onto only 3 bases, regardless of the system size.

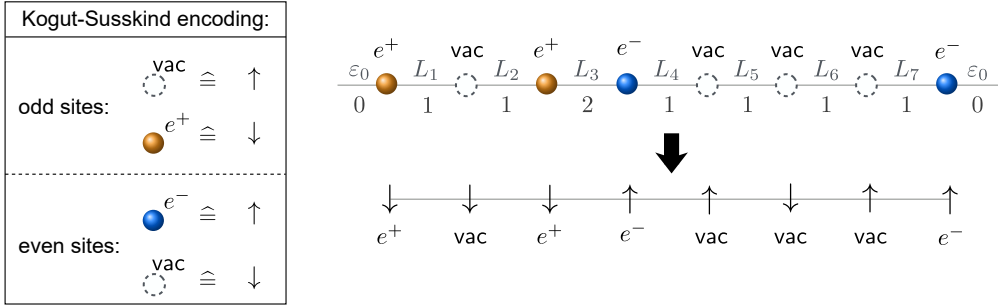


**Figure 7.8.: Encoding of the lattice Schwinger model in a chain of qubits.** The box shows the encoding of particles ( $e^+/e^-$ ) and vacuum (vac) into spins. The two spin states  $\uparrow/\downarrow$  in combination with the parity of each site, define the existence or absence of fermions. The right pictogram illustrates a specific product state for eight lattice sites in the Schwinger model and its translation into the spin configuration. The symbols  $\varepsilon_0$  and  $L_i$  and the corresponding numbers below, denote the electric fields, building up between the sites: We set the background field  $\varepsilon_0 = 0$ . Positively charged particles increase the field by one unit, negatively charged particles reduce it, whereas empty sites (vac) do not alter the electric field.

### On symmetries of the target Hamiltonian and the quantum resource

Matching symmetries between the experimental resources and the target model is highly beneficial for the overall efficiency of VQS. In particular, preserving symmetries reduces the Hilbert space to the relevant symmetry sector (Fig. 7.9) – which again reduces the number of variational parameters required to sample this space. On the other hand preserving symmetries in the resource that are not present in the target model can trap

the algorithm in a symmetry sector.

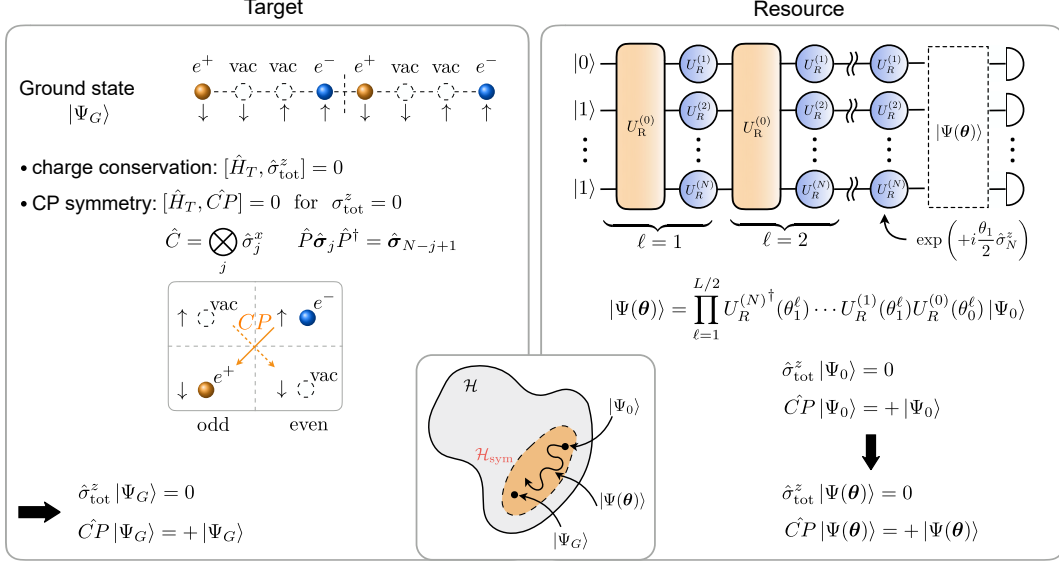


**Figure 7.9.: Symmetry considerations for the target Hamiltonian and the quantum resource.** The left-hand panel shows the Schwinger spin model in the Kogut-Susskind formulation where matter fields are represented by spin degrees of freedom. We investigate the ground state of  $\hat{H}_T$  restricted to the symmetry sector with quantum numbers  $\hat{\sigma}_{\text{tot}}^z = 0$  and  $\hat{C}\hat{P} = +1$ . The right-hand panel shows the native resources of our ion trap platform. They can be exploited to engineer symmetry preserving quantum circuits specifically tailored to the Schwinger model. The realization of an approximate XY-Hamiltonian (orange boxes  $U_R^{(0)}$ ), as given in Eq. (7.11), protects the  $\hat{\sigma}_{\text{tot}}^z$  symmetry. Single-Qubit rotations around the  $z$ -axis (blue circles  $U_R^{(j)}$ ) can be forced to be  $\hat{C}\hat{P}$ -symmetric by linking the rotation angles between the left and the right half of the chain according to  $\theta_\ell^n = -\theta_\ell^{N-n+1}$ . Such a circuit will protect the target symmetries, restricting the variational search only within the portion of Hilbert space of our interest (illustrated in the inset). Note that each unitary  $U_R^{(0)}$ , as well as each set of  $\{U_R^{(j)}\}$  with  $j = 1, \dots, N$  defines one *layer* of the quantum circuit. In this illustration,  $|\Psi(\theta)\rangle$  is generated by  $L$  such layers, so we call it a circuit of depth  $L$ .

The Schwinger Hamiltonian  $\hat{H}_T$  exhibits charge conservation symmetry  $[\hat{H}_T, \hat{\sigma}_{\text{tot}}^z] = 0$ , with  $\hat{\sigma}_{\text{tot}}^z = \sum_j \hat{\sigma}_j^z$ . Due to this symmetry, matter and antimatter are only created or annihilated as particle-antiparticles *pairs*. The specific symmetry subspace of our interest is the sector with zero total magnetization  $\hat{\sigma}_{\text{tot}}^z = 0$ , which includes the Néel state  $\uparrow\downarrow \dots \uparrow\downarrow$  (corresponding to the bare vacuum). Within this charge symmetry sector, the Schwinger model also retains  $\hat{C}\hat{P}$  symmetry:  $[\hat{H}_T, \hat{C}\hat{P}] = 0$ , which combines charge conjugation ( $C$ ) and spatial reflection ( $P$ ). In the Kogut-Susskind formalism, this operation can be implemented only for a lattice with even length  $N$ , as spatial reflection around a bond effectively maps the particle sublattice into the antiparticle sublattice, and vice versa. Since particles and antiparticles have opposite spin encod-

ings, all the spins must be flipped upon reflection, i.e. undergo a  $\sigma^x$  operation (Fig. 7.9). More mathematical details on the mapping and the symmetries of the Hamiltonian, are given in the Supplementary Material of Ref. [16].

Having summarized the symmetries of the target model, we have to implement them on our resource quantum simulator, consisting of up to  $N = 20$   $^{40}\text{Ca}^+$  ions, confined in a linear Paul trap. We first prepare the ions in a simple product state  $|\Psi_0\rangle$ . Specifically, we choose a Néel-ordered state, e.g.  $|\Psi_0\rangle = |\uparrow\downarrow\cdots\uparrow\downarrow\rangle$  that lies within the zero-magnetization sector. Our quantum simulator has two main quantum resources that preserve the symmetries of the target Hamiltonian:

- The XY-Hamiltonian

$$\hat{H}_R^{(0)} = \sum_{i=1}^{N-1} \sum_{j=i+1}^N J_{ij} (\hat{\sigma}_i^+ \hat{\sigma}_j^- + \hat{\sigma}_i^- \hat{\sigma}_j^+) + B \sum_{i=1}^N \hat{\sigma}_i^z \quad (7.11)$$

is realized using a bichromatic laser beam that off-resonantly couples all ions to the transverse modes of motion [116]. Here,  $J_{ij} \simeq J_0/|i-j|^\alpha$  are long-range anti-ferromagnetic couplings with tunable interaction range  $\alpha$ , and  $B$  is an effective, uniform magnetic field. This Hamiltonian is capable of creating *highly entangled states*, while protecting the  $z$ -magnetization. Additionally,  $\hat{H}_R^{(0)}$  is  $\hat{C}\hat{P}$  invariant within the zero-magnetization sector. This is visible in the interaction matrix, which is symmetric under reflection  $J_{i,j} = J_{N+1-j, N+1-i}$ .

- Single-qubit rotations around the  $z$ -axis

$$\hat{H}_R^{(j)} = \frac{\Delta_0}{2} \hat{\sigma}_j^z$$

are realized by a steerable, strongly focused off-resonant laser beam which induces an AC-Stark shift  $\Delta_0$ .

With these Hamiltonians we form a quantum circuit of alternating *layers* of unitary operations, to generate a family of variational trial states  $|\Psi(\boldsymbol{\theta})\rangle$  (see Fig. 7.9, right panel): The odd layers consist of the entangling operation  $U_R^{(0)}(\theta) = \exp(-i\theta\hat{H}_R^{(0)})$  where the control parameter  $\theta$  sets the duration of the time-evolution, while the even layers contain the local operators  $U_R^{(j)}(\theta) = \exp(-i\sum_{j=1}^N \theta\hat{H}_R^{(j)})$  acting on every site  $j$ . The single-qubit operations are forced to preserve  $\hat{C}\hat{P}$  by matching the rotation angle at site  $j$  with the rotation angle at site  $(N+1-j)$ , specifically

$$\theta^{(j)} = -\theta^{(N+1-j)}.$$

Both unitaries keep the state in a decoherence-free subspace with respect to the major experimental sources of decoherence [60]. The preservation of  $\hat{C}\hat{P}$  symmetry reduces the number of variational parameters for each single-qubit layer to  $N/2$ , while restricting the global search to the symmetry sector of interest. Furthermore, as the number of lattice sites increases, we expect the Schwinger model to exhibit approximate translational symmetry within a *bulk-region*  $\mathcal{B}$  in the centre of the lattice. We incorporate this symmetry, by enforcing  $\theta^{(j)} = \theta^{(j+2)}$  for all  $\{j, j+2\} \in \mathcal{B}$ , i.e. far from the ends of the ion chain. This reduces the number of variational parameters further, essentially making the number of parameters per layer non-scaling with the system size.

### On scalability

In our VQS framework, the number of variational parameters  $\theta$  scales linearly with the number of layers  $n_{\text{layers}}$ , at fixed size  $N$ . Therefore  $n_{\text{layers}}$ , also referred to as *circuit depth*, is a good quantifier of the variational complexity of the quantum simulation. For system sizes up to  $N = 12$  sites, we can determine the exact ground state of the target Hamiltonian on a classical computer, via exact diagonalization. With this, we can quantify the precision of a variational simulation by calculating the infidelity of the variationally optimized state with the exact ground state of the model.

We run the variational ground state simulation on a classical computer, and identify a minimal circuit depth  $n_{\text{req}}$  required to prepare the VQS state at a given precision, e.g. 5% infidelity. The observed scaling behaviour suggests that the variational complexity of the Schwinger ground state is polynomial – not exponential – in the system size  $N$ , ultimately making our VQS procedure scalable. Although we have simulated the scaling properties only up to 12 lattice sites, we expect our findings to be valid for larger and more complex systems. In particular, the appearance of a translationally invariant bulk region for large systems results in a system-size-independent number of variational parameters per circuit layer.

### 7.3.2. Optimization algorithm

Efficient variational quantum simulation relies on an advanced global optimization algorithm, which is specifically suited for finding the global minimum in a high-dimensional and gradient-free landscape, the space of parameters  $\theta$ . In particular, this space only reveals itself through inherently noisy measurements of quantum observables, while typically featuring multiple local minima. In the project presented here, we employ a variant of the dividing rectangles (DIRECT) algorithm [187, 188]: it divides the parameter space into regions called *hypercells*, which are represented by a single cost

function evaluation taken in its interior as illustrated in Figs. 7.10 a) and b). Cells are subdivided into smaller cells, if they are considered sufficiently promising to harbour the global minimum, prioritizing cells with low energy values, as well as cells with large sizes (Figs. 7.10 c) and d)). The cell size is an important quantity in the algorithm's decision making, because larger cells have more unexplored territory. Therefore, they are statistically more likely to contain the global minimum, compared to small cells. For a full optimization run, we assign a total budget of (up to)  $10^5$  calls to the quantum simulator. A single call involves the variational preparation of a trial state and the projective measurement of the qubits in a given basis. In order not to waste the finite iteration budget on high-energy points, we initially invest only a low number (30) of measurement repetitions per basis at each unexplored point. The low number of initial samples typically suffices to provide a rough estimation of the energy on which the algorithm can base its subsequent decisions. If two similarly sized cells are competing for a subdivision step, that is, if it is unclear which function value is lower due to the statistical uncertainty<sup>59</sup>, the algorithm can request refinement steps<sup>60</sup>. Those additional measurements are then combined with the previous ones, to reduce the statistical error and to increase the probability of correct decisions. The DIRECT algorithm attempts to balance between those phases of *exploitation* (refining a promising point) and *exploration* of the unknown areas in parameter space, which ensures that the algorithm does not get stuck in local minima and ultimately finds the global minimum.

During an optimization run, the algorithm maintains an internal representation, called *metamodel*, of the energy landscape in the form of a Gaussian Process [181]: This machine learning approach models the experimental data points as Gaussian functions and uses their joint distribution to obtain a continuous function of the energy landscape. The variance of the data functions implicate a probability distribution of metamodel functions, such that the Gaussian process yields predictions for the mean values as well as uncertainties of the energy landscape. The optimization algorithm uses this metamodel in the decision for subdividing hypercells, as well as for sampling at the predicted global minimum in exploration steps.

In our experiment, the variational algorithm continues requesting measurements from the quantum device until the allocated resource budget is exhausted. Another stopping criterion would be given by stationarity, that is, the algorithm terminates, if the pre-

<sup>59</sup>The measurements are affected by intrinsic statistical errors, introduced by the finite number of projective measurements (shot noise), temporal fluctuations in the experimental controls (control noise), and infidelities in the initial Néel state preparation.

<sup>60</sup>The algorithm selects when to perform the refinement steps and how many measurements to spend in this stage, based on methods from decision theory and Optimal Computing Budget Allocation (OCBA).

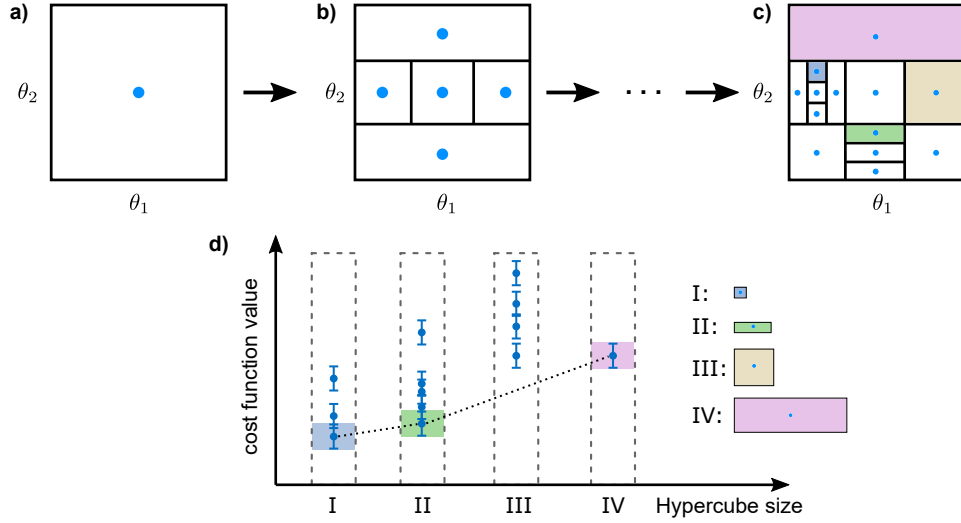


**Figure 7.10.: Schematics on the optimization algorithm.** Panels a)-c) illustrate the sequence of the optimization algorithm: **a)** Sampling the center of the hypercube in the parameter space spanned by  $\theta_1$  and  $\theta_2$ . **b)** Sampling along each dimension in parameter space and divide into smaller hyper-cubes. **c)** Evaluating the cost functions and identifying promising cubes (here marked by colors), as illustrated in panel **d)**: based on elements from decision theory (OCBA), the algorithm compares the cost function values and decides which cubes to subdivide and investigate further. One of the largest boxes (pink) is always added to the promising cubes with low cost function values (blue and green), in order to explore unknown areas.

dicted minimum of the metamodel is no longer changing as more iterations are added. For more details regarding the optimization algorithm, contact our collaborators from the theory department<sup>61</sup>.

### 7.3.3. Variational Schwinger ground state search for 20 qubits

We perform variational optimization to the ground state of the lattice Schwinger model with 20 qubits. After preparing the initial Néel state with a fidelity of 91(3)%, we apply a quantum circuit of depth 6, consisting of 3 entangling and 3 single-qubit rotation layers (as defined in the subsection *On symmetries of the target Hamiltonian and the quantum resource*). The entangling operations are realized by long-range spin-spin interactions, following an approximate power-law decay  $J_{ij} \simeq J_0/|i-j|^\alpha$ , with  $J_0 \approx (2\pi) 30$  Hz and an exponent  $\alpha = 0.98$ . This coupling is achieved by setting the bichromatic laser frequencies to be  $\pm(\omega_{com} + \delta)$  from the qubit transition, where  $\omega_{com} = (2\pi) 2.71$  MHz is the highest radial mode frequency and  $\delta = (2\pi) 0.04$  MHz. Additionally, both components of the bichromatic laser are shifted by  $\delta_B = (2\pi) 3$  kHz from the qubit transition,

<sup>61</sup>The optimization algorithm was advanced in the group of Prof. Peter Zoller, primarily by Rick van Bijnen, at the Institute of Quantum Optics and Quantum Information.

generating the effective transverse  $B$ -field in the system as defined in Eq. (7.11). We approximate translational invariance in a bulk region of 14 central sites, resulting in a total of 15 variational parameters  $\theta$ . The control variables  $\theta$  adjust the duration of the time-evolution under the spin-spin interaction, and the individual single-qubit rotation angles. Finally, we perform spin rotations prior to spatially resolved fluorescence detection, in order to project the quantum state into 3 different measurement bases  $x$ ,  $y$  and  $z$ . Those projective measurements yield the correlation functions in Eq. (7.10) which are necessary for evaluating the energy  $E(\theta) \equiv \langle \Psi(\theta) | \hat{H}_T | \Psi(\theta) \rangle$ .

The entire experimental sequence is repeated 30-200 times and the statistical average is taken. We partially correct for decoherence and imperfect initial state preparation by post-selecting on the measurements in the  $z$ -basis. This means, that we retain only those 70% of the measurements which lie within the zero-magnetization subspace. The results are subsequently passed to a classical computer, which runs the optimization routine and returns the control parameters  $\theta$  to the quantum device, in form of a sequence script file. In each iteration  $i$  of the optimization loop, the classical computer supplies a new set of  $\theta_i$ . Note that the experimental control system calibrates itself every 10 minutes to correct for slow drifts of the experimental parameters such as laser frequency, the positioning of the ion chain, and drift of the addressing laser beam.

The resulting optimization trajectory for  $m = 0.9$  and  $w = \bar{g} = 1$  is shown in Fig. 7.11 a), where the energy  $E(\theta_i)$  is plotted as a function of the iteration number  $i$  of the optimization loop. The coloring of the energy values  $E(\theta_i)$  serves for visualizing the different trial states  $|\Psi(\theta_i)\rangle$ , prepared during the optimization run: the color-code indicates the Euclidian distance  $|\Delta\theta|$ , of each set  $\theta_i$  to the parameter vector  $\theta_{\text{best}}$  with the highest theoretical fidelity  $\mathcal{F} = |\langle \Psi_G | \Psi_{\text{Sim}}(\theta_i) \rangle|^2$ . Here,  $|\Psi_G\rangle$  defines the exact ground state and  $|\Psi_{\text{Sim}}(\theta_i)\rangle$  the variational wave function as simulated numerically using the parameters  $\theta_i$  from the experiment. The graph in Fig. 7.11 c) illustrates the trend of this fidelity reaching up to 0.8. The algorithm maintains an internal metamodel of the energy landscape, that is continuously updated as more experimental data is gathered (c.f. Section 7.3.2). The red solid line in Fig. 7.11 a) indicates the **current estimate of the ground state energy**, extracted from this metamodel, with the shaded area as the  $2\sigma$  confidence interval of the prediction. As visualized in Fig. 7.11 b), the employed search algorithm continuously explores new regions in parameter space, leading to a large spread in the sampled energies. Initially, a local minimum appears (i), for which the cell size is reduced for fine sampling. However, that region is finally surpassed by a more promising region, labelled as (ii). Fig. 7.11 d) illustrates how well the experimental results agree with theoretical simulations for

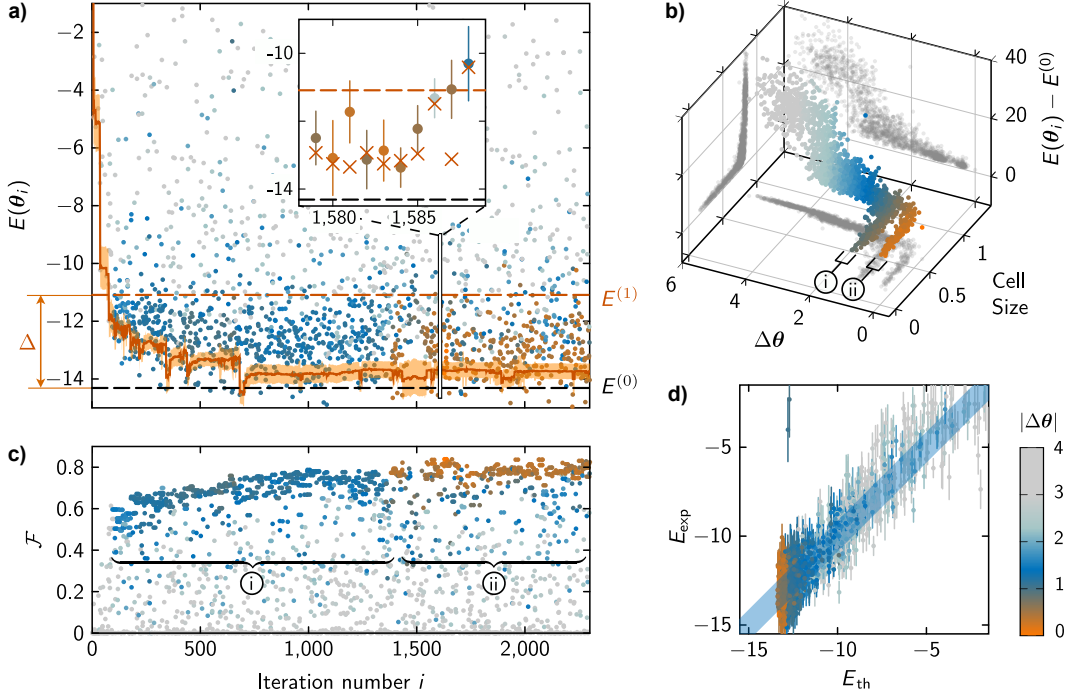


**Figure 7.11.: Variational ground state search with 20 ions.** **a)** Convergence of experimental energies  $E(\theta) \equiv \langle \Psi(\theta) | \hat{H}_T | \Psi(\theta) \rangle$  vs. iteration number  $i$ . The algorithm refines a potential minimum, but also keeps exploring new regions of the parameter space, leading to high energy values, even in the later stages of the run. The color-coding of the Energy values  $E(\theta_i)$  indicates the Euclidian distance,  $|\Delta\theta|$  of  $\theta_i$  to the parameter vector  $\theta_{\text{best}}$  with the highest theoretical fidelity (see panel c)). The solid red line is the current estimate of the ground state energy and its  $2\sigma$  uncertainty (shaded area), extracted from the algorithm's internal metamodel (see text).  $\Delta$  denotes the exact gap between the energy of ground state,  $E^{(0)}$ , and first excited state,  $E^{(1)}$ . Inset: Zoom into a late stage of the optimization, where dots show experimental data with statistical errorbars, and crosses show numerically simulated values. **b)** Visualization of sampled energy landscape relative to  $E^{(0)}$ , vs. parameter distance  $\Delta\theta$  and the corresponding cell size in the optimization algorithm. Distinct local minima are visible as 'fingers', marked (i) and (ii), extending towards smaller cell sizes, indicating fine sampling of the parameter space near a local minimum. **c)** Theoretical fidelities  $\mathcal{F}$  of the many-body wavefunctions (see text), with a rough indication of the local minima (i), (ii) b). **d)** Correlation between experimentally measured energy  $E_{\text{exp}}$  versus numerically simulated energy  $E_{\text{th}}$ , showing agreement within  $2\sigma$  (blue shaded area).

corresponding trial states  $|\Psi(\theta_i)\rangle$ . Typical statistical error bars are drawn as a blue band of thickness  $2\sigma$ , in which 55% of the data points accumulate.

A similar optimization run for 16 ions found multiple local minima and reached a final fidelity approaching 0.9. We attribute the increase in fidelity with lower number of ions, to less decoherence and a higher fidelity in the preparation of the initial state.

### 7.3.4. Quantum phase transition for 8 qubits

Next, we study a quantum phase transition of the Schwinger model for 8 lattice sites. Specifically, we monitor the change of the order parameter

$$\langle \hat{\mathcal{O}} \rangle = \frac{1}{2N(N-1)} \sum_{i,j>i} \langle (1 + (-1)^i \hat{\sigma}_i^z)(1 + (-1)^j \hat{\sigma}_j^z) \rangle \quad (7.12)$$

as a function of the mass  $m$  of the matter. The observable  $\langle \hat{\mathcal{O}} \rangle$  describes the probability of the lattice to be filled with electron-positron pairs, where the limit  $m \rightarrow +\infty$  correspond to the bare vacuum, and  $m \rightarrow -\infty$  to full proliferation of electron-positron pairs (see insets in Fig. 7.12 a)). The critical point of the Schwinger model with zero background field  $\epsilon_0 = 0$  and  $w = \bar{g} = 1$  occurs at negative bare mass  $m_c \sim -0.7$  [189].

Experimentally, we probe the phase transition by performing the following steps for each mass  $m$ : We prepare a different initial state, depending on whether the mass is below or above the critical point:  $|\downarrow\uparrow \dots \downarrow\uparrow\rangle$  and  $|\uparrow\downarrow \dots \uparrow\downarrow\rangle$  for  $m < m_c$  and  $m > m_c$ , respectively. In both cases, the Néel states are prepared with a fidelity of 98(2)%. Then, we follow the same optimization routine and measurement scheme as described in Section 7.3.3, to variationally prepare the ground state of the system. The parameters for the entangling layers of the quantum circuit are  $J_{ij} \approx (2\pi) 37$  Hz and  $\alpha = 1.34$ . For each trial state, prepared during the optimization, we calculate the observable  $\langle \hat{\mathcal{O}} \rangle$  and derive  $\langle \hat{\mathcal{O}} \rangle_{\text{avg}}$  as the weighted average over all states according to their energies and statistical error bars<sup>62</sup>. This procedure is repeated for various masses  $m$  in order to determine the full phase transition. Note that the optimization can be accelerated by re-evaluating previously sampled data for different values of  $m$  – which only changes the pre-coefficients in the summation of the measurement results (c.f. Eqs. (7.10)).

The experimental results are shown in Fig. 7.12 a), compared with theoretical calculations from exact diagonalization. For the trial states of most masses  $m$  we apply quantum circuits of depth 4 (10 parameters), and run the optimization routine for 2000 iterations. However, we found that the two points in proximity to the phase transition require an additional entangling layer (amounting to a circuit depth of 5) and about 5000 iterations of the optimization routine to enable convergence of the energies towards the theoretically expected ground state energy. We further measure the second-order Rényi entropy  $S_A^{(2)} = -\log_2 \text{Tr}(\rho_A^2)$  [104] to quantify entanglement across the phase

<sup>62</sup>The weighting factor corresponds to the probability for each trial state to be the closest to the ground state. To estimate this, we perform Monte Carlo sampling of all trial states, based on their measured energies and error bars. The weighting factor is determined by counting how often the energy minimum of all Monte Carlo samples occurs in each trial state distribution.

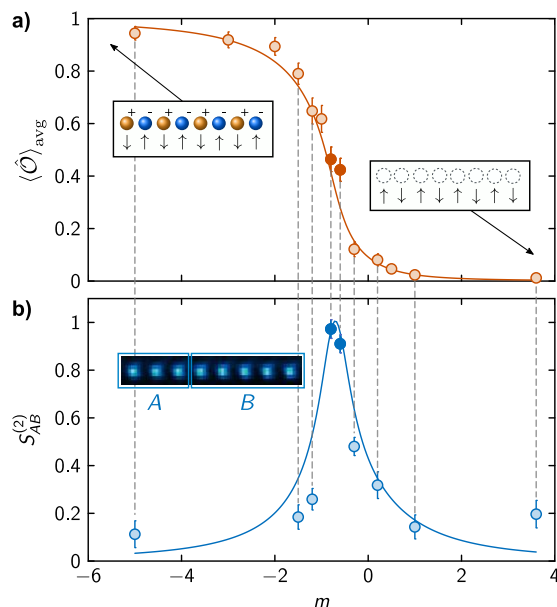


**Figure 7.12.: Quantum phase transition under varying mass  $m$ .** **a)** Order parameter  $\langle \hat{O} \rangle_{\text{avg}}$  as a function of mass. Circles represent experimental data, where each point is derived from all trial states of a full variational optimization run. Light-colored circles are based on a variational quantum circuit of depth 4, while for the dark-colored circles we used a circuit of depth 5. The solid line is a theoretical result from exact diagonalization. The insets visualize the bare vacuum and full filling of the 8-site lattice with electron-positron pairs, for the limits  $m \rightarrow \pm\infty$ , respectively. The critical point occurs at  $m_c \approx -0.7$ . **b)** Second-order Rényi entanglement entropy  $S_{AB}^{(2)}$ , with bipartition  $A$ – $B$  in the inset. Error bars correspond to one standard deviation of  $\langle \hat{O} \rangle_{\text{avg}}$  and  $\text{Tr}(\rho_A^2)$ , respectively.

transition (Fig. 7.12 b)). Here,  $\rho_A$  is the reduced density matrix in the bipartition  $A$ – $B$  shown in the inset. At the critical point we observe an increased entanglement entropy of the variationally prepared ground state. This is in agreement with the additionally required entangling layer in the variational quantum circuit for these points.

### 7.3.5. Algorithmic error bars

Finally, we want to give a quantitative measure for the success of the variational simulation by estimating the error  $\mathcal{E}$  of the approximate ground-state energy  $E(\boldsymbol{\theta}) \equiv \langle \hat{H}_T \rangle_{\boldsymbol{\theta}}$ . For this, we determine the variance of the target Hamiltonian  $\mathcal{E}^2(E, \boldsymbol{\theta}) = \langle (\hat{H}_T - E)^2 \rangle$ . For an exact eigenstate,  $\mathcal{E}^2$  is zero. However, for an approximate wave function  $|\Psi(\boldsymbol{\theta})\rangle$ , as prepared in our VQS, it provides an uncertainty estimate of the energy, according to the bound  $|E_\ell - E(\boldsymbol{\theta})| \leq \mathcal{E}(E(\boldsymbol{\theta}), \boldsymbol{\theta})$ , with  $E_\ell$  the exact eigenstate energy closest to  $E(\boldsymbol{\theta})$ . We define the uncertainty  $\mathcal{E}$  as **algorithmic error** because it includes statistical errors, systematic drifts as well as the errors due to the finite depth of the variational

quantum circuit. Thereby it corresponds to the cumulative uncertainty of the variational quantum algorithm. Comparing  $\mathcal{E}$  to the energy gap  $\Delta_{\text{exp}}$  between the ground state and the first excited state, provides us with a quantitative measure for the quality of the approximate eigenstate and the self-consistency of the quantum simulation.

In the experiment, we perform a full optimization run for the Schwinger ground state with 8 qubits and  $m = 0.1, w = \bar{g} = 1$ . The data is shown in Fig. 7.13 a), where the best approximate ground state (marked with ⑥) has a theoretical overlap of 0.95 with the exact ground state and a corresponding energy of  $E(\boldsymbol{\theta}_{\text{opt}}) = -3.24 \pm 0.36$ . The difference  $E(\boldsymbol{\theta}_{\text{opt}}) - E^{(0)}$  to the exact ground state energy  $E^{(0)}$ , corresponds to  $11\% \pm 18\%$  of the energy gap  $\Delta_{\text{exp}} = 2.11 \pm 0.24$ . The energy gap  $\Delta_{\text{exp}}$  itself is determined experimentally via a quantum subspace expansion strategy (see Appendix M). We then select six trial states, marked by the squares in the optimization curve, for which we measure the variances  $\mathcal{E}^2(E(\boldsymbol{\theta}_{\text{opt}}), \boldsymbol{\theta}) = \langle (\hat{H}_T - E(\boldsymbol{\theta}_{\text{opt}}))^2 \rangle$ . That is, we determine the variance of the target Hamiltonian  $\hat{H}_T$  under each trial state  $|\Psi(\boldsymbol{\theta})\rangle$ , with respect to the best approximate ground state energy  $E(\boldsymbol{\theta}_{\text{opt}})$ . Compared to Eq. (7.10), the term  $\langle \hat{H}_T^2 \rangle$  contains additional observables such as  $\hat{\Lambda}_X^2, \hat{\Lambda}_Y^2, \hat{\Lambda}_Z^2$  as well as the anticommutators  $\{\hat{\Lambda}_Z, \hat{\Lambda}_X\}$  and  $\{\hat{\Lambda}_X, \hat{\Lambda}_Y\}$ , which include three- and four-body correlations. This amounts to total of  $3N = 24$  projective measurements. Fig. 7.13 b) shows the algorithmic error  $\mathcal{E}(E(\boldsymbol{\theta}_{\text{opt}}), \boldsymbol{\theta})$ , in units of the experimental energy gap  $\Delta_{\text{exp}}$ . The graph demonstrates that the variational routine converges to an eigenstate, manifested by the asymptotically decreasing algorithmic error with a value of  $\mathcal{E}/\Delta_{\text{exp}} = 0.64 \pm 0.20$  for the best trial state (marked with ⑥). Finding a state whose algorithmic error  $\mathcal{E}$  is smaller than the energy gap  $\Delta_{\text{exp}}$  to the next excited state proves that the quantum simulator provides self-consistent results. In other words, this is a quantitative self-verification of the quantum simulation.

We investigate the dependence of the algorithmic error  $\mathcal{E}$  on the circuit depth using numerical simulations on a classical computer: Fig. 7.13 c) shows that the lowest achievable algorithmic error decreases, as the circuit depth increases.

## 7.4. Conclusion

This chapter introduced the quantum-classical feedback loop, which builds the basis of variational quantum simulation (VQS), and presented two experimental applications: First, we employed the variational quantum eigensolver algorithm to prepare molecular ground states of  $\text{H}_2$  and  $\text{LiH}$ . We compared different methods for mapping the fermionic Hamiltonian to a system of qubits in a trotterized way and studied molecular

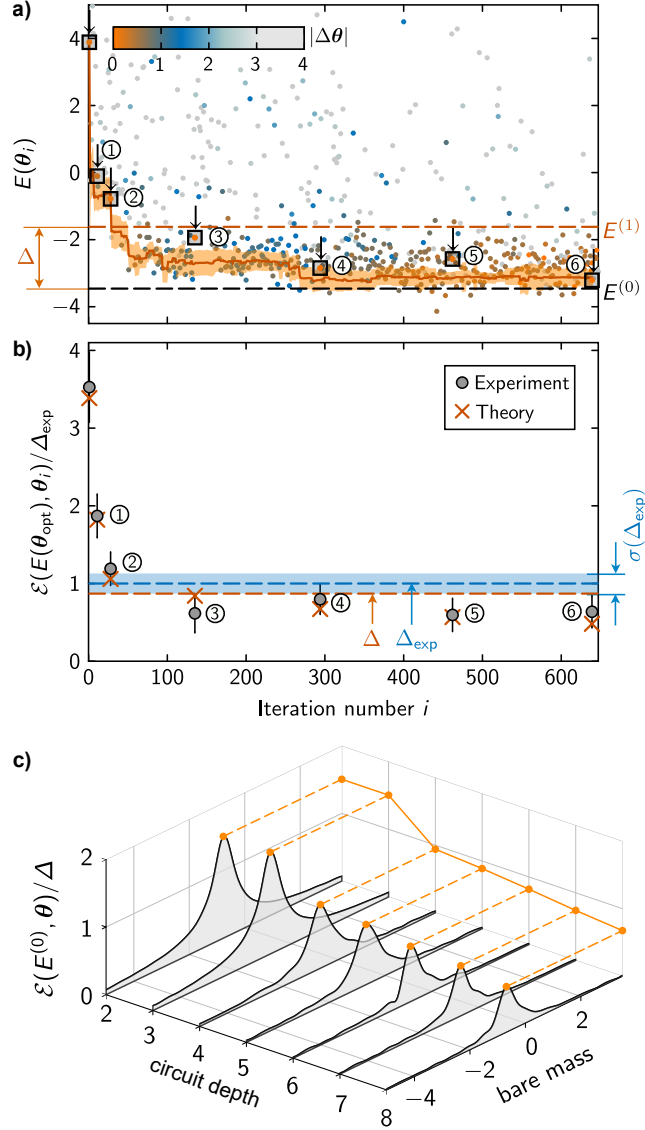


**Figure 7.13.: Algorithmic error bars.** **a)** Optimization trajectory for the 8-qubit Schwinger model with  $m = 0.1, w = \bar{g} = 1$ . The energies  $E(\theta) \equiv \langle \hat{H}_T \rangle_\theta$  of the trial states are plotted as a function of the iterations of the optimization algorithm (c.f. Fig. 7.11). **b)** Algorithmic error  $\mathcal{E}$  in units of the experimentally determined energy gap  $\Delta_{\text{exp}}$  for 6 selected trial states, as indicated by squares in panel a). Crosses show numerical simulation, filled circles are data with statistical error bars. For comparison, the exact energy gap  $\Delta$  and the experimental energy gap with uncertainty  $\sigma(\Delta_{\text{exp}})$ , are indicated. **c)** Numerical simulations of ground state optimization experiments. The algorithmic error is plotted against the circuit depth of the algorithm and complexity of the model (bare mass  $m$ ). The error decreases for increasing circuit depth, and increase in proximity of the critical point (orange dots), where the eigenstates are more entangled, requiring deeper circuits to maintain a high precision.

energy potentials as a function of the internuclear distance. Further we investigated the influence of measurement noise and decoherence. For this trotterized approach of VQS, further work is needed specifically in the mitigation of gate errors and the scalability of the quantum circuits if we are to approach classically intractable calculations.

An alternative approach is presented as the second application in the chapter: This method is based on the heuristic generation of trial states, using unitary operations that are more tailored to the available analog quantum hardware (single-qubit rotations of arbitrary angles around the z-axis, and spin-spin interactions with variable evolution time). This approach forgoes the requirement of realizing the targeted Hamiltonian directly in the laboratory, thus allowing to study a wide variety of previously intractable target models. We demonstrated this in the variational ground state preparation of the lattice Schwinger model, for up to 20 qubits – a task which is out of reach for current analog and digital quantum simulators.

A key challenge for variational quantum simulators is the scaling to larger system sizes, which is limited by the available quantum computing hardware, as well as by a rapid increase in the number of variational parameters. Moreover, the number of measurements needed for the classical computer to successfully navigate the high-dimensional energy landscape, rapidly increases with system size. In this second application, we demonstrated how VQS can be scaled up for lattice models by incorporating intrinsic symmetries of the Hamiltonian into the trial states. Within this project, our collaborators from the theory department developed an advanced global optimization algorithm specifically suited for noisy, high-dimensional and gradient-free problems. Finally, we targeted the long-standing problem of evaluating or verifying the results of the variational quantum simulation. We compared the algorithmic error of the measured ground state energy with the energy gap to the first excited state, proving self-consistency of the quantum simulator. Our approach and techniques apply immediately to a broad class of lattice models in condensed matter and high-energy physics, as well as programmable quantum simulators on other platforms.

The definite determination of the stopping criterion of the optimization algorithm is a challenging open question. Up to now, a typical stopping criterion for optimization algorithms is the comparison against a fixed goal. However, this only translates the problem to how to define this goal, ideally independent of a priori knowledge of the system, and not based on comparisons with classical simulations. The stopping criterion we applied in our second application, is to continue the optimization until an allocated resource budget is exhausted: The algorithm has a finite, total measurement budget that it can spend during the optimization process. It autonomously decides how to

distribute this budget between new unexplored points and refinement re-evaluations on promising points, to reduce the statistical errors. Another criterion involves the evaluation of stationarity: the optimization has converged, if the proposed solution is no longer improving as more points in the cost-function landscape are sampled. The proposed solution could for instance be the minimum of the parameter landscape, as predicted by a metamodel.

## 8. Summary and Outlook

Over the past decade, much research has been directed towards the realization of quantum devices with tens of qubits, in order to show the first practical application in which quantum simulators outperform their classical counterparts. As soon as quantum simulators succeed to solve classically intractable problems, we will be concerned with important tasks: Can we trust the result and how can we verify it? This goes hand in hand with the necessity to develop efficient tools to characterize large quantum systems.

The work presented here, covered five publications in the field of quantum simulation with tens of qubits. It targeted the long-standing problem of verifying quantum simulation results as well as the challenge of many-body state characterization. All discussed experiments were performed with  $^{40}\text{Ca}^+$  ions confined in a linear, macroscopic Paul trap at the IQOQI Innsbruck. The excellent control over all quantum degrees of freedom and the comparably simple mechanism for trapping and manipulating tens of ions, renders them a suitable platform for quantum simulators. The applied quantum circuits focus on arbitrary single-qubit rotations, spin-spin interactions with tunable interaction range and two-, three- and four-qubit MS entangling gates.

In the following, I summarize the content, the results and the conclusions of the individual chapters and close this final chapter with an outlook. After an introductory motivation in Chapter 1, the theoretical framework of quantum information science and the use of trapped  $^{40}\text{Ca}^+$  ions as qubits and pseudospins was discussed. Chapter 3 presented the three variants of quantum simulation and detailed both the theory and experimental tools for the realization of quantum simulation with trapped ions: from the bare laser-atom interaction, over the coupling to the motion of a trapped ion, to laser-induced spin-spin interactions with tunable interaction range. Chapter 4 reported on the technical innovations to the existing setup which allowed Doppler cooling and coherent manipulation of up to 51 qubits, in-sequence intensity stabilization of the addressing and the collective qubit-manipulation path, as well as simultaneous single-ion addressing with automatized calibration. Further, it presented EIT cooling and PG cooling as two efficient methods for sub-Doppler cooling of long ion strings. These

technical advances pave the way to more complex quantum simulations with even longer strings of ions.

The last three chapters focused on the main experimental projects that I carried out during my doctoral research: Chapter 5 reported on a detailed characterization of large complex states in our quantum simulator. The quantum states have been generated from time evolving Néel states under the spin-spin interaction Hamiltonian. We were able to extract genuine multipartite entanglement witnesses, from the small set of measurements for constructing the reduced density matrices of all groups of three neighbouring particles. For some evolution times, entanglement could be witnessed for all groups of up to four neighbouring qubits. The second part of this chapter presented the experimental realization of MPS tomography, a scheme that can accurately estimate many-qubit states of a broad class of quantum systems with an effort that scales at most polynomially with the number of particles. This tomography method is suited for states in which significant quantum correlations only exist over a maximum distance. We applied MPS tomography to successfully reconstruct and verify dynamical states of our quantum simulator towards classically intractable regimes. For the first time, we estimated states comprising up to 14 entangled and individually-controlled spins – a size beyond the practical limits of full quantum state tomography – performing measurements in only 27 bases. Even if the obtained fidelity lower bound was conservative, direct fidelity estimation proved that MPS tomography provided an accurate estimate of the 14-spin quench state. Therefore, this tomography scheme could be applied to obtain a first estimate of a state, and then apply direct fidelity estimation or Renyi entropy measurements for further characterization.

Chapter 6 discussed the transport behaviour of a spin-excitation through a network of interacting qubits. We studied the interplay between coherent transport, disorder and environment-induced noise with 10 qubits. In contrast to previous experiments on quantum transport, our qubits are coupled by a long-range interaction and disorder as well as noise are fully controllable with respect to their amplitude and spectral structure. This allowed us to see a large range of transport phenomena in a single system: we observed effects of Anderson localization in the absence of noise, an increased transport efficiency – known as environment assisted quantum transport (ENAQT) – at intermediate noise levels, and finally suppression of quantum transport under strong noise due to the quantum Zeno effect. We further found that in the regime where ENAQT is most effective the transport is mainly diffusive, displaying coherences only at very short times. The chapter closes with the observation that the spectral structure of non-Markovian dephasing strongly influences quantum transport, with the possibility

---

to reach efficiencies as high as with white noise while maintaining long-lived coherences.

Finally, Chapter 7 presented two experimental applications of variational quantum simulation (VQS). After introducing the quantum-classical feedback loop, which builds the basis of VQS, I discussed the variational preparation of molecular ground states. Using the quantum eigensolver algorithm, we studied molecular energy potentials of  $H_2$  and LiH as a function of the internuclear separation. The observed influence of measurement noise and decoherence revealed that this trotterized approach of VQS needs further work in the mitigation of gate errors and the scalability of the employed quantum circuits. The second part of this chapter focused on an alternative approach, which is based on the heuristic generation of variational trial states, using unitary operations that are more tailored to our analog quantum hardware. This approach forgoes the requirement of realizing the targeted Hamiltonian directly in the experiment, thus allowing to study a wide variety of previously intractable target models. We demonstrated this in the ground state preparation of the lattice Schwinger model, with up to 20 qubits. A key challenge for variational quantum simulators is the scaling to larger system sizes, which is limited by the available quantum computing hardware, as well as by a rapid increase in the number of variational parameters. We demonstrated how VQS can be scaled up for lattice models by incorporating intrinsic symmetries of the Hamiltonian into the trial states. Furthermore, we targeted the long-standing problem of verifying the results produced by the variational quantum simulator. Our approach and techniques apply immediately to a broad class of lattice models in condensed matter and high-energy physics, as well as programmable quantum simulators on other platforms. Another challenging open question is the definite determination of the stopping criterion of the optimization algorithm. The stopping criterion we chose in our second application, is to continue the optimization until an allocated resource budget is exhausted. The algorithm autonomously decided how to distribute this budget between new unexplored points and refinement re-evaluations on promising points, to reduce the statistical errors. Another criterion would involve the evaluation of stationarity: the optimization has converged, if the proposed solution is no longer improving as more points in the cost-function landscape are sampled. The proposed solution could for instance be the minimum of the parameter landscape, as predicted by a metamodel.

The Appendix focuses on the implementation of certain gates in our experiment, on pulse and measurement sequences and other mathematical or experimental tools that have been applied in the projects discussed in this thesis.

Regarding future experiments with long strings of ions, the optical properties of the 729 nm beam, currently used for the global qubit manipulation, has to be improved.

F. Kranzl found that the beam is not propagating perfectly perpendicular to the ion string and the wavefront of the beam has a curvature of tens of millimeters. These properties alter the coupling efficiency depending on the ion position, which compromises the quality of the spin-spin interaction in particular for long ion strings and low axial confinement. Besides that, we would prefer higher beam intensities to increase the spin-spin interaction strength. At the time of writing this thesis, a SolsTis ECD-X system from MSquared was brought into service. This laser system produces 790 nm light which is then frequency-doubled to 395 nm for realizing Raman-gates in our experiment. This will allow us to define the qubit in the Zeeman levels of the ground state, and benefit from largely reduced spontaneous emission. Thanks to the short wavelength of the Raman laser, the Lamb-Dicke factor increases by a factor of two - yielding a factor of four in the spin-spin coupling efficiency. Another factor of two is gained due to the two-photon process of the Raman transition. Details on this setup and related experiments will be discussed in the forthcoming PhD thesis of T. Brydges [60]. A near-future improvement of the setup involves the replacement of the current maintenance-intensive 729 nm system from Coherent, with a high-intensity system from MSquared, which was shown to generate a comparable laser linewidth [58]. Furthermore, the current pulse box, and accordingly the control software, will have to be replaced, because we are at the very limit regarding the number of digital outputs and radio-frequency sources. As a far-future modification, the quantum simulation experiment would largely benefit from a new version of the ion trap, for which the heating rate of the axial COM mode is about two orders of magnitude lower [190] than in our current trap, for which we measure 2000 phonons/s per ion at 130 kHz trapping frequency. This sums up to 100 000 phonons/s for a 50-ion string, extending the qubits' wavepackets beyond the addressing beam within tens of milliseconds after cooling, which in turn results in poor single-qubit gates. Ultimately, the ion loading technique could be upgraded from calcium-oven to ablation target loading. The latter method is already applied in other experiments in our group where it allows for reloading pure calcium ions much faster after a chemical reaction event. This would greatly increase the duty cycle of experiments with long ion strings and be the last step to full automation.

## Acknowledgements

I thank Rainer and Christian (Roos) for the opportunity to carry out my doctoral studies on such a highly developed, successful quantum experiment. Your sense and enthusiasm for the beauty of physics strongly influenced me and my work. I thank you for the patient explanations of the theoretical background to our experiments and that I could concentrate on the bare physics, instead of struggling with politics and finances. I am proud to have been part of distinguished projects based on your brilliant ideas. Moreover, I feel honoured that you allowed me to also pursue experiments of personal interest.

I also want to express gratitude towards the computer administrators, the mechanical and electronic workshop and the administrative personnel in IQOQI and at the university, especially Elisabeth, Klaus, Ad.Dir. Markus R. Knabl and Patricia. Thank you that you free us from technical obstacles and the huge bureaucratic efforts in academia, such that we can fully focus on our research.

Good human relations have always been an important topic for Rainer, inviting us to numerous events outside working life, like our group retreat in Obergurgl or the famous BBQs. In this research group I experienced an amazing working environment, in which I always felt welcome and started every working day with joy. I thank all the experts in electronics, optics, computer science and obviously physics, that supported me with guidance and resources – and I apologize that I don't list everyone by name. However, I want to mention a few outstanding people: Cornelius Hempel, who introduced me to the highly complex interplay in the laboratory and taught me sedateness and patience when facing technical problems. Petar Jurcevic, who filled the days in the laboratory with energy and good ideas. Moreover, I thank the younger PhD students Tiff and Florian as well as our PostDoc Manoj for the exchange of knowledge and the numerous funny moments in the laboratory. I also love to think back to the relaxing breaks full of philosophical discussions about God and the world with Milena, Leni, Dominik, Manoj, Lata, Florian and Tuomas. Finally, I thank everyone else that accompanied me during the last years in Innsbruck and everyone that still holds on our friendship back in South Tyrol. Every single one of you has enriched me scientifically and personally. I am glad to have such amazing friends!

Meinen größten Dank richte ich an meine Familie und Christian (Romen). All die Jahre, die ich in Innsbruck verbracht habe, habt ihr mich bedingungslos unterstützt. Geduldig habt ihr auch meine Aufregung über gelungene Experimente und einige verrückten Aktionen ausgehalten. Wenn es mal nicht so lief wie geplant, fand ich stets ein aufmerksames Ohr und ermunternde Worte. Eure Erziehung und Unterstützung

hat mich zu einem glücklichen, selbstbewussten Menschen gemacht. Dadurch und in dem Wissen, dass ihr als unerschütterliches Fundament immer hinter mir steht, konnte ich die große Herausforderung dieses Doktoratsstudiums meistern.

# A. List of publications

## Publications discussed in this thesis

1. B. P. Lanyon\*, C. Maier\*, M. Holzäpfel, T. Baumgratz, C. Hempel, P. Jurcevic, I. Dhand, A. S. Buyskikh, A. J. Daley, M. Cramer, M. B. Plenio, R. Blatt, C. F. Roos – *Efficient tomography of a quantum many-body system*, Nature Physics **13**, 1158 (2017).
2. C. Hempel\*, C. Maier\*, J. Romero, J. McClean, T. Monz, H. Shen, P. Jurcevic, B. P. Lanyon, P. Love, R. Babbush, A. Aspuru-Guzik, R. Blatt, C. F. Roos – *Quantum Chemistry Calculations on a Trapped-Ion Quantum Simulator*, Phys. Rev. X **8**, 031022 (2018).
3. N. Friis, O. Marty, C. Maier, C. Hempel, M. Holzäpfel, P. Jurcevic, M. B. Plenio, M. Huber, C. F. Roos, R. Blatt, B. P. Lanyon – *Observation of Entangled States of a Fully Controlled 20-Qubit System*, Phys. Rev. X **8**, 021012 (2018).
4. C. Maier, T. Brydges, P. Jurcevic, N. Trautmann, C. Hempel, B. P. Lanyon, P. Hauke, R. Blatt, C. F. Roos – *Environment-Assisted Quantum Transport in a 10-qubit Network*, Phys. Rev. Lett. **122**, 050501 (2019).
5. C. Kokail\*, C. Maier\*, R. van Bijnen\*, T. Brydges, M. K. Joshi, P. Jurcevic, C. A. Muschik, P. Silvi, R. Blatt, C. F. Roos, P. Zoller – *Self-verifying variational quantum simulation of lattice models*, Nature **569**, 355 (2019)
6. M. K. Joshi, A. Fabre, C. Maier, T. Brydges, D. Kiesenhofer, H. Hainzer, R. Blatt and C. F. Roos – *Polarization-gradient cooling of 1D and 2D ion Coulomb crystals*, New J. Phys. **22**, 103013 (2020).

## Further publications

7. P. Jurcevic, P. Hauke, C. Maier, C. Hempel, B. P. Lanyon, R. Blatt, C. F. Roos – *Spectroscopy of Interacting Quasiparticles in Trapped Ions*, Phys. Rev. Lett. **115**, 100501 (2015).
8. R. Lechner, C. Maier, C. Hempel, P. Jurcevic, B. P. Lanyon, T. Monz, M. Brownnutt, R. Blatt, C. F. Roos – *Electromagnetically-induced-transparency ground-state cooling of long ion strings*, Phys. Rev. A **93**, 053401 (2016).
9. P. Jurcevic, H. Shen, P. Hauke, C. Maier, T. Brydges, C. Hempel, B. P. Lanyon, M. Heyl, R. Blatt, C. F. Roos – *Direct Observation of Dynamical Quantum Phase Transitions in an Interacting Many-Body System*, Phys. Rev. Lett. **119**, 080501 (2017).
10. G. Higgins, W. Li, F. Pokorny, C. Zhang, F. Kress, C. Maier, J. Haag, Q. Bodart, I. Lesanovsky, M. Hennrich – *Single Strontium Rydberg Ion Confined in a Paul Trap*, Phys. Rev. X **7**, 021038 (2017).
11. T. Brydges\*, A. Elben\*, P. Jurcevic, B. Vermersch, C. Maier, B. P. Lanyon, P. Zoller, R. Blatt, C. F. Roos – *Probing Rényi entanglement entropy via randomized measurements*, Science **364**, 260 (2019).
12. A. Elben, P. Jurcevic, B. Vermersch, R. van Bijnen, C. Kokail, T. Brydges, C. Maier, M. K. Joshi, R. Blatt, C. F. Roos, P. Zoller – *Cross-Platform Verification of Intermediate Scale Quantum Devices*, Phys. Rev. Lett. **124**, 010504 (2020).
13. M. K. Joshi, A. Elben, B. Vermersch, T. Brydges, C. Maier, P. Zoller, R. Blatt and C. F. Roos – *Quantum Information Scrambling in a Trapped-Ion Quantum Simulator with Tunable Range Interactions*, Phys. Rev. Lett. **124**, 240505 (2020).

## B. Experimental implementation of MS gates

### B.1. Implementation of full Mølmer-Sørensen gates

The following chapter contains a tutorial-style documentation of how to implement a fully entangling Mølmer-Sørensen gate, specifically in our experiment:

1. **Check the power balancing of the bichromatic light field components:**

This step should only be necessary in case of changes in the RF power connections. The fiber AOM should ensure the optical balance of the bichromat frequency components. The QFP script: *balance\_bichr.qsc* shifts the components of the bichromatic beam on resonance one at a time, via the double-pass AOM frequency, and measures the coupling strength in terms of a pi-time. Using the “free Rabi fit” (in our QFP Analysis tool), you can quickly analyze the Rabi flops (a “free Rabi fit” is necessary, because the minimal pulse length is not zero, due to Blackman pulse shaping). Adjust the RF power of MAC 1 or 2 (indicated by (a) in Fig. B.1), in order to obtain similar pi-times, e.g. pi-times of (6.18, 6.14)  $\mu s$  indicates power balanced components.

2. **Accurate determination of axial COM frequency:** Scan the bichromat frequencies around the approximate COM frequency to get the precise value for the corresponding bichromat RF power, as it is then used for the gate. The applied sequence is the following: first bichromat pulse with phase 0 followed by a second bichromat pulse with phase  $\pi$ . Scan the bichromat frequencies (*MAC1&2 frequency* variable, see Fig. B.1 label b)) with high resolution. The FWHM of the dip is about 1 kHz, for a bichromat pulse length of about half the entangling gate time. You will find a dip where the frequencies are resonant with the COM frequency. The obtained value is then copied into the *SB* panel in the *Bichromat controls* tab of QFP (Fig. B.1 label c)).

3. **Determining the bichromat detuning:** We choose the bichromat detuning  $\Delta$  based on the equation in Refs. [27, 93]:  $\Delta = \Omega'2 \frac{1}{\sqrt{N}} \eta$ , where N is the number

of ions and  $\eta$  is the Lamb-Dicke factor of a single ion. The QFP tab *Bichromat* offers a calculator (Fig. B.1 label d)) to compute the required detuning  $\Delta$  and corresponding gate time  $t_{\text{gate}}$  from the parameters: Pi-time of the bichromat, number of ions, COM frequency (e.g. 1.35 MHz) and angle of incidence of the bichromatic beam (e.g.  $0^\circ$  for the beam coming through the tip electrodes). For the example of this tutorial, I calculate the desired detuning to be  $\Delta = (2\pi) 9.6$  kHz, which corresponds to a gate time of  $t_{\text{gate}} = 2\pi/\Delta = 104 \mu\text{s}$ . In this time, the first circle in phase space is closed. Note that the coupling strength in the equation above is given by  $\Omega' = (2\pi) 81.4$  kHz (i.e. “Boulder notation”,  $\Omega_B = 1/(4 \cdot \text{pi-time}) = (2\pi) 40.7$  kHz vs. our usual “Innsbruck notation”,  $\Omega' = 1/(2 \cdot \text{pi-time}) = (2\pi) 81.4$  kHz). After inserting the calculated detuning into the *Bichromat controls* panel, Fig. B.1 label e), a first scan of the bichromatic pulse length yields the measurements in Fig. B.2 a). We want to observe the probability to find no population of the D state  $p(2)$ , a single ion populating the D state  $p(1)$  and both ions populating the D state  $p(0)$ .

4. **Determining the gate time:** The gate time can be determined more accurately by scanning the pulse-length of the bichromatic pulse, using two gates in a row and finding the point where all population is in the S state again ( $p(2)$  is maximum).
5. **Fine tuning of the coupling strength:** Next, we want to ensure that the crossing point of  $p(0)$  and  $p(2)$ , (i.e. the superposition of both ions in S and both ions in D), occurs at the time when the circle in phase space closes ( $p(1)$  minimum). For this, we scan the overall RF power of the bichromatic beam, which corresponds to scanning the power of the bichromat transitions object. Therefore, it is advisable to set the power to, say -1 dB to start with, to allow for some leeway in terms of the overall power.
6. **Compensating AC-Stark shifts:** Finally, we need to compensate for the AC-Stark shift, induced by the bichromatic light field. With a pulse length corresponding to the gate time  $t_{\text{gate}}$ , we either use power imbalancing of the bichromat components or center line detuning. In the first case we imbalance the RF powers send to the bichromat AOM (e.g. keeping MAC1 fixed and scanning the MAC2 power, and then the other way around). In the latter case, the frequency shift of the bichromat transition object in QFP is scanned around 0 Hz. The scanning variable is called *bic\_shift* (typically referred to as “center line detuning”) and shown in Fig. B.1 label f). Optimum AC-Stark shift compensation is achieved at the minimum of the  $p(1)$  population. Also in this case, it is more precise to

connect two gates in series, and maximize the  $p(2)$  population instead. The final result is shown in Fig. B.2 b).

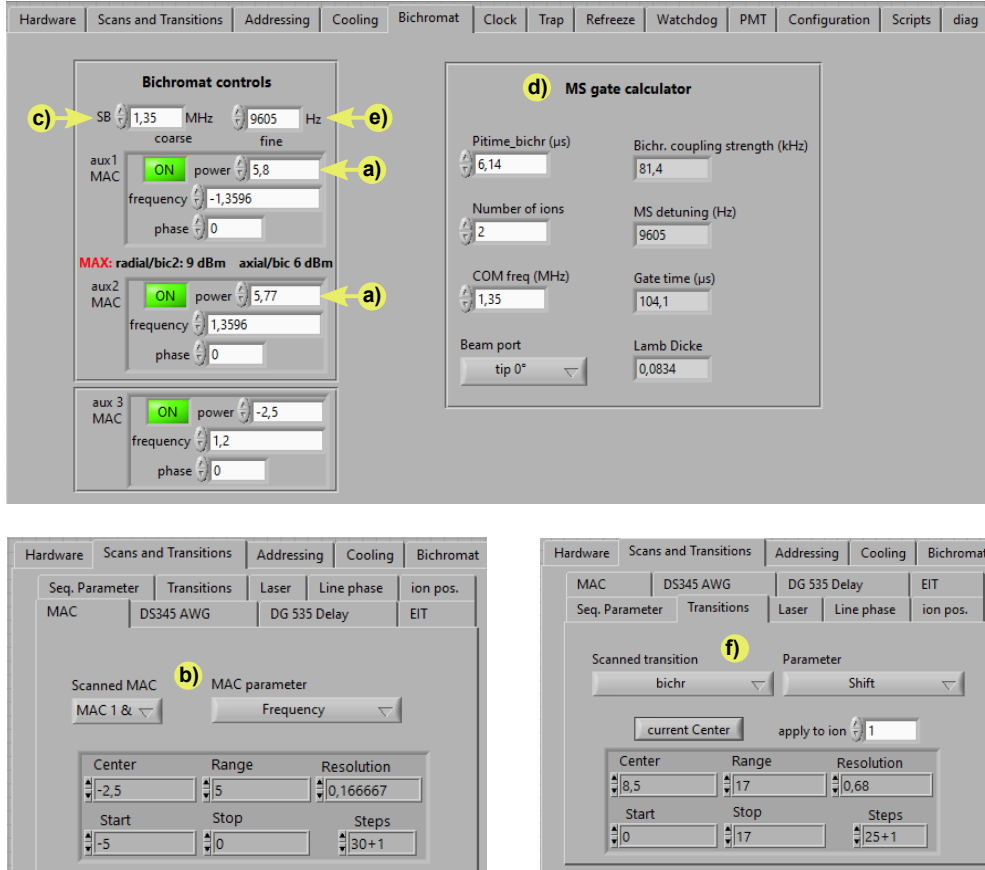


**Figure B.1.:** Most important tabs and fields in QFP, for implementing a Mølmer-Sørensen entangling gate.

## B.2. Determining the gate fidelity

The implementation of entangling gates for more ions does not differ from the two-ion case, although the analysis of the population behaviour is different. Fig. B.3 shows the evolution of population probabilities during the implementation of an MS gate for three and four qubits.

**Gate fidelity for even ion numbers:** For even numbers of ions, the MS gate generates a GHZ state at the gate time  $t_{\text{gate}}$ . In this case, we can infer the state fidelity right away by measuring (i) the population probabilities, averaged over many ( $>1000$ ) experimental repetitions (Fig. B.2 c)) and (ii) the parity contrast, which is related to

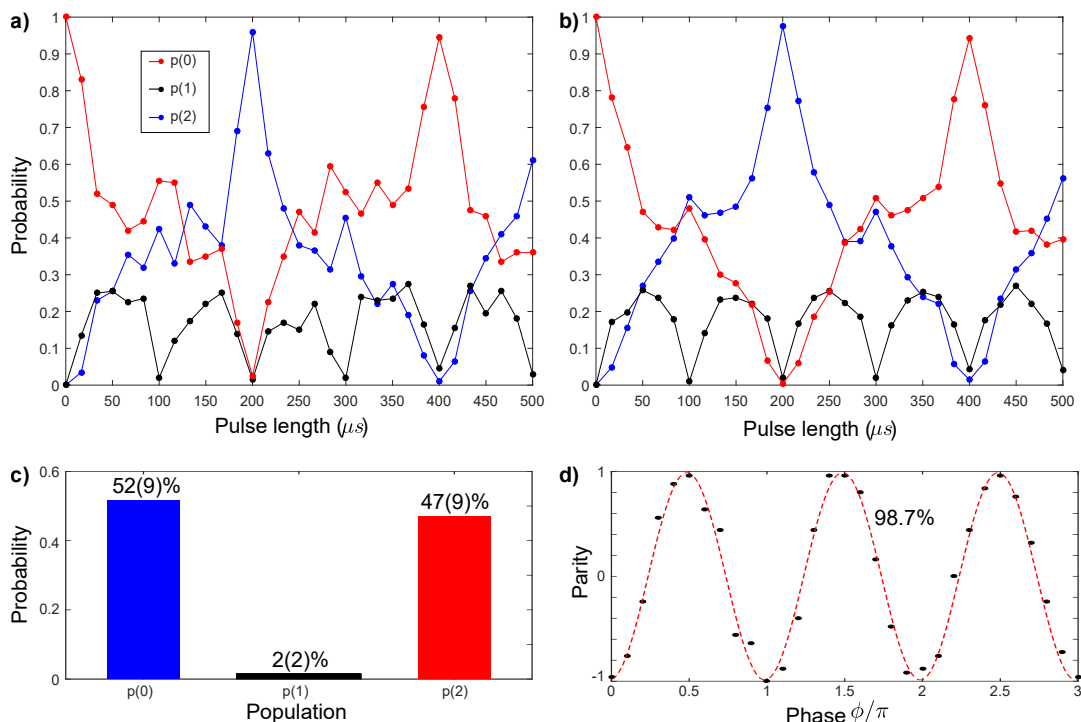


**Figure B.2.: Implementation and analysis of a 2-ion Mølmer-Sørensen gate.** a)-b) Steps during the setup, as described in the main text. Connected circles denote the probabilities of measuring no population of the D state ( $p(0)$ , red), one of the two ions populating the D state ( $p(1)$ , black) and both ions populating the D state ( $p(2)$ , blue). c) Population probabilities, averaged over 1500 experimental repetitions. d) Parity flops with a contrast of 98.7%.

the coherence of the GHZ state. It is evaluated by adding a  $\pi/2$  carrier pulse with variable phase  $\phi$ , after the MS gate and then measuring the contrast  $C$  of the parity flops (Fig B.2 d):

```
rf_729(1,bic_length,0*math.pi,"bichr")
rf_729(1,0.5,phase*math.pi,"carrier")
```

The finally obtained GHZ state fidelity is given by  $\mathcal{F} = (p(0) + p(2) + C)/2 \approx 99\%$ .

**Gate fidelity for odd ion numbers:** In the case of an odd number of ions we need to add a  $\pi/2$  carrier pulse right after the entangling gate, in order to generate a GHZ state and infer a gate fidelity. Note that you have to calibrate the carrier phase with respect to the bichromat beforehand. This can be done by implementing the pulse sequence

```
rf_729(1,0.5,-0.5*math.pi,"carrier")
rf_729(1,bic_length,bic_phase*math.pi,"bichr")
rf_729(1,0.5,0.5*math.pi,"carrier")
```

in which first a  $\sigma_x$  eigenstate is created and then the *bic\_phase* adjusted such that the bichromatic light field has no effect and the second rotation around +Y axis brings the population back to the ground state.

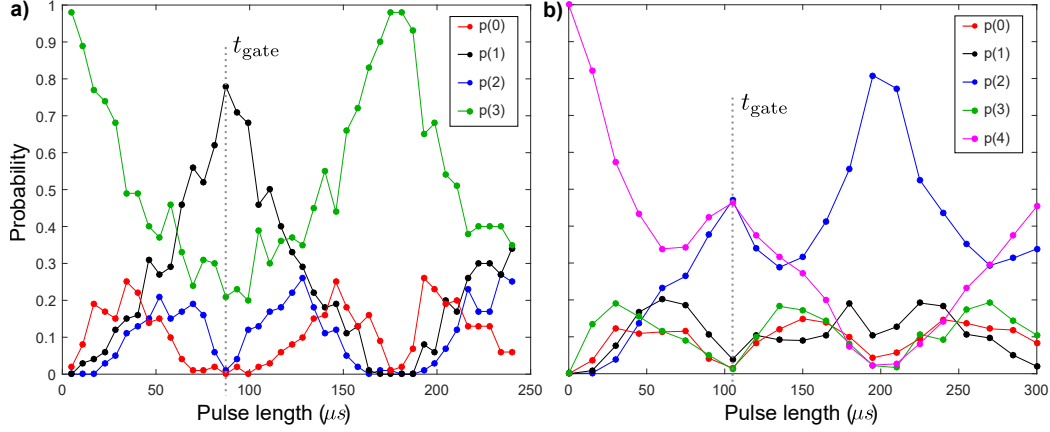


**Figure B.3.:** Temporal evolution of the population probabilities during an MS gate for three (a) and four (b) qubits. Population  $p(0)$  denotes the state where all ions are in S, while the highest population  $p(3)$  (or  $p(4)$ ) describe the state with all ions in the excited state D. The gate times are highlighted by dotted lines.

### B.3. Implementation of half-entangling gates on three ions

Steps 1-3 of the fully entangling gate (Section B.1) are the same: we measure the coupling strength of the bichromatic beam, determine the corresponding COM mode frequency, and use the gate calculator to estimate a detuning  $\Delta$  and gate time  $T$ . Using these values an MS gate occurs and accordingly the first circle in phase space closes, at time  $T = 2\pi/\Delta$ . Like for the implementation of fully entangling gates, we want to optimize gate time, overall power and center-line detuning of the bichromat: instead of using two fully entangling gates in a row and maximizing the population in S, you should use four half-entangling gates.

**Theoretical method:** Let us consider that we double the detuning  $\Delta' = 2\Delta$ , and at the same time we increase the coupling strength of the bichromat by  $\Omega' = \sqrt{2}\Omega$  (corresponding to raising the laser intensity by a factor of 2). At time  $T$ , the acquired geometric phase  $\Phi(T) \sim \frac{(\eta\Omega)(\eta\Omega)}{\Delta} \cdot T$  equals twice the phase at time  $T' = 2\pi/\Delta' = T/2 \Rightarrow \Phi(T') = \frac{1}{2} \cdot \Phi(T)$ , meaning that the circle in phase space has closed *twice* (see Fig. B.4) and we have a half-entangling gate at time  $T/2$ .

**Experimental realization:** In our experiment, increasing the power of the bichromat (and thereby  $\Omega$ ) by a given precise factor is not so easy. Alternatively, we can

keep  $\Omega$  constant and simply increase the detuning by  $\Delta' = \sqrt{2}\Delta$ . With this, also the gate time  $T$  changes and has to be remeasured. The right settings are found when the maximum of population  $p(1)$  coincides with the (second) minimum of  $p(0)$  and  $p(2)$  at the new gate time.

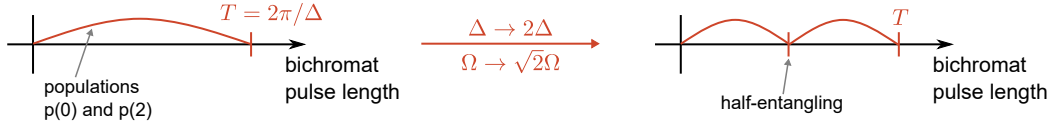


**Figure B.4.:** Relation between the parameters of a fully- and a half-entangling gate.

## C. Composite pulse sequences for single-qubit rotations

The following Mathematica simulations compare fidelity of the single-qubit flips for single-qubit addressing with a normal AC-addressing pulse sequence (Listing C.1) and with composite pulse sequence (Listing C.2). It shows that a 15% error in the Rabi frequency of the global pulses has a smaller impact to single-qubit flips when using composite pulse sequences, such that the fidelity increases from  $\sim 95\%$  to  $\sim 99.7\%$

Listing C.1: Single-qubit rotations without composite pulse

```
(* define rotation angle of the first global pulse *)
T = Pi/2;
(* include 15 percent rotation angle error *)
T = T*(1 - 0.15);
(* define phase of the first global pulse *)
Phi0 = 0;
(* define unitary of the first global pulse *)
Ux0 = ( {
  {Cos[T/2], -I*Exp[-I*Phi0]*Sin[T/2]},
  {-I*Exp[I*Phi0]*Sin[T/2], Cos[T/2]}
} );

(* define rotation angle of the single-qubit addressed pulse *)
P = Pi;
(* define unitary of the single-qubit addressed pulse *)
Uz = ( {
  {Exp[-I*P/2], 0},
  {0, Exp[I*P/2]}
} );

(* define the phase of the second global pulse *)
Phi1 = Pi;
(* define unitary of the second global pulse *)
Ux1 = ( {
  {Cos[T/2], -I*Exp[-I*Phi1]*Sin[T/2]},
  {-I*Exp[I*Phi1]*Sin[T/2], Cos[T/2]}
} );

(* define initial state *)
p0 = ({{0}, {1}});
```

```
(* apply all three unitaries sequentially to the initial state *)
p2 = Ux1.Uz.Ux0.p0;
(* calculate fidelity / overlap with a perfect qubit flip *)
Norm[{1, 0}.p2]^2

0.945503
```

### Listing C.2: Single-qubit rotations with composite pulse

```
(* define pulse parameters *)
T = Pi/2;
T = T*( 1 - 0.15);
Phi0 = 0;
Phi1 = Pi;
P = Pi;
p0 = ({{0},{1}});

(* unitaries of the composite pulse sequence, applied sequentially to initial
state *)
c0 = ( {
  {Cos[T/2], -I*Exp[-I*Phi0]*Sin[T/2]},
  {-I*Exp[I*Phi0]*Sin[T/2], Cos[T/2]}
} ).p0;
c1 = ( {
  {Cos[T/2], -I*Exp[-I*Pi/2]*Sin[T/2]},
  {-I*Exp[I*Pi/2]*Sin[T/2], Cos[T/2]}
} ).c0;
c2 = ( {
  {Exp[-I*P/2], 0},
  {0, Exp[I*P/2]}
} ).c1;
c3 = ( {
  {Cos[T/2], -I*Exp[-I*3*Pi/2]*Sin[T/2]},
  {-I*Exp[+I*3*Pi/2]*Sin[T/2], Cos[T/2]}
} ).c2;
c4 = ( {
  {Cos[T/2], -I*Exp[-I*Phi1]*Sin[T/2]},
  {-I*Exp[I*Phi1]*Sin[T/2], Cos[T/2]}
} ).c3;
(* calculate fidelity / overlap with a perfect qubit flip *)
Norm[{1, 0}.c4]^2

0.99703
```

## D. Tutorial for simultaneous single-ion addressing with an AWG

In the following I explain the four most important considerations and programs for performing simultaneous single-ion addressing. An arbitrary waveform generator (AWG) is used to generate a waveform with multiple frequency components

$$y = \sum_{i=1}^N A_i \cdot \sin(\omega_i^{RF} \cdot t) \quad (\text{D.1})$$

This waveform is sent to the AOD and generates multiple laser beams, each targeting a different ion and shifted by 60 – 90MHz with respect to the qubit transition. The RF amplitude  $A_i$  for each beam can be regulated independently, resulting in individually adjustable AC-Stark shifts on all ions simultaneously, reaching up to a few kHz.

1. **Identify the radio frequencies**  $\omega_i^{RF}$  related to the deflection angle to target the individual ions  $i$ , using pulse box DDS2 as RF source.
2. **Calibrate the inhomogeneity**<sup>63</sup> **in the intensity profile** over the  $N$ -ion string. This should be done once for each experimental condition (e.g. number of ions and trapping parameters) and can then be used for all associated measurements. In this step, the list of radio frequencies  $\omega_i^{RF}$  is handed over to the AWG, which produces a waveform with  $N$  frequencies and plays it in a *continuous loop*. The python script to do this is called `i0_AC_shift_calibration.py`. The waveform is then applied to the ions, e.g. using the following command in a QFP sequence:

```
rf_729(1,0.5,0*math.pi,"carrier") % global pi/2 pulse, phase=0
ttl_set("ionshuttle2",1) % sets TTL 11 to high voltage
seq_wait(wait_time)
ttl_set("ionshuttle2",0) % sets TTL 11 to low voltage
rf_729(1,0.5,1*math.pi,"carrier") % global pi/2 pulse, phase=pi
```

<sup>63</sup>The inhomogeneous intensity profile is mainly caused by clipping of the largely expanded addressing beam on the focusing optics.

This laser pulse sequence applies the corresponding component of the AWG-waveform to each of the  $N$  ions for the length of the variable *wait\_time*, resulting in individual AC-Stark Rabi flops on all ions simultaneously. Due to the inhomogeneous intensity profile, all ions have different pi-times, as shown in Fig. D.1 a). The Rabi flops are analyzed using the *Addressing error* fit function in our analysis software. This provides us with a line containing the pi-time for the individual ions.

In the following these pi-time differences “calibrated out” with an according correction factor for each RF amplitude  $A_i$  in Eq. (D.1). With this, we can then apply arbitrary AC-Stark shift patterns, e.g. we can homogenize the Rabi frequencies as shown in Fig. D.1 b).

3. **Convert an array of desired AC-Stark shifts into a calibrated RF waveform.** The python program used to generate arbitrary RF waveforms is called `i2_precalculate_waveforms.py`. It accepts simple matlab arrays, where the ion number  $N$  defines the number of columns. The optional rows correspond to time segments, required in the case of temporally varying waveforms, such that the number of rows corresponds to the number of AC-Stark shift changes in a waveform. The matlab script `i1_calc_dynamic_AC_shifts.m` gives an example of how to generate such a matlab array. In here, the variable *rabi\_ratio* calibrates the Rabi frequencies, as described at the end of step 2. Further, the matlab program takes into account that the laser intensity (and with it the desired AC-Stark shift strength or the single-qubit Rabi frequency) is not linear in the RF-amplitude which is applied to the AOD. We empirically observe the following relation<sup>64</sup>:  $A_i = 21.53 \cdot x^{-0.535}$ , where  $A_i$  is the RF amplitude required to obtain a AC-Stark pi-time  $x_i$ . In addition to the matlab array of RF amplitudes, the program `i2_precalculate_waveforms.py` asks for the *pulse length* of the time segments, so how long each arrangement of AC-Stark shifts is played. Note that each time segment should be played for at least  $10 \mu\text{s}$ , because we want to distinguish waves within 100 kHz frequency difference, which can be discriminated only after a runtime of at least  $10 \mu\text{s}$ . For static waveforms one can simply use  $100 \mu\text{s}$ , and select the appropriate trigger option (see item 4). Moreover, a wave should have at least 10 sample points during one oscillation period. For waves with frequencies between 50 – 100MHz, this is fulfilled at a temporal resolution of

<sup>64</sup>Note that this relation does depend on the employed AOD and the coupling of the laser beam to it. The relation has to be retaken for the new AOD system, built by L. Perenthaler for enabling 50-qubit addressing.

1 ns, or in other words 1 GS/s. Finally, the python program automatically dumps redundant laser power, not required on the ions, in an additional 50 MHz component, with an amplitude of  $x = 1 - \sum_{i=1}^N A_i/N$ , as given in the code lines 55–56. The empirically determined factor  $y = 0.01 \cdot x^3 - 0.0828 \cdot x^2 + 0.3752 \cdot x + 0.0405$  corrects for the non-linear relation between intensity and RF amplitude for this 50 MHz component.

For long waveforms (several tens of ms) the python program can take several minutes to produce the desired waveform. Therefore it is nice to outsource this task to a separate computer, while running the experiment. This script saves the waveform in the “.npz” format under the specified name.

4. **Set the desired trigger option and run the experiment.** The final script one needs to run during an experiment is called `i3_generate_AC_shifts.py`. It reads in the .npz file which was created in step 3 and defines how to trigger/gate the AWG output. For static AC-Stark shifts, we use the *gated* trigger. Waveforms for static AC-Stark shifts consist of a single time segment of typically 100  $\mu$ s. The gated trigger will continuously replay the waveform during the high voltage period of TTL 11. For temporally modulated AC-Stark shifts, we use the *single-start* trigger, which plays a waveform once, after a single trigger event from TTL 11. Those waveforms consist of many time segments, of typically 10  $\mu$ s each. One also need to hand over the .mat file with the RF amplitudes (generated in step 3) because from this file the AWG extracts how long the entire waveform sequence should be. Finally, the AWG is included into an experimental sequence by calling the command:

```
t11_set("ionshuttle2",1) % sets TTL 11 to high voltage
% the part of your sequence during which the AWG should be on
t11_set("ionshuttle2",0) % sets TTL 11 to low voltage
```

Fig. D.1 c) shows the cross-talk between neighbouring ions, when driving AC-Stark Rabi flops on every second ion in a 10-ion string. The associated addressing error  $\epsilon = \Omega_{i\pm 1}/\Omega_i$  is given by the ratio of the Rabi frequencies  $\Omega_i$  of the considered ions, and lies below 1%.

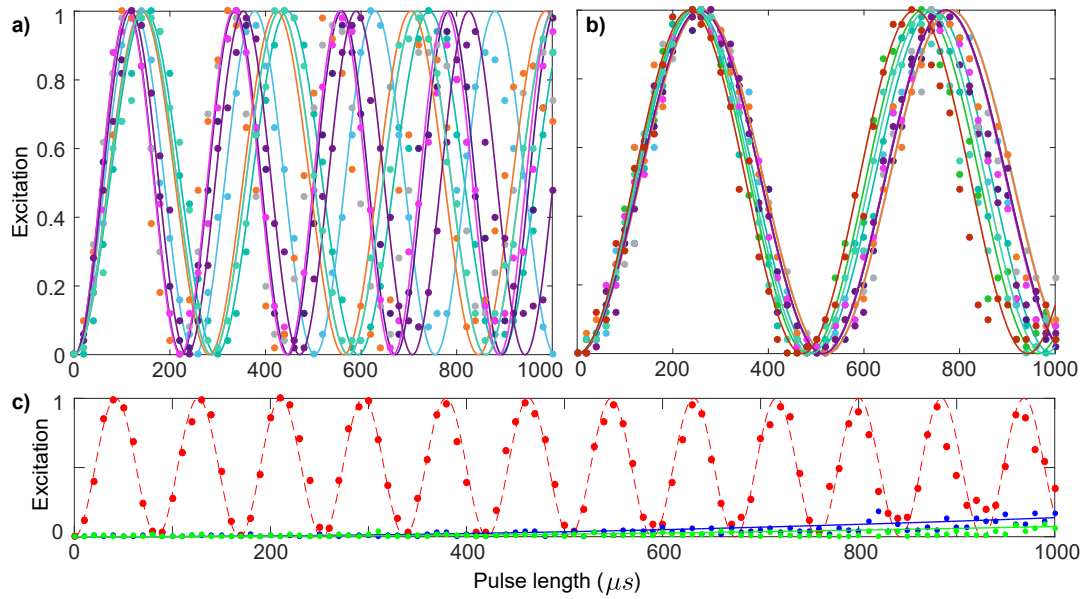


**Figure D.1.: Addressed AC-Stark Rabi flops using the AWG.** **a)** Simultaneous addressed Rabi flops on a 10-ion string. The inhomogeneous intensity profile over the ion string causes a multiplicity of Rabi frequencies. **b)** Example of equalized Rabi frequencies after calibration (step 2 above). Here, the collective Rabi frequency was chosen to be 60% of the lowest frequency measured in a). **c)** Addressing error associated with cross-talk for a 10-ion string, trapped at  $\omega_z = (2\pi) 217 \text{ kHz}$  axial frequency. Every second ion in string is addressed, but only ion 4 (blue), 5 (red) and 6 (green) are shown, for simplicity.

## E. Automatized addressing calibration

Listing E.1 shows an example of a qsc-script that automatically interlaces measurements by a clock-measurement every 2-3 minutes, and a calibration of the individual ion pi-times every 10 minutes. The corresponding functions are defined in the “Script manager.vi” in QFP. Lines 3-5 load the pulse-sequence python file and scan the experimental parameter “meas\_type” from 0 to 2. After four experiment scans, the clock-measurements are performed, corresponding to commands 9-24. This process is repeated nine times, such that after  $9 \cdot 4$  measurements, the addressing calibration takes place. The ion position is measured by the camera in lines 28-34, and corrected in line 35. The commands 43-50 finally scan a multiplication factor, named “AOD\_frequency”, for each ion’s addressing pi-time, fit it a Gaussian function via the command “fitlastscan()”, and update the individual ion pi-times automatically via “get\_single.ion\_AOD\_position()”. The updating is only performed for fit results with an amplitude  $> 0.35$ , a FWHM  $> 0.45$  and a resulting pi-time multiplication factor between 0.65 and 1.45. With this we avoid feedback of faulty fits, caused e.g. by statistical fluctuations.

Listing E.1: Example for a qsc-script with automatized calibration

```
1 for clock_run 1 9 1
2   for variational_step 1 4 1
3     LoadSequence ..\measurements\Experiments\2018_Variational\20
         IonOptimisation\CurrentSequence.py
4     SetLocalPar SuppressDisplay 0
5     scan Seq.Floats.meas_type,0,2,2, save=yes, queue=last, rnd=no, exp=1
6     Pause
7   endfor
8   %%%%%%%%%%%%%%%%%%%%%%%%%%%%%%%%%%%%%%%%%%%%%%%%%%%%%%%%%%%%%%%%%%%%%%%%%
9   LoadSequence protected\clock_measurement.py
10  GetPhysPar RamseyTime gl.rt
11  GetPhysPar B gl.B
12  GetPhysPar Bfet gl.Bfet
13  GetPhysPar f_0 gl.f_0
14  GetPhysPar f_c gl.f_c
15
16  SetLocalPar SuppressDisplay 1
17  SetLocalPar Cycles 100
```

```
18   SetLocalPar Seq.Floats.ramsey_time gl.rt
19   SetLocalPar Seq.Floats.pulse_length 0.5
20   SetVariable (dummy) cam_for_clock_off()
21
22   scan Seq.Floats.meas_type,1,4,3,save=temp,queue=first
23   SetVariable (gl.r11,gl.r12,gl.r21,gl.r22) MeanExcitation()
24   SetVariable (status) ClockEvaluation()
25   Pause
26 endfor
27 %%%%%%%%%%%%%%%%%%%%%%%%%%%%%%%%%%%%%%%%%%%%%%%%%%%%%%%%%%%%%%%%%%%%%%%%%%
28 SetLocalPar SuppressDisplay 1
29 SetVariable (dummy) camera_off()
30 LoadSequence protected\refpic_on.py
31 SetVariable (dummy) camdata_off()
32 SetVariable (dummy) CamComm_ref_full_data()
33 scan Seq.Floats.det_time,5000,5001,1,save=temp,queue=first
34 SetVariable (dummy) GetIonPositionShift()
35 SetVariable (dummy) CorrectPositionShift()
36 SetVariable (dummy) CamComm_ref_full_bg()
37
38 scan Seq.Floats.det_time,5000,5001,1,save=temp,queue=first
39 SetVariable (dummy) camdata_on()
40 SetVariable (dummy) camera_on()
41 Pause
42
43 SetLocalPar Cycles 50
44 LoadSequence 2018_variational\Calibrate_SIA.py
45 SetLocalPar SuppressDisplay 0
46 scanforfit Seq.Floats.AOD_frequency, 0.55,1.45,20,save=yes,queue=first,exp=1
47 SetVariable (dummy) fitlastscan()
48 SetVariable (dummy) get_single_ion_AOD_position()
49 SetLocalPar Transitions
50 SetGlobalPar Transitions
51 Pause
```

## F. Implementation of Rapid Adiabatic Passage

Rapid Adiabatic Passage (RAP) can e.g. be used to determine the mean phonon number of a particular motional mode of an ion crystal, to prepare Fock states and to generate Dicke states. A detailed discussion on the theoretical background and achieved experimental results is given in Ref. [107]. Here, I want to shortly summarize the idea and describe the required tools for implementing RAP in our experiment.

The method uses a frequency-chirped and intensity-shaped laser pulse, to adiabatically transfer the population from one state  $\psi_1$  to another state  $\psi_2$ , without remaining population in intermediate states. The laser properties is changed slow enough that the system can follow an evolving wave function *adiabatically*. *Rapid* refers to the fact that the time scales of the property change are small compared to the timescales defining the system (i.e. radiative lifetime and coherence time). Lets consider a two-level system with levels  $\psi_1$ ,  $\psi_2$ , interacting coherently with a laser pulse of detuning  $\Delta$  and Rabi frequency  $\Omega$ . In the rotating wave approximation such a system is described by the Hamiltonian

$$H(t) = \hbar \begin{pmatrix} 0 & \frac{1}{2}\Omega(t) \\ \frac{1}{2}\Omega(t) & \Delta(t) \end{pmatrix}.$$

The two eigenstates (in the rotating frame) are given by

$$\begin{aligned} \Phi_+(t) &= \psi_1 \sin[\Theta(t)] + \psi_2 \cos[\Theta(t)] \\ \Phi_-(t) &= \psi_1 \cos[\Theta(t)] - \psi_2 \sin[\Theta(t)] \end{aligned}$$

with the angle  $\Theta(t) = \frac{1}{2} \arctan[\Omega(t)/\Delta(t)]$  and associated eigenenergies  $\epsilon_{\pm}(t) = \frac{1}{2}[\Delta(t) \pm \sqrt{\Delta^2(t) + \Omega^2(t)}]$ . As depicted in Fig. F.1 a)-b), we can adiabatically evolve an eigenstate such that it undergoes a transition from one level to the other

$$\begin{aligned} \psi_1 &\longrightarrow \Phi_+(t) \longrightarrow \psi_2 \\ -\psi_1 &\longrightarrow \Phi_-(t) \longrightarrow \psi_1 \end{aligned}$$

where the passage is adiabatic if

$$\begin{aligned} |\langle \dot{\Phi}_+ | \Phi_- \rangle| &\ll |\epsilon_+ - \epsilon_-| \\ \Rightarrow \frac{1}{2} |\dot{\Omega}\Delta - \Omega\dot{\Delta}| &\ll (\Omega^2 + \Delta^2)^{3/2}. \end{aligned}$$

This condition can be achieved, using a smooth laser pulse with large Rabi frequency  $\Omega$  and/or large detuning  $\Delta$ . In other words, a long laser pulse with a frequency chirp across the resonance transition  $\psi_1 \leftrightarrow \psi_2$ , and a shaped intensity (Fig. F.1 c)).

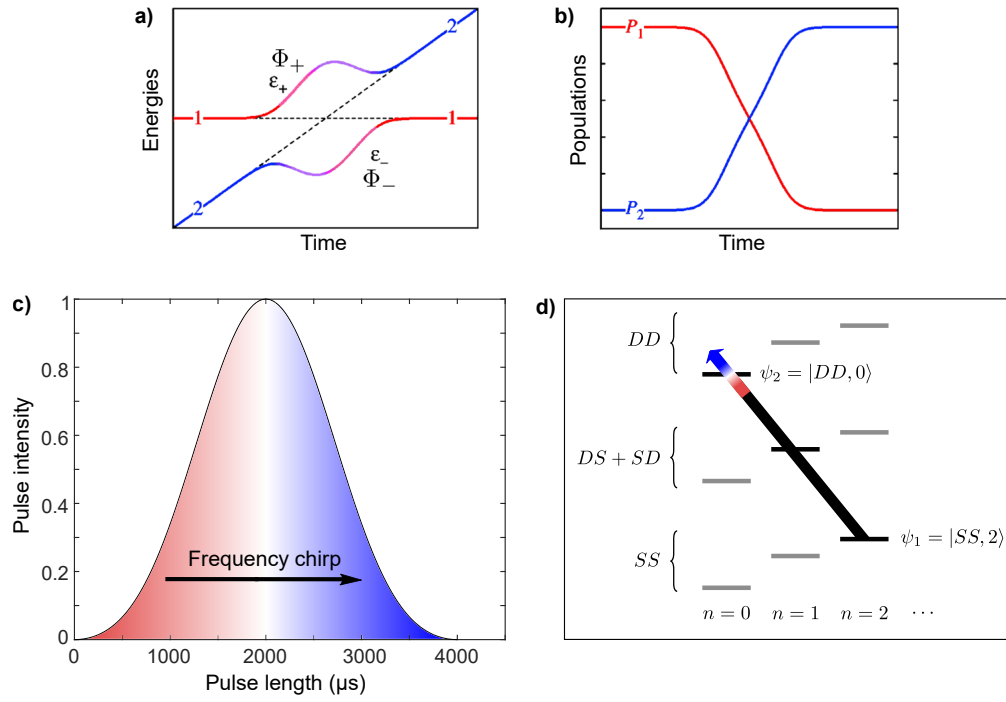


**Figure F.1.: Schematic diagrams on Rapid Adiabatic Passage.** **a)** Avoided crossing in the adiabatic evolution of eigenstates  $\Phi_{\pm}$ . Here, 1 and 2 denote the levels  $\psi_1$  and  $\psi_2$  respectively. **b)** Population transfer from  $\psi_1 \rightarrow \psi_2$  during a RAP. **c)** Laser pulse for RAP, featuring a long pulse length, a linear frequency chirp (colored area), and a Blackman-shaped intensity. **d)** Two-qubit level diagram depicting the functionality of a RAP pulse for motional state analysis. With the transfer  $\psi_1 \rightarrow \psi_2$ , the number of phonons  $n = 2$  is transferred to  $n$  collective excitations  $D$  in the ion string.

In our experiment, we applied RAP e.g. to measure the motional state population of a long ion crystal [107, 109]. In this case, the levels are represented by  $\psi_1 = |SSS \dots, n\rangle$  and  $\psi_2 = |DDD \dots, 0\rangle$ , where  $S$  and  $D$  describe the electronic (qubit) states of an ion and  $n$  describes the number of phonons in the system (Fig. F.1 d)). Fig. F.2 a) shows the motional state analysis of an 18-ion crystal with trapping frequencies

---

$\{\omega_x, \omega_y, \omega_z\} = 2\pi \{2.71, 2.68, 0.21\}$  MHz. RAP was implemented on the red sideband of the lowest-frequency radial mode at  $(2\pi) 2.08$  MHz. This mode was selected because it is spectrally well separated from other modes. Moreover, this mode has a lower heating rate than the radial COM modes, allowing a slower frequency sweep for the RAP. The laser pulse had a duration of 4 ms, a linear frequency chirp of 38 kHz across the red sideband transition, and the intensity was shaped according to a Blackman function. This pulse properties are set in the transition objects of our experiment software (QFP), as shown in Fig. F.2 b). Most importantly, the setting **slope** defines the rising and falling time of the Blackman shaping (selected in the field **Shaping**), and the field **span** defines the frequency span, over which the RAP pulse is chirped: 38 kHz means that the pulse sweeps from -38 kHz to +38 kHz over the transition defined in the field **Shift** (this should be the sideband transition on which the RAP is performed). The laser pulse was applied to all ions simultaneously, using the beam port perpendicular to the ion string. At the end of the sequence, the electronic state of each ions was detected by the EMCCD camera. The number of collective excitations in the ion string corresponds to the number of phonons prior to the RAP pulse.

Note that the same scheme can be applied on the blue sideband, in order to create Fock states (states with a well-defined number of quanta) or on the red sideband with  $n = 1$ , for generating Dicke-states (multipartite entangled states).

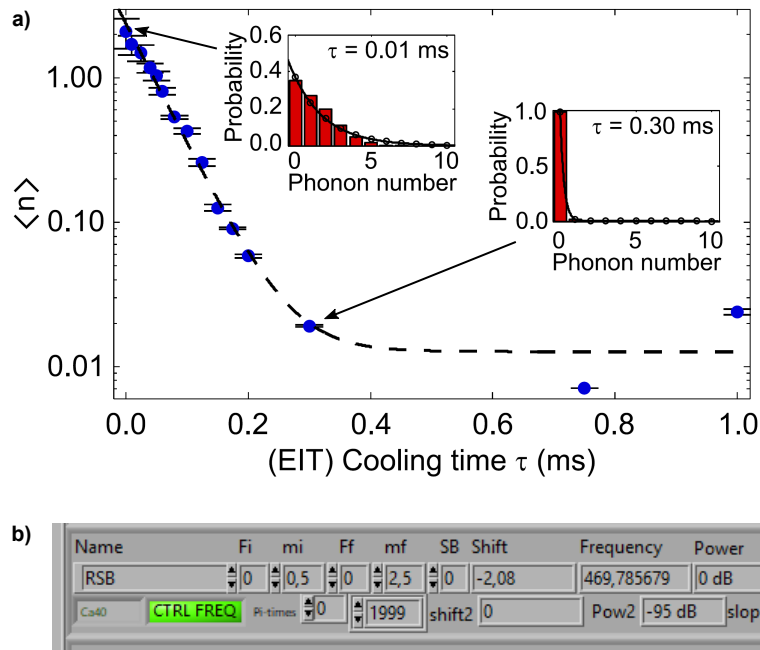


**Figure F.2.:** a) EIT cooling dynamics for an 18-ion crystal. The histograms in the inset are gathered via RAP on the radial motional mode at  $(2\pi)$  2.08 MHz and show the probability for finding a given number of excited ions. The mean phonon numbers  $\langle n \rangle$  in the main graph are determined by fitting a thermal distribution to the phonon-number distribution (solid line) of the histograms. This plot was taken from R. Lechner's thesis [107]. b) Screenshot from a transition object in our experiment software. The important fields for defining the RAP parameters (see text) are the Shift, Shaping, slope and span.

## G. Classical rate equation for transport dynamics under dephasing noise

The main idea for arriving at a classical rate equation is to adiabatically eliminate the coherences between sites, an approximation which becomes valid at times larger than the inverse dephasing rate. We start from the full master equation for our system, which reads

$$\dot{\rho} = -i[H, \rho] + \mathcal{L}\rho, \quad (\text{G.1})$$

with the Lindblad superoperator for dephasing noise  $\mathcal{L}X = \sum_i \frac{\gamma_i}{2} (2\sigma_i^+ \sigma_i^- X \sigma_i^+ \sigma_i^- - \sigma_i^+ \sigma_i^- X - X \sigma_i^+ \sigma_i^-)$ .

In the single-excitation subspace and in the case where noise and disorder dominate over the hopping terms, it is convenient to work in the basis spanned by the states  $|i\rangle = \sigma_i^+ |\Downarrow\rangle$ , with  $i = 1 \dots N$  and  $|\Downarrow\rangle$  the fully polarized state. In this basis, the excitation probabilities (‘populations’) evolve as

$$\dot{\rho}_{ii} = -i \sum_{\ell \neq i} (H_{i\ell} \rho_{\ell i} - \rho_{i\ell} H_{\ell i}), \quad (\text{G.2})$$

where we define  $\rho_{ij} = \langle i | \rho | j \rangle$  and analogously for  $H_{ij} = \langle i | H | j \rangle$ . The coherences for  $i \neq j$  evolve as

$$\begin{aligned} \dot{\rho}_{ij} &= -i \left( \sum_{\ell \neq i} H_{i\ell} \rho_{\ell j} - \sum_{\ell \neq j} \rho_{i\ell} H_{\ell j} \right) \\ &+ \left[ -i(H_{ii} - H_{jj}) - \frac{\gamma_i + \gamma_j}{4} \right] \rho_{ij}. \end{aligned} \quad (\text{G.3})$$

Here, the terms  $H_{i\ell} = J_{i\ell}$  ( $i \neq \ell$ ) describe the hoppings and  $H_{ii} = 2B_i$  the on-site disorder (up to a constant).

Under the assumption that the diagonal terms  $H_{ii}$  and  $\gamma_i$  are the dominating energy scales, we can adiabatically eliminate the coherences. Formally, this amounts to setting their time-derivatives to zero, which becomes valid on the ‘slow’ time scales on which the populations evolve,  $t \gg 1 / \left| i(H_{ii} - H_{jj}) + \frac{\gamma_i + \gamma_j}{4} \right|$ .

Solving the Eq. (G.3) for  $\dot{\rho}_{ij} = 0$  to leading order in the hoppings, i.e., assuming  $H_{ij} \ll |i(H_{ii} - H_{jj}) + \frac{\gamma_i + \gamma_j}{4}|$ , we obtain  $\rho_{ij} = \frac{H_{ij}(\rho_{jj} - \rho_{ii})}{H_{ii} - H_{jj} - \frac{\gamma_i + \gamma_j}{4}}$ . Inserting this expression into Eq. (G.2), we obtain the result

$$\dot{\rho}_{ii} = \sum_{\ell \neq i} \Gamma_{\ell i} (\rho_{\ell\ell} - \rho_{ii}), \quad (\text{G.4})$$

with  $\Gamma_{\ell i} = \frac{\frac{\gamma_i + \gamma_\ell}{2} H_{i\ell} H_{\ell i}}{(H_{ii} - H_{\ell\ell})^2 + (\frac{\gamma_i + \gamma_\ell}{4})^2}$ . By setting  $\gamma_i = \gamma \forall i$ , this set of coupled differential equations describes the diffusive evolution of the populations  $p_i = \rho_{ii}$  according to the classical rate equation (6.3) given in the main text.

In the regime of large noise, the diffusive rate Eq. (G.4) predicts a decrease of transport efficiency with increasing  $\gamma$  independent of  $B_{\max}$ , in accordance with the experimental observations. In the regime of ENAQT and for  $\gamma < J_{\max}$ , however, more complex models are required to obtain reliable predictions, since coherences play an important role in this regime at short times (see, e.g. Fig. 6.3 b)).

## H. Generating Gaussian Random Processes with arbitrary spectra

The following Matlab code [H.1](#) generates a sequence  $U$  of values from a Gaussian stationary process with a specified spectral density function  $S$ . In our experiment,  $S$  is chosen to be a Lorentzian distribution with center  $S_0$  and width  $g$ :  $S(\omega) = \frac{1}{2\pi} \cdot \frac{g}{g^2 + (\omega - S_0)^2}$ . Note that in the experiment we can only apply a set of  $N$  AC-Stark shifts to the ions. Following the algorithm in Ref. [\[163\]](#),  $S$  is discretized into  $M$  parts, where  $M \gg N$ . Then random values  $W$  are drawn from a Gaussian distribution with zero mean and unit variance. The noise sequence "dynamic\_noise", obtained from the algorithm, is a set of "random" variables with the desired power spectral density  $S$ . Finally, all values of the sequence "dynamic\_noise" are multiplied by a particular factor, to reach the desired noise amplitude. Then all  $N$  values are converted to actual RF amplitudes (as explained in Section [4.4.1](#)) and applied to the experiment as AC-Stark shifts.

Program [H.2](#) is used to graphically compare the generated random noise with the ideal, desired spectral density function. The result is shown in [Fig. H.1](#).

Listing H.1: Gaussian Random Processes with arbitrary spectra

```
clear all
% define variables;
dt = 100*10^(-6); % time-stepsize in s, realized in the experiment
S0 = 590.0; % Frequency center of the Lorentzian peak in 1/s
g = 200; % Width of the Lorentzian peak in 1/s
M = 5*10^3; % Number of points for discretizing the spectral density function S
fmax = 20000; % maximum frequency over which I want to define S

W = randn(1,M); % M random values drawn from a gaussian distribution with mean =
0, unit variance

% construct the sequence U following Percivals algorithm, to get a random noise
with Lorentzian spectral density function S = 1/pi*(1/2*g./((1/2*g)^2+(x-x0)
.^2))
U_j = zeros(1,M);
js = 0:M-1;
fj = js./M*fmax;
```

```

U_j(1) = sqrt(Spec_dens_Lorentz(fj(1),S0,g,1))*W(1)*sqrt(dt);
k = 2;
while (k >= 2) && (k < M/2+1)
    U_j(k) = sqrt(1/2*Spec_dens_Lorentz(fj(k),S0,g,1))* (W(2*k-1) + 1i*W(2*k-1))
        *sqrt(dt);
    k = k+1;
end

U_j(M/2+1) = sqrt(Spec_dens_Lorentz(fj(M/2+1),S0,g,1))*W(M)*sqrt(dt);
k = M/2+2;
while (k > M/2+1) && (k <= M)
    U_j(k) = conj(U_j(M+1-k+1));
    k = k+1;
end

% now generate the real-valued noise itself:
for t = 0:M-1
    U_t(t+1) = 1/sqrt(M)*sum( U_j.*exp(-1i*fj.*t*dt));
end
U_real(:) = real(U_t);

% only take the first N values of U_t, where N is given by "total time of
    experimental sequence / dt"
N = 600;
dynamic_noise(:) = U_real(1:N);

```

### Listing H.2: Compare constructed noise with ideal spectral density function

```

% Use Periodogram eq. (7) in Percivals paper to generate a spectrum
ww = 0:fj(M)/M:fj(M);
for l = 1:length(ww)
    summand = 0;
    for tt = 1:N % only take the first N values of U_t
        summand = summand + (U_real(tt))*exp(-1i*ww(l)*(tt-1)*dt);
    end
    test_spec(l) = abs(summand)^2/N;
end

figure(1)
hold on
plot(ww,Spec_dens_Lorentz(ww,S0,g,1)*dt,'-r','LineWidth',2) % ideal spectral
    density function
hold on
plot(ww,test_spec,'.-')

```

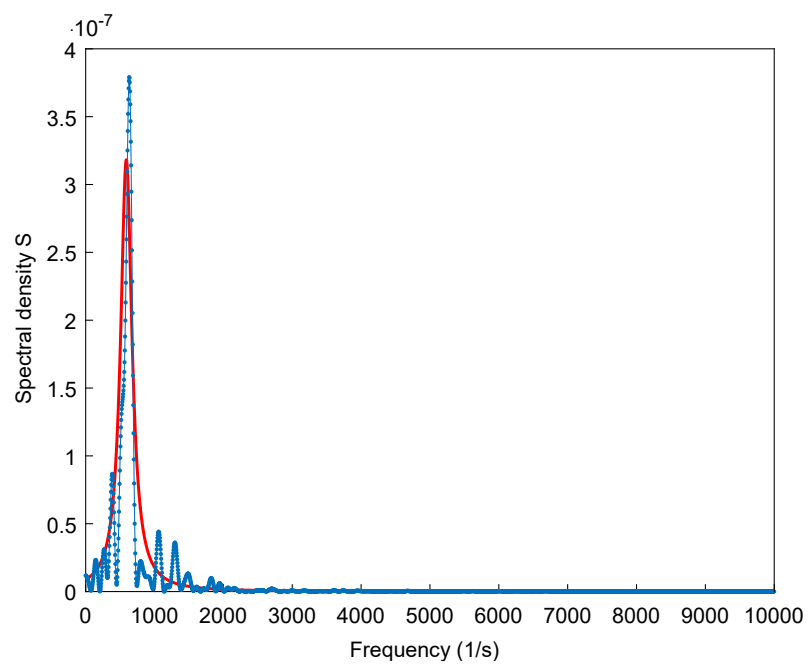


**Figure H.1.:** Graphical comparison of the ideal, desired spectral density function  $S$  (red) with the spectral density generated from random noise (connected blue dots).

# I. Measuring local reductions for MPS tomography

MPS tomography requires the ability to estimate the local reduced density matrices of all blocks of  $k$  neighbouring spins. On a linear chain of  $N$  spins, there are  $N - k + 1$  such blocks. The straightforward method to reconstruct a single block uses the set of all  $k$ -fold tensor products of the three Pauli operators  $X = \sigma_x$ ,  $Y = \sigma_y$ ,  $Z = \sigma_z$  and the identity operator  $\mathbb{1}$ . Applying these  $4^k$  observables to each block, amounts to a total of  $(N - k + 1)4^k$  measurements. For example, a two-qubit reduction ( $k = 2$ ) can be reconstructed from 16 expectation values:

$$\begin{aligned}
 &\langle X_1 X_2 \rangle \quad \langle X_1 Y_2 \rangle \quad \langle X_1 Z_2 \rangle \quad \langle X_1 \mathbb{1}_2 \rangle \\
 &\langle Y_1 X_2 \rangle \quad \langle Y_1 Y_2 \rangle \quad \langle Y_1 Z_2 \rangle \quad \langle Y_1 \mathbb{1}_2 \rangle \\
 &\langle Z_1 X_2 \rangle \quad \langle Z_1 Y_2 \rangle \quad \langle Z_1 Z_2 \rangle \quad \langle Z_1 \mathbb{1}_2 \rangle \\
 &\langle \mathbb{1}_1 X_2 \rangle \quad \langle \mathbb{1}_1 Y_2 \rangle \quad \langle \mathbb{1}_1 Z_2 \rangle \quad \langle \mathbb{1}_1 \mathbb{1}_2 \rangle .
 \end{aligned} \tag{I.1}$$

However, we can reuse measurements: For example,  $\langle Z_1 X_2 \rangle$  can also be used to extract the expectation values  $\langle Z_1 \mathbb{1}_2 \rangle$  and  $\langle \mathbb{1}_1 X_2 \rangle$ . This allows us to project each spin into the eigenstates of the three Pauli operators using only  $3^k$  bases measurements on the entire system of  $N$  spins. With this, the measurement settings in example (I.1) reduce to:

$$\begin{aligned}
 &\langle X, X \rangle \quad \langle X, Y \rangle \quad \langle X, Z \rangle \\
 &\langle Y, X \rangle \quad \langle Y, Y \rangle \quad \langle Y, Z \rangle \\
 &\langle Z, X \rangle \quad \langle Z, Y \rangle \quad \langle Z, Z \rangle .
 \end{aligned} \tag{I.2}$$

Those  $3^k$  measurement settings have to be repeated for each of the  $N - k + 1$  local blocks on the chain. Independent measurements, performed on each local block while remaining spins are ignored, would require  $(N - k + 1)3^k$  measurement settings. However, applying a clever combination of the observables to the entire chain, reduces the total number of measurement settings further: Specifically, for each of the  $3^k$  measurement settings, we split the system into  $\lceil N/k \rceil$  blocks and replicate the same settings

on each of the blocks. In our experiment, we set  $k = 3$ , i.e., we perform measurements in  $3^3 = 27$  different bases on  $N$  spins:

$$\begin{array}{ll}
 \langle Z, Z, Z, Z, Z, Z, Z, \dots \rangle & \langle Z, Z, X, Z, Z, X, Z, \dots \rangle \\
 \langle Z, Z, Y, Z, Z, Y, Z, \dots \rangle & \langle Z, X, Z, Z, X, Z, Z, \dots \rangle \\
 \langle Z, X, X, Z, X, X, Z, \dots \rangle & \langle Z, X, Y, Z, X, Y, Z, \dots \rangle \\
 \langle Z, Y, Z, Z, Y, Z, Z, \dots \rangle & \langle Z, -Y, X, Z, -Y, X, Z, \dots \rangle \\
 \langle Z, Y, Y, Z, Y, Y, Z, \dots \rangle & \langle X, Z, Z, X, Z, Z, X, \dots \rangle \\
 \langle X, Z, X, X, Z, X, X, \dots \rangle & \langle X, Z, Y, X, Z, Y, X, \dots \rangle \\
 \langle X, X, Z, X, X, Z, X, \dots \rangle & \langle X, X, X, X, X, X, X, \dots \rangle \\
 \langle X, X, -Y, X, X, -Y, X, \dots \rangle & \langle X, Y, Z, X, Y, Z, X, \dots \rangle \\
 \langle X, -Y, X, X, -Y, X, X, \dots \rangle & \langle X, Y, Y, X, Y, Y, X, \dots \rangle \\
 \langle Y, Z, Z, Y, Z, Z, Y, \dots \rangle & \langle -Y, Z, X, -Y, Z, X, -Y, \dots \rangle \\
 \langle Y, Z, Y, Y, Z, Y, Y, \dots \rangle & \langle -Y, X, Z, -Y, X, Z, -Y, \dots \rangle \\
 \langle -Y, X, X, -Y, X, X, -Y, \dots \rangle & \langle Y, X, Y, Y, X, Y, Y, \dots \rangle \\
 \langle Y, Y, Z, Y, Y, Z, Y, \dots \rangle & \langle Y, Y, X, Y, Y, X, Y, \dots \rangle \\
 \langle Y, Y, Y, Y, Y, Y, Y, \dots \rangle &
 \end{array}$$

## J. Singular Value Decomposition

An arbitrary matrix  $M$  of dimensions  $[N_A \times N_B]$  can be decomposed into  $M = USV^\dagger$  [132], where  $U$  has dimension  $[N_A \times \min(N_A, N_B)]$  and has orthonormal columns.  $S$  is of dimension  $[\min(N_A, N_B) \times \min(N_A, N_B)]$ , and is diagonal with non-negative entries  $S_{aa} \equiv s_a$  (the so-called *singular values*). The number  $r$  of non-zero singular values is the *rank* of  $M$ . Finally,  $V^\dagger$  is of dimension  $[\min(N_A, N_B) \times N_B]$  and has orthonormal rows.



**Figure J.1.:** Bipartition of “universe”  $AB$  into subsystems  $A$  and  $B$ .

An example application of SVD is the *Schmidt decomposition*, a very compact representation of a state based on the bipartition of the system “universe” into two subsystems  $A$  and  $B$ : We can rewrite any pure state with respect to a bipartition (Fig. J.1):

$$|\psi\rangle = \sum_{i=1}^{\dim(\mathcal{H}_A)} \sum_{j=1}^{\dim(\mathcal{H}_B)} \Psi_{ij} |i\rangle_A |j\rangle_B .$$

Here,  $\{|i\rangle_A\}$  and  $\{|j\rangle_B\}$  are orthonormal bases of  $A$  and  $B$ , and the coefficients are written as entries of matrix  $\Psi$ . Applying SVD to the matrix

$$\Psi_{ij} = \sum_{a=1}^{\min(N_A, N_B)} U_{ia} S_{aa} V_{aj}^* ,$$

results in the Schmidt decomposition of the state

$$|\psi\rangle = \sum_{a=1}^r s_a |a\rangle_A |a\rangle_B ,$$

with  $|a\rangle_A = \sum_i U_{ia} |i\rangle_A$  and  $|a\rangle_B = \sum_j V_{ja}^* |j\rangle_B$ .

## K. Hartree-Fock method for deriving molecular orbitals

The following summary is based on Refs. [173, 191]. The quantum mechanical description of the electronic structure of molecules treats electrons as moving under the influence of the nuclei. The spatial and energetic properties of electrons are described as molecular orbitals, which surround two or more atoms. In molecular orbital theory, the electrons are often considered as stochastically independent. In this case, the  $N$ -body electronic wavefunction is approximated by the so-called Slater determinant  $\varphi$  – an anti-symmetrized product wavefunction which consists of  $N$  one-electron molecular orbitals  $\phi_i$ :

$$\varphi(\mathbf{x}_1, \mathbf{x}_2, \dots, \mathbf{x}_N) = \frac{1}{\sqrt{N!}} \begin{vmatrix} \phi_1(\mathbf{x}_1) & \phi_2(\mathbf{x}_1) & \dots & \phi_N(\mathbf{x}_1) \\ \phi_1(\mathbf{x}_2) & \phi_2(\mathbf{x}_2) & \dots & \phi_N(\mathbf{x}_2) \\ \vdots & \vdots & \ddots & \vdots \\ \phi_1(\mathbf{x}_N) & \phi_2(\mathbf{x}_N) & \dots & \phi_N(\mathbf{x}_N) \end{vmatrix} \equiv |\phi_1, \phi_2, \dots, \phi_N\rangle. \quad (\text{K.1})$$

Here,  $\mathbf{x}_i$  denotes the position and spin of the  $i$ -th electron. The anti-symmetry ensures the Pauli principle, by changing sign upon exchange of two electrons. The Hartree-Fock method is a numerical technique to calculate the individual molecular orbitals  $\phi_i$  and thereby the entire electronic structure of the molecule:

- We begin with defining an ansatz basis  $\{\tilde{\phi}_i\}$  of molecular orbitals. A common basis set are the so-called Slater-type orbitals (STO), which consist of linear combinations of atomic orbitals (LCAO).

$$\tilde{\phi}_i = \sum_{\alpha} c_{\alpha i} \chi_{\alpha}. \quad (\text{K.2})$$

The atomic orbital functions,  $\chi_{\alpha}$ , can be represented by Gaussian functions, such that a linear combination of e.g. three (or six) Gaussian functions constructs a set of Slater-type orbitals named STO-3G (or STO-6G). In the example of molecular hydrogen  $\text{H}_2$ , we can construct a minimal basis, if each hydrogen atom contributes

a 1s orbital. The molecular orbitals are assembled by adding the corresponding two atomic wavefunctions: In-phase addition results in a lower energy  $\sigma_{1s}$  bonding orbital with increased electron density between the nuclei, while out-of-phase addition in an energetically higher lying  $\sigma_{1s}^*$  anti-bonding orbital, associated with a depletion in electron density between them.

- The chosen basis  $\{\tilde{\phi}_i\}$  is then used to construct the “Fock operator”  $\hat{F}$ , a single-electron operator which approximates the true  $N$ -body Hamiltonian by including the effects of electron-electron repulsion only in an average way: Electrons do not interact pairwise, but each electron interacts with a mean-field, collectively generated by all other electrons.

$$\hat{F} = \hat{H}_{\text{core}} + \sum_{i=1}^{N/2} [2\hat{J}_i - \hat{K}_i], \quad \text{with}$$

$$\hat{H}_{\text{core},i} \phi_i(\mathbf{x}_1) = \left[ -\frac{\nabla_i^2}{2} - \sum_n \frac{Z_n}{r_{in}} \right] \phi_i(\mathbf{x}_1),$$

$$\hat{J}_i \phi_i(\mathbf{x}_1) = \sum_{p=1}^N \phi_i(\mathbf{x}_1) \int \frac{\phi_p^*(\mathbf{x}_2) \phi_p(\mathbf{x}_2)}{r_{12}} d\mathbf{x}_2,$$

$$\hat{K}_i \phi_i(\mathbf{x}_1) = \sum_{p=1}^N \phi_p(\mathbf{x}_1) \int \frac{\phi_p^*(\mathbf{x}_2) \phi_i(\mathbf{x}_2)}{r_{12}} d\mathbf{x}_2.$$

Here,  $\hat{H}_{\text{core},i}$  is called the one-electron core Hamiltonian,  $\hat{J}_i$  is the Coulomb operator, which describes the inter-electron repulsion for electrons in the same  $i$ -th orbital, and  $\hat{K}_i$  is the exchange operator, defining the exchange energy upon electron swapping. With this, the Schrödinger equation turns into a system of  $N$  coupled one-particle equations – the Hartree-Fock equations:

$$\hat{F} |\phi_i\rangle = \varepsilon_i |\phi_i\rangle, \quad (\text{K.3})$$

with the molecular orbitals  $|\phi_i\rangle$  and the related orbital energies  $\varepsilon_i$ .

- The goal is to variationally optimize the coefficients  $c_{\alpha i}$  in the orbitals  $\tilde{\phi}_i$  towards the true eigenfunctions  $\phi_i$ , which solve the Hartree-Fock equation. The optimization procedure seeks to minimize the total energy  $\tilde{E}$  of the respective Slater determinant  $\tilde{\varphi}$ :  $\tilde{E} = \langle \tilde{\varphi} | \hat{F} | \tilde{\varphi} \rangle \geq E_{\text{exact}}$ . The Fock operator itself is constructed from the orbitals  $\tilde{\phi}_i$ , such that each updated set of molecular orbitals also updates the Fock operator. In this way, the Hartree-Fock orbitals are optimized iteratively until the change in total electronic energy  $\tilde{E}$  reaches a predefined threshold. The

resultant Slater determinant, constructed from the lowest-energy set of molecular orbitals, represents the Hartree–Fock ground state wave function  $\varphi_{\text{HF}}$ .

## L. Translating UCC operators to quantum gates

In order to translate the UCC operators into Mølmer-Sørensen and single-qubit gates, we employ a technique first demonstrated in Ref. [192], formulae 10-12: Consider arbitrary tensor products of Pauli operators  $A$  and  $B$  with  $[A, B] \neq 0$  we have:

$$\exp(-i\alpha A) \exp(i\theta B) \exp(i\alpha A) = \exp(i\theta B'),$$

with  $B' = \exp(-i\alpha A) B \exp(i\alpha A)$  and using the fact that Pauli operators are self-inverse:

$$B' = (\mathcal{I} \cos \alpha - iA \sin \alpha) B (\mathcal{I} \cos \alpha + iA \sin \alpha).$$

With the knowledge that  $A$  and  $B$  do not commute and therefore must anticommute we obtain:

$$B' = B \cos 2\alpha - \frac{i}{2}[A, B] \sin 2\alpha.$$

Specifically, for  $\alpha = \pi/4$  and the example of the  $H_2$  molecule under BK transformation we find:

$$\begin{aligned} \exp(-i\theta \sigma_1^y \sigma_j^x) &= \exp\left(i\theta \frac{[\sigma_1^x \sigma_j^x, \sigma_1^z]}{2}\right) \\ &= \exp\left(-i\frac{\pi}{4} \sigma_1^x \sigma_j^x\right) \exp(-i\theta \sigma_1^z) \exp\left(i\frac{\pi}{4} \sigma_1^x \sigma_j^x\right) \\ &= \exp\left(i\frac{\pi}{4} \sigma_1^x \sigma_j^x\right) \exp(-i(\theta + \pi) \sigma_1^z) \exp\left(i\frac{\pi}{4} \sigma_1^x \sigma_j^x\right). \end{aligned}$$

## M. Estimation of the energy gap via quantum subspace expansion

We experimentally estimate the energy gap between the ground state and the first excited state by adopting a quantum subspace expansion approximation, commonly used in quantum chemistry [172]. The method relies, on having a good approximant of the ground state of the target Hamiltonian. In our case, this is given by the variationally optimized state  $|\Psi(\boldsymbol{\theta}_{\text{opt}})\rangle$  with the highest overlap with the exact ground state. The corresponding approximate ground state energy is  $E(\boldsymbol{\theta}_{\text{opt}}) = \langle \Psi(\boldsymbol{\theta}_{\text{opt}}) | \hat{H}_T | \Psi(\boldsymbol{\theta}_{\text{opt}}) \rangle$ . We then construct an excitation subspace by applying a set of symmetry-preserving, low-energy excitation operators  $\hat{O}_q$  onto the state:  $\hat{O}_q |\Psi(\boldsymbol{\theta}_{\text{opt}})\rangle$ . The corresponding measurements provide us with the effective Hamiltonian  $H_{q,q'}^{\text{eff}} = \langle \Psi(\boldsymbol{\theta}_{\text{opt}}) | \hat{O}_q \hat{H}_T \hat{O}_{q'} | \Psi(\boldsymbol{\theta}_{\text{opt}}) \rangle$ , as well as the overlap matrix  $M_{q,q'} = \langle \Psi(\boldsymbol{\theta}_{\text{opt}}) | \hat{O}_q \hat{O}_{q'} | \Psi(\boldsymbol{\theta}_{\text{opt}}) \rangle$ . The solution of the generalized eigenproblem

$$\sum_{q'} H_{q,q'}^{\text{eff}} v_{q'}^{(k)} = \lambda_{(k)} \sum_{q'} M_{q,q'} v_{q'}^{(k)}, \quad (\text{M.1})$$

with real eigenvalues  $\lambda_{(k)} \leq \lambda_{(k+1)}$ , yields the approximate energy levels. At this stage,  $\lambda_{(0)}$  is an improved approximation of the ground state energy and  $(\lambda_{(1)} - \lambda_{(0)})$  is an estimator for the energy gap.

The most relevant excitations  $\hat{O}_q$  for constructing the quantum subspace of the Schwinger model include processes of a single, nearest-neighbour, electron-positron pair creation or annihilation. Such processes preserve the global charge conservation symmetry. To protect the  $\hat{C}\hat{P}$  symmetry, we tailor these excitations to be explicitly  $\hat{C}\hat{P}$ -symmetric:

$$\hat{O}_j = \hat{\sigma}_j^x \hat{\sigma}_{j+1}^x + \hat{\sigma}_j^y \hat{\sigma}_{j+1}^y + \hat{\sigma}_{N-j}^x \hat{\sigma}_{N+1-j}^x + \hat{\sigma}_{N-j}^y \hat{\sigma}_{N+1-j}^y, \quad (\text{M.2})$$

for  $j$  from 1 to  $N/2$ , while  $\hat{O}_0 = \mathbb{1}$ . According to this prescription, each operator of the form  $\hat{O}_j \hat{H}_T \hat{O}_{j'}$  can be decomposed in a sum of Pauli operator strings, which can be measured via  $n$ -body correlators. Note that this elementary subspace expansion

requires a number of measurement bases that scales as  $\propto N^2$ , to reconstruct the full matrices  $H_{j,j'}^{\text{eff}}$  and  $M_{j,j'}$ .

## Bibliography

- [1] M. Ben Yahia, et al., Nature Materials **18**, 496 (2019), URL <https://doi.org/10.1038/s41563-019-0318-3>.
- [2] M. A. Abdel-Rahman, et al., Scientific Reports **9**, 4535 (2019), URL <https://doi.org/10.1038/s41598-019-40890-2>.
- [3] A. Marais, et al., Journal of The Royal Society Interface **15**, 20180640 (2018), URL <https://royalsocietypublishing.org/doi/abs/10.1098/rsif.2018.0640>.
- [4] M. Hilbert and P. López, Science **332**, 60 (2011), URL <https://science.sciencemag.org/content/332/6025/60>.
- [5] R. Feynman, International Journal Of Theoretical Physics **21**, 467 (1982), URL <http://dx.doi.org/10.1007/BF02650179>.
- [6] I. M. Georgescu, et al., Rev. Mod. Phys. **86**, 153 (2014), URL <https://link.aps.org/doi/10.1103/RevModPhys.86.153>.
- [7] R. Blatt and C. F. Roos, Nature Physics **8**, 277 (2012), URL <https://doi.org/10.1038/nphys2252>.
- [8] J. W. Britton, et al., Nature **484**, 489 (2012), URL <https://doi.org/10.1038/nature10981>.
- [9] A. Browaeys and T. Lahaye, Nature Physics **16**, 132 (2020), URL <https://doi.org/10.1038/s41567-019-0733-z>.
- [10] H. Bernien, et al., Nature **551**, 579 (2017), URL <https://doi.org/10.1038/nature24622>.
- [11] J. Zhang, et al., Nature **551**, 601 (2017), URL <https://doi.org/10.1038/nature24654>.

- 
- [12] A. Kandala, et al., *Nature* **549**, 242 (2017), URL <https://doi.org/10.1038/nature23879>.
- [13] C. Hempel, et al., *Phys. Rev. X* **8**, 031022 (2018), URL <https://link.aps.org/doi/10.1103/PhysRevX.8.031022>.
- [14] E. F. Dumitrescu, et al., *Phys. Rev. Lett.* **120**, 210501 (2018), URL <https://link.aps.org/doi/10.1103/PhysRevLett.120.210501>.
- [15] N. Klco, et al., *Phys. Rev. A* **98**, 032331 (2018), URL <https://link.aps.org/doi/10.1103/PhysRevA.98.032331>.
- [16] C. Kokail, et al., *Nature* **569**, 355 (2019), URL <https://doi.org/10.1038/s41586-019-1177-4>.
- [17] M. Fox, *Quantum Optics, An Introduction* (Oxford University Press, 2006), ISBN 0198566735.
- [18] R. Horodecki, et al., *Rev. Mod. Phys.* **81**, 865 (2009), URL <https://link.aps.org/doi/10.1103/RevModPhys.81.865>.
- [19] G. Vidal and R. F. Werner, *Phys. Rev. A* **65**, 032314 (2002), URL <https://link.aps.org/doi/10.1103/PhysRevA.65.032314>.
- [20] D. David and P. Roger, *Proceedings of the Royal Society of London. A. Mathematical and Physical Sciences* **400**, 97 (1985), URL <https://doi.org/10.1098/rspa.1985.0070>.
- [21] M. A. Nielsen and I. L. Chuang, *Quantum Computation and Quantum Information* (Cambridge University Press, 2000), ISBN 0521635039.
- [22] D. P. DiVincenzo, *Phys. Rev. A* **51**, 1015 (1995), URL <https://link.aps.org/doi/10.1103/PhysRevA.51.1015>.
- [23] K. Mølmer and A. Sørensen, *Phys. Rev. Lett.* **82**, 1835 (1999), URL <https://link.aps.org/doi/10.1103/PhysRevLett.82.1835>.
- [24] E. Solano, et al., *Phys. Rev. A* **59**, R2539 (1999), URL <https://link.aps.org/doi/10.1103/PhysRevA.59.R2539>.
- [25] A. Sørensen and K. Mølmer, *Phys. Rev. A* **62**, 022311 (2000), URL <https://link.aps.org/doi/10.1103/PhysRevA.62.022311>.

- 
- [26] J. I. Cirac and P. Zoller, Phys. Rev. Lett. **74**, 4091 (1995), URL <https://link.aps.org/doi/10.1103/PhysRevLett.74.4091>.
- [27] G. Kirchmair, et al., New Journal of Physics **11**, 023002 (2009), URL <https://iopscience.iop.org/article/10.1088/1367-2630/11/2/023002>.
- [28] V. M. Schäfer, et al., Nature **555**, 75 (2018), URL <https://doi.org/10.1038/nature25737>.
- [29] M. Kjaergaard, et al., Annual Review of Condensed Matter Physics **11**, 369 (2020), URL <https://doi.org/10.1146/annurev-conmatphys-031119-050605>.
- [30] M. Veldhorst, et al., Nature **526**, 410 (2015), URL <https://doi.org/10.1038/nature15263>.
- [31] P. W. Shor, Phys. Rev. A **52**, R2493 (1995), URL <https://link.aps.org/doi/10.1103/PhysRevA.52.R2493>.
- [32] A. M. Steane, Phys. Rev. Lett. **77**, 793 (1996), URL <https://link.aps.org/doi/10.1103/PhysRevLett.77.793>.
- [33] J. Chiaverini, et al., Nature **432**, 602 (2004), URL <https://doi.org/10.1038/nature03074>.
- [34] P. Schindler, et al., Science **332**, 1059 (2011), URL <http://science.sciencemag.org/content/332/6033/1059>.
- [35] N. Metropolis and S. Ulam, Journal of the American Statistical Association **44**, 335 (1949), pMID: 18139350, URL <https://www.tandfonline.com/doi/abs/10.1080/01621459.1949.10483310>.
- [36] Z. Hradil, Phys. Rev. A **55**, R1561 (1997), URL <https://link.aps.org/doi/10.1103/PhysRevA.55.R1561>.
- [37] M. Ježek, et al., Phys. Rev. A **68**, 012305 (2003), URL <https://link.aps.org/doi/10.1103/PhysRevA.68.012305>.
- [38] R. Blume-Kohout, New Journal of Physics **12**, 043034 (2010), URL <https://iopscience.iop.org/article/10.1088/1367-2630/12/4/043034>.

- 
- [39] T. Monz, Ph.D. thesis, Leopold-Franzens University Innsbruck (2011), URL [https://quantumoptics.at/images/publications/dissertation/monz\\_diss.pdf](https://quantumoptics.at/images/publications/dissertation/monz_diss.pdf).
- [40] M. Cramer, et al., Nature Communications **1**, 149 (2010), URL <https://doi.org/10.1038/ncomms1147>.
- [41] T. Baumgratz, et al., Phys. Rev. Lett. **111**, 020401 (2013), URL <https://link.aps.org/doi/10.1103/PhysRevLett.111.020401>.
- [42] D. Gross, et al., Phys. Rev. Lett. **105**, 150401 (2010), URL <https://link.aps.org/doi/10.1103/PhysRevLett.105.150401>.
- [43] D. L. Donoho, IEEE Transactions on Information Theory **52**, 1289 (2006), URL <https://ieeexplore.ieee.org/document/1614066>.
- [44] E. J. Candes and T. Tao, IEEE Transactions on Information Theory **52**, 5406 (2006), URL <https://ieeexplore.ieee.org/document/4016283>.
- [45] C. Schwemmer, et al., Phys. Rev. Lett. **113**, 040503 (2014), URL <https://link.aps.org/doi/10.1103/PhysRevLett.113.040503>.
- [46] C. A. Riofrío, et al., Nature Communications **8**, 15305 (2017), URL <https://doi.org/10.1038/ncomms15305>.
- [47] A. Shabani, et al., Phys. Rev. Lett. **106**, 100401 (2011), URL <https://link.aps.org/doi/10.1103/PhysRevLett.106.100401>.
- [48] A. V. Rodionov, et al., Phys. Rev. B **90**, 144504 (2014), URL <https://link.aps.org/doi/10.1103/PhysRevB.90.144504>.
- [49] S. T. Flammia and Y.-K. Liu, Phys. Rev. Lett. **106**, 230501 (2011), URL <https://link.aps.org/doi/10.1103/PhysRevLett.106.230501>.
- [50] M. P. da Silva, et al., Phys. Rev. Lett. **107**, 210404 (2011), URL <https://link.aps.org/doi/10.1103/PhysRevLett.107.210404>.
- [51] D. P. DiVincenzo, Fortschritte der Physik **48**, 771 (2000), URL [https://doi.org/10.1002/1521-3978\(200009\)48:9/11<771::AID-PROP771>3.0.CO;2-E](https://doi.org/10.1002/1521-3978(200009)48:9/11<771::AID-PROP771>3.0.CO;2-E).

- 
- [52] C. F. Roos, Ph.D. thesis, Leopold-Franzens University Innsbruck (2000), URL [https://quantumoptics.at/images/publications/dissertation/roos\\_diss.pdf](https://quantumoptics.at/images/publications/dissertation/roos_diss.pdf).
- [53] P. A. Barton, et al., Phys. Rev. A **62**, 032503 (2000), URL <https://link.aps.org/doi/10.1103/PhysRevA.62.032503>.
- [54] T. Hänsch and A. Schawlow, Optics Communications **13**, 68 (1975), URL <http://www.sciencedirect.com/science/article/pii/0030401875901595>.
- [55] D. Wineland and H. Dehmelt, Bulletin of the American Physical Society **20**, 637 (1975), ISSN 0003-0503, Proposed  $10^{14}\Delta\nu < \nu$  Laser Fluorescence Spectroscopy on  $\text{Tl}^+$  Mono-Ion Oscillator III, URL <https://tf.boulder.nist.gov/general/pdf/2208.pdf>.
- [56] F. Diedrich, et al., Phys. Rev. Lett. **62**, 403 (1989), URL <https://link.aps.org/doi/10.1103/PhysRevLett.62.403>.
- [57] C. Roos, et al., Phys. Rev. Lett. **83**, 4713 (1999), URL <https://link.aps.org/doi/10.1103/PhysRevLett.83.4713>.
- [58] R. Stricker, Master's thesis, Leopold-Franzens University Innsbruck (2017), URL [https://quantumoptics.at/images/publications/diploma/master\\_stricker.pdf](https://quantumoptics.at/images/publications/diploma/master_stricker.pdf).
- [59] T. Ruster, et al., Applied Physics B **122**, 254 (2016), URL <https://doi.org/10.1007/s00340-016-6527-4>.
- [60] T. Brydges, PhD thesis in preparation during the writing of this work., URL <https://quantumoptics.at/en/publications/ph-d-theses.html>.
- [61] A. H. Burrell, et al., Phys. Rev. A **81**, 040302 (2010), URL <https://link.aps.org/doi/10.1103/PhysRevA.81.040302>.
- [62] H. G. Dehmelt, IEEE Transactions on Instrumentation and Measurement **31**, 83 (1982), URL <https://ieeexplore.ieee.org/document/6312526>.
- [63] C. Hempel, Ph.D. thesis, Leopold-Franzens University Innsbruck (2014), URL [https://quantumoptics.at/images/publications/dissertation/hempel\\_diss.pdf](https://quantumoptics.at/images/publications/dissertation/hempel_diss.pdf).

- 
- [64] E. J. Salumbides, et al., Phys. Rev. A **83**, 012502 (2011), URL <https://link.aps.org/doi/10.1103/PhysRevA.83.012502>.
- [65] W. Paul, Rev. Mod. Phys. **62**, 531 (1990), URL <https://link.aps.org/doi/10.1103/RevModPhys.62.531>.
- [66] R. F. Wuerker, et al., Journal of Applied Physics **30**, 342 (1959), URL <https://doi.org/10.1063/1.1735165>.
- [67] D. J. Wineland, et al., Journal of research of the National Institute of Standards and Technology **103**, 259 (1998), URL <https://www.ncbi.nlm.nih.gov/pmc/PMC4898965/>.
- [68] D. Leibfried, et al., Rev. Mod. Phys. **75**, 281 (2003), URL <https://link.aps.org/doi/10.1103/RevModPhys.75.281>.
- [69] R. J. Cook, et al., Phys. Rev. A **31**, 564 (1985), URL <https://link.aps.org/doi/10.1103/PhysRevA.31.564>.
- [70] M. Combescure, Annales de l'I.H.P. Physique théorique **44**, 293 (1986), URL <http://eudml.org/doc/76320>.
- [71] L. S. Brown, Phys. Rev. Lett. **66**, 527 (1991), URL <https://link.aps.org/doi/10.1103/PhysRevLett.66.527>.
- [72] D. James, Applied Physics B **66**, 181 (1998), URL <https://doi.org/10.1007/s003400050373>.
- [73] I. Buluta and F. Nori, Science **326**, 108 (2009), URL <http://science.sciencemag.org/content/326/5949/108>.
- [74] H. F. Trotter, Proc. Amer. Math. Soc. **10**, 545 (1959), URL <https://doi.org/10.2307/2033649>.
- [75] S. Lloyd, Science **273**, 1073 (1996), URL <http://science.sciencemag.org/content/273/5278/1073>.
- [76] K. R. Brown, et al., Npj Quantum Information **2**, 16034 (2016), URL <https://doi.org/10.1038/npjqi.2016.34>.
- [77] C. G. Almudever, et al., in *13th International Conference on Design Technology of Integrated Systems In Nanoscale Era (DTIS)* (2018), pp. 1–1, URL <https://ieeexplore.ieee.org/document/8368579>.

- [78] P. Jurcevic, et al., Phys. Rev. Lett. **119**, 080501 (2017), URL <https://link.aps.org/doi/10.1103/PhysRevLett.119.080501>.
- [79] P. J. J. O'Malley, et al., Phys. Rev. X **6**, 031007 (2016), URL <https://link.aps.org/doi/10.1103/PhysRevX.6.031007>.
- [80] A. Peruzzo, et al., Nature Communications **5**, 4213 (2014), URL <https://doi.org/10.1038/ncomms5213>.
- [81] C. Cohen-Tannoudji, et al., *Quantum Mechanics, Volume 2* (Wiley VCH, 1991), ISBN 0471164356.
- [82] G. Kirchmair, Ph.D. thesis, Leopold-Franzens University Innsbruck (2010), URL [https://quantumoptics.at/images/publications/dissertation/kirchmair\\_diss.pdf](https://quantumoptics.at/images/publications/dissertation/kirchmair_diss.pdf).
- [83] C. Cohen-Tannoudji, et al., *Quantum Mechanics, Volume 1* (Wiley VCH, 1991), ISBN 0471164356.
- [84] R. Loudon, *The Quantum Theory of Light* (Oxford University Press, 2000), ISBN 0198501765.
- [85] I. V. Hertel and C.-P. Schulz, *Optical Bloch Equations. In: Atoms, Molecules and Optical Physics 2* (Springer, Berlin, Heidelberg, 2015), ISBN 978-3-642-54313-5, URL [https://doi.org/10.1007/978-3-642-54313-5\\_10](https://doi.org/10.1007/978-3-642-54313-5_10).
- [86] D. James, Fortschritte der Physik **48**, 823 (2000), URL [https://doi.org/10.1002/1521-3978\(200009\)48:9/11<823::AID-PROP823>3.0.CO;2-M](https://doi.org/10.1002/1521-3978(200009)48:9/11<823::AID-PROP823>3.0.CO;2-M).
- [87] P. Jurcevic, Ph.D. thesis, Leopold-Franzens University Innsbruck (2017), URL [https://quantumoptics.at/images/publications/dissertation/Jurcevic\\_Dissertation.pdf](https://quantumoptics.at/images/publications/dissertation/Jurcevic_Dissertation.pdf).
- [88] S. Stenholm, Rev. Mod. Phys. **58**, 699 (1986), URL <https://link.aps.org/doi/10.1103/RevModPhys.58.699>.
- [89] J. Eschner, et al., J. Opt. Soc. Am. B **20**, 1003 (2003), URL <http://josab.osa.org/abstract.cfm?URI=josab-20-5-1003>.
- [90] K. Kim, et al., New Journal of Physics **13**, 105003 (2011), URL <https://iopscience.iop.org/article/10.1088/1367-2630/13/10/105003>.

- 
- [91] S.-B. Zheng, Phys. Rev. A **58**, 761 (1998), URL <https://link.aps.org/doi/10.1103/PhysRevA.58.761>.
- [92] C. Hempel, et al., Nature Photonics **7**, 630 (2013), URL <https://doi.org/10.1038/nphoton.2013.172>.
- [93] C. F. Roos, New Journal of Physics **10**, 013002 (2008), URL <https://iopscience.iop.org/article/10.1088/1367-2630/10/1/013002>.
- [94] P. Jurcevic, et al., Phys. Rev. Lett. **115**, 100501 (2015), URL <https://link.aps.org/doi/10.1103/PhysRevLett.115.100501>.
- [95] K. Kim, et al., Phys. Rev. Lett. **103**, 120502 (2009), URL <https://link.aps.org/doi/10.1103/PhysRevLett.103.120502>.
- [96] D. Porras and J. I. Cirac, Phys. Rev. Lett. **92**, 207901 (2004), URL <https://link.aps.org/doi/10.1103/PhysRevLett.92.207901>.
- [97] P. Nevado and D. Porras, Phys. Rev. A **93**, 013625 (2016), URL <https://link.aps.org/doi/10.1103/PhysRevA.93.013625>.
- [98] A. Kaplan, et al., Phys. Rev. A **66**, 045401 (2002), URL <https://link.aps.org/doi/10.1103/PhysRevA.66.045401>.
- [99] G. Kirchmair, Master's thesis, Leopold-Franzens University Innsbruck (2006), URL [https://quantumoptics.at/images/publications/diploma/diplom\\_kirchmair.pdf](https://quantumoptics.at/images/publications/diploma/diplom_kirchmair.pdf).
- [100] J. Benhelm, Ph.D. thesis, Leopold-Franzens University Innsbruck (2008), URL [https://quantumoptics.at/images/publications/dissertation/benhelm\\_diss.pdf](https://quantumoptics.at/images/publications/dissertation/benhelm_diss.pdf).
- [101] F. Zähringer, Ph.D. thesis, Leopold-Franzens University Innsbruck (2012), URL [https://quantumoptics.at/images/publications/dissertation/zaehringer\\_diss.pdf](https://quantumoptics.at/images/publications/dissertation/zaehringer_diss.pdf).
- [102] S. T. Gulde, Ph.D. thesis, Leopold-Franzens University Innsbruck (2003), URL [https://quantumoptics.at/images/publications/dissertation/gulde\\_diss.pdf](https://quantumoptics.at/images/publications/dissertation/gulde_diss.pdf).
- [103] L. Perntaler, Master thesis in preparation during the writing of this work., URL <https://quantumoptics.at/en/publications/master-diploma-theses.html>.

- [104] T. Brydges, et al., *Science* **364**, 260 (2019), URL <https://science.sciencemag.org/content/364/6437/260>.
- [105] M. K. Joshi, et al., *New Journal of Physics* **22**, 103013 (2020), URL <https://iopscience.iop.org/article/10.1088/1367-2630/abb912>.
- [106] I. E. Linington and N. V. Vitanov, *Phys. Rev. A* **77**, 010302 (2008), URL <https://link.aps.org/doi/10.1103/PhysRevA.77.010302>.
- [107] R. Lechner, Ph.D. thesis, Leopold-Franzens University Innsbruck (2016), URL [https://quantumoptics.at/images/publications/dissertation/lechner\\_diss.pdf](https://quantumoptics.at/images/publications/dissertation/lechner_diss.pdf).
- [108] G. Morigi, et al., *Phys. Rev. Lett.* **85**, 4458 (2000), URL <https://link.aps.org/doi/10.1103/PhysRevLett.85.4458>.
- [109] R. Lechner, et al., *Phys. Rev. A* **93**, 053401 (2016), URL <https://link.aps.org/doi/10.1103/PhysRevA.93.053401>.
- [110] D. J. Wineland, et al., *J. Opt. Soc. Am. B* **9**, 32 (1992), URL <http://josab.osa.org/abstract.cfm?URI=josab-9-1-32>.
- [111] J. I. Cirac, et al., *Phys. Rev. Lett.* **70**, 556 (1993), URL <https://link.aps.org/doi/10.1103/PhysRevLett.70.556>.
- [112] G. Birkel, et al., *Europhysics Letters (EPL)* **27**, 197 (1994), URL <https://iopscience.iop.org/article/10.1209/0295-5075/27/3/005>.
- [113] A. Fabre, Master's thesis, Leopold-Franzens University Innsbruck and École Polytechnique (2018).
- [114] G. Morigi, *Phys. Rev. A* **67**, 033402 (2003), URL <https://link.aps.org/doi/10.1103/PhysRevA.67.033402>.
- [115] T. Baumgratz, et al., *New Journal of Physics* **15**, 125004 (2013), URL <https://iopscience.iop.org/article/10.1088/1367-2630/15/12/125004>.
- [116] P. Jurcevic, et al., *Nature* **511**, 202 (2014), URL <http://www.nature.com/doi/10.1038/nature13461>.
- [117] P. Hauke and L. Tagliacozzo, *Phys. Rev. Lett.* **111**, 207202 (2013), URL <https://link.aps.org/doi/10.1103/PhysRevLett.111.207202>.

- 
- [118] E. H. Lieb and D. W. Robinson, *Comm. Math. Phys.* **28**, 251 (1972), URL <https://projecteuclid.org:443/euclid.cmp/1103858407>.
- [119] B. Nachtergaele and R. Sims, in *IAMP News Bulletin* (2010), pp. 22–29, URL <http://arxiv.org/abs/1102.0835>.
- [120] M. Cheneau, et al., *Nature* **481**, 484 (2012), URL <https://doi.org/10.1038/nature10748>.
- [121] F. G. S. L. Brandão and M. Horodecki, *Nature Physics* **9**, 721 (2013), URL <https://doi.org/10.1038/nphys2747>.
- [122] F. G. S. L. Brandão and M. Horodecki, *Communications in Mathematical Physics* **333**, 761 (2015), URL <https://doi.org/10.1007/s00220-014-2213-8>.
- [123] B. P. Lanyon, et al., *Nature Physics* **13**, 1158 (2017), URL <http://dx.doi.org/10.1038/nphys4244>.
- [124] N. Friis, et al., *Phys. Rev. X* **8**, 021012 (2018), URL <https://link.aps.org/doi/10.1103/PhysRevX.8.021012>.
- [125] C. H. Bennett, et al., *Phys. Rev. A* **53**, 2046 (1996), URL <https://link.aps.org/doi/10.1103/PhysRevA.53.2046>.
- [126] M. B. Plenio, *Phys. Rev. Lett.* **95**, 090503 (2005), URL <https://link.aps.org/doi/10.1103/PhysRevLett.95.090503>.
- [127] C. Sabín and G. García-Alcaine, *The European Physical Journal D* **48**, 435 (2008), URL <http://dx.doi.org/10.1140/epjd/e2008-00112-5>.
- [128] C. Lancien, et al., *Journal of Physics A: Mathematical and Theoretical* **48**, 505302 (2015), URL <https://iopscience.iop.org/article/10.1088/1751-8113/48/50/505302>.
- [129] B. Jungnitsch, et al., *Phys. Rev. Lett.* **106**, 190502 (2011), URL <https://link.aps.org/doi/10.1103/PhysRevLett.106.190502>.
- [130] M. Hofmann, et al., *Journal of Physics A: Mathematical and Theoretical* **47**, 155301 (2014), URL <https://iopscience.iop.org/article/10.1088/1751-8113/47/15/155301>.
- [131] H. Häffner, et al., *Nature* **438**, 643 (2005), URL <https://doi.org/10.1038/nature04279>.

- [132] U. Schollwöck, *Annals of Physics* **326**, 96 (2011), january 2011 Special Issue, URL <http://www.sciencedirect.com/science/article/pii/S0003491610001752>.
- [133] E. T. Jayne, *Probability Theory: The Logic of Science* (Cambridge University Press, 2003), ISBN 0-511-06589-2.
- [134] I. H. Kim, *On the informational completeness of local observables* (2014), [arXiv:1405.0137](https://arxiv.org/abs/1405.0137), URL <http://arXiv.org/abs/1405.0137v1>.
- [135] G. S. Engel, et al., *Nature* **446**, 782 (2007), URL <http://dx.doi.org/10.1038/nature05678>.
- [136] H. Lee, et al., *Science* **316**, 1462 (2007), URL <http://science.sciencemag.org/content/316/5830/1462>.
- [137] F. Caruso, et al., *The Journal of Chemical Physics* **131**, 105106 (2009), URL <https://aip.scitation.org/doi/abs/10.1063/1.3223548>.
- [138] S. Huelga and M. Plenio, *Contemporary Physics* **54**, 181 (2013), URL <https://doi.org/10.1080/00405000.2013.829687>.
- [139] N. Lambert, et al., *Nature Physics* **9**, 10 (2013), URL <http://dx.doi.org/10.1038/nphys2474>.
- [140] F. Fassioi, et al., *Journal of The Royal Society Interface* **11**, 20130901 (2014), URL <http://rsif.royalsocietypublishing.org/content/11/92/20130901>.
- [141] P. W. Anderson, *Phys. Rev.* **109**, 1492 (1958), URL <https://link.aps.org/doi/10.1103/PhysRev.109.1492>.
- [142] P. W. Anderson, *Rev. Mod. Phys.* **50**, 191 (1978), URL <https://link.aps.org/doi/10.1103/RevModPhys.50.191>.
- [143] P. Rebentrost, et al., *New Journal of Physics* **11**, 033003 (2009), URL <https://iopscience.iop.org/article/10.1088/1367-2630/11/3/033003>.
- [144] S. Mostame, et al., *New Journal of Physics* **14**, 105013 (2012), URL <http://stacks.iop.org/1367-2630/14/i=10/a=105013>.
- [145] S. Viciani, et al., *Phys. Rev. Lett.* **115**, 083601 (2015), URL <https://link.aps.org/doi/10.1103/PhysRevLett.115.083601>.

- [146] D. N. Biggerstaff, et al., Nature Communications **7**, 11282 (2016), URL <http://dx.doi.org/10.1038/ncomms11282>.
- [147] R. d. J. León-Montiel, et al., Scientific Reports **5**, 17339 (2015), URL <http://dx.doi.org/10.1038/srep17339>.
- [148] A. Potočnik, et al., Nature Communications **9**, 904 (2018), URL <https://doi.org/10.1038/s41467-018-03312-x>.
- [149] D. J. Gorman, et al., Phys. Rev. X **8**, 011038 (2018), URL <https://link.aps.org/doi/10.1103/PhysRevX.8.011038>.
- [150] N. Trautmann and P. Hauke, Phys. Rev. A **97**, 023606 (2018), URL <https://link.aps.org/doi/10.1103/PhysRevA.97.023606>.
- [151] C. Maier, et al., Phys. Rev. Lett. **122**, 050501 (2019), URL <https://link.aps.org/doi/10.1103/PhysRevLett.122.050501>.
- [152] F. Rieke, et al., *Spikes: Exploring the Neural Code* (A Bradford Book - MIT Press, 1999), ISBN 9780262181747, URL <https://mitpress.mit.edu/books/spikes>.
- [153] S. Miller and D. Childers, *Probability and Random Processes* (Academic Press, New York, 2004), ISBN 978-0-12-172651-5, URL <https://doi.org/10.1016/B978-0-12-172651-5.X5000-3>.
- [154] Bootstrapping is a technique to assign measures of accuracy (e.g. variance) to sample data and relies on random sampling with replacement [193, 194]. In our experiment, a single data set is composed of  $L$  realizations with random disorder and noise. Step (1) of the bootstrapping is to sample  $L - 2$  realizations from our data set and compute the mean  $\bar{\eta}$ . Then step (1) is repeated  $B$  times to come up with estimates  $\bar{\eta}_1, \bar{\eta}_2, \dots, \bar{\eta}_B$ . Finally the standard deviation of all  $B$  estimates corresponds to the standard error of the data set.
- [155] G. S. Engel, Procedia Chemistry **3**, 222 (2011), 22nd Solvay Conference on Chemistry, URL <http://www.sciencedirect.com/science/article/pii/S1876619611000684>.
- [156] I. Kassal, et al., The Journal of Physical Chemistry Letters **4**, 362 (2013), URL <https://doi.org/10.1021/jz301872b>.

- [157] E. Romero, et al., *Nature Physics* **10**, 676 (2013), URL <http://dx.doi.org/10.1038/nphys3017>.
- [158] A. Chenu and G. D. Scholes, *Annual Review of Physical Chemistry* **66**, 69 (2015), URL <https://doi.org/10.1146/annurev-physchem-040214-121713>.
- [159] R. Huang, et al., *Nature Physics* **7**, 576 (2011), URL <http://dx.doi.org/10.1038/nphys1953>.
- [160] F. A. An, et al., *Nature Communications* **8** (2017), URL <https://doi.org/10.1038/s41467-017-00387-w>.
- [161] A. Schreiber, et al., *Phys. Rev. Lett.* **106**, 180403 (2011), URL <https://link.aps.org/doi/10.1103/PhysRevLett.106.180403>.
- [162] S. Gopalakrishnan, et al., *Phys. Rev. Lett.* **119**, 046601 (2017), URL <https://link.aps.org/doi/10.1103/PhysRevLett.119.046601>.
- [163] D. B. Percival, *Computing Science and Statistics* **24**, 534 (1992), URL <http://citeseerx.ist.psu.edu/viewdoc/summary?doi=10.1.1.52.4747>.
- [164] L. Levi, et al., *Nature Physics* **8**, 912 (2012), URL <http://dx.doi.org/10.1038/nphys2463>.
- [165] H. Yichen, et al., *Annalen der Physik* **529**, 1600318 (2016), URL <https://onlinelibrary.wiley.com/doi/abs/10.1002/andp.201600318>.
- [166] C.-J. Lin and O. I. Motrunich, *Phys. Rev. B* **97**, 144304 (2018), URL <https://link.aps.org/doi/10.1103/PhysRevB.97.144304>.
- [167] M. Fu, et al., in *Proceedings - Winter Simulation Conference* (2008), pp. 27–38, URL <https://ieeexplore.ieee.org/document/4736053>.
- [168] A. Aspuru-Guzik, et al., *Science* **309**, 1704 (2005), URL <https://science.sciencemag.org/content/309/5741/1704>.
- [169] M. Reiher, et al., *Proceedings of the National Academy of Sciences* **114**, 7555 (2017), URL <https://www.pnas.org/content/114/29/7555>.
- [170] Y. Wang, et al., *ACS Nano* **9**, 7769 (2015), URL <https://doi.org/10.1021/acsnano.5b01651>.

- [171] Y. Shen, et al., Phys. Rev. A **95**, 020501 (2017), URL <https://link.aps.org/doi/10.1103/PhysRevA.95.020501>.
- [172] J. I. Colless, et al., Phys. Rev. X **8**, 011021 (2018), URL <https://link.aps.org/doi/10.1103/PhysRevX.8.011021>.
- [173] T. Helgaker, et al., *Second Quantization* (John Wiley & Sons, Ltd, 2014), chap. 1, pp. 1–33, ISBN 9781119019572, URL <https://onlinelibrary.wiley.com/doi/abs/10.1002/9781119019572.ch1>.
- [174] P. Jordan and E. P. Wigner, *Über das Paulische Äquivalenzverbot* (Springer Berlin Heidelberg, 1993), pp. 109–129, ISBN 978-3-662-02781-3, URL [https://doi.org/10.1007/978-3-662-02781-3\\_9](https://doi.org/10.1007/978-3-662-02781-3_9).
- [175] S. B. Bravyi and A. Y. Kitaev, Annals of Physics **298**, 210 (2002), URL <http://www.sciencedirect.com/science/article/pii/S0003491602962548>.
- [176] A. Tranter, et al., International Journal of Quantum Chemistry **115**, 1431 (2015), URL <https://onlinelibrary.wiley.com/doi/abs/10.1002/qua.24969>.
- [177] A. Tranter, et al., Journal of chemical theory and computation **14**, 5617 (2018), URL <https://www.ncbi.nlm.nih.gov/pmc/articles/PMC6236472/>.
- [178] T. Helgaker, et al., *Molecular Electronic-Structure Theory* (Wiley, 2002), ISBN 978-1-118-53147-1.
- [179] J. A. Nelder and R. Mead, The Computer Journal **7**, 308 (1965), URL <https://doi.org/10.1093/comjnl/7.4.308>.
- [180] K. E. Vugrin, Ph.D. thesis, Virginia Polytechnic Institute and University (2005), URL <http://hdl.handle.net/10919/27515>.
- [181] C. E. Rasmussen and C. K. I. Williams, *Gaussian Processes for Machine Learning* (MIT Press, 2006), ISBN 0-262-18253-X, URL <http://www.gaussianprocess.org/gpml/chapters/RW.pdf>.
- [182] M. Otten and S. K. Gray, npj Quantum Information **5**, 11 (2019), URL <https://doi.org/10.1038/s41534-019-0125-3>.
- [183] R. Babbush, et al., Phys. Rev. X **8**, 011044 (2018), URL <https://link.aps.org/doi/10.1103/PhysRevX.8.011044>.

- 
- [184] E. A. Martinez, et al., *Nature* **534**, 516 (2016), URL <https://doi.org/10.1038/nature18318>.
- [185] J. Schwinger, *Phys. Rev.* **128**, 2425 (1962), URL <https://link.aps.org/doi/10.1103/PhysRev.128.2425>.
- [186] C. Hamer, et al., *Nuclear Physics B* **208**, 413 (1982), URL <http://www.sciencedirect.com/science/article/pii/0550321382902292>.
- [187] D. R. Jones, et al., *Journal of Optimization Theory and Applications* **79**, 157 (1993), URL <https://doi.org/10.1007/BF00941892>.
- [188] H. Liu, et al., *Engineering Optimization* **47**, 1441 (2015), URL <https://doi.org/10.1080/0305215X.2014.971777>.
- [189] T. M. R. Byrnes, et al., *Phys. Rev. D* **66**, 013002 (2002), URL <https://link.aps.org/doi/10.1103/PhysRevD.66.013002>.
- [190] M. Guggemos, Ph.D. thesis, Leopold-Franzens University Innsbruck (2017), URL [https://quantumoptics.at/images/publications/dissertation/2017\\_guggemos\\_diss.pdf](https://quantumoptics.at/images/publications/dissertation/2017_guggemos_diss.pdf).
- [191] C. D. Sherrill, *An Introduction to Hartree-Fock Molecular Orbital Theory*, School of Chemistry and Biochemistry, Georgia Institute of Technology (2000), URL <http://vergil.chemistry.gatech.edu/notes/hf-intro/hf-intro.pdf>.
- [192] M. Müller, et al., *New Journal of Physics* **13**, 085007 (2011), URL <https://iopscience.iop.org/article/10.1088/1367-2630/13/8/085007>.
- [193] R. W. Johnson, *Teaching Statistics* **23**, 49 (2001), URL <https://onlinelibrary.wiley.com/doi/abs/10.1111/1467-9639.00050>.
- [194] B. Efron, *The Annals of Statistics* **7**, 1 (1979), URL <https://projecteuclid.org/euclid.aos/1176344552>.